

STENT DESIGN AND ARTERIAL MECHANICS:
PARAMETERIZATION TOOLS USING THE FINITE ELEMENT METHOD

A Thesis

by

JOSE JULIAN BEDOYA CERVERA

Submitted to the Office of Graduate Studies of
Texas A&M University
in partial fulfillment of the requirements for the degree of

MASTER OF SCIENCE

May 2006

Major Subject: Biomedical Engineering

STENT DESIGN AND ARTERIAL MECHANICS:
PARAMETERIZATION TOOLS USING THE FINITE ELEMENT METHOD

A Thesis

by

JOSE JULIAN BEDOYA CERVERA

Submitted to the Office of Graduate Studies of
Texas A&M University
in partial fulfillment of the requirements for the degree of

MASTER OF SCIENCE

Approved by:

Chair of Committee, James E. Moore Jr.

Committee Members, John C. Criscione

Matthew W. Miller

Head of Department, Gerard L. Cote

May 2006

Major Subject: Biomedical Engineering

ABSTRACT

Stent Design and Arterial Mechanics:

Parameterization Tools Using the Finite Element Method. (May 2006)

Jose Julian Bedoya Cervera, B.S., Florida International University

Chair of Advisory Committee: Dr. James E. Moore Jr.

Vascular stents are medical devices used to treat stenoses – blockages in arteries that restrict blood flow. Most commonly, stents are made out of stainless steel or nitinol, and are delivered to the afflicted sites via catheter-based delivery systems. Usually, stents are balloon-expandable or self-expanding. In order for the treated vessel to remain patent, it is necessary that the stents be oversized to prevent flow-induced or pressure-induced stent migration. Furthermore, stents must be rigid enough to prevent the collapse of the vessel, allowing the free passage of blood. However, it has been observed that the presence of the stent in the artery triggers adverse biological responses such as neointimal hyperplasia, often times culminating in restenosis. Extensive research external to this investigation has elucidated evidence to suggest that the abnormally high stresses imparted to the arterial wall as a result of stenting are an important factor in the treatment and development of cardiovascular diseases. Furthermore, normal physiologic diameter fluctuations between systole and diastole produce beneficial biological responses in the artery wall. The primary purpose of this study was to investigate specific stent design criteria that minimize the stress field in the arterial wall to mitigate the impact of restenosis. Commercially available finite element software was used to design the stents

parametrically, and perform the stress analysis on a hyperelastic arterial model, including the effects of contact between the artery and stent. Seven stent geometries were uniquely defined by varying strut-spacing, ring amplitude, and crown radii of curvature. Stent designs with large strut spacing, large ring amplitude and a greater than zero radius of curvature imparted the less severe stress field in the arterial wall as well as maximizing vessel deflection between systole and diastole. In contrast, stents with small strut spacing, small amplitudes and zero radius of curvature at the crowns imparted significantly higher stresses. The small strut spacing and small amplitude created stiffer stents, preventing the artery from experiencing physiologic diameter fluctuations between systole and diastole. Evidence presented herein suggests that strut spacing should be as wide as possible without causing pillowing of the arterial wall into the stent.

To my wonderful family. Without them, all is meaningless.

ACKNOWLEDGMENTS

It is a great honor to acknowledge publicly and in writing the people who have helped me in this journey. First and foremost my dear wife, Nathalia, my source of inspiration and confidence. Her endless and unceasing support have guided me through sometimes bewildering paths. My son, Daniel Felipe, while in the womb gave me the inspiration to believe in dreams, and now empowers me with the realization of those dreams and many more to come. I thank my parents, Michael and Gladis Bedoya; Nathalia's parents, Gustavo and Betty De La Hoz; Michael and Cindy Moreno; Jimmy and Peggy Moore, John and Margaret Criscione, and many other former graduate students with families, (i.e., "survivors") for all of their support, true empathy, points of view, and lessons learned.

It goes without saying that my mentor, Jimmy Moore, who entrusted me with the opportunity to attend graduate school and work for him, originally in Miami at Florida International University, and now here at Texas A&M University has proved to be more than simply a mentor, but also a valued friend. Frankly put, words of even great literary figures could not express my gratitude and friendship towards him. I am also indebted to Michael Moreno for all his good fatherly advice and patience throughout the years. I am very appreciative of John Criscione for his valuable time, patience, guidance and expert advice on constitutive models. I would also like to thank Dr. Miller for obtaining porcines from the Texas A&M University Vet School for the experiments. Additionally, thanks to Galen, Caleb and Dr. Nelson from the Vet School.

Finally, but certainly not least, I owe much of my sanity, experimental methods - and more! - to my lab mates, Clark Meyer, Shiva Yazdani, Luke Timmins, Joao Soares, Filippo Piffaretti, Matt Magnuson, John Nieves, Danny Acero, as all of them provided valuable insight, much needed help, and great friendships. Luciano Machado, thanks for your friendship, kind words and reminding me that things in the end will turn out ok. Quando o bicho pega e nao solta, lembre que "Deus e pai, ..." e voce ja sabe o resto.

TABLE OF CONTENTS

	Page
ABSTRACT	iii
ACKNOWLEDGMENTS.....	vi
TABLE OF CONTENTS	viii
LIST OF FIGURES.....	x
LIST OF TABLES	xiv
1. INTRODUCTION	1
2. CONSTITUTIVE LAWS.....	7
2.1 Fundamental Definitions –Kinematics	7
2.2 Strain	10
2.3 Stress	12
2.4 Assumptions in the Development of a Constitutive Model	15
3. EXPERIMENTAL METHODS.....	25
3.1 Need for Experimental Methods	25
3.2 Harvest of Porcine Carotids and Specimen Preparation	25
3.3 Computer Aided Vascular Experimentation (CAVE).....	27
3.4 Deformation Measurements	30
3.5 Data Acquisition System and Experimental Control	31
3.6 Experimental Data Analysis.....	41
4. THE FINITE ELEMENT METHOD AND ITS USE IN MSC PATRAN/MARC	47
4.1 Variational Principles in Mechanics	48
4.2 The Finite Element Method.....	49
4.3 Virtual Work Principle	50
4.4 Stationary Principle of Total Potential Energy	52
4.5 FEM Formulation and Implementation Using MSC.Patran and MSC.Marc.....	58
4.6 Numerical Integration Techniques	61
4.7 Treatment of Contact in MSC.Patran and MSC.Marc	62
4.8 Functional Forms for Strain Energy Density Functions in Patran and Marc.....	68
4.9 Nonlinear Solution Methods	70
4.10 Stented Artery Model Creation in MSC.Patran	72

	Page
4.11 Data Analysis Methods	84
4.12 Mesh Convergence and Mesh Convergence Criteria	87
4.13 General Effects of Stenting – Numerical Models	97
5. RESULTS.....	99
5.1 Assessment of Hoop Stresses on the Intima During Diastole.....	99
5.2 Assessment of Radial Stresses on the Intima During Diastole	111
5.3 Assessment of Maximum Principal Stresses on the Intima During Diastole.....	120
5.4 Assessment of Hoop Stresses on the Intima During Systole	122
5.5 Assessment of Radial Stresses on the Intima During Systole.....	130
5.6 Assessment of Hoop Stresses on the Adventitia During Systole	134
5.7 Assessment of RZ Shear Stresses on the Intima During Diastole.....	140
5.8 Assessment of Radial Displacements on the Intima During Diastole.....	143
6. SUMMARY	150
6.1 Interpretation of Results During Diastole at the Intima	151
6.2 Interpretation of Results During Systole at the Intima.....	157
6.3 Cyclical Deflection Results	159
6.4 Radial Displacement During Diastole at the Intima.....	162
7. LIMITATIONS, FUTURE DIRECTIONS AND CONCLUSIONS	165
7.1 Limitations	165
7.2 Future Directions.....	168
7.3 Conclusions	169
REFERENCES.....	171
APPENDIX A	177
APPENDIX B	210
VITA	244

LIST OF FIGURES

FIGURE	Page
3.1 Top view drawing of CAVE device without tubing and cables.....	28
3.2 Front view drawing of CAVE device without tubing and cables	29
3.3 Block diagram of control and feedback system of the re-designed CAVE device	32
3.4 Force calibration plot	33
3.5 Pressure calibration plot	34
3.6 Video dimension analyzer calibration plot.....	35
3.7 LVDT calibration plot.....	36
3.8 Preconditioning force-diameter data for porcine right common carotid.....	38
3.9 Preconditioning pressure-diameter data for porcine right common carotid.....	39
3.10 Experimental data for right common porcine carotid for all stretch ratios	40
3.11 Comparison of pressure predicted by manipulation of equation 3.1 and constants in table 3.3, and experimental pressure data.....	45
3.12 Comparison of experimental data and data predicted by manipulating equation 3.1 with constants in table 3.3	46
4.1 Illustration of a 20-noded hexahedral element.....	56
4.2 Illustration of friction model implemented in MSC.Patran and MSC.Marc....	64
4.3 Illustration of a NURBS surface in Patran	67
4.4 Illustration of the Newton-Rhapson method	71

FIGURE	Page
4.5	Solution procedure implemented in MSC.Marc 73
4.6	Quarter model of the artery modeled used to save computational resources and time 75
4.7	Generic stent showing the three parameters of interest..... 79
4.8	Stents analyzed in this study 81
4.9	Illustration of relative position of stent and artery after translate boundry condition 83
4.10	Graphical representation of the application of boundary conditions for this boundary value problem 83
4.11	Stress colormap result for stent 1B1 84
4.12	Illustration of modified stent lengths 86
4.13	Illustration of relative element lengths for mesh densities..... 91
4.14	Comparison of increasing mesh density between mesh “A” and mesh “B” 93
4.15	Class II critical hoop stress variation between “A” and mesh “B” for stent 1A1 94
4.16	Critical class I radial stress comparison for mesh “A” and mesh “B” 95
4.17	Differences observed between mesh “A” and mesh “B” for class II critical radial stresses for stent 1A1 96
4.18	Mesh refinement effect on radial displacement results for stent 1A1 at the intima during systole and diastole 97

FIGURE	Page
4.19 Impact of implanting a stent in an isotropic hyperelastic artery relative to displacements	98
5.1 Hoop stress plots of stent designs used in this study.....	101
5.2 Class III critical hoop stress threshold reveals stent 2A3 to have the lowest intimal area affected by class III hoop stresses.....	105
5.3 Binary class III critical hoop stress maps of stents at the intima during diastole	107
5.4 Critical hoop stress	108
5.5 Binary critical class II hoop stress maps at the intima during diastole	110
5.6 Radial stress components for stented artery models at the intima during diastole	112
5.7 Class I critical radial stress at the intima during diastole	115
5.8 Binary critical class I radial stress at the intima during diastole for stented artery models.....	117
5.9 Class II critical radial stresses reveal additional information about the stent designs	119
5.10 Binary critical class II radial stresses at the intima during diastole for stented artery models.....	121
5.11 Comparison of results obtained for the critical maximum principal stresses and the critical hoop stresses	124

FIGURE	Page
5.12 Comparison of class III critical hoop stresses at the intima during systole and diastole.....	126
5.13 A comparison in relative increase in incidence of class II critical hoop stresses when pressure is increased from diastole to systole	128
5.14 Class I critical radial stresses at the intima according to stent design during systole and diastole	132
5.15 Comparison of class II critical radial stresses at the intima according to stent design during systole and diastole	135
5.16 Summary of class I critical hoop stresses on the adventitia during systole for the stent designs conceived in this study	139
5.17 Class II critical hoop stresses on the adventitia during systole	141
5.18 RZ component of shear stress at the intima during diastole for all stents evaluated in this thesis.....	142
5.19 Displacement maps of all stents at the intima during diastole	145
5.20 Displacement plots of small spaced stents at intima during diastole and systole	149

LIST OF TABLES

TABLE	Page
3.1 Measurements of pig carotid used in CAVE devices at various configurations	26
3.2 Summary of calibration plot characteristics	37
3.3 Summary of constants obtained for equation 3.1	43
4.1 Summary of binary restenosis rates from Kastrati et al., 2001	77
4.2 Summary of stents studied in this thesis	80
4.3 Summary of the third phase of the stent-artery model mesh refinement study	90
4.4 Summary of mesh densities for each test stent	92
5.1 Critical hoop stress	103
5.2 Critical radial stress	114
5.3 Critical maximum principal stress	125
5.4 Summary of critical hoop stresses at the intima during systole for all stents analyzed in this thesis	128
5.5 Distribution of radial critical stresses according to stent design on the intima during systole	134
5.6 Summary of incidence of classes I, II and III critical hoop stresses on the adventitia during systole.....	137

1. INTRODUCTION

Cardiovascular diseases have been the number one killer in the United States since the year 1900 –except for year 1918. In 2001, 64,400,000 Americans, or 22.6% of the total population, suffered at least one type of cardiovascular disease. Mortality figures from that same year also reveal that of the total 2,400,000 deaths of all causes, cardiovascular diseases contributed to 1,408,000 or 58.6% of all deaths. The total cost associated with cardiovascular diseases in the year 2004 amounted to USD\$368.4 billion. More lives in the United States are claimed each year by cardiovascular diseases than the next five leading causes of death combined (American Heart Association, 2004).

Atherosclerosis is a progressive asymptomatic disease characterized by the narrowing and hardening of arteries that may result in eventual blockage causing ischemia to tissues and organs. While the risk factors for atherosclerosis are diffuse (use of tobacco products, hypercholesterolemia and high levels of other lipids, physical inactivity, obesity and diabetes mellitus), the disease strikes specific locations in the vasculature including arteries in the coronary, carotid, femoral, popliteal, renal and iliac circulation.

Forms of treatment for blocked coronary arteries include bypass surgery, angioplasty, and stenting. Bypass surgery performed in the heart consists of diverting the

blocked blood flow through an alternate path in order to replenish the heart muscle.

The shortcomings for this form of treatment include high degree of invasiveness to the patient, long hospital stays, very long recovery periods, and extremely high cost (American Heart Association, 2004). Angioplasty in the coronary arteries consists of making a small incision in the femoral artery and guiding a balloon catheter to the site of treatment. Once the catheter has been delivered to the proper site, it is expanded by a pressure of up to 15 atmospheres. This unblocks the artery by pushing the atheromatous plaque into the arterial wall. Unfortunately, the forced mechanical expansion of the lumen and the contact with the balloon catheter may cause damage to the artery. The endothelial denudation triggers a thrombotic response which leads to platelet adherence to the subendothelial surface, and contraction of the elastic fibers in the internal and external elastic laminae due to the mechanical damage may cause up to a 40% lumen loss (Woods and Marks, 2004). In a clinical setting, the physician is guided by the amount of acute gain achieved with no measurable indication whether injury has occurred – acute gain is defined as the relative increase in luminal diameter with reference to the diseased state immediately after the procedure (Kuntz et al., 1993). Moreover, weeks to months after the procedure, 40% of the patients treated once again developed a stenosis (appropriately termed “restenosis”) many times requiring repeat procedures (Fleisch and Meier, 1999). Despite its shortcomings, angioplasty is still considered an improvement relative to bypass surgery mainly due to its decreased invasiveness and cost.

A stent is characterized as being a tubular mesh used to prop open an occluded lumen. The stents may be expanded by the assistance of an angioplasty balloon catheter (316L stainless steel), or they may be self-expanding – hyperelastic Nitinol – (Duerig et al., 2000). Although there are many applications for stents (esophageal, biliary, etc.), in this thesis they pertain to a cardiovascular environment. The recent advent of stents in the cardiovascular realm began in 1969 by Dotter, whereby stents were conceived to improve the outcome angioplasty. In a one year clinical trial (Benestent); the outcome of patients receiving angioplasty alone and the Palmaz-Schatz stent were compared. The study consisted of 516 patients of which 259 underwent angioplasty and stenting and 257 underwent angioplasty alone. It was found that 40% of the patients that underwent angioplasty had the need to undergo repeat angioplasty due to restenosis. The stent group had a lower restenosis rate of 30% (Versaci et al., 1997). Currently it is generally recognized that stenting is an improvement to angioplasty in large vessels with short lesions (Mudra et al., 1997). However, patients with diabetes, complex coronary artery disease, and other complicating factors increase the risk of in-stent restenosis substantially (Woods and Marks, 2004).

To reduce the risk of in-stent restenosis even further, stents were being coated not just with passive (oxides), but also active surface coatings (platelet inhibiting agents). Passive coatings (gold, polylactic acid, etc.) were used with the idea to minimize surface defects, while active coatings (abciximab, heparin, etc.) were used to reduce the incidence of thrombotic events. The latter advancement in stent design reduced the incidence of acute thrombosis in model patients (Topol et al., 2002; Harrington et al.,

1995). Yet, despite the successful application of these agents, restenosis rates were only slightly lowered (Woods and Marks, 2004). Use of drug-eluting stents followed with drugs such as Sirolimus (i.e., Rapamycin), Everolimus, Tacrolimus and Paclitaxel being used to inhibit vascular smooth muscle cell proliferation. It was clinically obvious that there had been an improvement to being treated with drug-eluting stents rather than a bare metal stent. The RAVEL trial (Morice et al., 2002) showed binary restenosis rates of 26.6% for patients who received a bare metal stent (118), versus a 0% binary restenosis rate for patients receiving a Sirolimus eluting stent (120). Yet, there have been other trials such as the DELIVER trial – Paclitaxel – (Guidant Reports Preliminary Results of DELIVER Clinical Trial, 2003) reported an insignificant difference in restenosis rates between bare metal stents and drug-eluting stents – 21% and 16%, respectively. Moreover the SIRIUS trial (Moses et al., 2002) reported insignificant differences between in-stent restenosis at the edges of the stent.

Meanwhile, there have been efforts to model and design stents computationally, as it had already been recognized that stent design affects restenosis (Kastrati et al., 2001; Rogers and Edelman, 1995; Rogers et al., 1998). Linear elastic models by Rogers et al. (1998) modeled balloon expansion with stent and artery contact using a 2-dimensional model. Investigators such as Migliavacca and colleagues (Petrini et al., 2004; Migliavacca et al., 2002; Migliavacca et al., 2005) have focused mostly on the characterization of mechanical properties of stents. Prendergast and colleagues (Lally et al., 2005) modeled the stent-artery interaction of commercially available stents (NIR – Boston Scientific; S7 – Medtronic AVE) on an idealized stenosed artery. Furthermore,

they created a simplified restenosis algorithm that would simulate the process of neointimal hyperplasia and restenosis. Holzapfel et al. (2002) modeled the balloon expansion of a full 3-dimensional anisotropic diseased artery. In separate investigations, Holzapfel characterized anisotropic plaque properties (Holzapfel et al., 2004) and subsequently modeled a 3-dimensional stent-artery interaction with parameterized commercially available stents in a severely diseased iliac artery with 8 different vascular tissues. All the aforementioned computational studies have yielded useful information regarding the process of stenting. Nevertheless, none of the above studies have provided stent design criteria for future stent generations. Herein, we propose a new method to evaluate stents computationally, by parameterizing¹ original stent geometries reminiscent of commercially available stents in a non-diseased 3-dimensional model of the stent-artery interaction. Moreover, stent geometries will be uniquely defined by using three parameters which are: strut spacing – implicated in influencing platelet deposition (Robaina et al., 2003) – radius of curvature at the stent crowns, and amplitude (along the longitudinal axis of stents) of the corrugated sinusoid-like rings. Additionally, we have characterized the mechanical properties of a porcine common carotid artery with a hyperelastic isotropic constitutive model in order to evaluate how variations in geometric stent configurations will affect the stress fields imparted to the artery after stent deployment. Our aim is to elucidate stent design criteria by considering the effects of

¹ Holzapfel et al., 2005 also parameterized stent geometries. However, due to the high specificity inherent in utilizing diseased arterial geometries, it is not possible to generalize the impact of one stent to other morphologies. Furthermore, we are attempting to elucidate stent design criteria to design future stents, and in this process, we consider that by using a non-diseased artery, one is able to generalize to a greater extent how variations in geometric features present in stents will affect the host artery.

contact between the stent and the artery by minimizing the stresses imparted, and maximizing the cyclical stretch experienced by an artery between systole and diastole.

2. CONSTITUTIVE LAWS

The field of solid mechanics is the study of material (solid) response to applied loads and the quantification of these. In the cardiovascular system there is no exception to this premise. In order to study material response to applied loads, constitutive relations are needed. These relations describe how stress and strain are related. In order to arrive at this definition, more fundamental entities must be introduced.

2.1 Fundamental Definitions –Kinematics

The study of deformable kinematics entails the quantification of motion of bodies and their interior. In this pursuit, it is useful to characterize bodies of interest as a collection of particles (Humphrey, 2002). Furthermore, it is of interest to measure the positions of these particles and be able to compare their current positions to earlier reference positions. This approach is known as the Lagrangian approach where the independent variables (\mathbf{X}, t) represent particle location in the reference configuration and time, respectively. The Eulerian approach is also useful and the independent variables (\mathbf{x}, t) represent particle location in the current configuration and time, respectively (note that bold here indicates vectorial or tensorial variables). The relationship between the current and the reference configuration is described using the deformation gradient \mathbf{F} with the following definition in equation 2.1a:

$$d\mathbf{x} = \mathbf{F} \cdot d\mathbf{X} . \tag{2.1a}$$

Alternatively in index notation relative to a Cartesian coordinate system,

$$dx_{iA} = F_{iA} dX_A. \quad (2.1b)$$

Where subscripts i and A denote the basis vectors of the coordinate systems in which the current and reference configurations are respectively defined. From equations 2.1a and 2.1b it is evident that

$$\mathbf{F} = \frac{\partial \mathbf{x}}{\partial \mathbf{X}}. \quad (2.2)$$

The displacement vector is defined as the difference in position between the current and reference configuration, namely

$$\mathbf{u} = \mathbf{x} - \mathbf{X}. \quad (2.3)$$

Similarly, the displacement gradient tensors are defined as

$$\mathbf{H} = \frac{\partial \mathbf{u}}{\partial \mathbf{X}}, \quad (2.4)$$

$$\mathbf{h} = \frac{\partial \mathbf{u}}{\partial \mathbf{x}}, \quad (2.5)$$

and

$$\mathbf{F} = \mathbf{I} + \mathbf{H}, \quad (2.6)$$

$$\mathbf{F}^{-1} = \mathbf{I} - \mathbf{h}, \quad (2.7)$$

where equations 2.4 and 2.5 describe the Lagrangian and Eulerian displacement gradient tensors respectively. Moreover, \mathbf{F} may also be described by equations 2.6 and 2.7. It is of interest to mention that the deformation gradient is a transformation, or a mapping of the positions of particles in bodies between the current and reference configurations. The differential notation is used because particle positions of two particles, are connected by differential line segments (Humphrey, 2002). Moreover, rotations are also described by the deformation gradient since in general it cannot be assumed that particles in the reference configuration will retain the same orientation or magnitude in the current configuration (Humphrey, 2002).

A fundamental characteristic of a constitutive relation is that it is valid regardless of physical orientation of the material. The deformation gradient \mathbf{F} is a “two-point tensor” that depends on the physical orientation of the material; it is not symmetric, and may contain rigid body motion contributions undesirable to descriptions of strain (Humphrey, 2002). In order to overcome these difficulties, the development of constitutive models is done using one-point symmetric tensors free from rigid body motion. These are respectively the right and left Cauchy-Green Stretch tensors shown below

$$\mathbf{C} = \mathbf{F}^T \cdot \mathbf{F} \quad (2.8)$$

$$\hat{\mathbf{B}} = \mathbf{F} \cdot \mathbf{F}^T \quad (2.9)$$

where \mathbf{C} is defined in the reference configuration and $\hat{\mathbf{B}}$ is defined in the current configuration (see Humphrey, 2002 and Chadwick, 1976 for more details in continuum mechanics).

2.2 Strain

As mentioned above, strain quantities require descriptions independent of rigid body translation and rotation. There are several strain measures that possess this characteristic. Using equations 2.1a, 2.1b, 2.8, 2.9, the following expressions for Lagrangian and Eulerian strains respectively, are obtained:

$$\mathbf{E} = \frac{1}{2}(\mathbf{C} - \mathbf{I}) \quad (2.10)$$

$$\mathbf{e} = \frac{1}{2}(\mathbf{I} - \mathbf{B}^{-1}). \quad (2.11)$$

When pure rigid body motion occurs, the differential line segments in equations 2.1a and 2.1b are equal to one another and \mathbf{F} has a value of \mathbf{I} and therefore \mathbf{E} and \mathbf{e} describe only strains. After some manipulation and use of equations 2.4 – 2.7 the following strain representations are obtained:

$$\mathbf{E} = \frac{1}{2}(\mathbf{H} + \mathbf{H}^T + \mathbf{H}^T \cdot \mathbf{H}) \quad (2.12)$$

$$\mathbf{e} = \frac{1}{2}(\mathbf{h} + \mathbf{h}^T - \mathbf{h}^T \cdot \mathbf{h}). \quad (2.13)$$

In the case of small deformation theory, the quadratic terms of equations 2.12 and 2.13 are negligible in comparison to the linear terms (Humphrey, 2002; Slaughter, 2002). In the case of large deformation theory as is the case of vascular and soft tissue

mechanics, equations 2.12 and 2.13 are employed in their full form and later incorporated in constitutive relations.

In addition to mapping differential line segments from reference to current configurations, it is also desirable to have a relationship that describes the mapping of differential areas and differential volumes. These relationships are crucial in the development of constitutive relations for hyperelastic materials such as soft tissues. Using the scalar triple product of spatial differential lines in a body and the definition of the determinant we arrive at the relationship between reference and current differential volumes (Bowen, 1989) as paraphrased by (Humphrey, 2002). Namely,

$$dv = (\det \mathbf{F}) dV, \quad (2.14)$$

which after rearranging yields

$$\det \mathbf{F} = \frac{dv}{dV}. \quad (2.15)$$

The relationship describing mapping of differential areas is known as Nanson's relation and is expressed as

$$\mathbf{n} da = J \mathbf{N} dA \mathbf{F}^{-1} \quad (2.16)$$

where \mathbf{n} is the unit normal in the current configuration and \mathbf{N} is the unit normal in the reference configuration. Therefore a more accurate physical description of Nanson's relation is the mapping of *oriented* areas from two configurations (Humphrey, 2002; Slaughter, 2002).

2.3 Stress

Intrinsic to the definition of stress are the definitions of force, oriented areas and traction vectors. A traction vector is defined by equation 2.17

$$\mathbf{T}^{(n)} \equiv \lim_{\Delta a \rightarrow 0} \left(\frac{\Delta \mathbf{f}}{\Delta a} \right) = \frac{d\mathbf{f}}{da} \quad (2.17)$$

where lower case implies current configuration of geometries, and da is a differential area element with an outward unit normal described by \mathbf{n} .

Stress is defined as force acting over an oriented area and is characterized by two vectorial directions and thus it is a second order tensor. Furthermore, there are multiple measures of stress relating the different configurations of a body. Nanson's relation will be key in the development of these different stress measures.

2.3.1 True Stress –Cauchy Stress

In the development of a constitutive equation, it is necessary to carry out experiments applying loads and observing displacements. Ideally, the material being studied must be subjected to the same environment in which it will be evaluated. Cauchy stress \mathbf{t} is defined as the force in the current configuration acting over an oriented area also in the current configuration. It operates on the normal vector \mathbf{n} of area da by transforming its orientation into the traction vector acting on that area (Humphrey, 2002)

$$\mathbf{T}^{(n)} = \mathbf{t} \cdot \mathbf{n} . \quad (2.18)$$

2.3.2 Nominal Stress –First Piola-Kirchhoff Stress

It is a complex task in soft tissue mechanics to know what configuration a material will conform to when it is loaded and consequently measurements of current areas are very difficult to obtain (Humphrey, 2002). For this purpose, the First Piola-Kirchhoff, or nominal stress is quite useful. Using the same convention as used previously, lower case variables are used to represent quantities in the current configuration and upper case variables are used to represent quantities in the reference configuration. Nominal stress is defined as the current force applied over the reference oriented area. For this purpose a new traction vector in terms of the reference configuration needs to be defined as

$$\mathbf{T}^{(N)} = \frac{d\mathbf{f}}{dA} \quad (2.19)$$

and

$$\mathbf{T}^{(N)} = \mathbf{N} \cdot \mathbf{P} \quad (2.20)$$

where dA is the elemental area in the reference configuration and \mathbf{N} is the normal unit vector of dA .

The utility of this measure of stress is evident in the simpler task of measuring actual forces but calculating stress with respect to the reference configuration. The main drawback of this type of stress is that in general it is not symmetric and because it is defined with respect to two configurations, it is a two-point tensor. Therefore, the utility of this measure of stress ends after experimentation (Humphrey, 2002). For constitutive law formulation, there is a need to derive a measure of stress that is defined in the

reference configuration and is also symmetric. In order to achieve this, one must use the deformation gradient tensor and map the current force vector into a “reference” force vector (Humphrey, 2002).

2.3.3 Second Piola-Kirchhoff Stress

Using equation 2.1a and multiplying it by \mathbf{F}^{-1} on both sides, one finds the inverse relationship

$$d\mathbf{X} = \mathbf{F}^{-1} \cdot d\mathbf{x}. \quad (2.21)$$

Similarly, one may transform the current force vector defined in equations 2.17 and 2.19 as

$$d\tilde{\mathbf{f}} = \mathbf{F}^{-1} \cdot d\mathbf{f} \quad (2.22)$$

and therefore a new traction vector is defined as

$$\tilde{\mathbf{T}}^{(N)} = \frac{d\tilde{\mathbf{f}}}{dA} \quad (2.23)$$

and

$$\tilde{\mathbf{T}}^{(N)} = \mathbf{N} \cdot \mathbf{S}. \quad (2.24)$$

\mathbf{S} in 2.24 is known as the Second Piola-Kirchhoff stress tensor. Unlike nominal stress, \mathbf{S} is symmetric and a one point tensor defined in the reference configuration which proves to be convenient for constitutive modeling. The drawback however is that \mathbf{S} has no direct physical meaning in large deformation theory since it is defined in the reference configuration, which geometrically is substantially different from the current configuration (Humphrey, 2002). Lastly, using Nanson’s relation and manipulating

equations 2.18-2.24 one can find a relationship between the aforementioned stress measures. Namely,

$$\mathbf{t} = \left(\frac{1}{J}\right) \cdot (\mathbf{F} \cdot \mathbf{P}) \quad (2.25)$$

$$\mathbf{P} = \mathbf{S} \cdot \mathbf{F}^T \quad (2.26)$$

$$\mathbf{t} = \left(\frac{1}{J}\right) \cdot (\mathbf{F} \cdot \mathbf{S} \cdot \mathbf{F}^T). \quad (2.27)$$

In this study, the stress measure of interest is true or Cauchy stress. The reason for this is the fact that contact mechanics invokes a non-linear relationship between the applied force and the observed displacement in the current configuration. Namely, the force depends on the displacement and the displacement depends on the force. Therefore, an iterative solution satisfying equilibrium conditions is required. For more detail on these stress derivations and their applications, see chapter 3 in Humphrey 2002, and chapter 14 in Reddy, 1993.

2.4 Assumptions in the Development of a Constitutive Model

2.4.1 The Continuum Assumption

In the most fundamental sense, all matter is composed of discrete material quanta such as atoms, protein molecules, individual cells and so forth (Slaughter, 2002). It is central to the continuum hypothesis that this idea of discrete particles can be neglected when studying matter that its length scale is several orders of magnitude larger than these discrete constituents. For example, an artery may be assumed to be continuous if

one is interested in analyzing the material response of the tissue as a whole and not individual cells. In making this assumption, if an infinitesimal volume of matter were to be considered, it would always be surrounded by other particles. In addition to this premise, other physical quantities must also be represented by fields that are continuous or in the least piecewise continuous (Humphrey, 2002).

2.4.2 Constitutive Law Formulations

In the process of formulating a constitutive relation there are several principles of continuum mechanics that must be satisfied. These include conservation laws (mass, linear and angular momenta, energy) and the entropy inequality (Humphrey, 2002). These basic postulates help one formulate a constitutive relation by restricting the form of this relation into something that abides by these governing physical laws. In the case of conservation of mass, the total mass of a body must remain unchanged from one configuration to another. Specifically,

$$\int_{\Omega_0} \rho_0 dV = \int_{\Omega_0} \rho dv \quad (2.28)$$

where Ω denotes domain and subscript ‘o’ and upper case denotes reference configuration and no subscript and lower case denotes current configuration. Bringing the right-hand-side of equation 2.28 to the left-hand-side and using the relationship established in equations 2.14-2.16 integrated over the reference domain we arrive at

$$\int_{\Omega_0} (\rho_0 - \rho J) dV = 0 . \quad (2.29)$$

Recognizing that dV is arbitrary and valid for all domains,

$$J = \frac{\rho_0}{\rho}. \quad (2.30)$$

Similarly, the balance of linear momentum equation in a Lagrangian approach is given by the following:

$$\frac{d}{dt} \int_{\Omega_0} \rho_0 \mathbf{v} dV = \int_{\Omega_0} \rho_0 \mathbf{b} dV + \int_{\partial\Omega_0} \rho_0 \mathbf{T}^{(N)} dA \quad (2.31)$$

where \mathbf{v} is the velocity vector and \mathbf{b} is a vector representing body forces (Humphrey, 2002). Equation 2.31 can be simplified by applying the divergence theorem and using the first Piola-Kirchhoff stress equation and further realizing that dV in 2.31 is arbitrary, we arrive at

$$\operatorname{div} \mathbf{P} + \rho_0 \mathbf{b} = \rho_0 \mathbf{a} \quad (2.32)$$

where \mathbf{a} is the acceleration of the particles in Ω_0 . Analogous to 2.32 is

$$\operatorname{div} \mathbf{t} + \rho_0 \mathbf{b} = \rho_0 \mathbf{a}, \quad (2.33)$$

which is in terms of the true (Cauchy) stress tensor. The balance of angular momentum, or the applied moments are balanced with the moment of momentum of the body. In the Lagrangian approach,

$$\frac{d}{dt} \int_{\Omega_0} (\mathbf{x} \times \rho_0 \mathbf{v}) dV = \int_{\Omega_0} (\mathbf{x} \times \rho_0 \mathbf{b}) dV + \int_{\partial\Omega_0} (\mathbf{x} \times \mathbf{T}^{(N)}) dA. \quad (2.34)$$

After some manipulation and once again realizing that equation 2.34 must be valid in an arbitrary domain dV , yields the results in terms of the described measures of stress;

$$\mathbf{F} \cdot \mathbf{P} = \mathbf{P}^T \cdot \mathbf{F}^T \quad (2.35)$$

and

$$\mathbf{t} = \mathbf{t}^T, \quad (2.36)$$

and

$$\mathbf{S} = \mathbf{S}^T \quad (2.37)$$

The preceding results provide a restriction on the constitutive relation written in terms of first and second Piola-Kirchhoff stresses and Cauchy stresses, necessitating that the indicated symmetries must be respected (Humphrey, 2002).

The conservation of energy has the following form:

$$\rho_0 \frac{d\varepsilon}{dt} = \mathbf{P}^T : \frac{d\mathbf{F}}{dt} - \text{div } \mathbf{q} + \rho_0 g \quad (2.38)$$

where \mathbf{q} is the heat flux vector, the third term on the right is a volumetric heating term, \mathbf{P} is the first Piola-Kirchhoff stress tensor, and $d\varepsilon/dt$ is the change in internal energy with respect to time. Equation 2.38 plays no role in the development for a constitutive relation applied to an isothermal process such as the one in this thesis. However, the entropy inequality provides important information and restrictions on constitutive laws on processes that are isothermal as well as more general temperature dependent events (Humphrey, 2002). Namely,

$$-\rho_0 \left(\frac{d\psi}{dt} + \eta \frac{dT}{dt} \right) + \mathbf{P}^T : \frac{d\mathbf{F}}{dt} - \left(\frac{1}{T} \right) \mathbf{q} \cdot \mathbf{grad}(T) \geq 0 \quad (2.39)$$

where ψ is the Helmholtz potential related to internal energy by $\varepsilon = \psi + \eta T$, η is the entropy and T is absolute temperature. For an isothermal process with no heat transfer,

2.39 reduces to

$$\left(-\rho_0 \frac{d\psi}{dt} + \mathbf{P}^T \right) : \frac{d\mathbf{F}}{dt} \geq 0 \quad (2.40)$$

For a hyperelastic material, the inequality in 2.40 is replaced with an equality because hyperelastic implies that the material is elastic and therefore the process is reversible

$$\left(-\rho_0 \frac{d\psi}{dt} + \mathbf{P}^T\right) : \frac{d\mathbf{F}}{dt} = 0 \text{ for all } \mathbf{F}. \quad (2.41)$$

Soft tissues clearly exhibit hysteresis, creep and stress-relaxation. Therefore, making the assumption that the material behaves reversibly can be justified by first ensuring that the material is tested after 10-15 cycles of pressure-diameter, force-elongation in an observed physiologic load range (this procedure is known as preconditioning in the literature) prior to constitutive formulation. Creep and stress-relaxation phenomena can be neglected if a viscoelastic material is considered as two separate materials, one for loading and the other for unloading. In this study, only the loading characteristic of the material is considered, and therefore the viscoelastic nature of the material is neglected. Furthermore, in this thesis we are interested in only the deformation of the body and not its history of deformation. Additionally, by virtue of local action (see Humphrey, 2002, p.90 for more details) and the fact that time is deemed irrelevant in this study by not including viscoelastic effects, we conclude that $\psi = \psi(\mathbf{F})$ and $d\psi/dt = \partial\psi/\partial\mathbf{F} : \partial\mathbf{F}/\partial t$, therefore,

$$\left(-\rho_0 \frac{d\psi}{d\mathbf{F}} + \mathbf{P}^T\right) : \frac{d\mathbf{F}}{dt} = 0 \text{ for all } \mathbf{F}. \quad (2.42)$$

Noting that \mathbf{F} can be arbitrary, its time derivative is also arbitrary and therefore the term inside the parenthesis must vanish. This implies that the first Piola-Kirchhoff stress tensor is derivable from the Helmholtz potential (which for the current study, the stress is also derivable from a strain energy density function), and is restricted to the

relationship in 2.43 for a hyperelastic material. This is illustrated by the following relationships:

$$\mathbf{P}^T = \rho_0 \partial \psi \partial \mathbf{F}, \quad (2.43a)$$

or,

$$\mathbf{P} = \rho_0 \partial \psi \partial \mathbf{F}^T \quad (2.43b),$$

(Humphrey ,2002).

Finally, in an isothermal process the Helmholtz potential and the strain energy are related by

$$\rho_0 \psi(\mathbf{F}) = W(\mathbf{F}). \quad (2.44)$$

One limitation of 2.44 is invoked by the fact that \mathbf{F} is an asymmetric two-point tensor and therefore violates the material frame indifference assumption in developing a suitable constitutive relation. However, using the relationships in equations 2.8 and 2.9, one can arrive to a strain energy density function that is a function of either the right Cauchy-Green stretch tensor \mathbf{C} or the left Cauchy-Green stretch tensor $\hat{\mathbf{B}}$. These kinematic quantities are symmetric one-point tensors without rigid body motion and therefore can be used in a constitutive formulation. Using 2.43 and 2.44 we can express

$$\mathbf{P} = 2 \cdot \frac{\partial W}{\partial \mathbf{C}} \cdot \mathbf{F}^T \quad (2.45)$$

and

$$\mathbf{t} = \frac{2}{J} \cdot \mathbf{F} \cdot \frac{\partial W}{\partial \mathbf{C}} \cdot \mathbf{F}^T. \quad (2.46)$$

2.4.2.1 Incompressibility Constraint

Equations 2.45 and 2.46 are valid for unconstrained hyperelastic materials. However, experiments dating from 1954 (Lawton), 1968 (Carew et al), 1969 (Dobrin and Rovick) and 1984 (Chuong and Fung) have shown that arterial tissue behaves nearly isochorically when subjected to isothermal physiologic loading. These observations impose a kinematic restriction onto the constitutive relation in which $J = 1$. This constraint needs to be enforced in the constitutive relation. In this study, the Lagrange multiplier method is used to enforce this condition. This yields the following expressions for stress:

$$\mathbf{t} = -p\mathbf{I} + \frac{2}{J} \cdot \mathbf{F} \cdot \frac{\partial W}{\partial \mathbf{C}} \cdot \mathbf{F}^T \quad (2.47)$$

where p represents the Lagrange multiplier.

2.4.2.2 Homogeneity Assumption

It is obvious from histological observations of arteries that they are not materially homogeneous. The distribution of individual constituents such as elastin, collagen and smooth muscle cells does indeed vary with position in the artery. Experiments performed by Roach and Burton (1957) showed that elastin and collagen were the primary contributors to this nonlinear characteristic. Elastin is a highly extensible protein that resembles linear elastic behavior (constant slope) although with finite deformations. Collagen is much stiffer and is thought to prevent acute overdistension in arteries (Humphrey, paper, 2003). In many instances, arteries are assumed to be materially homogeneous. Such a claim was made by Clark and Glagov (1985) by stating that

although the individual constituents are not distributed homogeneously, they are distributed in some sense with regularity within the layers. In this study, the artery is assumed to be distributed homogeneously. This assumption is a valid in the realm of what is being investigated which is the response of the artery wall as a whole and not the response of individual constituents.

2.4.2.3 Residual Stresses

In the realm of solid mechanics, determination of stress relies on the idea that all quantities must be compared to a reference configuration. With this idea in mind, it is of paramount importance to be able to identify this reference configuration in arterial mechanics. However, residual stresses were not included in the constitutive formulation due to a limitation with MSC.Patran only being able to implement residual stresses as linear superposition and not the multiplicative decomposition that is generally accepted. Therefore the inclusion of residual stresses as a linear superposition in this scenario would be meaningless. The implications of this shortcoming are addressed in section 7.

2.4.3 Material Nonlinearities

Sources of nonlinearities in arterial mechanics stem from geometric nonlinearities, loading nonlinearities and material nonlinearities. Although they can be classified as such, in practice nonlinearities are not discernible from one another. In most mathematical and physical scenarios, these nonlinearities are not uncoupled and their

effects are difficult to describe independently. However, one can learn fundamental qualities from observation and experimentation.

In order to more accurately predict arterial response to applied loads, the nonlinear character of the stress strain relationship exhibited by arteries must be included. In this study, arteries are characterized by performing pressure-diameter, force-elongation tests. Suitable strain energy functions must abide by restrictions imposed by the theory of continuum mechanics as well as the increasingly monotonic and characteristic of the loading curve. Unlike plastic, rubber and many other material behaviors, soft tissues do not exhibit limit point instabilities. For this reason, the functional form of the strain energy density function must be selected with care. Many commercial finite element packages have built in strain energy density functions commonly used for incompressible materials such as rubber. However, many of these functional forms have inflection points which lead to these limit point instabilities or bifurcating loads. For this reason, a polynomial not exhibiting limit point instabilities under the conditions of interest as a strain energy density function was used. Equation 2.48 is a generic example of the strain energy function used in this thesis,

$$W = C_{10} \cdot (I_1 - 3) + C_{01} \cdot (I_2 - 3) + C_{11} \cdot (I_1 - 3) \cdot (I_2 - 3) + C_{20} \cdot (I_1 - 3)^2 + C_{30} \cdot (I_1 - 3)^3 \quad (2.48)$$

where W denotes strain energy per unit volume, C_{10} , C_{01} , C_{11} , C_{20} , and C_{30} are material parameters determined by experimentation, I_1 is the first invariant of the left Cauchy-Green stretch tensor, and I_2 is the second invariant of the same tensor.

Contact mechanics introduces loading nonlinearities due to contact itself as well as geometric nonlinearities whereby the stiffness of the material is a function of the displacement and vice versa. Our experimental set-up did not include measurements associated with contact mechanics.

2.4.4 Material Symmetry – Isotropy

Finite element models included in this study will be assumed to behave isotropically, implying that material behavior is the same independent of loading axis and direction. Histologic observations however, clearly indicate that arteries are very structurally organized, elucidating the fact that arteries are anisotropic (Humphrey, 2002). However, in this thesis the main goal is to compare different stent designs and to evaluate how the variation of geometric parameters affects the stress distribution in the arteries. It is assumed that the stent is many times stiffer than the artery. Furthermore, this is a comparative study whereby use of an isotropic constitutive behavior is useful in assessing the different stress fields imparted to the artery.

2.4.5 Arterial Wall as a Passive Material

In this thesis, the artery will be analyzed as a passive material. Namely, upon excision, arteries were immediately taken back to the laboratory where they were refrigerated with PBS solution and material property testing will take place. Details pertaining to the experiment will be discussed in section 3.

3. EXPERIMENTAL METHODS

3.1 Need for Experimental Methods

In any type of analysis, it is necessary to have a theoretical background along with experimental methodology. As Humphrey (2002) has mentioned “one does not make sense without the other”. The mechanical properties of arteries, as has been alluded to in section 2, behave in a highly complex nonlinear manner. Philosophically, it is necessary to test mechanical properties of materials in the same way as it is being simulated in the finite element method in order for there to be any relevance in the sought results. Towards this end, porcine carotid arteries were harvested and tested in a computer controlled multi-axial testing device originally developed by Humphrey et al. (1993) and modified for this thesis. Computer controlled experimentation can be a significant improvement over non-computer-control experimentation. Namely, human error is limited to programming and wiring. Computer aided vascular experimentation (CAVE) greatly enhances the experimental repeatability, limits human error, and provides a mean for more complex experimentation to occur (Humphrey, 2002).

3.2 Harvest of Porcine Carotids and Specimen Preparation

Porcine common carotids were harvested with the aid of the School of Veterinary Medicine at Texas A&M University, College Station, TX. Pigs 2 years of age with an estimated weight between 180-200 lbs were anesthetized and subsequently euthanized. These pigs had congenital ventricular septal defects (VSD's) where there was a shunt

between the right and left ventricle. It was confirmed through the Veterinary School at Texas A&M University that these pigs otherwise were normotensive. In this study, it was important to measure the in vivo configuration as precisely as possible in order to have a more accurate representation in the creation of finite element models. Prior to harvest, measurements of the in vivo length of the common carotid were made using a caliper. Measurements of the axial length after harvest were also taken to determine the in vivo axial stretch ratio (see table 3.1 for the actual measurements). The in vivo diameter could not be measured accurately due to the compliance of the tissue and rigidity of the caliper. Both left and right common carotids were excised. Once both common carotid arteries were harvested, they were placed in phosphored buffered saline solution inside an iced styrofoam cooler and transported back to the laboratory where arteries were refrigerated at 4 °C. The arteries were cleaned and the perivascular tissue was carefully removed taking care not to damage the adventitia, or to puncture the artery wall.

Table 3.1

Measurements of pig carotid used in the CAVE device at various configurations.

	Intimal Radius (mm)	Adventitial Radius (mm)	Axial Length (cm)	Axial Stretch
In Vivo Configuration	Not available	Not available	6.10	1.60
Unloaded Configuration	1.196	2.509	3.8	1.0

3.3 Computer Aided Vascular Experimentation (CAVE)

A custom designed electromechanical multi-axial material characterization device originally developed by Humphrey et al (1993) was modified to more current technology. The device is able to extend, inflate and twist simultaneously a cylindrical specimen while acquiring pertinent load and deformation data in real time. The system consists of three subsystems. The first system consists of the hardware making up the device, and is comprised of micro-step motors (Anaheim Automation, CA) and peristaltic pumps (Harvard Apparatus, Cole Parmer), driving 2 carriages mounted on a twin web shaft moving in opposite directions. The second and third systems included a non-contacting diameter measuring system consisting of a video dimension analyzer (VDA), and a control and data acquisition system (National Instruments).

Figure 3.1 is a top view of the CAVE system, taken from Humphrey et al., 1993. The hardware consists of a horizontally oriented low friction twin shaft web system (H) with end supports (R) and middle supports (not shown for clarity), on which two carriages (Q) connected by left and right hand ball screws, (B) are driven in opposing directions by a micro-stepper motor (G) (Anaheim Automation, CA). The ball screws are attached to the carriages using aluminum L-brackets and ball nuts, a wafer coupling (E), and oil-impregnated thrust bearings (A) at the ends for support. A linear differential variable transformer –LVDT- (D) is rigidly connected to the carriages measuring the distance between the carriages, and the axial deformation of the artery. A second stepper motor (P) is mounted on one of the carriages with an aluminum L-bracket to control the twisting of the cylindrical specimen (L). A pressure transducer (I), a tension-

compression force transducer (J), and a torque transducer (O) are also rigidly attached to the carriages. The center-line of the pressure transducer corresponds to that of the specimen eliminating the need to determine the effect of a hydrostatic pressure. Additionally, the tubing of the pressure transducer suffers no tension, compression or torsion when the specimen is stretched or relaxed since it is rigidly attached to one of the “moving” carriages.

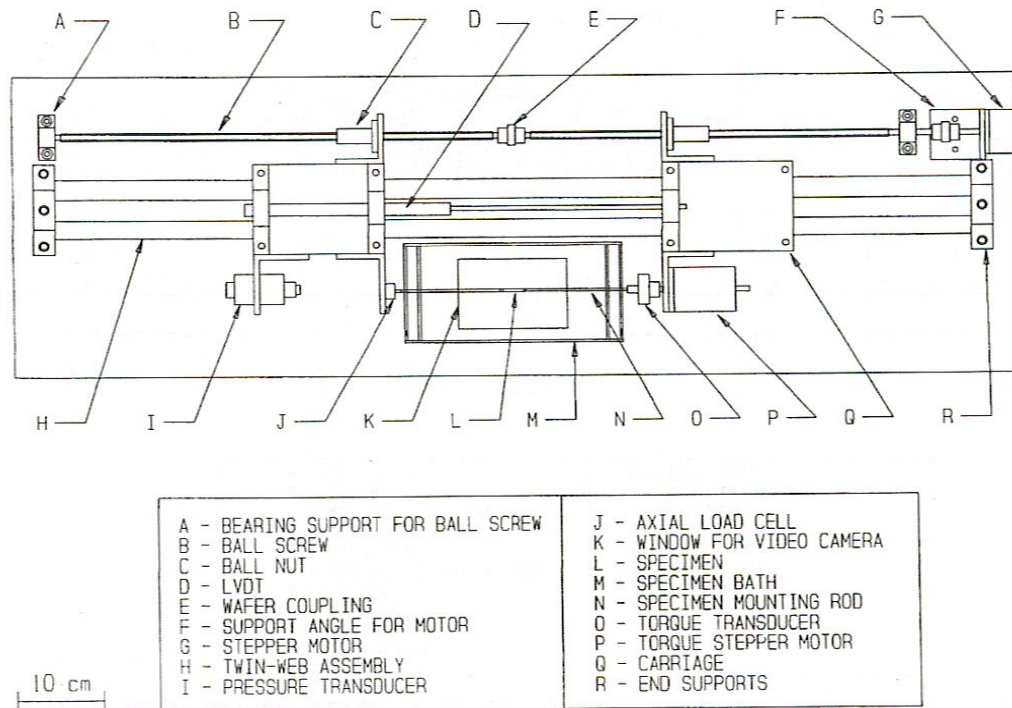


Fig. 3.1. Top view drawing of CAVE device without tubing and cables (Humphrey et al., 1993).

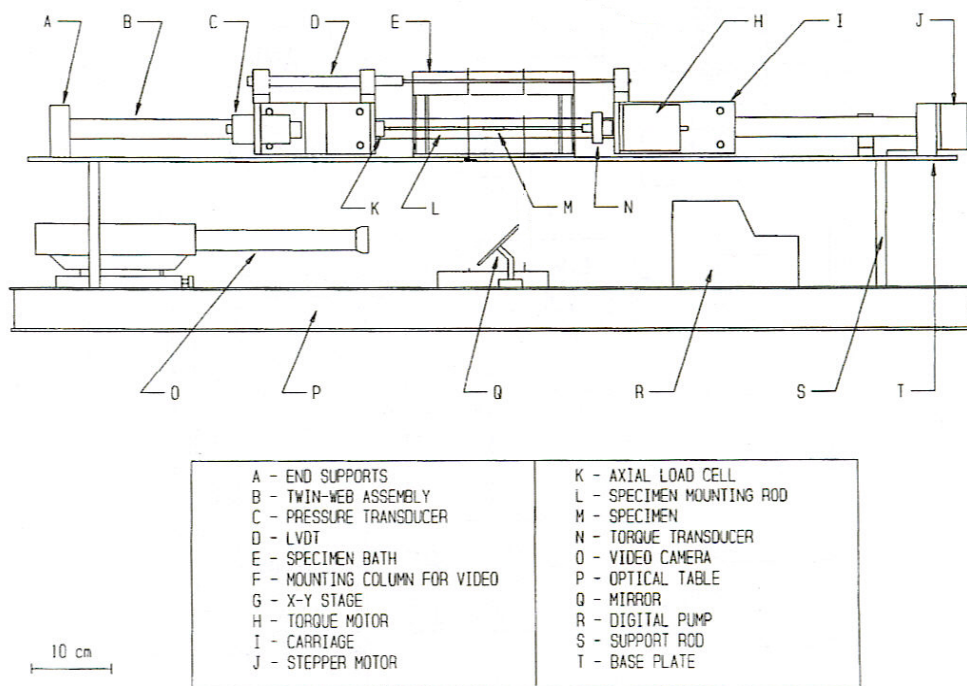


Fig. 3.2. Front view drawing of CAVE device without tubing and cables (Humphrey et al., 1993).

The specimen (L) is attached to the device using cylindrical Plexiglas mounting rods (N) and appropriately sized cannulae (not shown). The mounting rods are attached to the carriages through 1 mm clearance holes in the bath. The bath (M) has two chambers, and is circulated with a temperature controlled Phosphored Buffered Saline solution (PBS) using a heating pump (not shown). An outer chamber exists in the bath chamber (M) so that overflow PBS solution leaking through the mounting rods clearance holes is pumped back to the heating pump reservoir (not shown). All the sensors, optics,

and motor equipment are safeguarded from liquids to minimize corrosion with this circulating system.

In a front view of the CAVE system in figure 3.2, it can be appreciated that the system rests on top of an aluminum plate (T) with a cut out region measuring 9x15 cm where a CCD camera (O) and a 10 mm diameter optical mirror (Q) oriented at a 45°, capture the specimen (L) as the experiment takes place. The CCD camera along with a video dimension analyzer (VDA), track the diameter changes in real time. More details about the data acquisition system are explained in future sections. The aluminum plate is elevated 15 cm in height above an optical table (P) and supported with 16 support rods (S).

3.4 Deformation Measurements

Deformation of the diameter is measured in real time via the aforementioned CCD camera, a video dimension analyzer (VDA), a data acquisition system, a frame grabber board NI-1408 (National Instruments, TX), and a black and white monitor. The CCD camera outputs a signal to the VDA, which transmits the signal as an image to the monitor while also transmitting a voltage signal to the data acquisition system. The voltage signal from the VDA is linearly proportional to the deformation of the diameter while the experiment is taking place. The signal onto the black and white monitor is digitized into a pixel array where the white specimen (blood vessel) takes values of 255, while black values correspond to 0 (background). It is important that there is a good contrast between the specimen and the background in order to obtain adequate results.

The VDA detects this digital edge and tracks it as the vessel inflates and deflates. Custom software in LabView (National Instruments, Austin, TX) was written to do all the acquiring and processing of data in real time. The LVDT provided the change in displacement of the artery in the axial direction.

3.5 Data Acquisition System and Experimental Control

Unlike the original system in Humphrey et al. 1993, the current CAVE device uses only one computer to acquire and process the data, along with the aforementioned custom programmed graphical user interface in LabView. Analog signals from the load cells were transmitted to an amplifier and later to an A/D converter with a capacity of up to 16 channels at a combined sampling rate of 200ks/s and a 12-bit resolution on variable output ranges. In this study, 5 channels were used and the output range of the A/D converter was -5V to +5 V.

Accuracy of the load cells and the LVDT are 0.1 to 0.2%, and resolutions are 0.5g for the axial force transducer, 0.65 mmHg for the pressure transducer, 0.1 mm for the LVDT, and 0.02 mm for the VDA (Humphrey et al., 1993).

Inflation and extension of the specimen are induced by a Harvard Apparatus peristaltic pump (Mass), and an Anaheim Automation micro-stepper motor (Anaheim, CA). Although the aforementioned pump and motor are by hardware, designed to be open loop, they have the capability to be controlled in a closed loop format through software that transmits alphanumeric codes. The motor is controlled through a SMC40 indexer and a MBC10640 driver (Anaheim Automation, CA). The indexer card is

external to the computer, and communicates with the PC via a RS-232 serial port at 9600 baud. The Harvard Apparatus pump has its own microprocessor, and it communicates through a serial port also at a rate of 9600 baud. Figure 3.3 is a block diagram describing the control of the CAVE device.

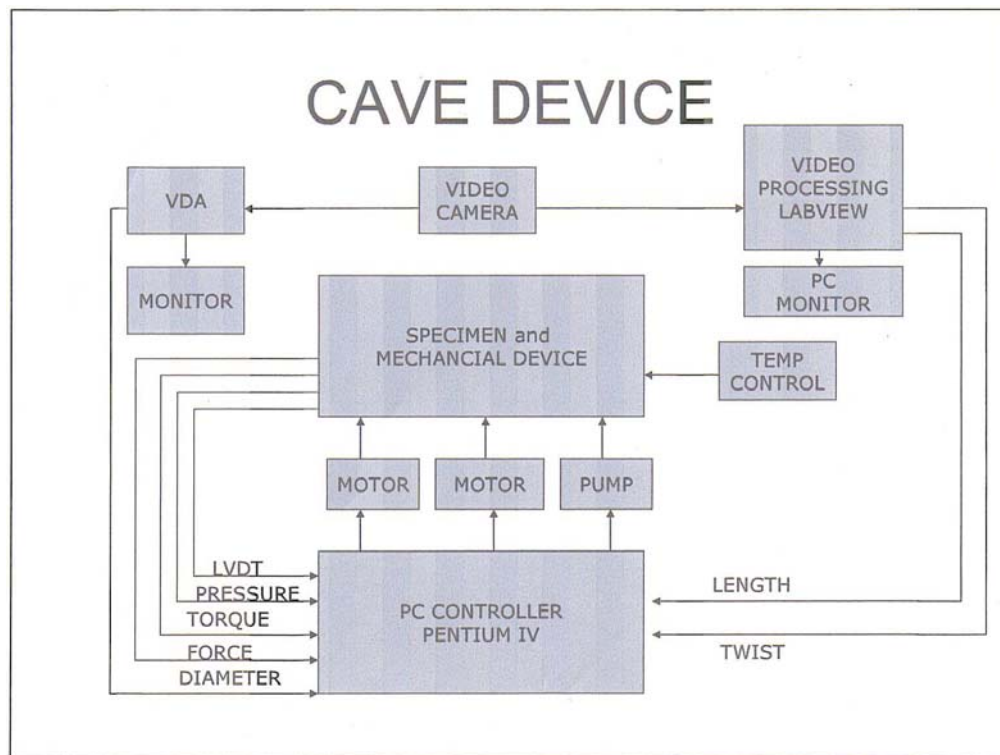


Fig. 3.3. Block diagram of control and feedback system of the re-designed CAVE device.

3.5.1 Calibration of Transducers

The force transducer was calibrated by mounting known weights with an effectively inextensible string to a frictionless pulley. Different known weights were

hung from the pulley, and readings were recorded from the data acquisition system. A linear least square regression was used to determine an equation that would fit the experimental data with the output of the force transducer as shown in figure 3.4.

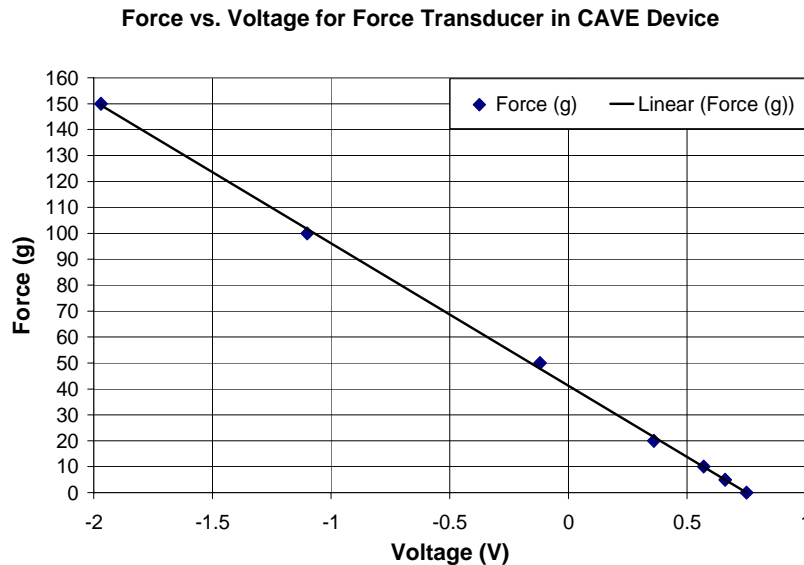


Fig. 3.4. Force calibration plot. Note the obvious linear relationship between force (g) and voltage. Known weights were hung on a hook rigidly attached to a lexan mounting rod threaded onto the tension-compression force transducer. Only tension data were generated.

The pressure transducer was calibrated in a similar way; namely, a syringe filled with water connected to the pressure sensor via Masterflex tubing was raised and lowered. The corresponding heights and outputs of the sensors were recorded. When the “column” of water could not be raised any higher, a mercury and bulb sphygmomanometer were used to obtain additional pressure data at higher ranges (0 – 250 mmHg). The calibration plot is shown below in figure 3.5.

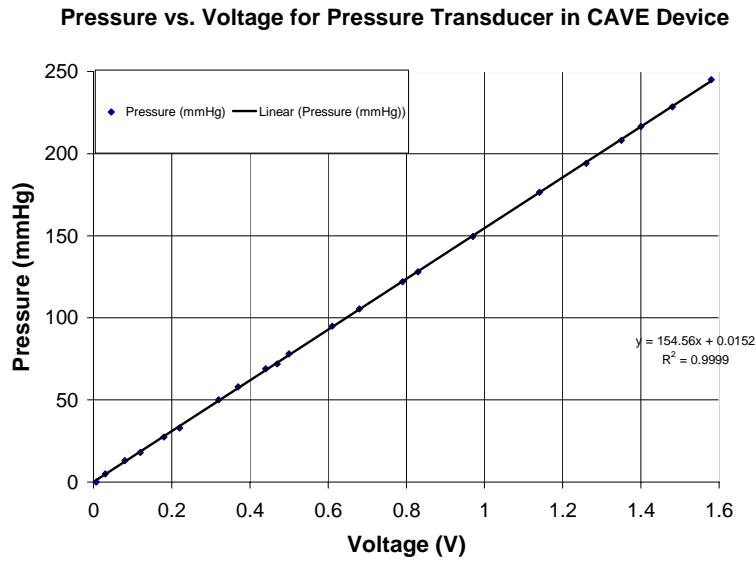


Fig. 3.5 Pressure calibration plot. Note the linear relationship between pressure and voltage.

The VDA was calibrated by placing a white Delrin stepped rod of known diameters submerged in the perfusing section of the CAVE system in the same optical plane as the experiment would have take place. The VDA was then used to obtain diameter measurements based on the white image with black background displayed on the monitor. Corresponding measurements of the different diameters were then recorded. These are shown in figure 3.6.

Diameter vs. Voltage for Video Dimension Analyzer in CAVE Device

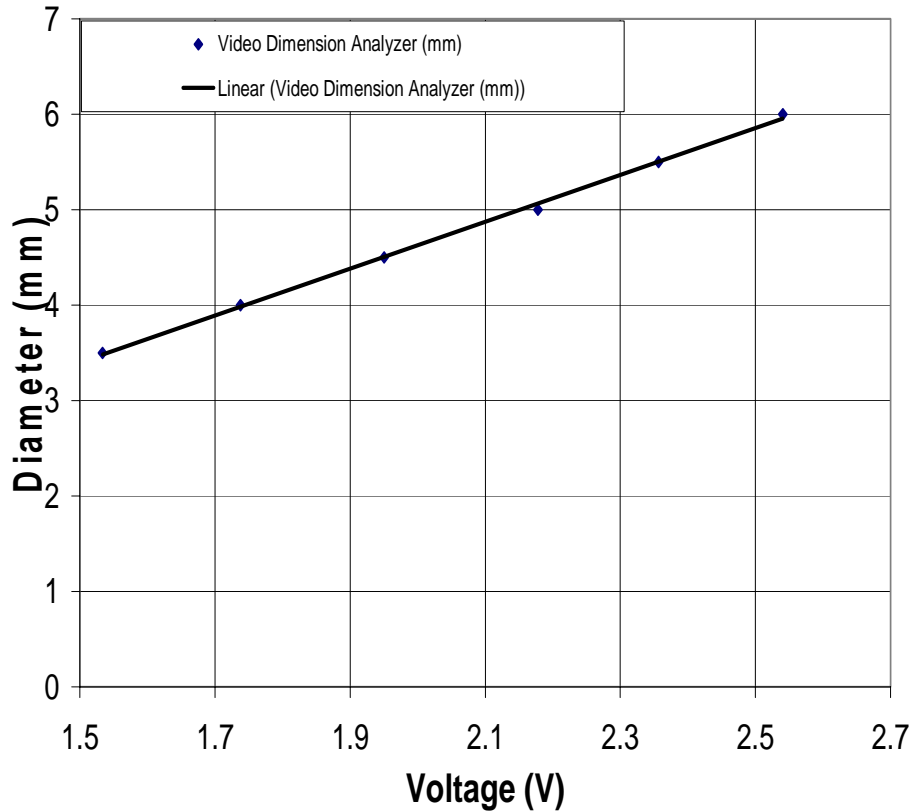


Fig. 3.6. Video dimension analyzer calibration plot. Note the linear relationship between the diameter and voltage.

The LVDT was calibrated by measuring the distance between the carriages with a caliper, and then using the step motor to increase the distance between the carriages. The resulting displacement was then measured and recorded along with the voltage output of the LVDT signal. This procedure was performed starting with the smallest feasible separation of the carriages and ending with the largest separation the sensor could handle. Figure 3.7 shows the LVDT calibration plot. The gauge length of the

arteries tested were adequately sized so that the LVDT was used in the calibrated range. Table 3.2 shows the summary of the linear least-squares regression equations as well as the “goodness of fit” parameter R^2 .

Carriage Separation vs. Voltage for LVDT in CAVE Device

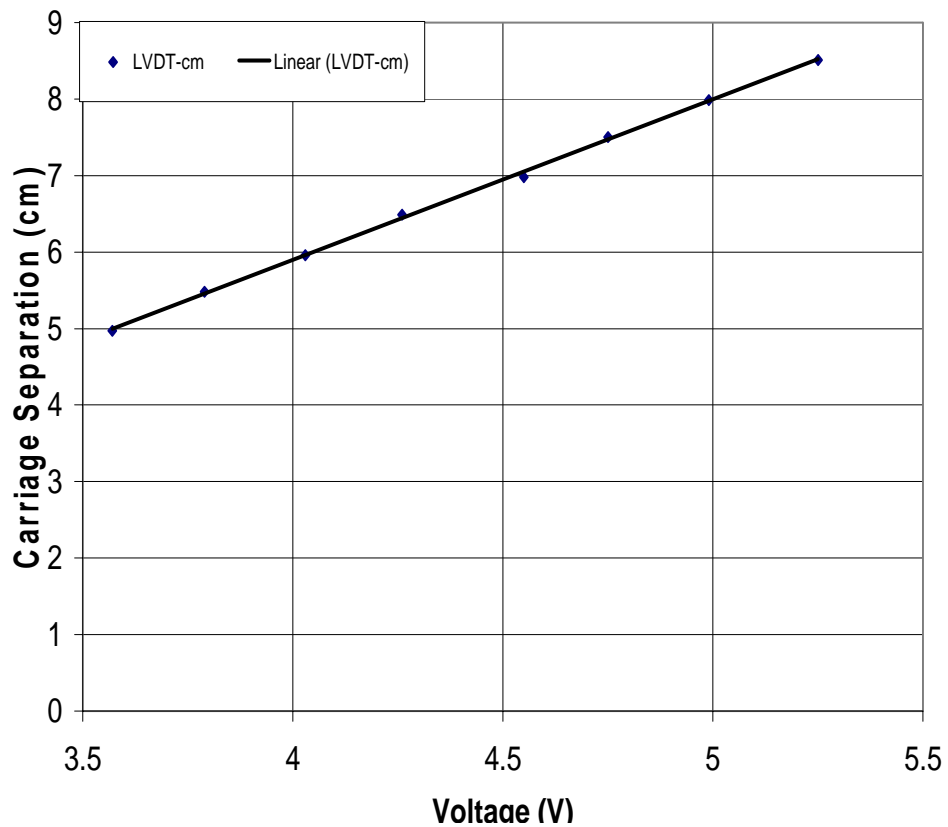


Fig. 3.7. LVDT calibration plot. Note the linear relationship between the carriage separation and voltage.

Table 3.2

Summary of calibration plot characteristics. The variable “y” indicates the predicted transducer output (i.e., force, pressure, etc.) and the variable “x” indicates the measured voltage while performing the calibration procedure.

	Linear Least Squares Regression Equation	Correlation Coefficient
Force Transducer	$y = -54.94x + 41.19$	$R^2 = 0.99$
Pressure Transducer	$y = 154.56x + 0.02$	$R^2 = 0.99$
Video Dimension Analyzer	$y = 2.45x - 0.28$	$R^2 = 0.99$
LVDT	$y = 2.10x - 2.49$	$R^2 = 0.99$

All calibrations for all sensors were performed once after verifying that the results were repeatable.

3.5.2 Constant Length Protocol

After removal of the perivascular tissue, the experiments on each specimen began. Then, the specimen was subjected to a constant length protocol; whereby the length is maintained constant while the artery is pressurized cyclically with the peristaltic pump. In order to make measurements, the specimen was first preconditioned at least 14 times at each axial stretch ratio to minimize the effects of hysteresis. After

preconditioning, a cycle of pressurization – depressurization was performed and recorded as data. Then a larger stretch ratio was preconditioned as previously described, and subsequent measurements followed. Only the loading curves were used as data for later curve fitting. Specimens were tested at axial stretch ratios ranging from 1.0 to 1.85 in increments of 0.10 or 0.05 at cyclic pressures of 0 – 160 mmHg (see figures 3.8, 3.9 and 3.10).

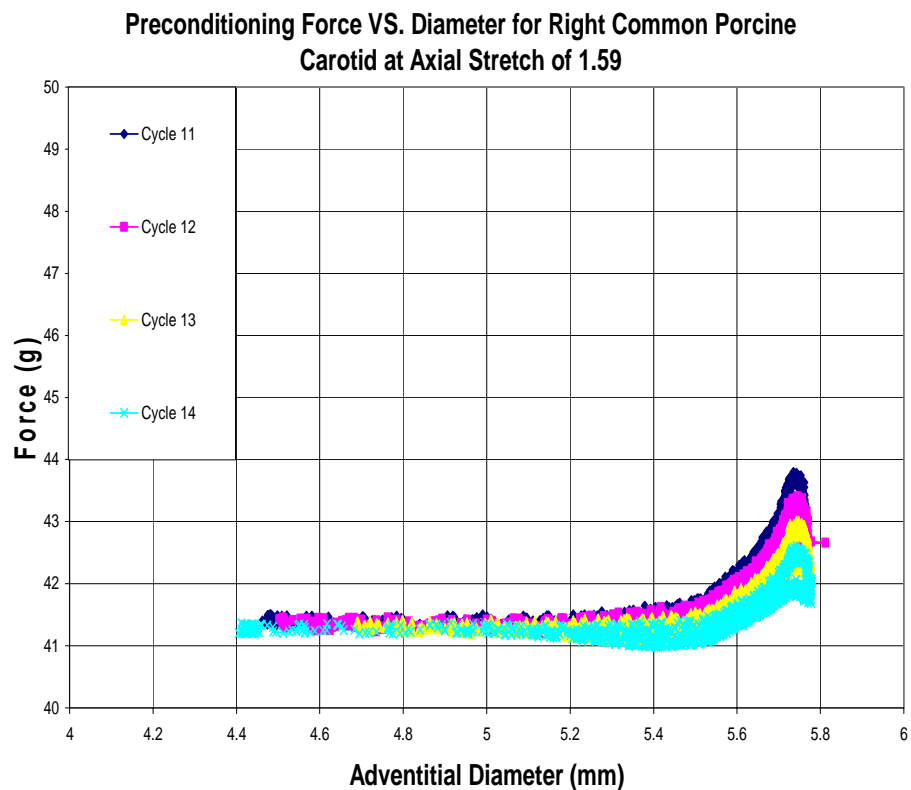


Fig. 3.8 Preconditioning force-diameter data for porcine right common carotid.

Preconditioning Pressure VS. Diameter for Right Common Porcine Carotid at Axial Stretch of 1.59

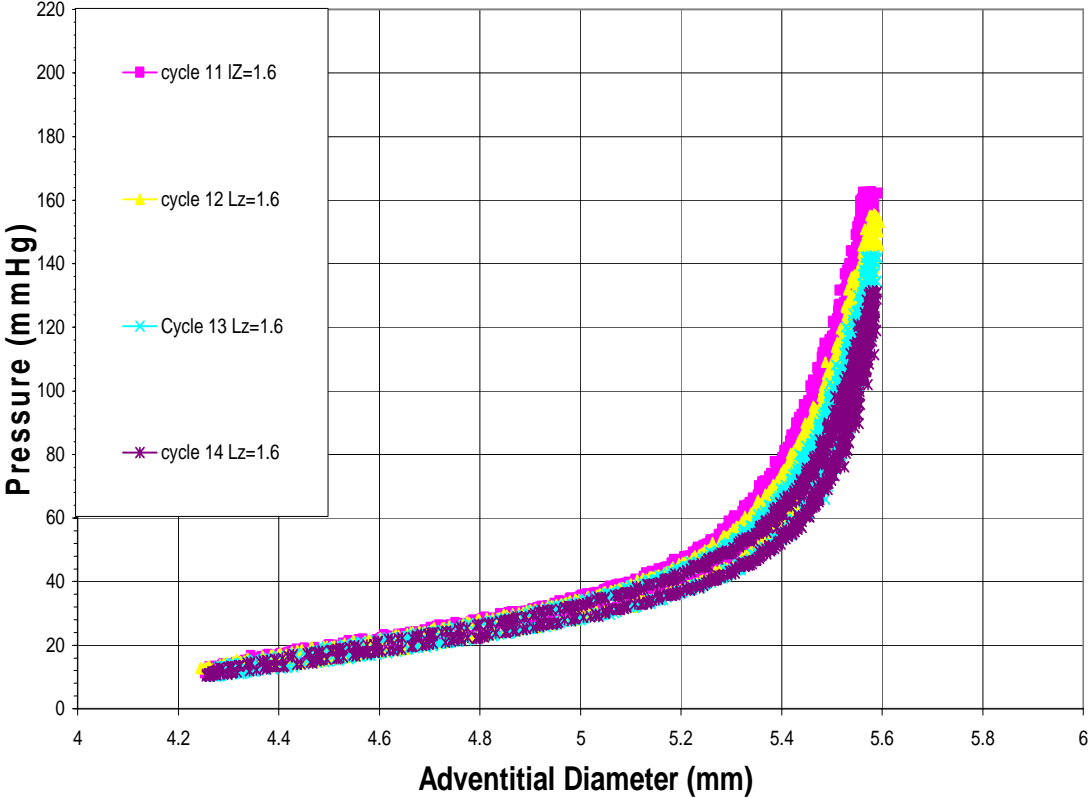


Fig. 3.9. Preconditioning pressure-diameter data for porcine right common carotid.

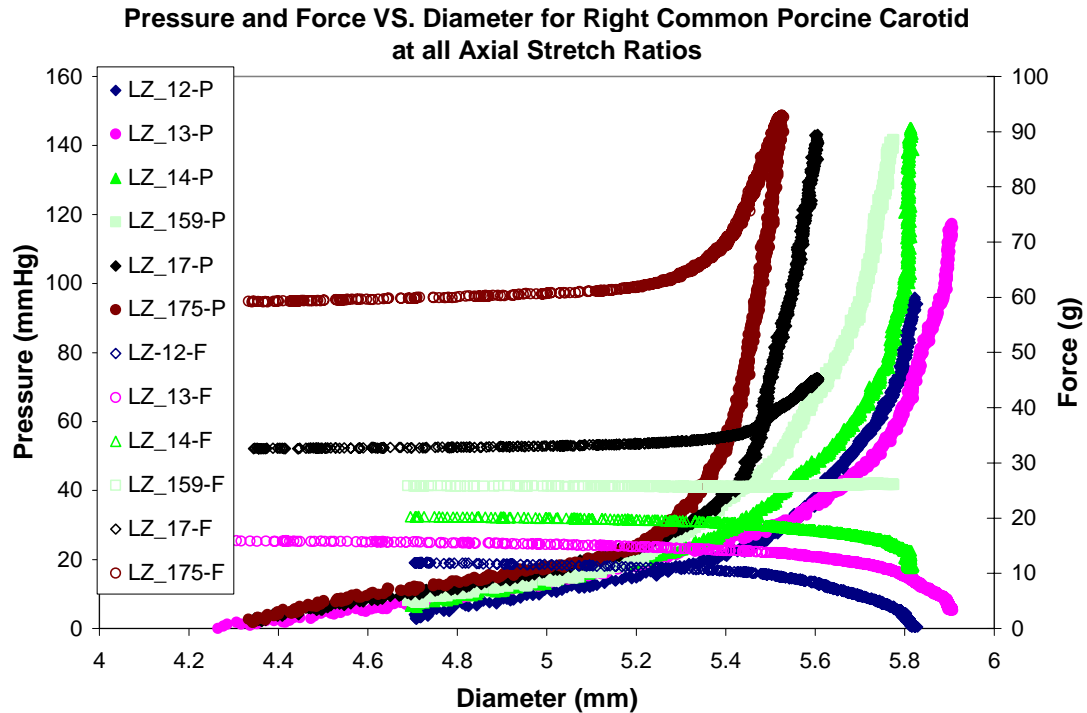


Fig. 3.10. Experimental data for right common porcine carotid for all stretch ratios. Axial stretch ratio 1.59 (nearly a straight line in the force diameter curve) was ultimately the axial stretch ratio used in the finite element analysis.

3.5.3 Residual Strain Measurements

Although the finite element programs MSC.Patran and MSC.Marc support inclusion of residual stress data in the linear elastic theoretical framework of superposition, they do not support residual stresses in a large deformation and large strain nonlinear finite elasticity theory framework. For this reason, residual strain measurements were not incorporated into the finite element study. However, for the

purpose of a parametric stent design study, it is postulated that exclusion of these quantities will not affect the ability to compare stent designs, and their imparted stress fields on the arterial wall.

3.5.4 Functional Form of Strain Energy Density Function

The functional form of the strain energy density function is of the form,

$$W = C_{10} \cdot (I_1 - 3) + C_{01} \cdot (I_2 - 3) + C_{11} \cdot (I_1 - 3) \cdot (I_2 - 3) + C_{20} \cdot (I_1 - 3)^2 + C_{30} \cdot (I_1 - 3)^3 \quad (3.1)$$

where I_1 is the first invariant of the left Cauchy-Green stretch tensor B , and C_{10} , C_{01} , C_{11} , C_{20} , C_{30}

3.6 Experimental Data Analysis

A Matlab program was developed to determine constants for a strain energy density function to be used in the finite element simulations. Unsuccessful attempts were made to fit the entire space of experimental data to the isotropic constitutive strain energy density function in 3.1. Namely, it was impossible to describe such large data variations (axial stretch ratios ranging from 1.0 to 1.85) with a polynomial equation which is only a function of the first two Cauchy-Green deformation invariants. In order to successfully model the anisotropic hyperelastic behavior of an artery in MSC.Patran, a user-subroutine in FORTRAN was to be developed. This was beyond the scope of this thesis and therefore, the best solution using equation 3.1 as a strain energy density function with an isotropic response was to determine the constants in equation 3.1 by

some other means. Furthermore, only the in vivo stretch ratio was used to find the aforementioned constants due to two main reasons:

- 1) The limited capacity of equation 3.1 only allows a small bandwidth of data to be modeled as opposed to the full spectrum of data.
- 2) The arterial response is highly anisotropic, and therefore, isotropic models are inherently limited when anisotropic data is fed into it.

However, it is pointed out that although these are significant limitations to modeling arterial mechanical response in the absolute – definite – sense, important information and insight can still be gained by studying an isotropic model. In particular, it will be shown that the current isotropic model in this thesis is still able to represent some anisotropy. Arteries in general are notoriously stiffer in the circumferential direction than in the axial direction. Therefore, it is expected that the hoop stresses will be the highest stresses a stented artery will experience since the presence of the stent affects most intensely the circumferential direction. Furthermore, it is thought that arteries cyclically pressurized at the in vivo stretch, will have a constant axial load response (Humphrey, 2002). Interestingly enough, in an analysis of anisotropic hyperelastic artery models performed by Holzapfel et al. (2002), it was been shown that the axial component of stress is lower. In this thesis, the axial stretch is 6 times greater than the hoop stretch. In our own models, the hoop stresses also resulted in the largest magnitude of stress – just as the anisotropic models are – despite the significant difference in axial and hoop stretch ratios (59% and 10% respectively).

Since attempts to fit constants in equation 3.1 using a non-linear regression Marquardt-Levenberg routine were ill-fated, constants were derived empirically. These are shown in table 3.3.

Table 3.3

Summary of constants obtained for equation 3.1.

Constants	Value
C_{10}	25,466
C_{01}	-11,577
C_{11}	-506
C_{20}	1703
C_{30}	1650

The pressure and axial load response given by the constants in table 3.3 are shown in figures 3.11 and 3.12. Note that the pressure obtained with the aforementioned constants and the experimental pressure yield the same hoop stretch value – corresponding to the same diameter) at systole (16 kPa). The pressure at diastole (10.66 kPa) however, is underestimated by our model, and therefore underestimates the stresses imparted to the vessel. In contrast to the pressure data, it was not possible to approximate the axial load data as accurately. Our model overestimates the axial load data by 100%

in the worst case, implying that the observed axial stresses calculated by Patran are higher than they would be had the axial load data been fitted properly. However, despite this limitation, our simulations still show that the circumferential stresses are higher in magnitude. In an anisotropic model, our hoop stresses would be higher, and our axial stresses would be lower. These limitations will be discussed further in section 6, as well as the implications in the results obtained in section 5. Lastly, despite our constants lacking the sought and idealized mathematical rigor, the pressure and axial load curves (in vivo) derived from the constants in table 3.3 and equation 3.1 are accommodating to the mechanical behavior and response observed during experimentation. It is important therefore to understand what is meant by predictive capability versus descriptive capability. The latter is not much more useful than using a table containing the original data. The former however, is useful in solving complex boundary value problems given physically realistic behaviors have been verified – such as obtaining a tensile stress in a material if it is stretched, and compressive behavior if it is compressed; and also, assessing the closeness of the numerical results obtained – i.e., how precise a calculation is (Humphrey, 2002). The fact that isotropy does not possess the characteristics to model a wide range of behavior of an anisotropic model, is an affirmation that whenever possible, anisotropy should be used in place of isotropy when describing the mechanical behavior of arteries. Should this not be possible, it is necessary to understand the limitations and restrictions imposed in order to benefit from any research. These limitations and implications on our results will be explained in section 6.

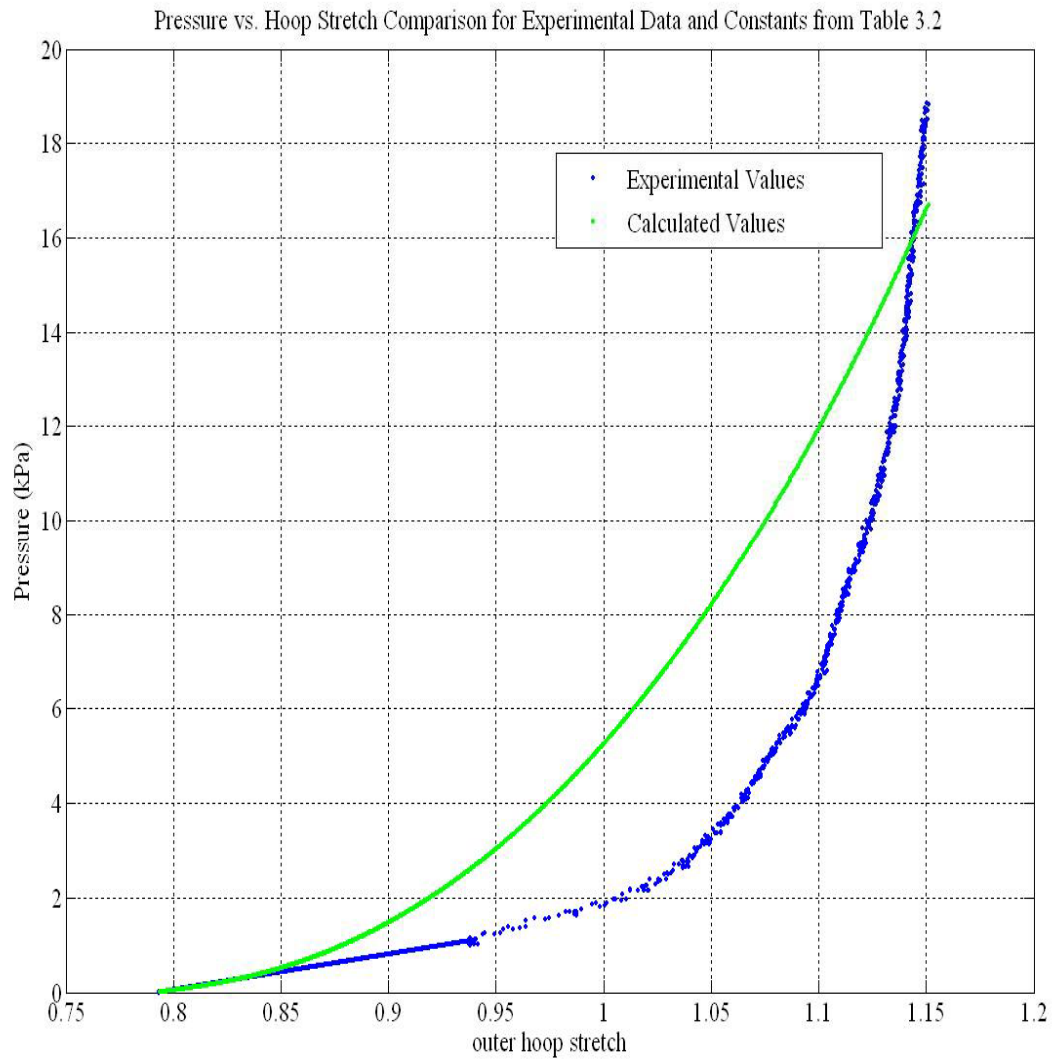


Fig. 3.11. Comparison of pressure predicted by manipulation of equation 3.1 and constants in table 3.3, and experimental pressure data.

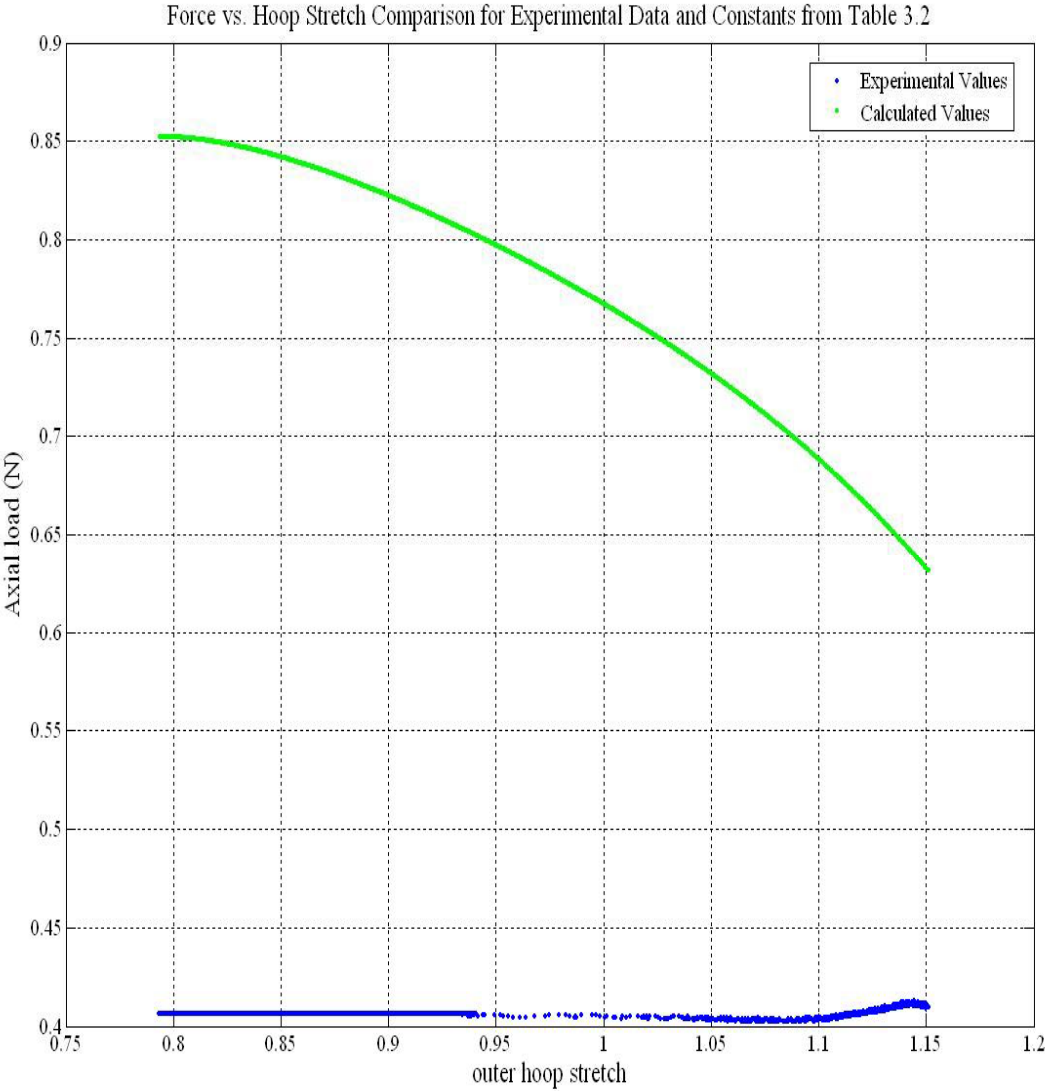


Fig. 3.12. Comparison of experimental data and data predicted by manipulating equation 3.1 with constants in table 3.3.

4. THE FINITE ELEMENT METHOD AND ITS USE IN MSC PATRAN/MARC

All physical phenomena, whether mechanical, biological, electromagnetic or chemical, can be described by the laws of physics (Reddy, 1993). While obtaining the governing equations of a system in any mathematical form may be difficult, obtaining an analytical solution that satisfies the prescribed boundary conditions and governing equations exactly is usually only possible for cases involving simple geometry. This difficulty has been undercut by the development of variational methods, and amongst them, the finite element method. All variational methods recast a problem in integral form that was originally formulated in differential form. An important consideration in this transition from differential to integral form, is that in the former, the governing equations must be satisfied exactly everywhere in the domain. In the integral form, the governing equations are satisfied over the averaged domain (Humphrey, 2002). As its name suggests, the finite element method consists of discretizing a domain into discrete yet adjacent subdomains or elements that are finite in size and simple in shape. It is this simplicity that makes it possible to determine approximate solutions to the boundary value problem of interest that is otherwise intractable to solve analytically. Depending on the class of problem, certain parameters of the solution are required to be continuous from element to element at specific points (known as nodes). Boundary conditions must be satisfied identically where they are specified. Because of the complex geometry, the problem of finding and comparing the stress fields imparted onto an artery by different stents requires the use of the finite element method. Additional complicating factors

include the nonlinear character of the mechanical properties of soft tissues, and discontinuous fields created by contact between the artery and the stent.

4.1 Variational Principles in Mechanics

Historically, variational principles in mechanics have been used to obtain approximate solutions using numerical methods to problems that are many times intractable to solve analytically. The solution procedure consists of assuming a solution in the form of a finite set of linearly independent functions with undetermined parameters. This assumed form is substituted in a functional to be minimized using variational calculus. For non-conservative systems, a functional may not exist, however, using the principle of virtual work (of actual loads moving through virtual (fictitious) displacements), a weak form of the governing differential equation can be developed and the application of weighted residual methods, the Ritz method will also result in a system of equations with undetermined parameters (Reddy, 1993).

In general, the solution to a continuum problem cannot be represented by a finite set of functions, and therefore it is intuitively obvious that weighted residual, Ritz and the finite element methods in fact yield approximate solutions. However, as more linearly independent terms are introduced in the assumed form of the solution of a well posed problem, a converged solution is attained (Reddy, 2002). The limitation of these non-finite element numerical methods is that the coordinate functions are difficult to obtain and they are dependent on the specified boundary conditions of the problem. Additionally, these functions can have any functional form so long as they describe the

geometry and the physics of the problem. Therefore, this method is not readily or easily adaptable to a computer program for automation. This gave rise to the development of the finite element method.

4.2 The Finite Element Method

The major difference between the finite element method and other variational principles, is that the continuum itself is discretized into smaller domains geometrically simple that the sought solution form of each element can be represented accurately by polynomial functions. Therefore, these sub-domains (finite elements) are easily implemented into a computer program whereby the coordinate functions and their coefficient matrices can be generated systematically, and are applicable to any problem independent of boundary conditions, discontinuities (or lack of), and material properties. The only requirement for a problem to be solved using FEM, is that a weak form of the governing differential equation can be formulated (Reddy, 2002). It is important to emphasize however, that the finite element method, although extremely versatile in its wide application to boundary value problems, imposes a restriction on the primary variables such that they are represented by the coordinate functions (polynomials). In addition, solutions to boundary value problems using the finite element method may change depending on the number of subdomains (elements). A mesh independence study is an integral part in any boundary value problem solved using the finite element method. Therefore, the finite element method should be used with care, and it should not

be thought of as a crutch for solving problems, rather it is a weapon that may cause harm if used inappropriately.

4.3 Virtual Work Principle

As explained in section 2, a configuration is understood to mean the positions of all particles contained in a body at any given time. A configuration is said to be admissible when it corresponds to a system in equilibrium as well as satisfying geometric constraints (Reddy, 2002). The virtual work principle stems from variations of these admissible configurations such that equilibrium as well as the geometric constraints of the system are still respected. There are various formulations of the virtual work principle. For the displacement formulation finite element methods it is “...the work done by actual forces through a virtual displacement of the actual configuration” (Reddy 2002, p.96). Alternatively, in the complementary virtual work principle, the virtual work is done by virtual forces in moving through actual displacements (Reddy 2002, p.97). A mixed formulation is an application of the virtual work principle where displacements and force or stress-like quantities are varied.

In this thesis, the augmented Lagrange multiplier method is used to enforce incompressibility giving rise to a spherical stress² (commonly misinterpreted as hydrostatic pressure (Humphrey, 2002)) in addition to displacements as primary (interpolated) variables.

A fundamental concept of the virtual work principle is that the variations are hypothetical, so in principle these variations need not be infinitesimal so long as equilibrium is still enforced, and geometric constraints are respected. Namely, a deformable body with volume V and surface S , is subject to geometric boundary conditions on S_1 and surface forces on S_2 . The virtual displacements on S_1 are necessarily zero,

$$S = S_1 \cup S_2 \quad (4.1)$$

$$S_1 \cap S_2 = \emptyset \quad (4.2)$$

$$\delta \mathbf{u} = 0 \text{ on } S_1 \quad (4.3)$$

$$\delta W = \mathbf{F} \cdot \delta \mathbf{u} \quad (4.4)$$

where $\delta \mathbf{u}$ represents the virtual displacement of the continuum in question and δW represents the corresponding virtual work. Virtual work is composed of two

² The stress tensor can be split into into two tensors; one of which describes dilatational stress components (spherical), and the deviatoric or distortional stress components. The decomposition is expressed as,

$$\boldsymbol{\sigma} = \begin{pmatrix} \sigma_m & 0 & 0 \\ 0 & \sigma_m & 0 \\ 0 & 0 & \sigma_m \end{pmatrix} + \begin{pmatrix} \sigma_{11} - \sigma_m & \sigma_{12} & \sigma_{13} \\ \sigma_{21} & \sigma_{22} - \sigma_m & \sigma_{23} \\ \sigma_{31} & \sigma_{32} & \sigma_{33} - \sigma_m \end{pmatrix} \text{ where } m \text{ represents mean spherical stress, and the}$$

subscripts 1,2,3 represent the face and direction of the shear stresses relative to a particle under stress commonly represented as a ‘‘cube’’.

components: virtual work done by external forces (applied loads) and virtual work done by internal forces (in the form of stresses). Equations 4.5 and 4.6 describe in general terms expressions for the latter and former respectively, where ρ is the mass density, \mathbf{f} are generalized body forces, \mathbf{t} are generalized traction forces, $\boldsymbol{\sigma}$ is the true Cauchy stress tensor, $\boldsymbol{\beta}$ is the symmetric gradient operator in the current configuration, and \mathbf{L} is the material moduli tensor in the current configuration. Equation 4.7 is the total virtual work expressed as the sum of external and internal virtual work (for more details on the derivations of these equations see Reddy 2002, p.97, p.184).

$$\delta W_E = -\left(\int_V \rho \mathbf{f} \cdot \delta \mathbf{u} dv + \int_{s_2} \mathbf{t} \delta \mathbf{u} ds\right) \quad (4.5)$$

$$\delta W_I = \int_V (\boldsymbol{\sigma}) : (\boldsymbol{\beta}(\delta \mathbf{u}) \mathbf{L} \boldsymbol{\beta}(\Delta \mathbf{u})) dv \quad (4.6)$$

$$\delta W = \delta W_I + \delta W_E \quad (4.7)$$

The negative sign in 4.5 is there by convention in that the work done on a body is considered to be negative and the work done by a body is considered positive.

Furthermore, equation 4.6 is also known as the *virtual strain energy density* in the current configuration, which is irrespective of the constitutive behavior (Reddy, 2002).

4.4 Stationary Principle of Total Potential Energy

Once a constitutive formulation is assumed, the principle of stationary total potential energy is obtained and is used to arrive at the displacement formulation finite element methods. For the problem at hand however, the assumption of incompressibility

renders traditional displacement based finite element methods ill-conditioned numerically. Therefore a modified functional must be formulated such that incompressibility is enforced while at the same time numerical stability is achieved. This modified principle, which is sometimes referred to as a “hybrid” or “mixed” variational method includes the aforementioned pressure-like term (or spherical stress) used to enforce incompressibility. Since incompressible materials have very distinct behaviors in bulk and shear, it is numerically favorable to decouple the dilatational deformation (volume changing) and the deviatoric deformation (volume preserving, or isochoric). This results in the following modified deformation gradient and left Cauchy-Green stretch tensor where J is the determinant of the deformation gradient \mathbf{F} :

$$\mathbf{F} = (J^{\frac{1}{3}} \cdot \mathbf{I}) \hat{\mathbf{F}} \quad (4.8)$$

$$\mathbf{C} = (J^{\frac{2}{3}} \cdot \mathbf{I}) \hat{\mathbf{C}} \quad (4.9a)$$

$$\mathbf{B} = (J^{\frac{2}{3}} \cdot \mathbf{I}) \hat{\mathbf{B}} \quad (4.9b)$$

where the quantities in parenthesis are associated with dilatational deformations, $\hat{\mathbf{F}}$, $\hat{\mathbf{C}}$ and $\hat{\mathbf{B}}$ are associated with deviatoric deformations, and \mathbf{I} represents the identity tensor (Holzapfel, 2000).

Following this multiplicative decomposition, the mixed formulation principle can be expressed as in equations 4.10:

$$\delta \Pi(\mathbf{u}, p) = \delta W_I + \delta W_E = 0, \quad (4.10a)$$

$$\begin{aligned} \delta\Pi(\mathbf{u}, p) = & \int_{\Omega} W_{dev}(\hat{\mathbf{B}}(\mathbf{u}) \cdot \delta\mathbf{u} + 3p \cdot (J(\mathbf{u})^{\frac{1}{3}} - 1)) \cdot \delta p \\ & - 9K(J^{\frac{1}{3}} - 1)dv + - \left(\int_{\Omega} p\mathbf{f} \cdot \delta\mathbf{u} dv + \int_{s_2} \mathbf{t} \cdot \delta\mathbf{u} ds + C_c \right) \end{aligned} \quad (4.10b)$$

where Π represents the total potential energy of the system, W represents the strain energy density function, p is the Lagrange multiplier (spherical stress), and K represents the bulk modulus which was introduced by a penalty parameter inherent in a perturbed (or augmented) Lagrange multiplier method. The term C_c represents the contact condition between the artery and stent and will be elaborated in the next section. Note that the terms including K and p vanish in the case of incompressibility, and are near zero (positive) as the material becomes slightly compressible, (MSC.Marc Volume A, 2004). It can be appreciated that only deviatoric deformations contribute to the strain energy. The key difference between equations 4.10b and 4.7 is that the former assumes a constitutive formulation. In particular (and in this thesis), the constitutive behavior of equation 2.47 in section 2 is substituted in 4.10b. Considering \mathbf{u}_o and p_o to be the solution to \mathbf{u} and p that satisfies equations 4.10a (i.e., $\delta\Pi = 0$), and substituting the approximations in 4.11 into 4.10b,

$$\mathbf{u}_o = \Sigma u_i^e \Psi_i^e, \text{ for } i = 1, 2, \dots, N \quad (4.11a)$$

$$p_o = \Sigma p_i^e \Psi_i^e, \text{ for } i = 1, 2, \dots, N \quad (4.11b)$$

we arrive at the expression

$$\delta \Pi(u_i^e, p_i^e) = 0, \text{ for } i = 1, 2, \dots, N. \quad (4.12a)$$

In 4.11 and 4.12, u_i^e and p_i^e are the (as of now unknown) nodal values of the primary variables being interpolated (i.e., displacements and spherical stresses), for which Ψ_i^e and ϕ_i^e are displacement and spherical stress coordinate functions (interpolating functions) respectively used in the e th element for the i th node. Equation 4.12a can be rewritten as

$$\frac{\partial \Pi}{\partial u_i^e} \delta u_i^e + \frac{\partial \Pi}{\partial p_i^e} \delta p_i^e = 0, \text{ for } i = 1, 2, \dots, N \quad (4.12b)$$

where the δu_i^e 's and δp_i^e are independent of each other and therefore 4.12c-d is equivalent to 4.12a-b (Humphrey, 2002).

$$\frac{\partial \Pi}{\partial u_i^e} \delta u_i^e = 0, \text{ for } i = 1, 2, \dots, N \quad (4.12c)$$

$$\frac{\partial \Pi}{\partial p_i^e} \delta p_i^e = 0, \text{ for } i = 1, 2, \dots, N \quad (4.12d)$$

In this thesis, the element type used was the 20-node hexahedral element, where the displacements are interpolated using quadratic Lagrange functions while the spherical stress is interpolated with a linear function. Figure 4.1 is a depiction of the 20-noded hexahedral element and its numbering scheme used.

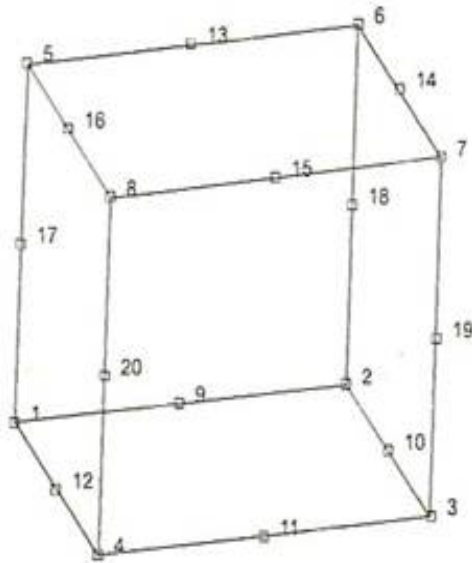


Fig. 4.1 Illustration of a 20-noded hexahedral element. Note the numbering scheme of the nodes. Each number corresponds to the appropriate equation number in equations 4.13 – 4.17.

This element has three displacement degrees of freedom per node and one additional degree of freedom (for the spherical stress) on every corner node. The displacement interpolating functions are described below:

For the corner nodes $i = 1, 2, \dots, 8$:

$$\Psi_i^e = \frac{1}{8} \cdot (1 + \xi \xi_i)(1 + \eta \eta_i)(1 + \zeta \zeta_i)(\xi \xi_i + \eta \eta_i + \zeta \zeta_i - 2). \quad (4.13)$$

For the mid-side nodes $i = 9, 11, 13, 15$:

$$\Psi_i^e = \frac{1}{4} \cdot (1 - \xi^2)(1 + \eta \eta_i)(1 + \zeta \zeta_i). \quad (4.14)$$

For the mid-side nodes $i = 10, 12, 14, 16$:

$$\Psi_i^e = \frac{1}{4} \cdot (1 - \eta^2)(1 + \xi\xi_i)(1 + \zeta\zeta_i). \quad (4.15)$$

For the mid-side nodes $i = 17, 18, 19, 20$:

$$\Psi_i^e = \frac{1}{4} \cdot (1 - \zeta^2)(1 + \xi\xi_i)(1 + \eta\eta_i). \quad (4.16)$$

The interpolating functions for the spherical stress are linear functions and are of the form:

$$\Psi_i^e = \frac{1}{8} \cdot (1 + \xi\xi^2)(1 + \eta\eta_i)(1 + \zeta\zeta_i) \text{ for } i = 1, 2, \dots, 8. \quad (4.17)$$

In 4.13 – 4.17, the Greek letters η , ξ , and ζ , represent an element-based natural orthonormal coordinate system with its origin located at the centroid of each element.

The transformation from the x-y-z space to the η - ξ - ζ space is used to facilitate integration techniques; they do not entail a physical coordinate transformation of the elements or boundary value problem being analyzed. In addition, the 20-noded hexahedron used herein employs the isoparametric formulation where the geometry and the displacement use the same degree of interpolation –quadratic in this case; and η , ξ , and ζ have a range of $\{\eta, \xi, \zeta\} \in [-1, 1]$ so that the resulting element is a unit cube. Since the boundary value problem is formulated in Cartesian components, the following transformation relates the x-y-z space and the η - ξ - ζ space:

$$x = x_i \Psi_i^e; \quad (4.18)$$

$$y = y_i \Psi_i^e; \quad (4.19)$$

$$z = z_i \Psi_i^e. \quad (4.20)$$

Note that only the quadratic interpolation functions are used to map the geometry.

4.5 FEM Formulation and Implementation Using MSC.Patran and MSC.Marc

Equations 4.11 represent a set of N linearly independent equations, represented in matrix form as

$$\begin{pmatrix} \mathbf{K}_u & \mathbf{K}_p \\ \mathbf{K}_p^T & \gamma \end{pmatrix} \{ \mathbf{U}_N \}_{1 \times N} = \{ \mathbf{F}_N \}_{1 \times N}. \quad (4.21)$$

Here $[\mathbf{K}_u]$ represents the the initial stiffness matrix and the material stiffness matrix, defined in Cartesian coordinates respectively as

$$(K_1)_{ij} = \int_{v_{n+1}} (\beta_{imn} L_{mnpq} \beta_{pqj}) \det \hat{J} dv, \quad (4.22)$$

$$(K_2)_{ij} = \int_{v_{n+1}} (\sigma_{kl} N_{i,k} N_{j,l}) \det \hat{J} dv. \quad (4.23)$$

In equations 4.22 and 4.23, β_{imn} is the symmetric gradient operator evaluated in the current configuration, σ_{kl} is the Cauchy stress tensor, $N_{i,k}$ and $N_{j,l}$ represent the interpolation function matrices, $\det \hat{J}$ is the determinant of the Jacobian transformation matrix required for the numerical integration techniques employed herein. Equations 4.24 and 4.25 describe this mapping:

$$\hat{J} = \begin{pmatrix} \frac{\partial X}{\partial \xi} & \frac{\partial Y}{\partial \xi} & \frac{\partial Z}{\partial \xi} \\ \frac{\partial X}{\partial \eta} & \frac{\partial Y}{\partial \eta} & \frac{\partial Z}{\partial \eta} \\ \frac{\partial X}{\partial \zeta} & \frac{\partial Y}{\partial \zeta} & \frac{\partial Z}{\partial \zeta} \end{pmatrix}, \quad (4.24)$$

$$\hat{J} = \begin{pmatrix} X_i \frac{\partial}{\partial \xi} (Ni)^e & Y_i \frac{\partial}{\partial \xi} (Ni)^e & Z_i \frac{\partial}{\partial \xi} (Ni)^e \\ X_i \frac{\partial}{\partial \eta} (Ni)^e & Y_i \frac{\partial}{\partial \eta} (Ni)^e & Z_i \frac{\partial}{\partial \eta} (Ni)^e \\ X_i \frac{\partial}{\partial \zeta} (Ni)^e & X_i \frac{\partial}{\partial \zeta} (Ni)^e & X_i \frac{\partial}{\partial \zeta} (Ni)^e \end{pmatrix}, \quad (4.25)$$

where $(Ni)^e$ represents the appropriate interpolation function (i.e., Ψ_i^e for displacement and Ψ_i^e for the spherical stress).

The tangent stiffness matrix in the current configuration is L_{ijkl} , is defined as,

$$L_{ijkl} = \left(\frac{I}{J}\right) F_{im} F_{jn} F_{kp} F_{lq} D_{mnpq}, \quad (4.26)$$

and it is convected to the current configuration through 4.27:

$$D_{mnpq} = 4 \left(\frac{\partial^2 W}{\partial C_{mn} \partial C_{pq}} \right) \quad (4.27)$$

$[\mathbf{K}_p]$ in 4.21 represents the incompressibility contribution to the stiffness matrix and it has the following form:

$$K_p = \int_{v_{n+1}} (C_{mn} \beta_{jmi} \det \hat{J}) dv, \quad (4.28)$$

where C_{mn} has been defined in 4.9a and β_{jmi} was defined in 4.22 – 4.23. The surface load vector is defined as

$$Q_i = \int_{S_{n+1}} N_i t_i \hat{J}_{2D} ds, \quad (4.29)$$

where N_i represent the appropriate interpolation function, t_i represents the traction vector and \hat{J}_{2D} represents the surface Jacobian as the norm of the cross product of two vectors defining an element surface as in 4.30.

$$\hat{J}_{2D} = |V_{,j} \times V_{,i}| \text{ for } i,j = 1,2,3. \quad (4.30)$$

The variable γ in equation 4.21 represents a small positive number inherent in the augmented Lagrange multiplier method used in 4.21 to render the system of equations positive-definite. Finally, \mathbf{R} represents the residual load vector for not satisfying equilibrium exactly. In this thesis, an increment was considered converged when \mathbf{R} reached 10% of the theoretical reaction loads used to enforce equilibrium exactly. It is important to note however, that in nonlinear analyses such as the boundary value problem in this thesis, there is a nonlinear relationship between the stiffness matrix $[\mathbf{K}]$, the unknown primary variable vector (displacement and spherical stress, one-dimensional array) $\{\mathbf{U}\}$, and the generalized load vector $\{\mathbf{F}\}$. Namely, 4.21 (condensing all stiffness matrix contributions into $[\mathbf{K}]$) should be explicitly expressed as

$$[\mathbf{K}(U_N)]\{U_N\} = \{\mathbf{Q}\} - \{\mathbf{R}\}, \quad (4.31)$$

where some subscripts have been omitted for clarity and the parentheses is meant to imply functional dependence between quantities.

The analysis framework used in MSC.Patran and MSC.Marc for nonlinear hyperelasticity with the incompressibility constraint is performed in the updated Lagrangian approach using Herrmann formulation finite elements, whereby the integrations are carried out in the current configuration at $t = n+1$ (MSC.Marc volume A, 2004). The strain measure is the true or logarithmic measure defined as

$$\varepsilon_{ij} = \frac{1}{2} \ln(B_{ij}), \quad (4.32)$$

or using the spectral decomposition theorem 4.32 can be expressed in terms of its principal values and directions as

$$\varepsilon_{ij} = \frac{1}{2} \ln(\lambda_A) n^A_i n^A_j \quad (4.33)$$

(MSC.Marc Volume A, 2004).

It is common practice in the finite element method to use numerical integration techniques to process all of the stiffness and load vector information. MSC.Marc uses standard Gauss quadrature.

4.6 Numerical Integration Techniques

It is common practice in the finite element method to use numerical integration techniques rather than analytical integration. MSC.Marc uses standard Gauss quadrature in order to evaluate all integral equations. All integrals defined previously are therefore integrated as,

$$\iiint \phi dv \approx \sum_k \sum_j \sum_i \phi \hat{J} W^i W^j W^k \quad (4.34)$$

or,

$$\iint \phi dv \approx \sum_j \sum_i \hat{J}_{2D} W^i W^j \quad (4.35)$$

where W^i , W^j , and W^k are weighting factors. Since this is a well known and documented technique, it is omitted in this manuscript. For detailed information, consult MSC.Marc Volume B, p. 2-21, Humphrey 2002, p. 232, Reddy 1993, p. 251.

4.7 Treatment of Contact in MSC.Patran and MSC.Marc

In this thesis, contact is being considered between the implanted stent and the artery using the deformable-deformable formulation in MSC.Marc. Contact is implemented in Marc directly and therefore no new Euler equations are generated from a Lagrange multiplier method and a semi-definite equation system is avoided (this was not the case in the enforcement of incompressibility). A penalty parameter although simpler to implement, due to the open-endedness of the magnitude of the penalty parameter, it can allow penetration to occur and contact is cannot be enforced exactly since a finite number must be provided (MSC.Marc Volume A, 2004). The contact constraint is therefore implemented directly into the stationary potential energy principle as noted in 4.10b.

Equation 4.36 describes the contribution of contact to the total potential energy equation

$$C_C = \int_a p_N(\mathbf{u})(u_A - u_B) \mathbf{n} da, \quad (4.36)$$

where p_N is the normal contact pressure load that depends upon the current configuration of bodies A and B in question. This contact pressure is defined by equation 4.37 where, f_N is the equilibrating reaction force between bodies A and B and da is the area of the element surface in contact (MSC.Marc Volume A, 2004).

$$p_N = \int f_N da . \quad (4.37)$$

The friction model available in MSC.Marc is the Coulomb friction model (MSC.Marc Volume A, 2004). In this thesis, the “glue” option was used where once a node contacts a patch on the opposite body, the eight nodes on the face of a 20-node hexahedral element and the contacting node have multi-point constraint equations that restrict the future motion to be strictly in the normal direction. In addition, the friction condition will contribute to the stiffness of the system and is calculated as in 4.38:

$$K_{ij} = \frac{\partial f_t}{\partial v_j} . \quad (4.38)$$

Although equation 4.38 adds non-symmetric stiffness contributions, these were taken to be symmetric to save computational time and memory as it was confirmed through experiments that these simulations differed less than 1% in the maximum principal Cauchy stress field in the artery. The constitutive equation for Coulomb friction in Marc is

$$f_t = \left(\frac{2\mu f_N}{\pi} \right) \arctan\left(\frac{v_j}{RVCNST} \right) \quad (4.39)$$

where μ is the coefficient of friction equal to one in the “glue” friction model, \arctan is the arctangent function and RVCNST varies between 1% and 10% of the sliding relative velocity v_j , depending on how close to convergence an increment is (MSC.Marc Volume A, 2004). Figure 4.2 is an illustration of the described friction model, where K has been defined in 4.38, F_1 and F_2 are the forces and u_1 and u_2 are the displacements at the respective locations.



Fig. 4.2. Illustration of friction model implemented in MSC.Patran and MSC.Marc. Taken from MSC.Marc Volume A, 2004.

Equilibrium of figure 4.3 yields equations 4.40 and 4.41:

$$K_1 u_1 - K_2 u_2 = F_1, \quad (4.40)$$

$$-K_1 u_1 + K_2 u_2 = F_2. \quad (4.41)$$

Similarly, 4.42 – 4.43 are in terms of the relative velocities,

$$K_1 v_1 - K_2 v_2 = F_{1t}, \quad (4.42)$$

$$-K_1 v_1 + K_2 v_2 = F_{2t}. \quad (4.43)$$

Equations 4.42 – 4.43 are calculated incrementally as

$$K_1 \delta v_1^i - K_2 \delta v_2^i = \Delta F_{1t}^i, \quad (4.44)$$

$$-K_1 \delta v_1^i + K_2 \delta v_2^i = \Delta F_{2t}^i, \quad (4.45)$$

and similarly,

$$K_1 \delta u_1^i - K_2 \delta u_2^i = \Delta F_{1t}^i, \quad (4.46)$$

$$-K_1 \delta u_1^i + K_2 \delta u_2^i = \Delta F_{2t}^i. \quad (4.47)$$

Since the problem being solved is considered to be static, velocities are derived from the displacement increments δu^i and the time increment Δt as

$$\delta v^i = \frac{\delta u^i}{\Delta t}. \quad (4.48)$$

The velocities are updated by adding the increments to v_1^i and v_2^i , where the superscript $i - 1$ refers to the beginning of iteration i .

$$v_1^i = \Delta v_1^{i-1} + \delta v_1^i, \quad (4.49)$$

$$v_2^i = \Delta v_2^{i-1} + \delta v_2^i. \quad (4.50)$$

Analogously with the displacements,

$$u_1^i = \Delta u_1^{i-1} + \delta u_1^i, \quad (4.51)$$

$$u_2^i = \Delta u_2^{i-1} + \delta u_2^i. \quad (4.52)$$

Finally, from equations 4.48 and 4.40, 4.41

$$\frac{1}{\Delta t} K^i \delta u_l^i = \Delta F i_l \quad (4.53)$$

$$\frac{1}{\Delta t} K^i \delta u_l^i = \Delta F i_2. \quad (4.54)$$

Contact is detected in Marc by tracking the nodes belonging to a contact body with a contact boundary condition. Contact occurs when two nodes are within a tolerance distance equal to 5% of the smallest element edge length of the bodies with contact boundary conditions. This is illustrated in equation 4.55:

$$(u_A - u_B) \mathbf{n} < TOL. \quad (4.55)$$

The aforementioned constraining equations are then applied to the appropriate nodes in contact. Stresses from the interpolation functions are then extrapolated to the Gauss integration points for normal stress calculation. Nodal sliding relative velocities are then calculated beginning with the converged value from the previous iteration. Once a node comes into contact, the “glue” or “stick” friction model then forces the relative sliding velocity to zero. The force and stiffness contributions are numerically integrated and extrapolated to the closest node and then added to the appropriate assembled equations. The contact bodies were defined by C^2 -continuous Non-Uniform Rational B-Splines surfaces (NURBS) – see figure 4.3- rendering an accurate calculation of the normal vector in 4.36.

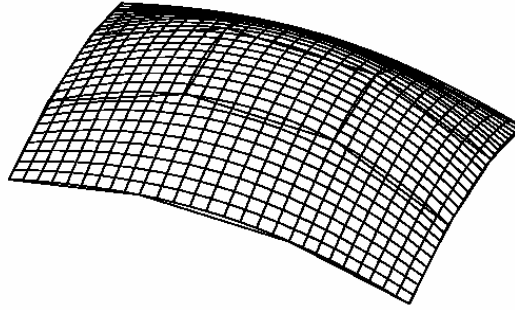


Fig. 4.3. Illustration of a NURBS surface in Patran. Note the difference between the mesh and the NURBS surface. The normal is calculated based on the NURBS surface.

In each iteration, MSC.Marc checks for penetration by solving 4.56, where K^T is the tangent stiffness matrix in the current configuration, δu_i is the converged displacement value and R_{i-1} are the residuals from the previous iteration subject to the tolerance value described in section 4.5.

$$K^T \delta u_i = R_{i-1}. \quad (4.56)$$

In the event that penetration has occurred, the displacement increment becomes

$$\Delta u_i = \Delta u_{i-1} + s \delta u_i \quad (4.57)$$

where s is a factor between zero and one required to avoid penetration in 4.59

$$s \in [0, 1], \quad (4.58)$$

$$(uA - uB)n < 0, \quad (4.59)$$

and the total displacement then becomes

$$\Delta U^n = \Delta u^{n-1} + \Delta U_i. \quad (4.60)$$

Contact status is based off of 4.59 and friction information. The final displacement calculated in 4.60 is used to calculate all strains and stresses. When global equilibrium is achieved (based on the criteria in section 4.5 and 4.6), the next increment is calculated (MSC.Marc Volume A, 2004).

4.8 Functional Forms for Strain Energy Density Functions in Patran and Marc

The functional form for strain energy density functions used in Patran and Marc to solve nonlinear elasticity problems with large strains and large deformations are expressed as functions of stretch ratios. Namely, these are kinematic quantities associated with characteristic geometric features such as the radius, circumference and length, in the case of a blood vessel; or for the edges of a block whose volume is enclosed in $\{X_i\}$ (i.e., $-1 \leq X_i \leq 1$ for $i = 1,2,3$). Although it is much more efficient to represent cylindrical-like objects in a cylindrical coordinate system, MSC.Patran and MSC.Marc have a limitation whereby contact mechanics of deformable bodies are not supported by cylindrical curvilinear interpolation functions during the duration of this study and its documentation. Therefore, although computationally more costly, the analyses must be carried out in a Cartesian coordinate system with orthonormal bases E_i for $i = 1, 2, 3$. A coordinate transformation is therefore required to view results in the more convenient cylindrical coordinate system. Stretch ratios are represented by the equation below,

$$\lambda_i = \frac{(L_i + u_i)}{L_i}, \quad (4.61)$$

where L_i represents the reference length and u_i represents subsequent deformation in the x-y-z space. The incompressibility constraint as a functions of stretch ratios is expressed as

$$\lambda_1 \lambda_2 \lambda_3 = 1. \quad (4.62)$$

This constraint may also be represented by the third invariant of the left (or right)

Cauchy-Green stretch tensor as

$$III = \lambda_1^2 \lambda_2^2 \lambda_3^2 = 1 \quad (4.63a)$$

or,

$$III = \frac{(e_{ijk} e_{pqr} B_{ip} B_{jq} B_{kr})}{6} = \det(B). \quad (4.63b)$$

The first and second invariants are represented as

$$I = \lambda_1^2 + \lambda_2^2 + \lambda_3^2 \quad (4.64a)$$

or

$$I = B_{ii}; \quad (4.64b)$$

$$II = \lambda_1^2 \lambda_2^2 + \lambda_1^2 \lambda_3^2 + \lambda_2^2 \lambda_3^2 \quad (4.65a)$$

or

$$II = \frac{B_{ij}B_{ij} - (B_{ii})^2}{2}. \quad (4.65b)$$

To simplify implementation of incompressibility constraint numerically, equation 4.10b is recast in terms of the first deviatoric left Cauchy-Green stretch tensor invariants \hat{I} , and the volumetric contribution as

$$W = W_{deviatoric} + W_{volumetric} \quad (4.66a)$$

$$W = C_{10}(\hat{I} - 3) + C_{20}(\hat{I} - 3)^2 + C_{30}(\hat{I} - 3)^3 + \frac{9k}{2}(J^{\frac{1}{3}} - 1)^2. \quad (4.66b)$$

4.9 Nonlinear Solution Methods

Nonlinear systems of equations can be extremely expensive in computational cost and time and usually require iterative solution methods in order to achieve equilibrium (MSC.Marc volume A, 2004). Since a numerical method cannot enforce equilibrium exactly, a residual load correction must be applied in order to maintain equilibrium below the tolerance threshold value. This prevents the residual from increasing from increment to increment and therefore any accumulation of unbalanced forces is avoided by this method (MSC.Marc volume A, 2004). Equation 4.67 is the basis for maintaining equilibrium in the Newton Rhapsion method (see figure 4.4) using the multi-frontal sparse direct solver,

$$K(u^n)\delta u^{n+1} = F(u) - R(u), \quad (4.67)$$

where u is the displacement, K is the tangent stiffness matrix, δu is the primary variable increment, F is the applied load vector, and R is the residual load vector from the internal stresses.

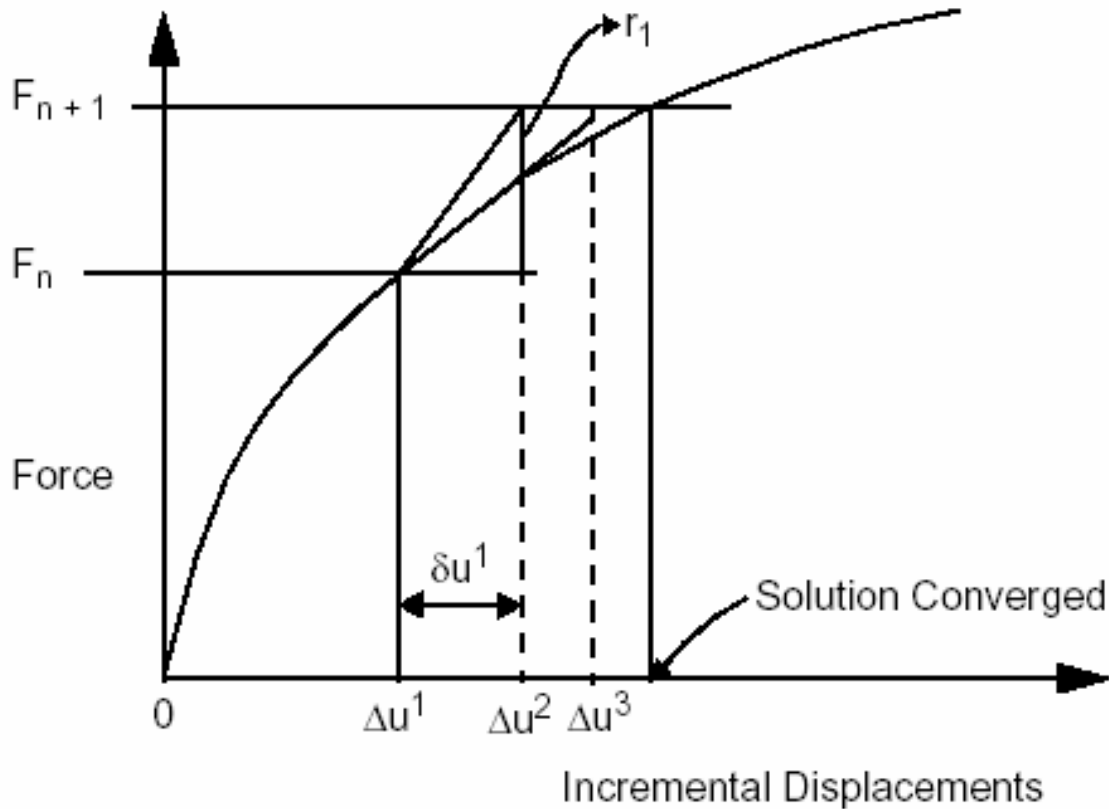


Figure 4.4. Illustration of the Newton-Raphson method.

The superscript n denotes the solution at the n th iteration. The solution for the $(n+1)$ th iteration is obtained by solving 4.68:

$$(\delta u)^{n+1} = [K(u^n)]^{-1} \{F(u)\} \quad (4.68)$$

subject to the tolerance threshold of 4.69:

$$\frac{|R|}{|F_{reaction}|} \leq TOL \quad (4.69)$$

Once a solution to 4.68 is found subject to 4.69, the total solution of the $(n+1)th$ increment is

$$\Delta u^{(n+1)} = \Delta u^n + \delta u \quad (4.70)$$

(MSC.Marc Volume A, 2004). Figure 4.5 is a flow diagram of the solution procedure employed in MSC.Marc.

4.10 *Stented Artery Model Creation in MSC.Patran*

The experimental measurements of the harvested arteries reported in section 3 were used to create numerical models in Patran using the Linux platform for parallel computation. The computer cluster used to solve this boundary value problem consists of a head node with dual 2.8 Ghz 32-bit processors, 4GB of random access memory (RAM), 4 200GB hard drives with a RAID level 5 as a data back-up and ASUS motherboards with 800 Mhz front side bus speed. The slave nodes (15) consisted of single 2.8 GHz 32-bit processors, 2GB of RAM, 80GB of hard disk space, and ASUS

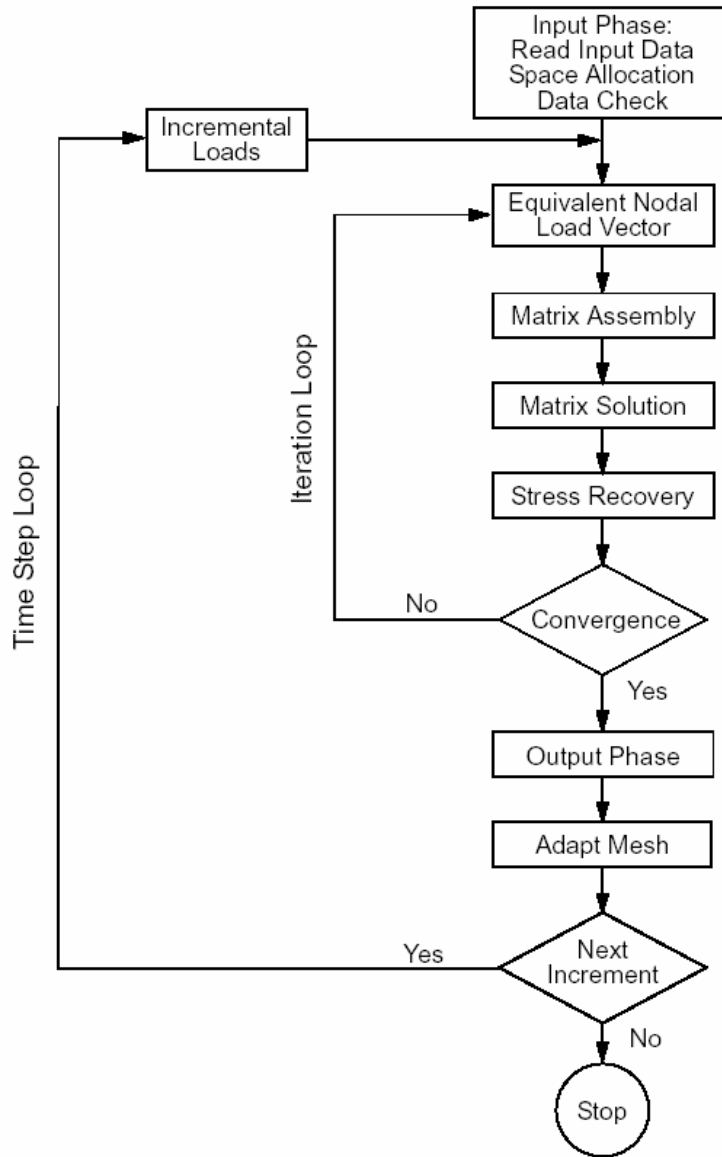


Fig 4.5. Solution procedure implemented in MSC.Marc. Taken from MSC.Marc Volume A, 2004.

motherboards with 800 Mhz of front side bus speed. The operating system of the computer cluster was RedHat 9. The Linux version of Patran was 2005 release a, and Marc 2005 release a.

4.10.1 Arterial Geometry Creation

The artery was approximated as a perfectly straight homogeneous round cylinder. The thickness of the arterial wall was assumed constant, and the measurements came from table 3.1. Due to axisymmetry, only a quarter of the circumference of the artery and stent were modeled to save computational memory and processing time (see figure 4.6).

The geometry of the blood vessel was generated by creating a point at a luminal vertex and sweeping it in the radial direction using the appropriate thickness measured in the reference configuration. The resulting line was then swept 90° in the circumferential direction and a surface was created. This surface was then extruded in the axial direction three stent lengths – the middle stent length was the contacting region – such that edge effects would disappear in the unstented portion of the vessel. Stent geometries were created through a custom parameterization technique developed with a Matlab program.

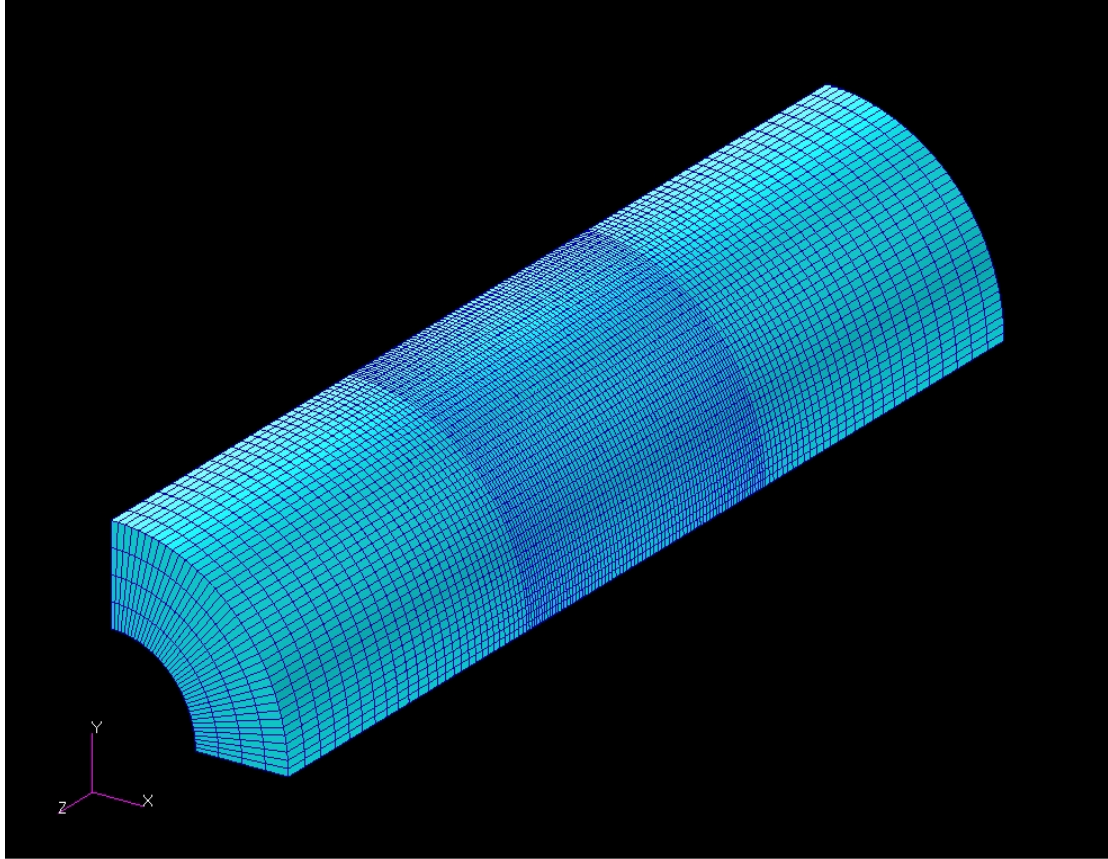


Fig. 4.6. Quarter model of the artery modeled used to save computational resources and time. The bottom edge corresponds to the 0° position and the edge facing to the left corresponds to the 90° position relative to a polar coordinate system. In-plane symmetry boundary conditions were applied to these edges restricting deformation to remain in their original plane.

4.10.2 Stent Geometry and Parameterization

Large scale clinical trials (Kastrati et al., 2001) demonstrated clinical evidence that in-stent restenosis rates depend on stent design. Table 4.1 summarizes the restenosis rates for stainless steel balloon expandable stents used in the above mentioned clinical trial. The clinical trial consisted of 4,510 unselected patients – exclusion criteria included failure of the procedure and an adverse outcome within the first month after the procedure. Restenosis was considered effective when there was a 50% or greater diameter stenosis at a 6-month follow-up. They performed a logistic regression model for restenosis where several risk factors were analyzed and compared. The results of this study showed that the greatest risk factor for a binary restenosis – 50% or greater diameter stenosis at 6-months – was small vessel diameter. Specifically, coronary arteries with a 2.7 mm diameter exhibited a 79% increase in risk for restenosis when compared with a 3.4 mm diameter coronary. The second strongest risk factor was stent design, as reported in the article: “... the strength of the predictive model is largely attributable to differences in stent design, and that these differences are highly responsible for the variability in the risk for restenosis ...” (Kastrati et al., 2001). Given this strong clinical data that stent design is a determining factor of restenosis, we used the finite element method to provide insight as to how restenosis rates can be improved by extracting biomechanical evidence and applying it to stent design. Rather than evaluating actual stent geometries used in Kastrati et al., (2001), we elected to determine specific design criteria by designing stents parametrically and comparing their biomechanical impact to numerical models of stented arteries.

Table 4.1

Summary of binary restenosis rates from Kastrati et al., 2001. Binary restenosis is defined as 50% or greater diameter stenosis at a 6-month angiographic follow-up. This clinical study included consisted of patients with exclusion criteria limited to procedural failure and adverse effects within a month of stent implantation. Total number of patients was 4,510 whereby stent design was found to be a strong independent factor influencing restenosis rates.

Stent	Binary Restenosis Rates
Guidant Multi-Link	20%
Jomed Jostent	25.8%
J&J Palmaz-Schatz	29%
PURA-A	30.9%
Inflow Steel	37.3%
NIR	37.8%
Inflow Gold	50.3%

4.10.2.1 *Stent Parameterization*

Stents were designed parametrically in order to classify and evaluate geometric features commonly seen in stent designs as deleterious or beneficial to the mechanical environment of a stented artery. It is expected that some of these features in specific

combinations are likely to be more detrimental than others to vessel patency. With such a parameterization technique, it is possible to optimize geometric characteristics of stents to create a more favorable mechanical environment that the artery is subjected to. The parameters of interest in this investigation were strut spacing (h), axial amplitude (f) and strut radius of curvature at the crown junctions (ρ)³ – see figure 4.7. Thus, stents studied herein were generic stent panels consisting of concentric rings of sinusoid-like curves linked by straight bars of varying lengths. Figure 4.7 is a depiction of such a generic stent identifying the parameterization technique. A matlab subroutine was written in order to create the stent designs automatically, checking to see if the geometries can actually exist. A separate program was then created to automatically generate three-dimensional stents in Patran. This technique provided automated design and generation of stents, requiring little intervention from the solid modeling perspective in Patran. These programs are available in appendix A.

All stent designs had a constant thickness of 100 microns (10E-06 meters) and an outer radius 10% larger than the intimal systolic radius of the artery with a value of 2.375 mm. The stents were given names with the objective to identify all three parameters easily and without the need to refer to actual measurements. An SRA – strut spacing, radius of curvature, amplitude – naming system was devised for this purpose. Spacing took values of either “1” or “2” to identify small or large spacings respectively

³ The radius of curvature is measured at the inner edge of the stent with a specified thickness. When referring to a stent with a 0 mm radius of curvature, it is the inner stent edge of ρ that is being described, while the radius of curvature on the outer edge is equal to the inner edge radius plus the stent strut thickness. As a side note, stents are created onto a manifold cylindrical surface in 3-D space and are then given a thickness by extruding the stent radially 0.10 mm. This information can be extracted from the aforementioned matlab subroutines available in appendix B.

(1.1875 mm vs. 2.375 mm). Similarly, radius of curvature is given an alphabetic symbol in order to make it simpler to recognize when reading this manuscript. The letters for radius of curvature are “Z” representing a zero radius of curvature, “A” represents 0.148 mm, and “B” represents 0.296 mm. The amplitude was given a numerical symbol with magnitude proportional to its actual value, where “1” represents 0.59375 mm, “2” represents 1.1875 mm, and “3” represents 1.78125 mm. Table 4.2 is a summary of the stent parameters studied herein, and figure 4.8 is a graphical depiction of the designed stents.

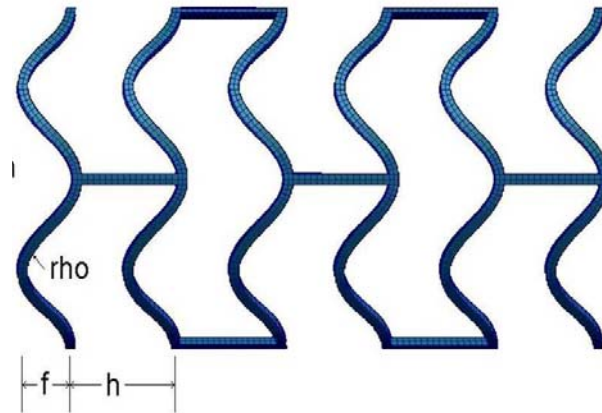


Fig. 4.7. Generic stent showing the three parameters of interest. F is the axial amplitude, h is connector bar length (or strut spacing), and ρ is radius of curvature at the crown junctions. These three parameters were varied incrementally to design new stents.

Table 4.2

Summary of stents studied in this thesis. Note that there is a stent naming protocol that identifies each stent corresponding to its three parameters. The naming protocol follows an SRA format (spacing, radius or curvature, amplitude). Spacing 1 represents 1.1875 mm, spacing 2 represents 2.375 mm. Radius of curvature (rho) takes the following values: Z represents 0 mm, A represents 0.148 mm and B represents 0.296 mm. Amplitudes (f) are represented as follows: 1 represents 0.59375 mm, 2 represents 1.1875 mm, and 3 represents 1.78125 mm.

Stent	Strut spacing in mm (h)	Axial amplitude in mm (f)	Radius of curvature in mm (rho)
1Z1	1.1875	0.59375	0
1A1	1.1875	0.59375	0.148
1B1	1.1875	0.59375	0.296
1B2	1.1875	1.1875	0.296
2Z3	2.375	1.78125	0
2A3	2.375	1.78125	0.148
2B2	2.375	1.1875	0.296

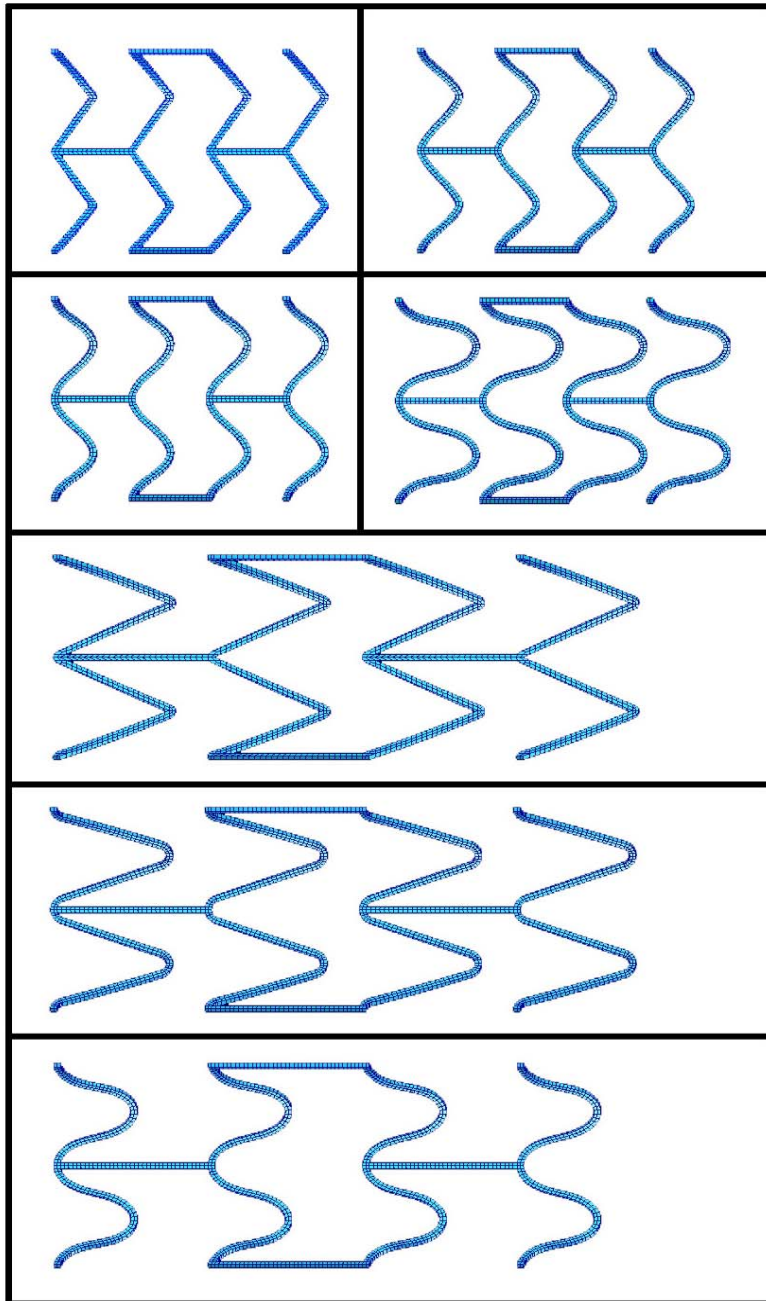


Fig.4.8. Stents analyzed in this study. From right to left beginning at the top: Stent 1Z1, 1A1, 1B1, 1B2, 2Z3, 2A3, 2B2. Note the variation in geometric parameters.

4.10.3 Application of Boundary Conditions

The boundary conditions applied to the boundary value problem included displacement boundary conditions, pressure, and contact. The vessel was stretched in the axial direction by 59% simulating the axial tethering that was measured in vivo (see table 3.1). Since a quarter model was used to save on computational time (see figure 4.6), it was necessary to apply boundary conditions on the arterial wall at the 0° and 90° positions such that when inflated, the artery would deform uniformly while the wall at those positions would remain in its original plane. The vessel was then inflated by applying a pressure of 225 mmHg. This pressure was determined by numerical experiments and it was found that this value dilated the artery enough such that the 10% oversized stent could be “implanted”. The stent was originally positioned outside the artery and then translated in the axial direction (see figure 4.9) such that the stent and artery mid-points along that direction coincided. The pressure was then reduced to systole and subsequently to diastole. Analytic contact⁴ occurs before systolic pressure is achieved – see figure 4.10 for a graphical representation of the application of boundary conditions. In the Windows version of Patran it is possible to simply alter the contact table such that during inflation load step, the artery is allowed to pass through the stent without making contact. In subsequent load steps the contact table can be modified and re-activated so that contact may occur during systole and diastole. However, the Linux version does not support modification of the contact table and therefore a stent

⁴ Analytic contact is defined by NURBS surfaces. NURBS stands for “non-uniform rational B-splines”, and they have C_2 continuity, defining the normal more accurately in the deformed configuration.

translation boundary condition was added. The boundary conditions on the stent beyond the translation step, included in plane deformation for the for the struts identical to those applied to the artery, and an analytical contact boundary condition.

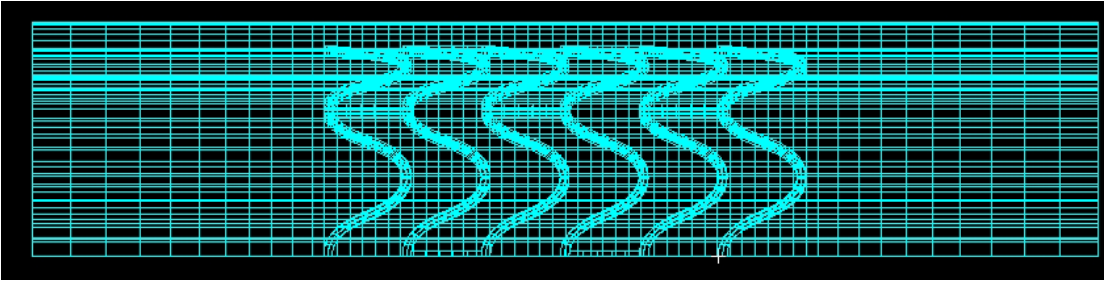


Fig. 4.9. Illustration of relative position of stent and artery after translate boundary condition.

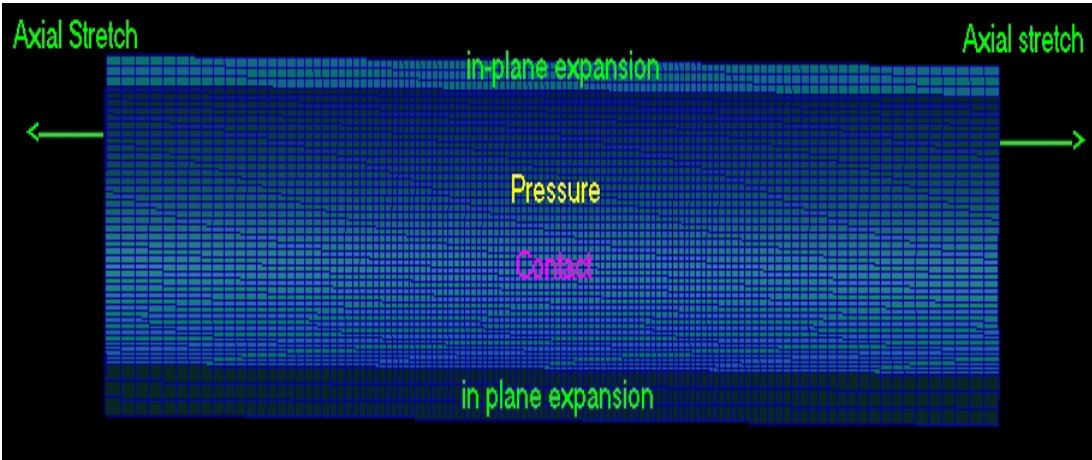


Fig. 4.10. Graphical representation of the application of boundary conditions for this boundary value problem. Note that the translation boundary condition is not shown.

4.11 Data Analysis Methods

Results of the finite element method with MSC.Patran and MSC.Marc are nodal values by default. The resulting table of nodal values can be plotted as a colormap of the model for qualitative analysis. The table can also be evaluated by manipulating the quantitative outputs. Both approaches are used herein to provide a more complete conception of the impact of stent design on stresses in the artery wall.

The symmetry boundary conditions necessary to take advantage of the reduced computational load, can cause edge effects due to the nature of the contact⁵ as seen in figure 4.11.

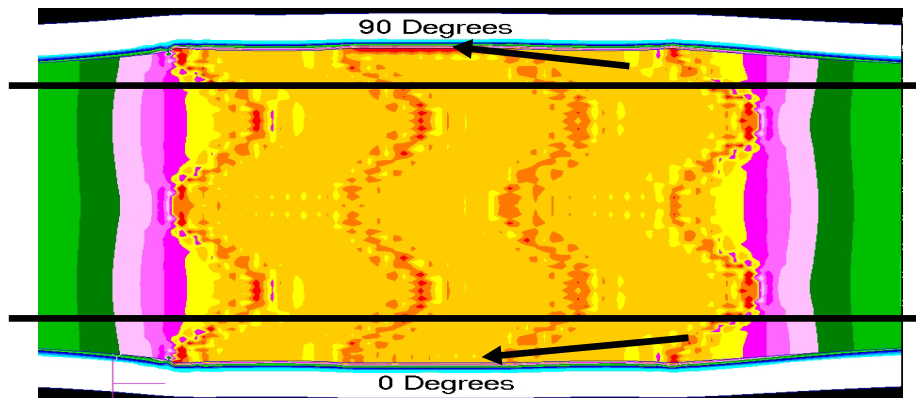


Fig. 4.11. Stress colormap result for stent 1B1. Note the absence of the connector bar stress imprint at the 0° position. For this reason, only the regions between 11.25° and 78.75° of all stents were analyzed quantitatively – between the black lines. Only stents 1B1 and 1B2 displayed this anomaly.

⁵ The contact boundary condition is not a symmetric one, and therefore it can occasionally cause anomalies in the results, such as those detected in two of the stented artery simulations.

These edge effects can cause erroneous data and were therefore avoided. The model represented 90° of the actual stented artery. Data from 11.25° to 78.75° were used for the quantitative analysis described below.

Seven stented artery models employing distinct variations of the stent parameters outlined above were developed. Data from the contacting arterial solid – which extended half a stent radius beyond the stented section – were acquired at diastolic and systolic pressures; on the intima and adventitia. A matlab subroutine was developed where the output variables of the arterial solid model in question – displacements and stresses – were sorted relative to spatial position. Once the data were sorted, stent edges were identified by a coordinate searching algorithm whereby the stented region was parsed into 4 equally axially spaced regions. The displacement and stress data of the parsed sections was then organized such that the first stented section (left edge of the first fourth of the stent) was appended to the left edge of the unstented artery model. The second and third pieces of the stent (50^{th} and 75^{th} percentiles respectively) were then consecutively inserted multiple times building a larger stented artery model than the original. When the new stented artery model reached close to 30 mm in length, the fourth and final piece of the stent was appended followed by the right edge of the unstented model. With this method, all stented artery models were nearly the same length. Figure 4.12 shows the final geometries of the stents – compare with figure 4.8 to see original relative stent sizes. This procedure provided an unbiased comparison relative to axial stent length.

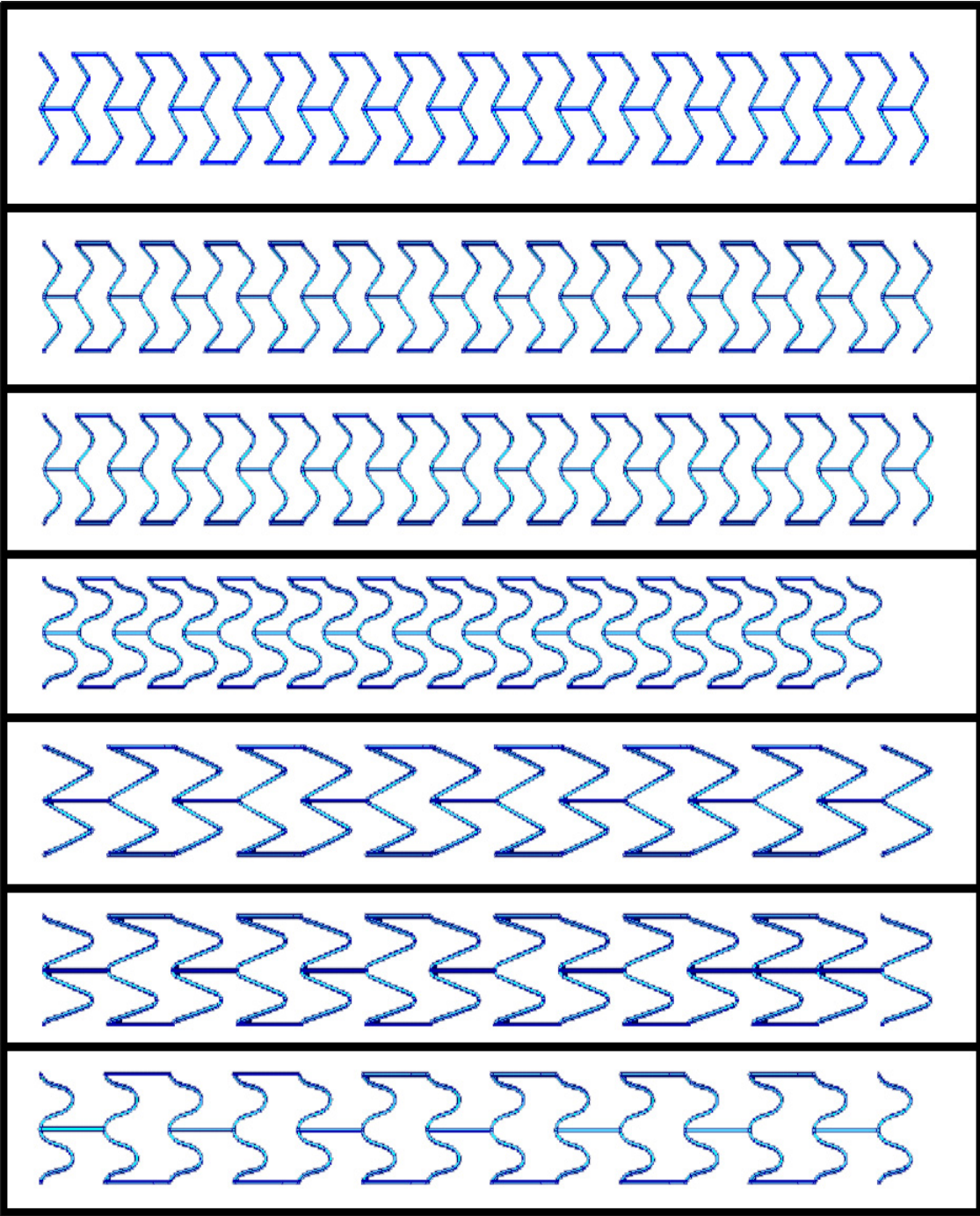


Fig. 4.12. Illustration of modified stent lengths. Note that all the stents are approximately the same size. From top to bottom: Stent 1Z1, 1A1, 1B1, 1B2, 2Z3, 2A3, 2B2.

The output stress data for the modified stented artery models – nodal values for hoop stress, radial stress and maximum principal stress – were then grouped into designated ranges designed to ease comparison of the colormap plots. Thus, the groupings are necessarily different for each stress measure. Using this data, a percent of the vessel “critically stressed” was calculated according to the groupings. The three groupings were designated as the following:

Class I critical stresses – highest threshold, indicates the highest stresses observed among all stents. Class I critical stresses are regions of maximum stress and therefore regions where an adverse biological response is most likely to occur.

Class II critical stresses – lower threshold than Class I, includes Class I data.

Class III critical stresses – the lowest threshold, includes class I and II data.

Using this classification system, the percent of the total nodes that correspond with these critical values is calculated as an approximation of the percent of the artery that is “critically stressed”. To be clear, the purpose of the aforementioned classifications is to facilitate comparison of stent designs. There are no implications whatsoever to biological response – they are merely regions where affliction is most likely to occur. Thus, class III stresses may be sufficient to induce unfavorable outcomes.

4.12 Mesh Convergence and Mesh Convergence Criteria

In finite element method studies, it is of paramount importance to exercise mesh refinement – increase the number of nodes of the model – in order to determine to what degree the solutions of primary and secondary variables change with increases in nodes.

Ideally, one performs mesh refinement until there is no change in the sought solution to primary and secondary variables.

The mesh convergence study in this thesis consisted of a three step process. The first step was to perform mesh refinements in the model of the artery alone – with no contact – observing the variation of maximum principal stress distributions. The second step was to perform refinements in stents themselves by applying a pressure load on the outside of the stent and observing changes in displacements⁶. The first step of the process – vessel mesh density study – was carried out by running simulations of a vessel being pressurized to 225 mmHg (30 kPa) and stretched by 59% in the axial direction - the measured in vivo length – while applying the aforementioned symmetry displacement boundary conditions in the xz and yz planes (see figure 4.6). The criterion used for the isolated vessel mesh convergence – alternatively, mesh independence – was that the maximum principal Cauchy stress field in the lumen and adventitia of the artery had to vary by less than 1%. The second step in the process, consisted of applying a pressure load of 450 mmHg (60 kPa) to the outside surface of the stent and observing changes in displacement. The mesh was deemed converged when changes in displacement were less than 1% in radial direction, which corresponded to stents with a 20-noded serendipity hexahedral element edge length of 0.10 mm. The third phase of the mesh convergence was to run stented artery models while increasing the mesh density of the artery until stresses in the artery varied the least possible. The elements used were also hexahedral 20-noded serendipity elements (see equations 4.13 – 4.17

⁶ Stent convergence criteria was based solely on changes in solutions to displacement and not on stresses because stress distributions in the stent were not of interest in this thesis.

and figure 4.1). Only the elements in the artery were increased, since the displacement of the stent was already converged, and stresses in the stent were not relevant to this study. In addition, the mesh in the vessel was not uniform to save computational time. The middle solid (where contact occurs) was meshed with a *two-way-bias* mesh where there were two element lengths that were specified (L1 and L2 in figure 4.13). The areas of compliance mismatch (edges of the middle solid) were meshed with the greatest density because these areas are expected to have the highest stresses due to contact. The end solids were meshed with a *one-way-bias* where also two element edge lengths were specified. The elements near the middle solid were the same size as the edges of the middle solid. The elements in the far end of the vessel were significantly larger once it was determined that it was unnecessary that they too remained small (based on convergence results). The results for the final mesh convergence are reported below in table 4.3 and figure 4.13.

Table 4.3

Summary of the third phase of the stent-artery model mesh refinement study. Refer to figure 4.13 for a qualitative depiction of L1 and L2. Note that only one of the end solid mesh densities is illustrated. The other end solid has the same densities, except L1 and L2 are interchanged. A mesh refinement from mesh “A” to mesh “B”, produced approximately a 40% increase in nodes.

Mesh	Number of Elements along the Specified Dimension			
	Radial	Circumferential	Axial (mid solid)	Axial (end solids)
A	4	28	L2 = 0.126 mm L1 = 0.08 mm	L2 = 0.351 mm L1 = 0.08 mm
B	4	40	L2 = 0.08 mm L1 = 0.052 mm	L2 = 0.351 mm L1 = 0.052 mm

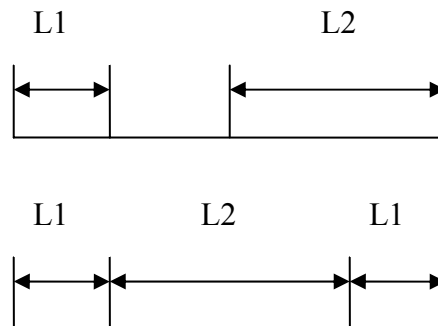


Fig. 4.13. Illustration of relative element lengths for mesh densities. Top illustration represents a one-way bias mesh used on the artery-end-solids. The bottom illustration represents the 2-way bias mesh used for the middle solid in figure 4.6.

Due to memory and other computational resource constraints associated with the Linux cluster, it was not possible to run all the simulations at a more refined mesh “B”. Furthermore, during the documentation of this thesis, it was not possible to re-submit all previous simulations that were analyzed in mesh “B” in the coarser mesh “A”. Ideally, all simulations would have been refined until the stress fields and data post-processing analysis techniques did not vary with an increase in the number of nodes. The next best solution would have been to analyze all finite element simulations with the same mesh density while having knowledge on how the behavior is at other mesh densities so that error can be assessed more precisely. However, our computer and time resource limitations only allowed us to run some simulations in mesh “A”, and some in mesh “B”. Table 4.4 summarizes which simulations were run with mesh “A” and mesh “B”.

Table 4.4.

Summary of mesh densities for each test stent. Note that stents with large spacing were all run on mesh “A” due to the increased size in artery which subsequently meant a very sharp increase in nodes. This increase in nodes proved impractical to run large spaced stent simulations in mesh “B”. Estimated computing times was approximately 50 days in the worst case attempted (stent 2B2).

Stent	Mesh
1Z1	B
1A1	B
1B1	B
1B2	B
2Z3	A
2A3	A
2B2	A

Below in figure 4.14 are bar graphs representing the differences between both meshes for stent 1A1 – small spacing, medium radius of curvature and small amplitude. Since stent designs are being compared relative to critical stresses, mesh convergence criteria is addressed in the same way.

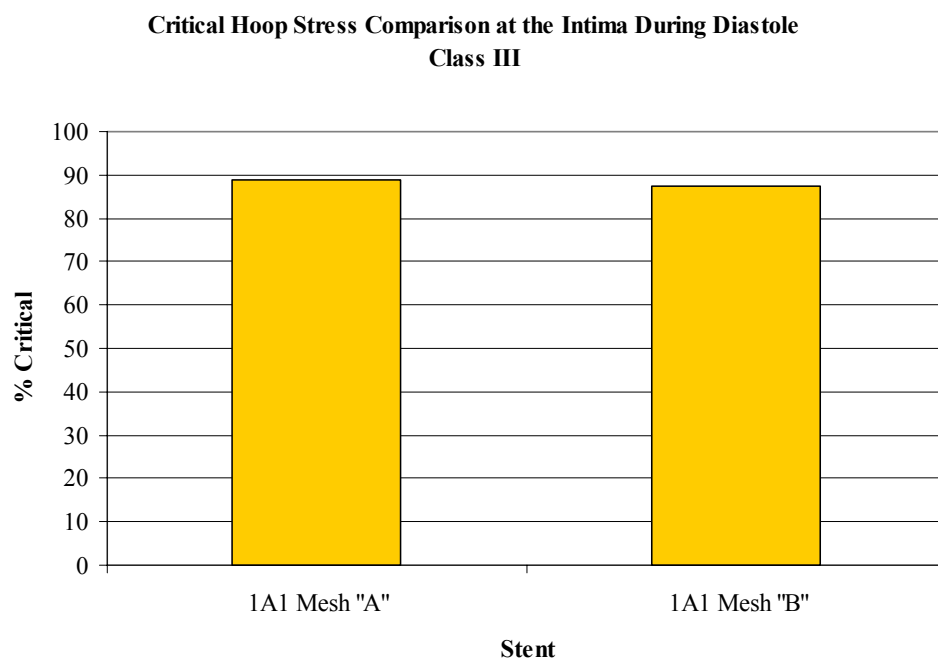


Fig. 4.14. Comparison of increasing mesh density between mesh “A” and mesh “B”. Note that the results are nearly identical in class III critical hoop stresses at the intima during diastole.

As can be appreciated from figure 4.14, refining the mesh from “A” to “B” in stent 1A1 has little effect on class III critical hoop stresses – close to 2% difference in critical stresses. When comparing class II critical hoop stresses during diastole, the intima in mesh “A” had approximately a 15% more area affected (see figure 4.15). It is expected that numerical models that were run on mesh “A” and not “B”, would likely decrease the class II critical hoop stresses imparted to the intima during diastole, likely improving our results in section 5.

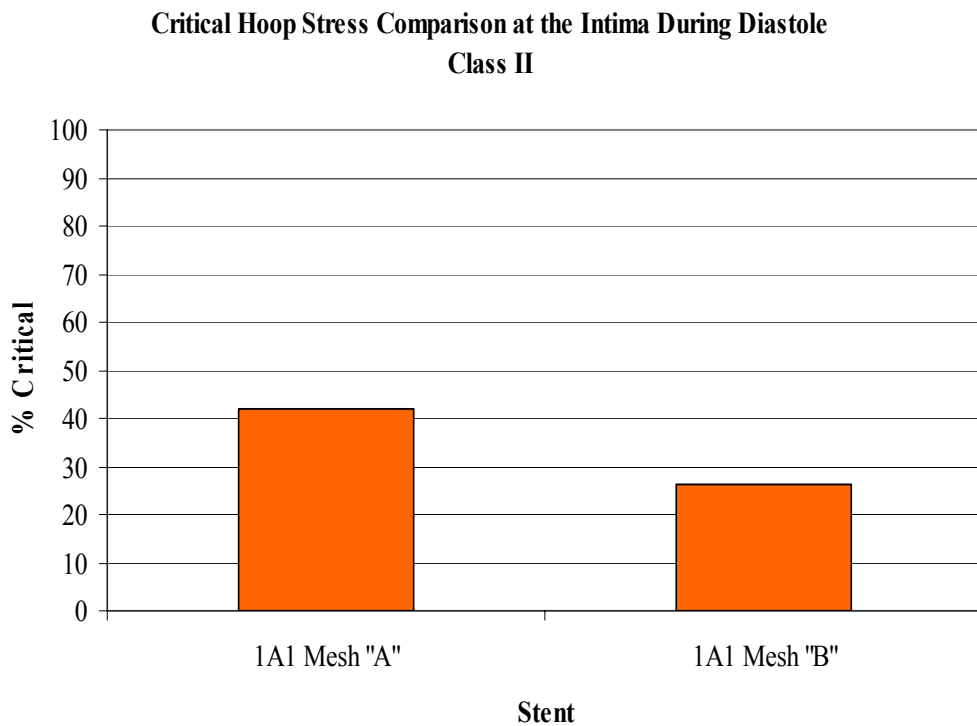


Fig. 4.15. Class II critical hoop stress variation between mesh “A” and mesh “B” for stent 1A1.

When comparing meshes in class I critical radial stresses (figure 4.16), there was a negligible difference in intimal area affected. Similarly, when comparing meshes relative to class II critical radial stresses, there was a 2.4% difference in areas affected (figure 4.17). Further mesh refinement is not expected to be significantly different.

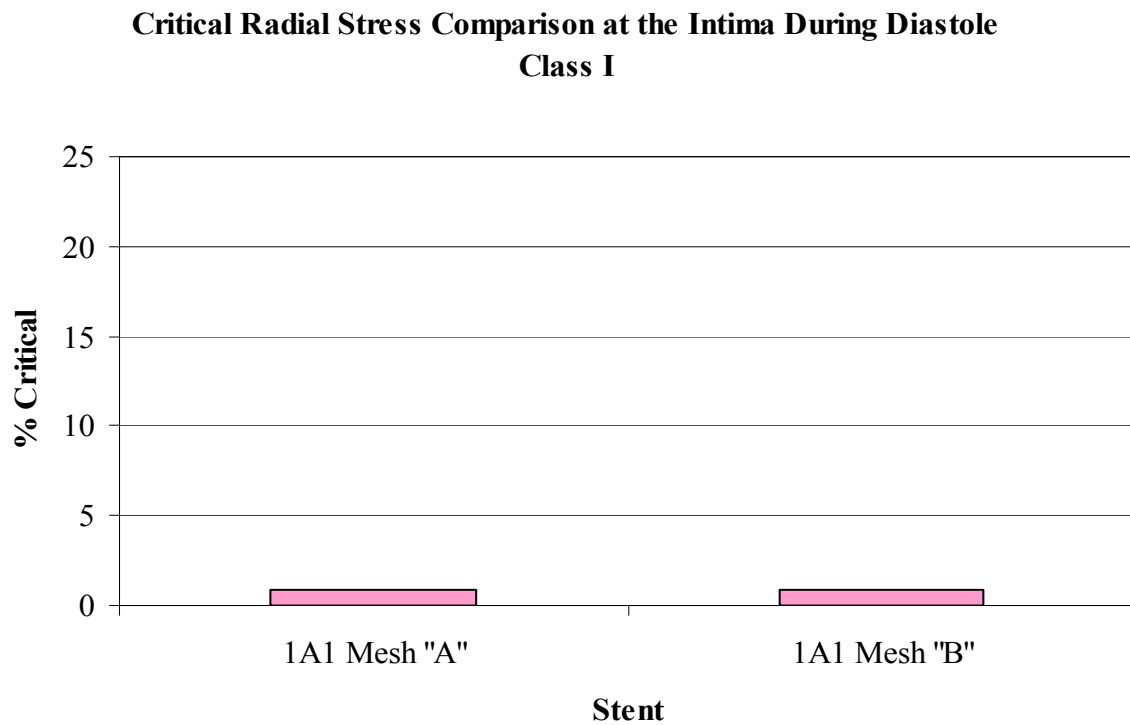


Fig.4.16. Critical class I radial stress comparison for mesh "A" (coarse mesh) and mesh "B" (fine mesh). There is a 0.01% difference in areas affected by this type of stress.

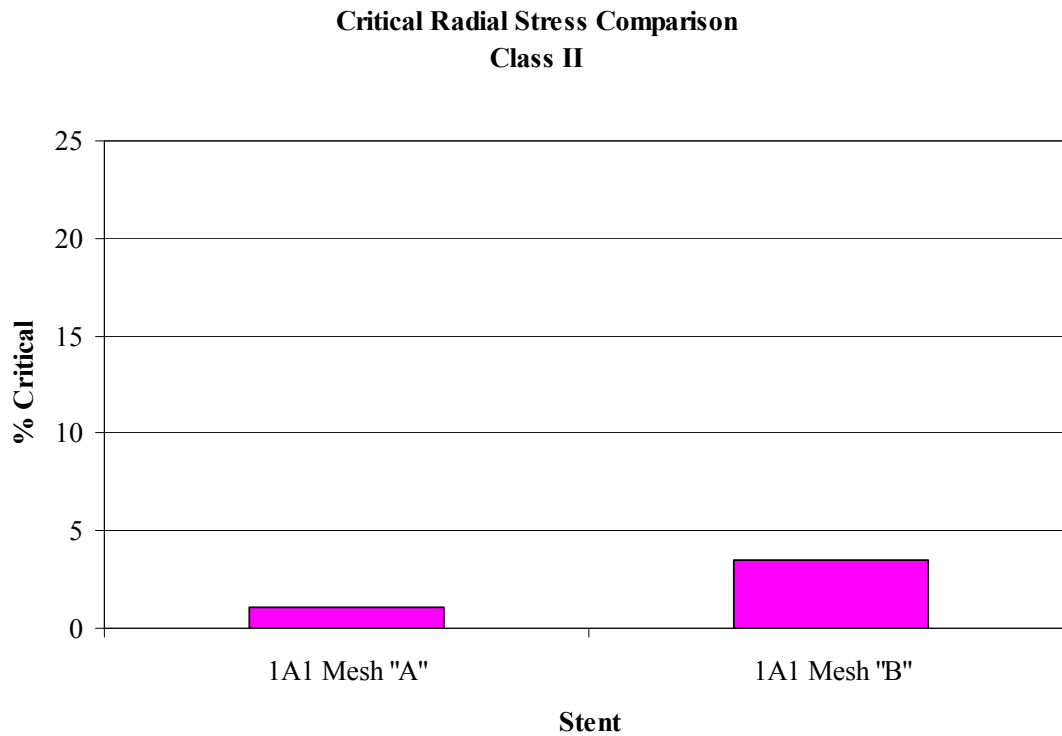


Fig.4.17. Differences observed between mesh “A” and mesh “B” for class II critical radial stresses for stent 1A1. Note the small increase in this type of stress associated with a finer mesh.

From this mesh convergence analysis, it is expected that the results for class II critical hoop stresses will be the most affected due to the limitation that not all models were run on the same mesh density. However, it will be shown that there are still discernible differences in stresses imparted to the artery wall that are due to stent design. Convergence tests during systole are not expected to change due to the predictable material response to an increase in pressure. Furthermore, if the adventitia were to be analyzed in a similar way as the intima, the mesh independence would be improved relative to the intima because there are no rough nonlinearities (contact) present in that

surface. Figure 4.18 shows how arterial radial displacement relative to the reference “unloaded” configuration in table 3.1.

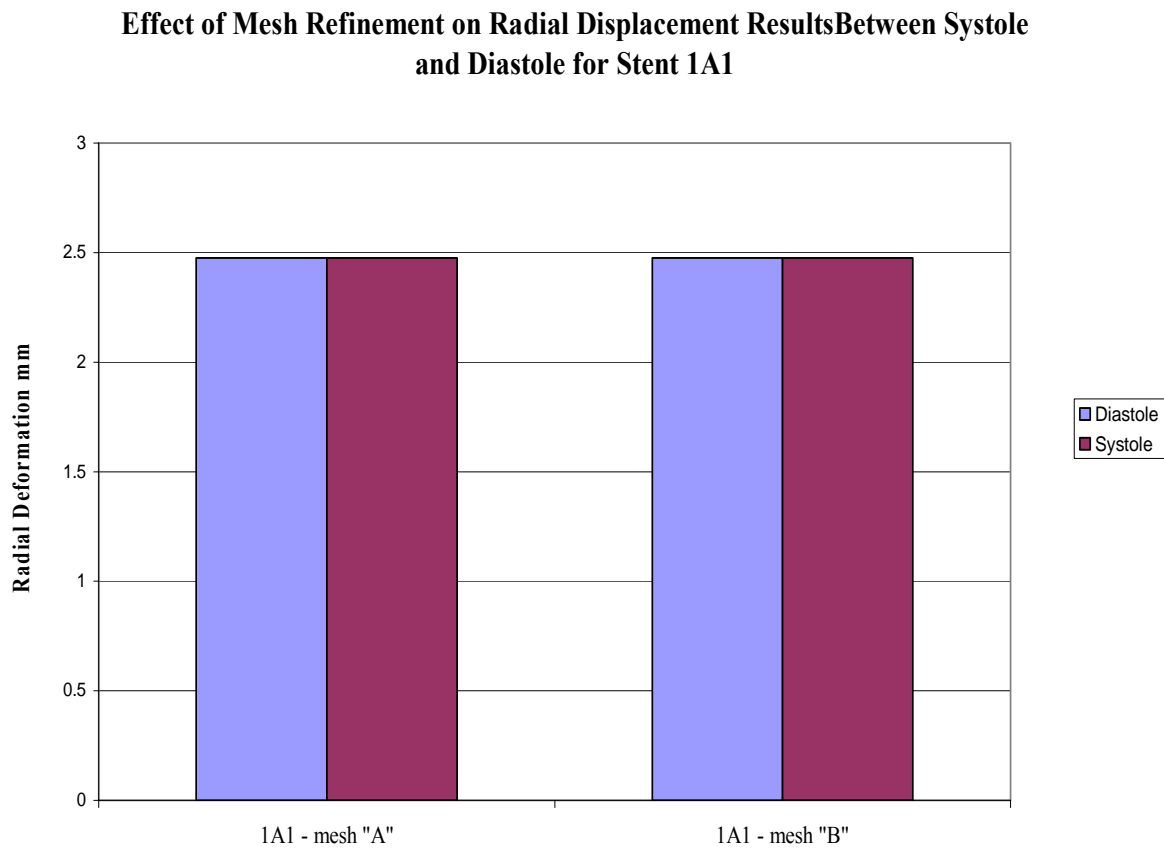


Fig. 4.18. Mesh refinement effect on radial displacement results for stent 1A1 at the intima during systole and diastole. Note that there is no difference in displacements from the coarser mesh A to the finer mesh B.

4.13 General Effects of Stenting – Numerical Models

The general effects on displacement associated with implanting a 10% oversized stent (relative to systolic intimal diameter) to an isotropic hyperelastic artery at the intima and adventitia are depicted in Figure 4.19.

Effect of Stenting on Intimal and Adventitial Radii For Selected Stents

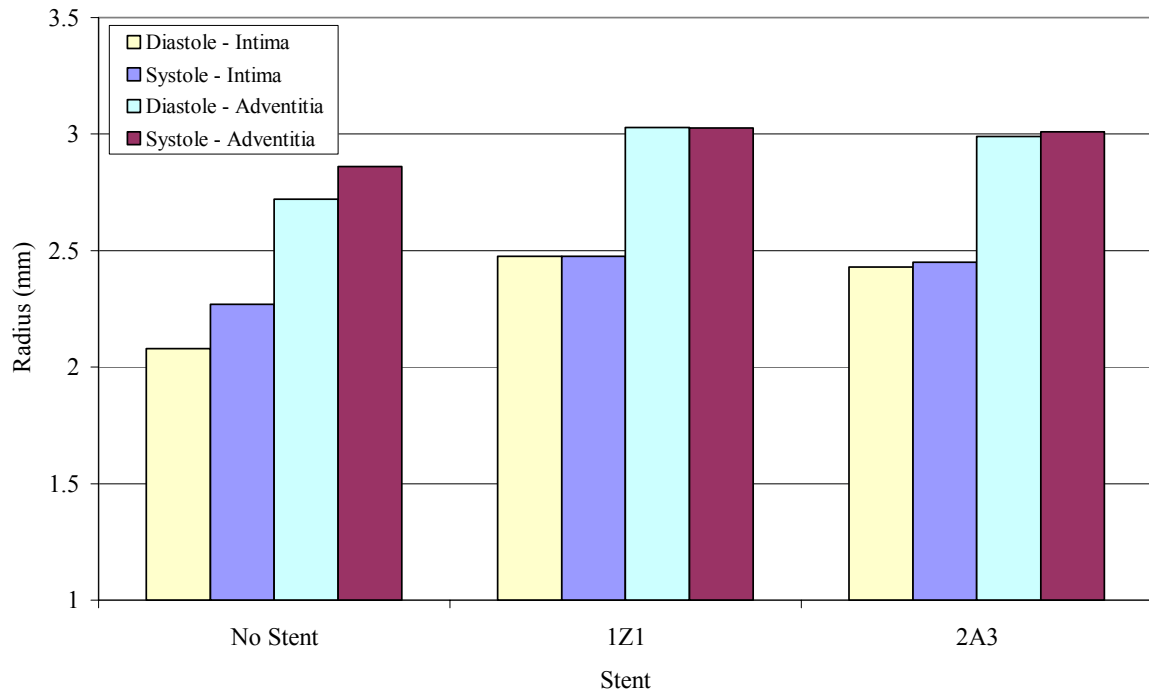


Fig. 4.19. Impact of implanting a stent in an isotropic hyperelastic artery relative to displacements. The 10% oversized stent had an outer radius of 2.47 mm. Note the increased rigidity of the artery as a result of stenting. Also, note the lack of cyclical stretch between systole and diastole at both intima and adventitia.

Note the stiff response of stented arteries - evidenced by a lack of difference in displacement. The stent design comparison results relative to stresses and displacements are described next.

5. RESULTS

The results of the simulations performed in this study indicate that the geometric properties of vascular stents influence the resulting stress field imposed on the artery. Regions of maximum stress are representative of the regions where an adverse biological response is most likely to occur. It will be shown that the hoop stresses have the greatest magnitude in the stented artery models studied herein as compared to other stress components, and therefore, hoop stresses dominate the make-up of maximum principal stresses. Since the documentation of this thesis, changes occurred in the critical stress thresholds for hoop stress described below (section 5.1). Please refer to appendix B for the journal publication version (submitted) of these stress threshold levels.

5.1 Assessment of Hoop Stresses on the Intima During Diastole

Results of the finite element method for stented arteries suggest that varying more than one parameter along the same path – consistently increasing or consistently decreasing all parameters – greatly enhances the differences that can be observed when comparing stent designs. Figure 5.1 shows hoop stress maps that different stents impart on the intima of the artery during diastole. In particular, note stent 2A3 how it has much lower stresses than any other stent analyzed in this study. It is evident that stent 2A3 has the majority of the intima affected by stresses from 390 kPa to 460 kPa (excluding the upper stress bound), whereas stents 1Z1, 1A1, 1B1 impart stresses on the order of 495 kPa to beyond 600 kPa. Stent 2A3 has large spacing (2.375 mm), a mid range radius of curvature (0.148 mm), and a large amplitude (1.78125 mm), whereas stents 1Z1, 1A1

and 1B1 have half the spacing, one third the amplitude of 2A3, and radii of curvature of 0 mm, 0.148 mm and 0.296 mm respectively. Radius of curvature “Z” has the sharpest stress concentration with respect to the radius (0 mm). While there is an observable stress pattern and magnitude difference in this range when comparing stents 1Z1, 1A1 and 1B1, the most dramatic difference can be appreciated from stent 2A3 to stents 1Z1, 1A1 and 1B1. Nevertheless, stents 1Z1, 1A1, and 1B1 look similar amongst themselves. Observing stent 1B2, the stresses on the intima that are above 565 kPa are reduced relative to stents 1Z1, 1A1 and 1B1. In order to discern differences such as in the latter example, a classification system of critical stresses was developed with no mechano-biological responses implied by any of the thresholds. This classification system is discussed next.

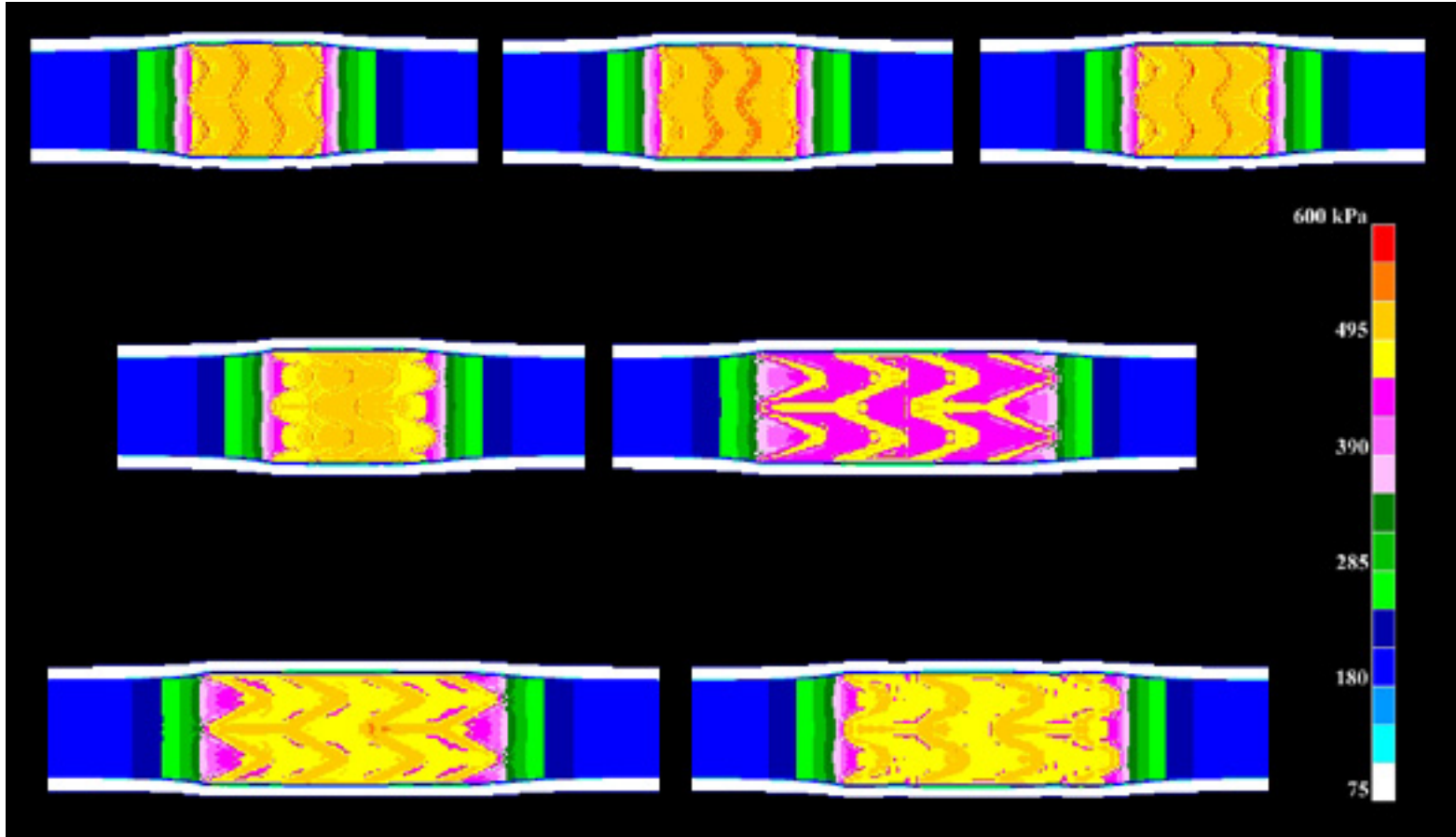


Figure 5.1. Hoop stress plots of stent designs used in this study. From left to right starting at the top: stent 1Z1, stent 1A1, stent 1B1, stent 1B2, stent 2A3, stent 2Z3, stent 2B2. Units are in kPa. Note how the stent “stress footprint” is evident on each stress map.



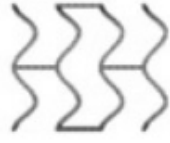
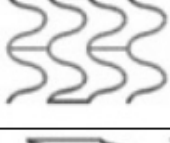



5.1.1 Critical Stress Definitions

Three classes of critical hoop stresses were defined to be as follows:

- a) Class I critical stresses – defined to be stresses that are above 565 kPa
- b) Class II critical stresses – defined to be stresses that are above 530 kPa (inclusive of class I).
- c) Class III critical stresses – defined to be stresses that are above 495 kPa (inclusive of classes I and II).

As a point of reference, the Law of Laplace – which represents the average hoop stress through the thickness of an artery – for our unstented artery model is 35 kPa. As can be appreciated, implanting a stent causes the stress at the intima to be over an order of magnitude greater than the average stress predicted by the Law of Laplace. Table 5.1 shows the numbers of nodal values at the intima as a percentage of each stented artery model at the intima that are in each critical stress class. Class I stresses are only evident in very small regions – less than 1.5 % in the worst case – thus, only the Class II and III thresholds will be analyzed.

Table 5.1. Critical hoop stress. Class I stresses are evident in arteries treated with stents 1Z1 and 1B1, though the area affected is relatively small (less than 1.5%). Lowering the critical threshold to Class II however, reveals important differences in stent design. Stent 1A1 induces the highest class II hoop stresses. Note that lowering the threshold further reveals stent 2A3 induces significantly lower critical stresses than any other stent.

Hoop Stress Comparison				
% Intimal Nodes Critically Stressed				
Stent	Stent Image	Class I (16XLaplace_{dias})	Class II (15XLaplace_{dias})	Class III (14XLaplace_{dias})
1Z1		1.48	17.08	81.59
1A1		0.03	26.30	87.39
1B1		1.37	17.20	82.46
1B2		0.09	4.59	72.15
2A3		0.00	0.00	6.44
2Z3		0.02	1.11	34.04
2B2		0.00	0.55	33.96

5.1.1.1 Class III Critical Hoop Stresses

At a class III threshold, it is revealed that stent 2A3 induces class III stresses in less than 6.5 % of the approximate intimal area, up to a 13.5 – fold decrease in the area affected relative to any other stent in this study.

Differences in stent design are magnified when varying more than one parameter simultaneously. It is interesting to note how the medium radius “A” with large spacing “2”, and large amplitude “3”, induced the lowest stresses (6.44 % stent 2A3); conversely, the same radius “A” with low spacing “1” and low amplitude “1” affected the highest intimal area amongst the stented artery models (87.39 % stent 1A1). When varying both radius and amplitude as in stents 2Z3 and 2B2, the class III hoop stresses affected 34.04 % and 33.96 % of the intima respectively.

When one looks at the effect of varying the spacing alone, it is revealed that stents with longer spacing (2.375 mm vs. 1.1875 mm) will give lower hoop stresses, as seen in figure 5.2 when comparing stents 1B2 to 2B2. This reduction in stresses corresponds to a greater than 50 % reduction in class III critical hoop stresses from 72.15 % to 33.96 %.

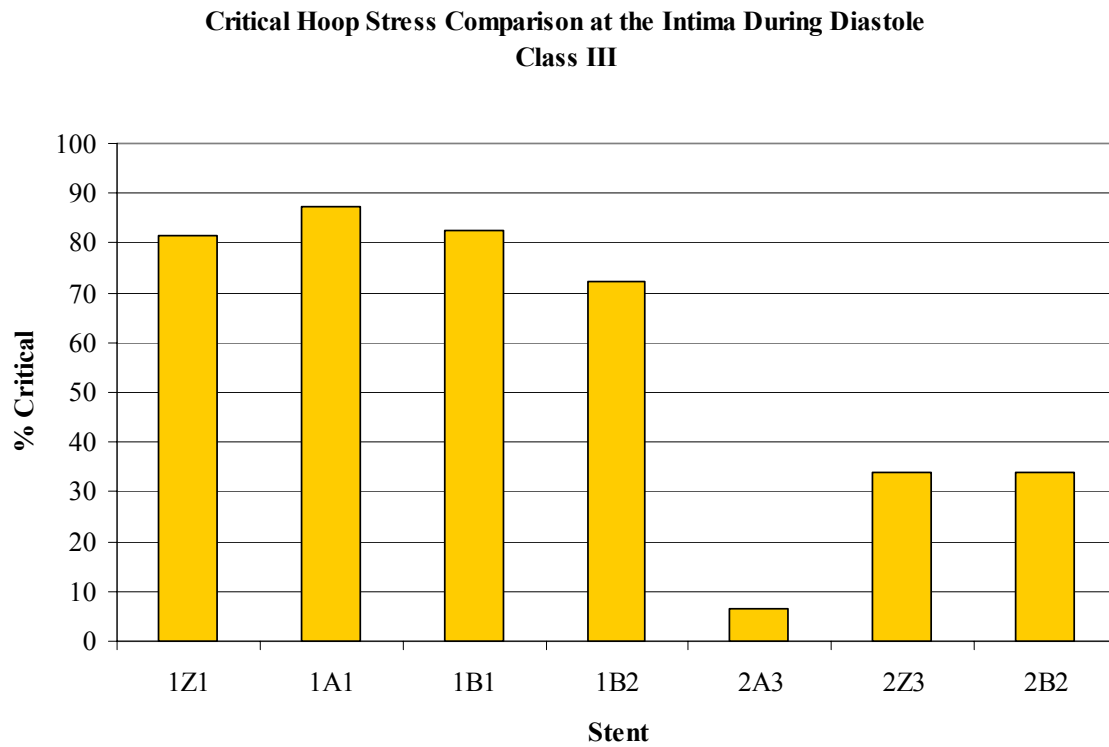


Fig. 5.2. Class III critical hoop stress threshold reveals stent 2A3 to have the lowest intimal area affected by class III hoop stresses. Note how the color of the bar graph for class III critical hoop stresses corresponds to the stress field map as in figure 5.1.

Similarly, when varying the radius of curvature by itself in stents with small spacing and amplitude as seen from stent 1Z1 to 1B1 (0 mm vs. 0.296 mm, respectively), nearly identical percentages of intimal area are affected by class III stresses (see figure 5.2 and table 5.1).

When analyzing the effect of varying the radius of curvature in stents with larger spacing and amplitude (stents 2A3, 2Z3) the stent with a 0 mm radius of curvature has nearly a 6 – fold increase in area affected by class III critical hoop stresses. This is also evident in figure 5.1 by observing the change in magnitude in the stress field of the stented intima. When varying the amplitude, as in the comparison between stents 1B2 and 1B1, the former induced class III stresses on 72.15% of the intima, while the latter induces class III stresses on 82.46% of the intima. Similar to the effect of increasing the spacing, increasing the amplitude has the effect of lowering the stresses.

Binary stress maps were plotted in order to facilitate visualization of the intimal area affected by class III critical hoop stresses. These are plotted in figure 5.3.

5.1.1.2 Class II Critical Hoop Stresses

Class II critical hoop stress threshold exposes additional differences masked in class III stresses in the design of stents 1Z1, 1A1 and 1B1. These stents induce class II critical stresses over relatively large areas as compared to other designs presented in this study (figure 5.4).

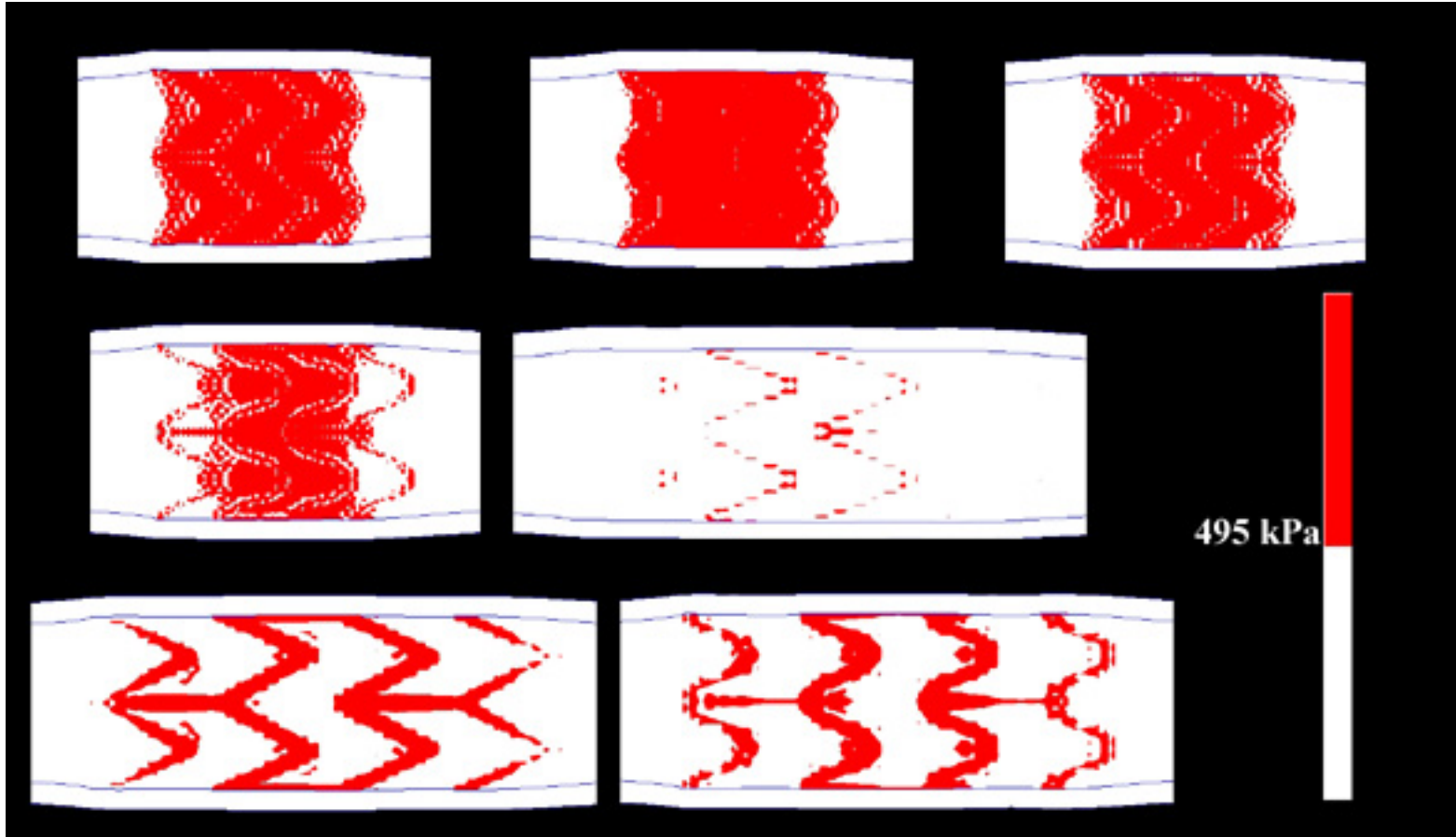


Figure 5.3. Binary class III critical hoop stress maps of stents at the intima during diastole. From left to right starting at the top: stent 1Z1, stent 1A1, stent 1B1, stent 1B2, stent 2A3, stent 2Z3, stent 2B2. Red denotes nodal hoop stress values that are above 495 kPa while white denotes nodal hoop stress values that are below 495 kPa. Note the marked difference in class III nodal hoop stress values in stent 2A3 relative to all other stented artery models. In general, stents with large spacing induce less class III critical hoop stresses than stents with small spacing.

**Critical Hoop Stress Comparison at the Intima During Diastole
Class II**

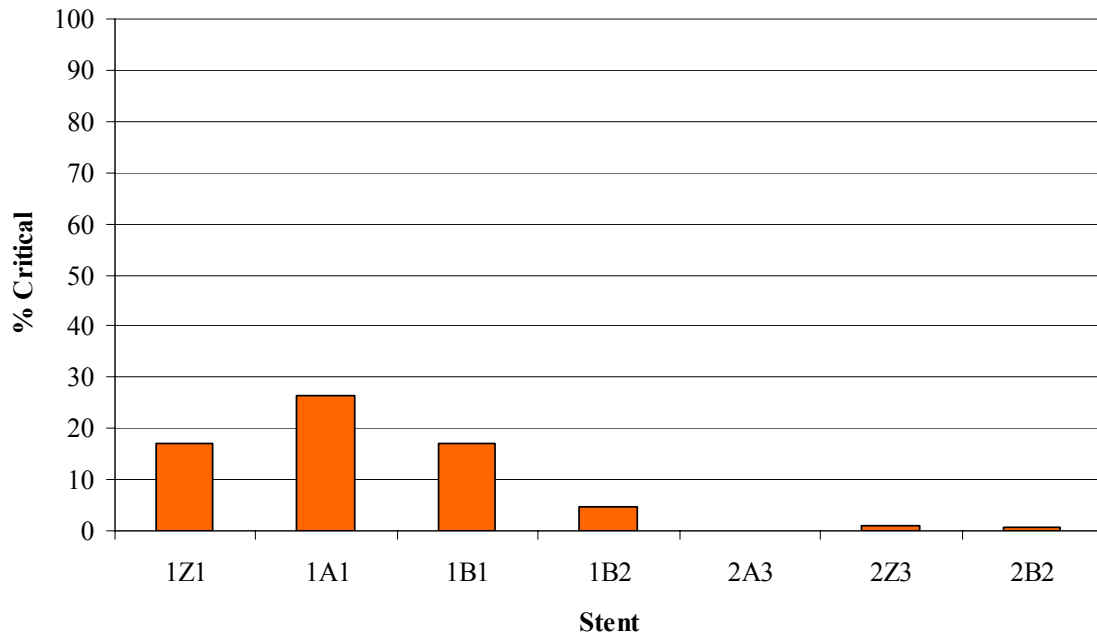


Figure 5.4. Critical hoop stress. Stents 1Z1, 1A1, and 1B1 – low spacing, low amplitude – represent designs that inflict the highest hoop stresses in the artery relative to the other designs.

Similar to the class III threshold, when varying more than one parameter simultaneously, noteworthy differences are revealed between stent designs. When comparing stents 1A1 and 2A3, it is revealed by table 5.1 that there is no class II stresses induced in the intima in the latter design, while the former design affects 26.30% of the intima with class II stresses. In fact, as was mentioned in the preceding section, stent 2A3 induced class III stresses (inclusive of class II stresses) on 6.44% of the intima. When comparing 2A3 to 2B2 – no change in spacing, increase in radius and decrease in

amplitude – an area of 0.55% is affected by the latter stent, attesting to the fact that when multiple parameters are varied, there are more noticeable differences.

Analyzing the effect of varying only the spacing as in stents 1B2 and 2B2, doubling the spacing causes an 8 – fold reduction of in class II stresses from 4.59% to 0.55%. Varying only the radius of curvature in small spaced stents (1A1, 1Z1, 1B1) it is revealed that similar to the class III hoop stresses, 1Z1 and 1B1 are very similar – affecting areas of 17.08% and 17.20% respectively in class II hoop stresses; and again as in class III hoop stresses, a radius of curvature of 0.148 mm (A) caused the highest incidence of class II stresses – 26.30%. In largely spaced stents – spacing “2” – stent 2Z3 registered 1.11% class II stresses whereas stent 2A3, as was mentioned earlier in this document, did not register any class II hoop stresses. Variations of amplitude are magnified when analyzing the stent designs relative to class II hoop stresses. Comparing stents 1B1 and 1B2, there is a reduction in class II stresses from 17.20% to less than 5% respectively. Class II critical hoop binary stress maps are plotted in figure 5.5.

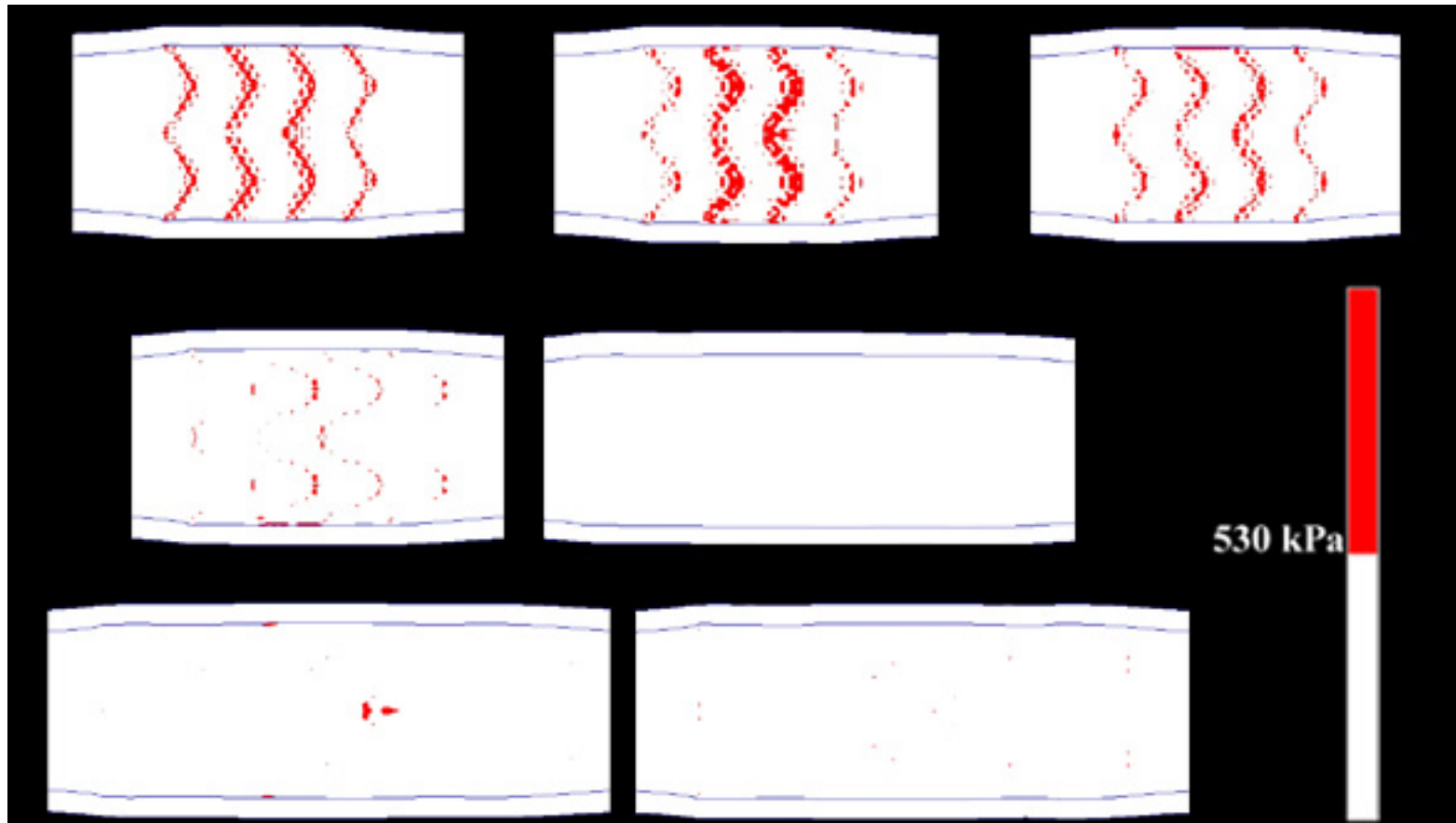


Figure 5.5. Binary critical class II hoop stress maps at the intima during diastole. From left to right starting at the top: stent 1Z1, stent 1A1, stent 1B1, stent 1B2, stent 2A3, stent 2Z3, stent 2B2. Red denotes nodal hoop stress values that are above 530 kPa while white denotes nodal hoop stress values that are below 530 kPa. Note the differences in class II nodal hoop stress values in stents with large spacing (2**) relative to stents with small spacing (1**). Stent 2A3 does not induce any class II hoop stresses. Differences of stents 1B2 relative to 1Z1, 1A1 and 1B1 is more evident in class II stresses than in class III stresses. Stent 1A1 induces the most class II critical hoop stresses.

5.2 Assessment of Radial Stresses on the Intima During Diastole

Similarly as the hoop stress analysis, radial stress fields will be shown for stented arteries at the intima during diastole. The critical stress definitions are shown below.

5.2.1 Critical Stress Definitions

Radial stresses in pressurized cylinders of any sort are compressive due to the pressure acting radially outward onto the the exposed surface. Under these circumstances, radial stresses are negative. Similar to hoop stresses, it is postulated that regions of highest (compressive) stress are likely candidates for initiating adverse biological responses. There are no biotransducing responses associated or implied with any of the stress thresholds.

- a) Class I critical stresses – defined to be stresses that are below – 120 kPa
- b) Class II critical stresses – defined to be stresses that are below – 100 kPa (inclusive of class I).
- c) Class III critical stresses – defined to be stresses that are below – 80 kPa (inclusive of classes I and II).

As a point of reference, diastolic pressure has a value equal to 10.66 kPa at the intima of the artery. It will be shown that the impact of stenting in the models analyzed herein notoriously increases the compressive stresses in some regions of the intima to over 20 times the diastolic pressure value. Figure 5.6 shows the radial stress component for all stented artery models analyzed in this thesis.

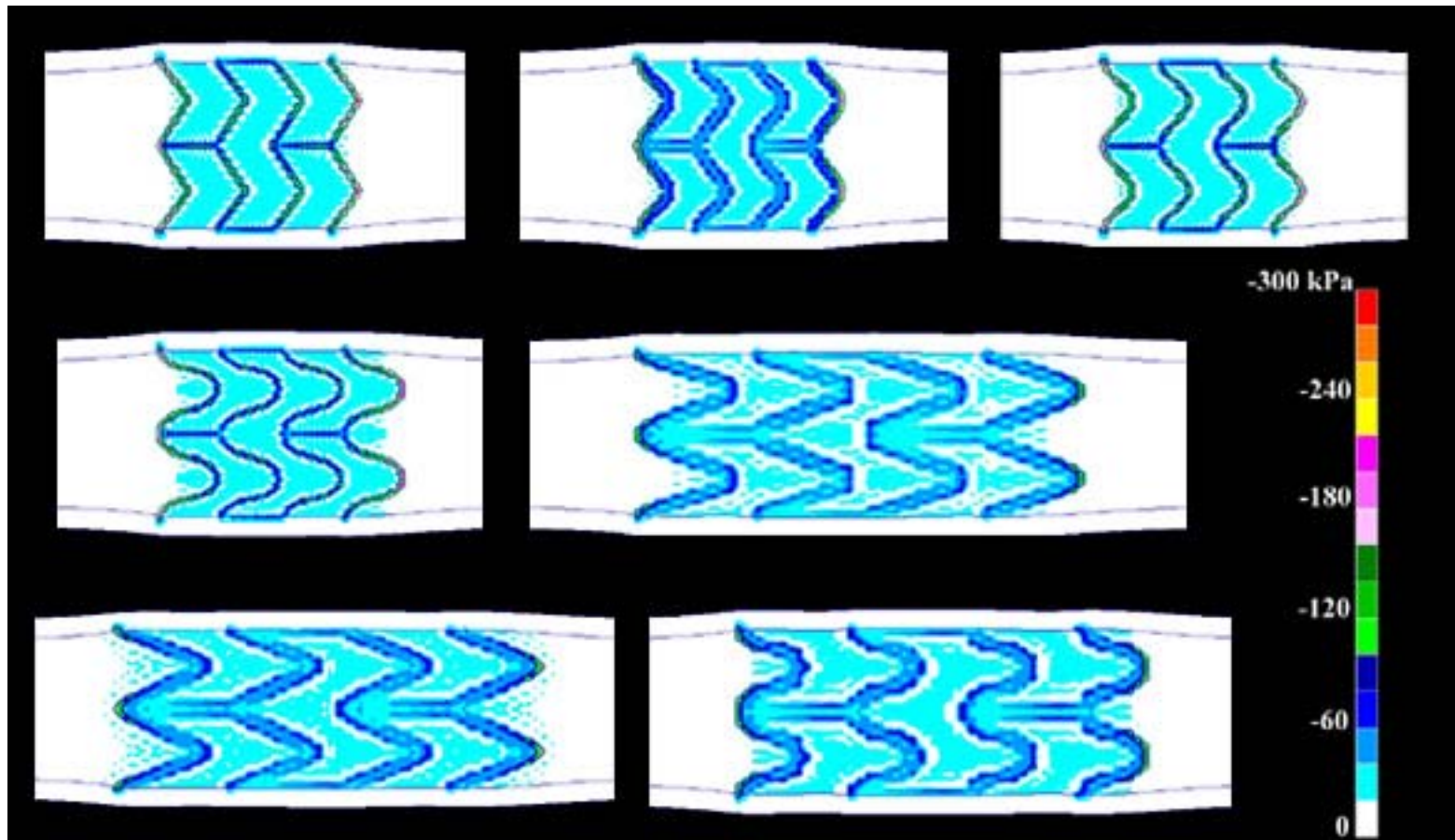





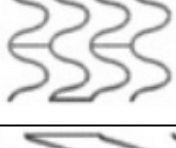



Figure 5.6. Radial stress components for stented artery models at the intima during diastole. From left to right starting at top: stent 1Z1, 1A1, 1B1, 1B2, 2A3, 2Z3, 2B2. Note the lower magnitude stresses in stents with large spacing.

With the exception of stent 1A1, stents with larger spacing induce a noticeable reduction in compressive stresses than stents with small spacing. Stents 1Z1 and 1B1 have similar stress imprints on the intima, revealing stresses in excess of -220 kPa at the edges of the stent. However, it can be appreciated that the edges of stent 1Z1 induce slightly higher compressive stresses than stent 1B1. Conversely, stents with large spacing have stresses on the order of -160 kPa at the edges of the stent. Table 5.2 and figure 5.7 show this information more clearly.

5.2.1.1 Class I Critical Radial Stresses

Stents with large amplitude and large spacing induce class I radial stresses on approximately 20 times less intimal area than stents with low amplitude and low. In particular, stent 1Z1 affects 8.46% of the intima while stent 2A3 affects only 0.44% of the intima with class I radial stresses. When comparing stents 1Z1 and 1B1 in figure 5.6, it can be appreciated that they affect the intima in nearly the same way. Yet, in contrast to the hoop stress analysis, stent 1A1 sets itself apart by affecting a small portion of the intima in class I radial stresses (0.85 %), while in hoop stresses it set itself apart by imparting the highest percentage of class II and class III hoop stresses. This fact makes stent 1A1 comparable to stents 2A3, and 2Z3 when it comes to class I radial stresses.

Table 5.2. Critical radial stress. Class I stresses are prevalent in arteries treated with stents 1Z1 and 1B1 affecting 8.46% of the analyzed intima, and 8.09% of the analyzed intima respectively. Stent 1A1, which displayed the highest hoop stresses, imparts 0.85% class I critical radial stresses on the analyzed lumen. Stent 2A3 imparts class I critical radial stresses on 0.44% of the intima in question.

Radial Stress Comparison				
% Intimal Nodes Critically Stressed				
Stent	Stent Image	Class I (11.25XP_{dias})	Class II (9.4XP_{dias})	Class III (7.5XP_{dias})
1Z1		8.46	10.89	13.70
1A1		0.85	3.50	12.57
1B1		8.09	10.81	13.19
1B2		5.27	11.06	14.55
2A3		0.44	1.70	7.79
2Z3		0.48	2.79	10.88
2B2		1.17	4.04	10.88

**Critical Radial Stress Comparison at the Intima During Diastole
Class I**

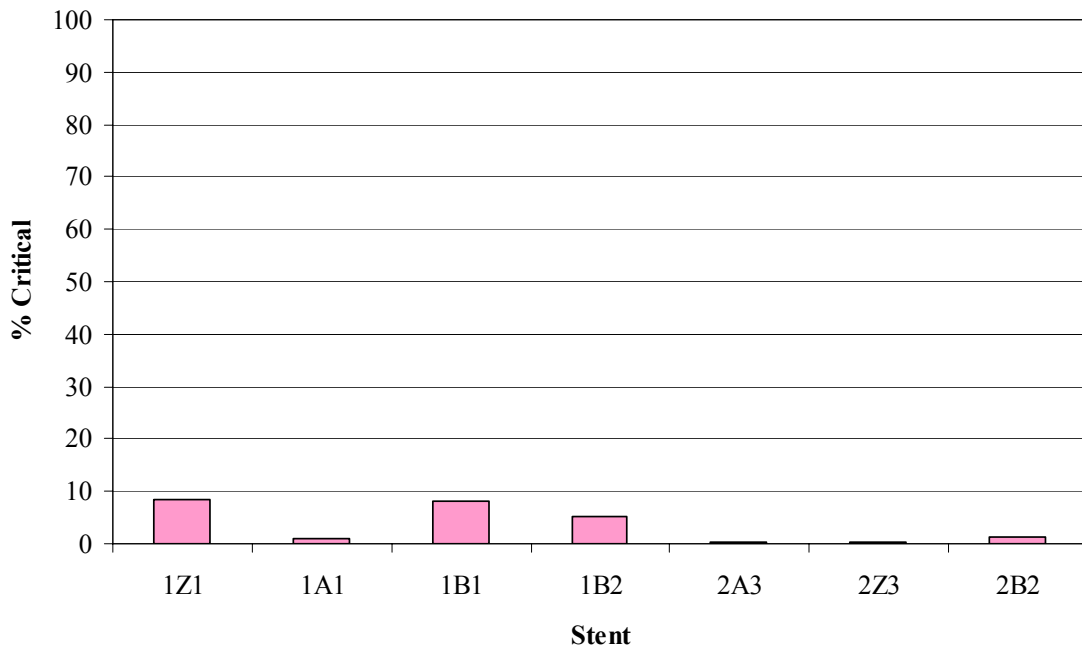


Figure 5.7. Class I critical radial stress at the intima during diastole. Stents 1Z1, 1B1, and 1B2 represent designs that inflict high radial stresses in the artery. Recall that stent 1A1 had the highest class II critical hoop stresses (small radius of curvature); here stent 1A1 is close to inducing the lowest class I critical radial stresses. Stents 2A3 and 2Z3 have the lowest class I critical radial stresses on the intima.

When varying spacing, stents 2*3 all have comparable areas affected by class I critical radial stresses – less than 1.2 % of the intimal area, whereas stents 1*1 have a large disparity with radius “A” affecting about a tenth of the area affected by stents 1Z1 and 1B1. When comparing stents 1B2, and 2B2, increasing the spacing by twice resulted in a decrease in stress from 5.27% to 1.17%.

A change in radius of curvature while all else is constant as in stents 2A3 and 2Z3, there is a negligible difference in intimal area affected by class I radial stresses. Conversely, as was mentioned above, 1A1 and 1Z1 differ by an order of magnitude in terms of areas affected by class I radial stresses.

A variation of the amplitude while all other parameters are constant, as in stents 1B1 and 1B2, has the effect of reducing the area affected by class I critical radial stresses. In this particular example, an amplitude of 1.1875 mm induced class I stresses to 5.27% of the intima, while an amplitude of 0.59375 mm induced class I stresses to 8.09% of the intima. Binary plots of class I critical radial stresses are shown in figure 5.8 where a spatial distribution of critical stresses can be appreciated.

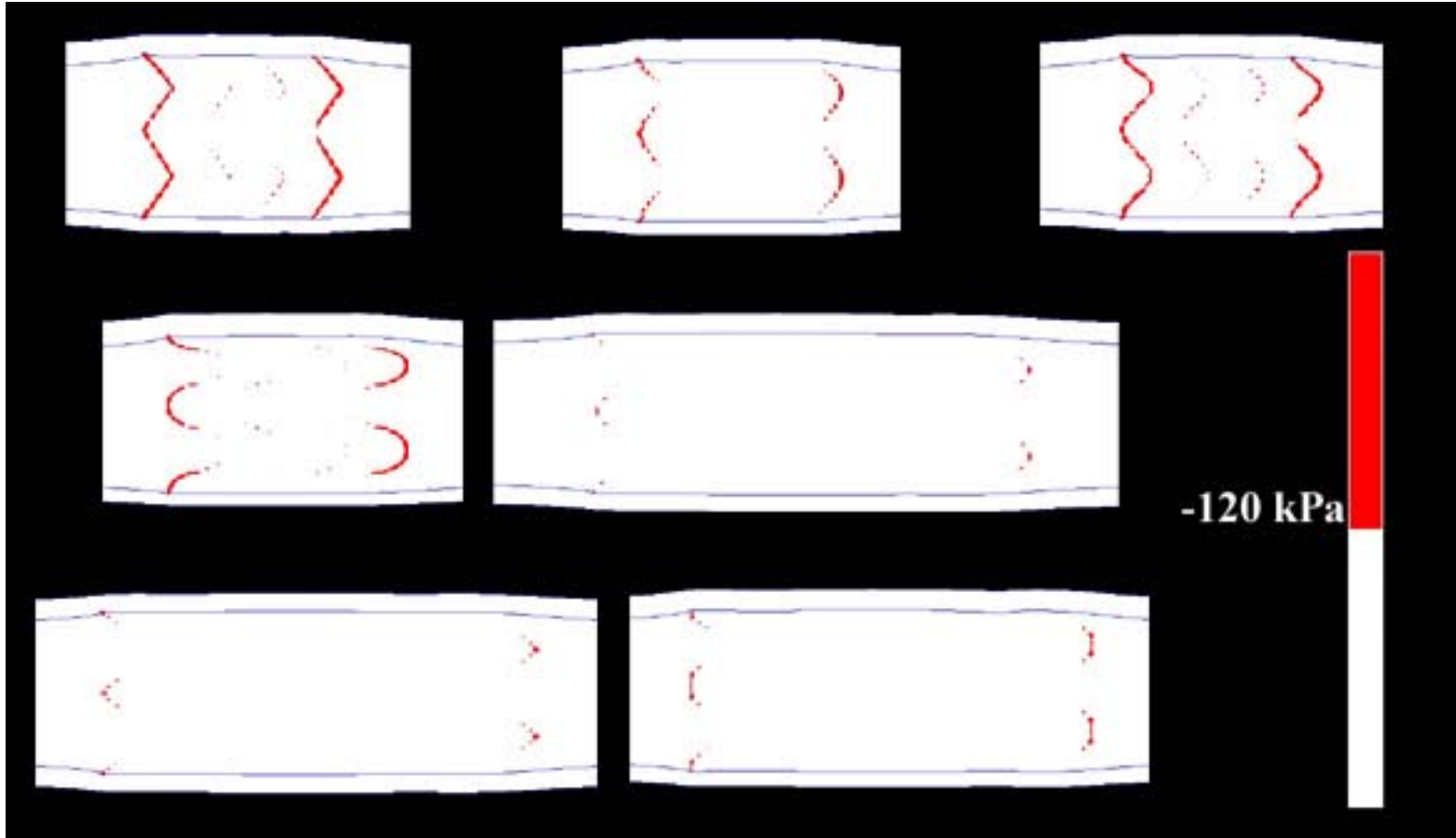


Fig. 5.8. Binary critical class I radial stress at the intima during diastole for stented artery models. From left to right starting at top: stent 1Z1, 1A1, 1B1, 1B2, 2A3, 2Z3, 2B2. White represents stresses that are above -120 kPa, and red represents stresses that are below -120 kPa. Note the lower incidence of critical stresses in stents with large spacing.

5.2.1.2 Class II Critical Radial Stresses

Class II radial stresses reveal features of stent 1B2 not seen in class I stresses. Specifically, stent 1B2 has the highest incidence of class II radial stresses. Trends in other stents however remain the same. Stent 2A3 is the stent with the lowest incidence of class II radial stresses, affecting 1.70% of the intima, while stent 1B2 produces higher class II radial stresses on 11.06% of the intima (see table 5.2 and figure 5.9). When comparing stents 1Z1 and 2Z3 (twice the spacing and three times the amplitude while radius is constant) results in a decrease in class II stresses from 10.89% of the intima affected to 2.79% of the intima affected. This trend is consistent with previous analyses of class I radial stress, and classes II and III hoop stresses that variation of more than one parameter exacerbates differences between stent designs. If instead one compares 1Z1 to 2A3, there is a further reduction in class II critical radial stresses – from 10.89% to 1.7% - attesting to the fact that a 0 mm radius of curvature will induce higher stresses on the arterial wall. However, similar to class I radial stresses, there is not a trend change or reversal relative to class II radial stresses between stents 1A1 and 2A3; the latter is still affecting roughly half as much intima as the former. Similarly, an increase in radius in conjunction with a decrease in amplitude as in stents 2A3 and 2B2 increased class II stresses from 1.70% to 4.04%.

**Critical Radial Stress Comparison at the Intima During Diastole
Class II**

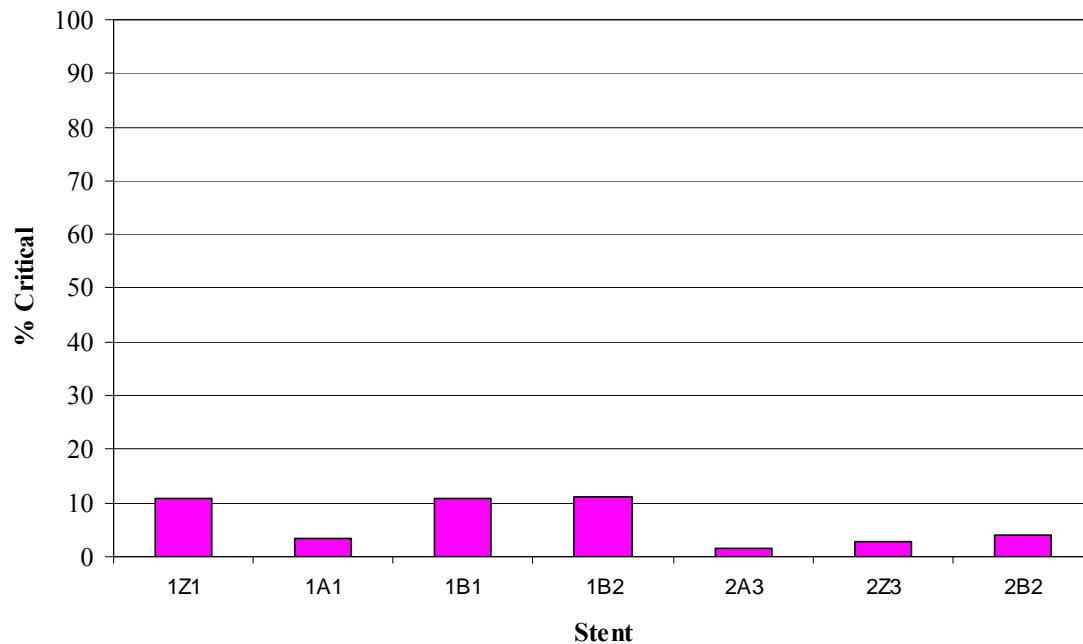


Fig. 5.9. Class II critical radial stresses reveal additional information about the stent designs. In particular stent 1B2 is now more similar to stents 1Z1 and 1B1.

Variation of only radius of curvature in stents with low amplitude and low spacing (1Z1, 1A1) reflects a more than 3 – fold difference between the intima affected, 10.89% versus 3.50% respectively. In stents with large spacing and large amplitude (2Z3, 2A3), the effect was less pronounced, producing a 1% difference, 2.79% and 1.70% respectively. Therefore, differences in stresses induced by the variation of radius

of curvature is also sensitive to the spacing and amplitude of the design. This fact was also prevalent across different stress classes and components discussed previously.

A 2 – fold increase in amplitude in stents 1B1 and 1B2 resulted in an increase in affected intima of 0.25% attesting further to the fact that a variation of more than one parameter will magnify differences between stent designs. Binary plots of class II radial stresses are shown in figure 5.10.

5.3 Assessment of Maximum Principal Stresses on the Intima During Diastole

Maximum principal stress is often the preferred measure of stress in finite element analysis because it represents the stress with the highest magnitude any given particle of a material is undergoing. Alternatively, the eigenvectors of the stress tensor represent the outward unit normals, and the eigenvalues represent the principal stresses acting in the direction of the corresponding eigenvector. There are three principal stresses in a three dimensional space and the terms “maximum”, “mid” and “minimum” describe their relative magnitudes. For the boundary value problem analyzed in this thesis – a pressurized cylinder with hyperelastic isotropic properties subjected to elongation and contact – the hoop stresses had the highest magnitude and therefore dominated the make-up of maximum principal stresses. Qualitatively, the behavior of maximum principal stresses is very close to the hoop stress behavior. For this reason, it will only be shown that these two different stress measures are very similar. However, the data is still presented in the same form as for hoop stresses.

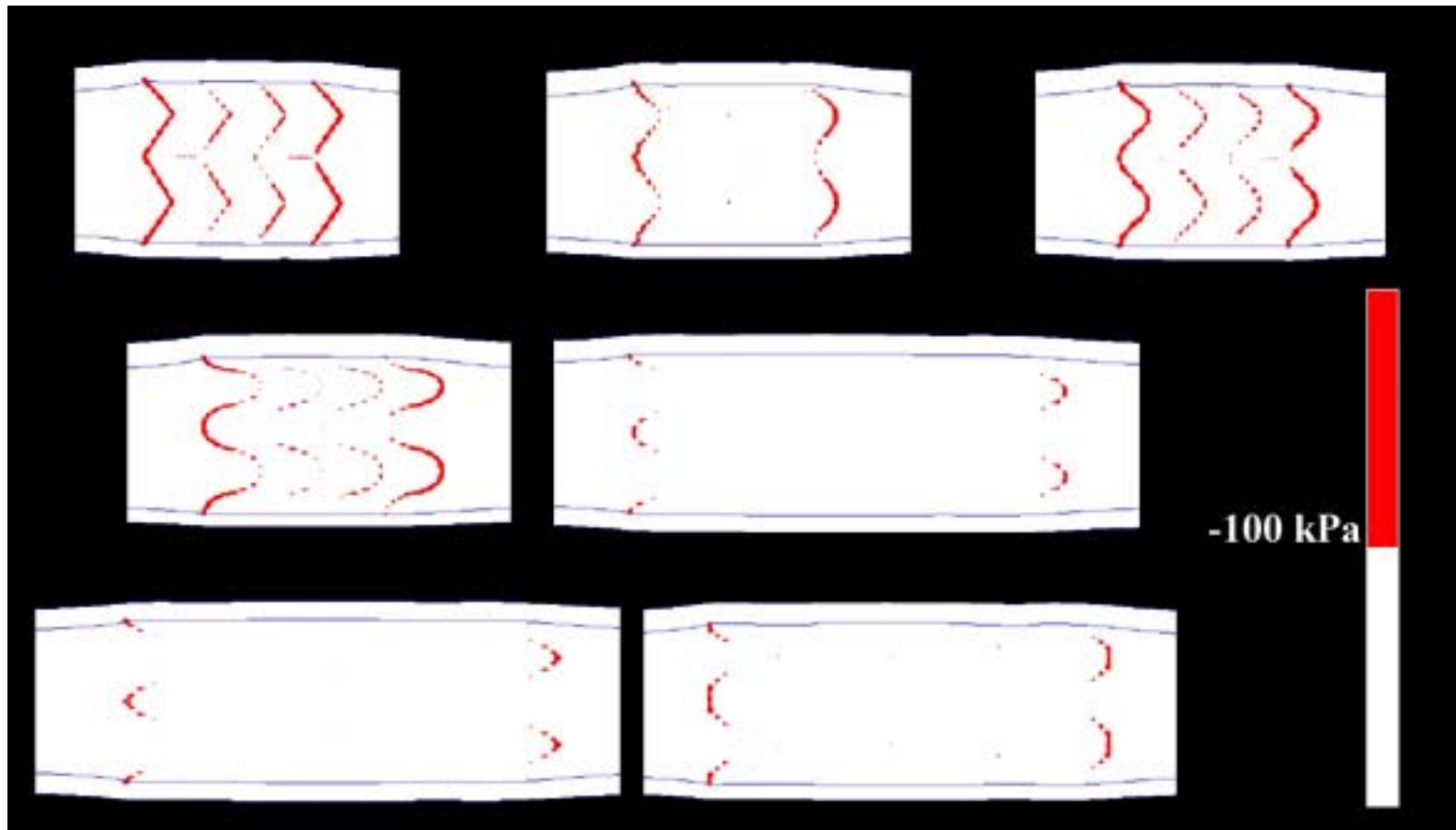


Fig. 5.10. Binary critical class II radial stresses at the intima during diastole for stented artery models. From left to right starting at top: stent 1Z1, 1A1, 1B1, 1B2, 2A3, 2Z3, 2B2. White represents stresses that are above -100 kPa, and red represents stresses that are below -100 kPa. Note the sparse population on the intima of class II critical radial stresses on largely spaced stents. In contrast to hoop stresses in figure 5.5, stent 1A1 imparts a low percentage of class II critical radial stresses – nearly the smallest relative to all the stents – 3.50%, as opposed to the highest percentage – 26.30%, in class II hoop stress.

5.3.1 Critical Stress Definitions

Critical stress definitions for maximum principal stress are the same as those for critical hoop stresses.

- a) Class I critical stresses – defined to be stresses that are above 565 kPa
- b) Class II critical stresses – defined to be stresses that are above 530 kPa (inclusive of class I).
- c) Class III critical stresses – defined to be stresses that are above 495 kPa (inclusive of classes I and II).

Table 5.3 shows the distribution of critical maximum principal stresses, and figure 5.13 shows the similarity with hoop stresses.

5.4 Assessment of Hoop Stresses on the Intima During Systole




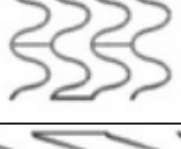
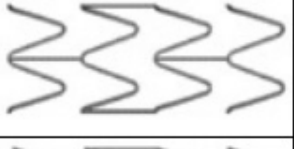


Results for hoop stresses at the intima during systole are presented in this section. By using the same classification system of critical stresses that was used for diastole at the intima, one is able to assess the influence of a change of pressure on stented arteries. A summary of this classification system is shown below.

5.4.1 Critical Stress Definitions

- a) Class I critical stresses – defined to be stresses that are above 565 kPa.
- b) Class II critical stresses – defined to be stresses that are above 530 kPa (inclusive of class I).
- c) Class III critical stresses – defined to be stresses that are above 495 kPa (inclusive of classes I and II).

Table 5.3

Critical maximum principal stress. These results are qualitatively similar to those obtained in the hoop stress analysis.

Critical Max Principal Stress Comparison				
% Intimal Nodes Critically Stressed				
Stent	Stent Image	Class I	Class II	Class III
1Z1		3.26	18.74	82.34
1A1		0.08	27.99	88.02
1B1		1.72	18.09	83.17
1B2		0.13	7.38	73.65
2A3		0.00	0.00	6.62
2Z3		0.00	1.41	35.09
2B2		0.03	0.78	35.77

As a point of reference, the Law of Laplace has a value of 61.56 kPa for our unstented artery model. Note the increase in magnitude of the Law of Laplace hoop stress value due to the increase in pressure. Table 5.4 shows the nodal values for each stented artery model that lie in each critical stress class. It is worth noting that the percentage of nodal values within class I critical hoop stresses decreased relative to the same values in diastole. Yet, systolic classes II and III values are now higher than the corresponding diastolic values. Since class I critical hoop stresses at the intima during systole affect less than 1% of the intimal area in question, they will not be discussed.

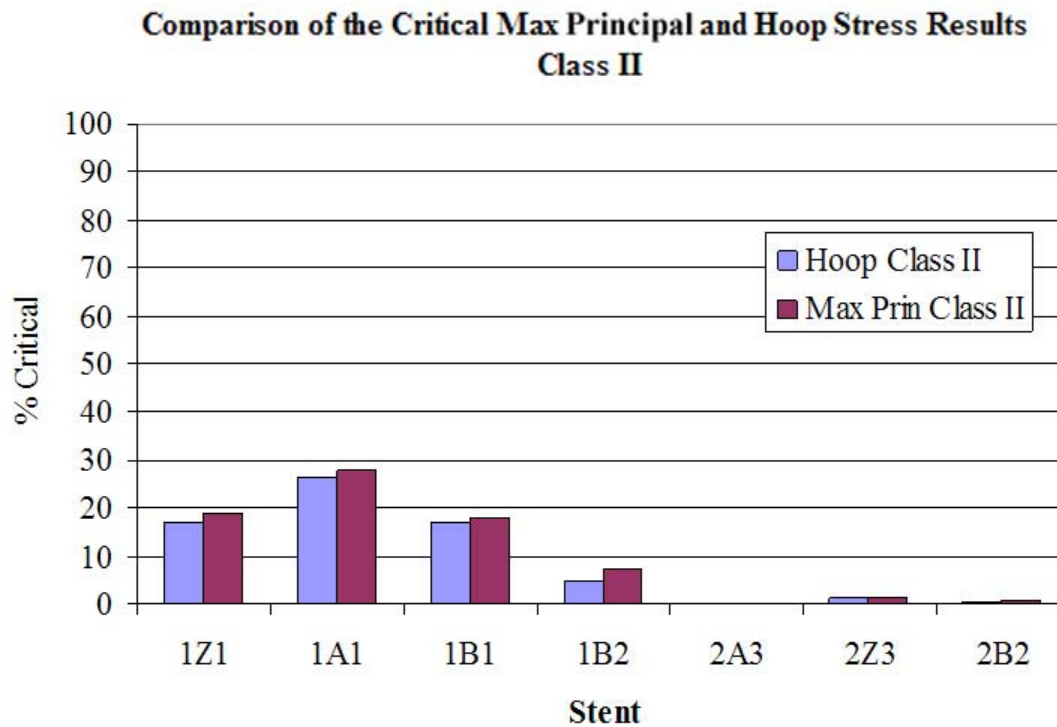









Fig. 5.11. Comparison of results obtained for the critical maximum principal stresses and the critical hoop stresses. The consistency between these results illustrates the dominance of the hoop component.

Table 5.4

Summary of critical hoop stresses at the intima during systole for all stents analyzed in this thesis. Similar to hoop stresses at the intima during diastole, class I critical hoop stresses has a very low incidence in all stents. Classes II and III display the same general trends as that observed at the intima during diastole.

Hoop Stress Comparison				
% Intimal Nodes Critically Stressed				
Stent	Stent Image	Class I ($9.2XLaplace_{sys}$)	Class II ($8.6XLaplace_{sys}$)	Class III ($8XLaplace_{sys}$)
1Z1		0.06	22.15	89.00
1A1		0.01	40.62	89.70
1B1		0.06	21.41	89.25
1B2		0.00	8.69	87.31
2A3		0.00	0.00	35.87
2Z3		0.00	20.99	84.84
2B2		0.00	0.97	82.16

5.4.1.1 Class III Critical Hoop Stresses

Analysis of class III critical hoop stresses reveal the same stent ranking observed in the intima during diastole. However, it is worth noting that these values are higher than those observed during diastole. Figure 5.12 presents this information more clearly.

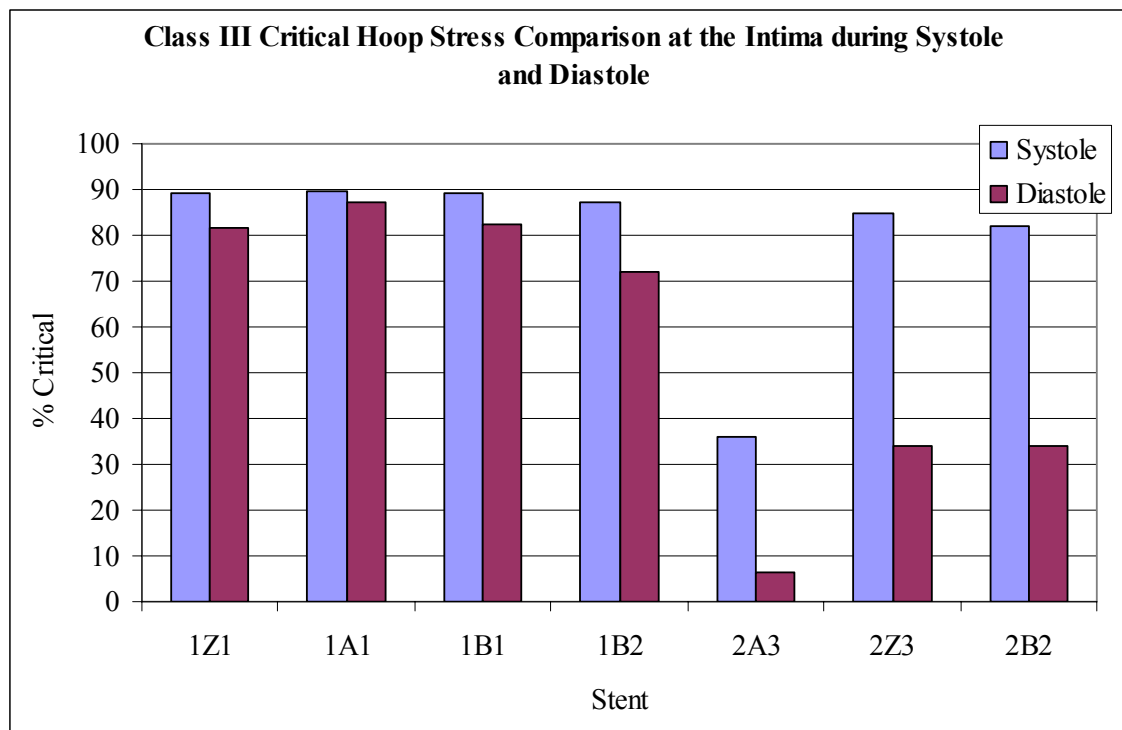


Fig. 5.12. Comparison of class III critical hoop stresses at the intima during systole and diastole.

Note that while the trends remain the same as in diastole, the systolic values are higher.

As can be appreciated from these results, an increase in pressure will cause a rise in nodal values to be present in class III critical hoop stresses. It is interesting to note how stent 2A3 still induces the least class III critical hoop stresses on the intima of the stented artery. Stent 2B2, inducing 82.16% class III critical hoop stresses, is the stent that is the closest to stent 2A3 relative to area affected, yet, it is still more than twice the area affected by stent 2A3. A much tighter distribution is observed in systole than in diastole with all stents – with the exception of 2A3 – all stents are within 6.84% of each other when it comes to intimal area affected.

Increasing the spacing during systole, as in stents 1B2 to 2B2 produced a less than 5% difference in intimal area affected – 87.31% and 82.16% respectively. An increase in amplitude while all other parameters are constant as in stents 1B1 to 1B2, resulted in a decrease in area affected from 89.25% to 87.31% respectively. When it came to a variation in radius of curvature, stents with small spacing and small amplitude all imparted similar class III hoop stresses to the intima – all affecting above 89% of the intima and stent 1A1 causing the highest percentage of class III stresses 89.70%. Conversely, unlike the intimal results at diastole, stent 2Z3 was very similar to stents with small spacing and small amplitude. Within the variational parametric space analyzed in this thesis, stents with a zero radius of curvature (radius “Z”) imparted high stresses in the intima during systole regardless of the other two parameters varied.

5.4.1.2 Class II Critical Hoop Stresses

An analysis of class II critical hoop stresses at the intima during systole reveals further details about stent designs that were not obvious during diastole. Figure 5.15 is a comparison of how class II critical hoop stresses changed when the pressure was increased from diastole to systole.

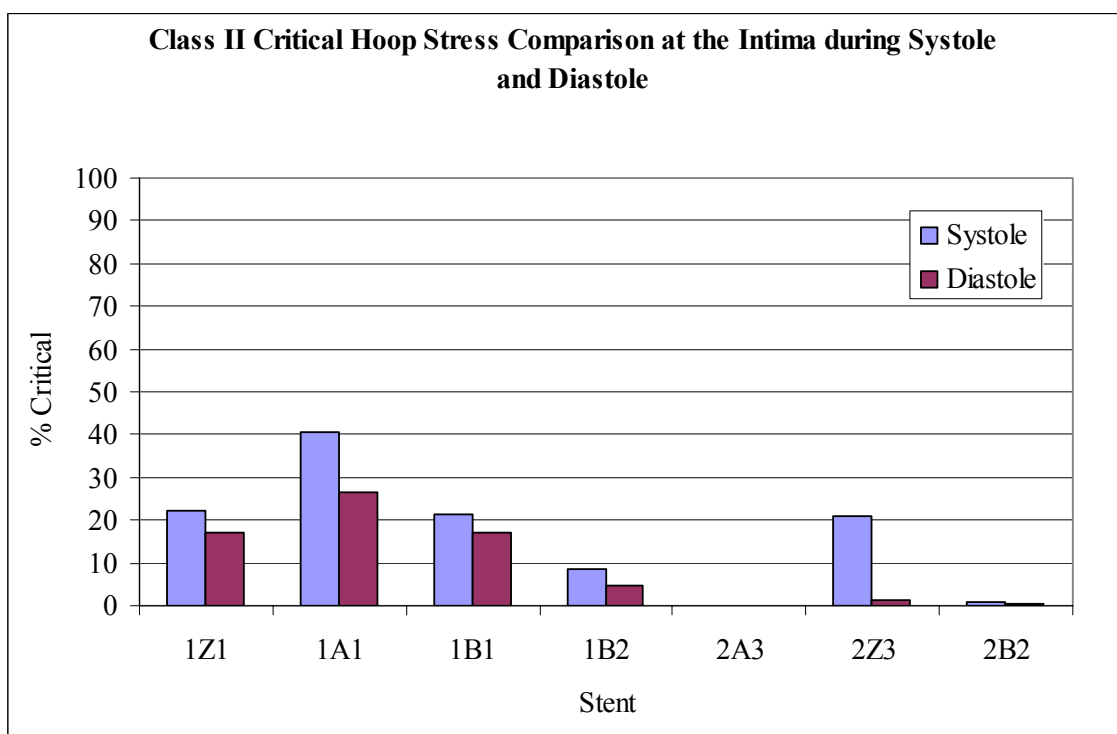


Fig. 5.13. A comparison in relative increase in incidence of class II critical hoop stresses when pressure is increased from diastole to systole. Note how stent 2Z3 (with a 0 mm radius of curvature) had the highest increase in stresses – approximately a 20 – fold increase.

It is interesting to note that additional information about stents with a 0 mm radius of curvature has been revealed. Stent 1Z1 had an increase from 17.08% to 22.15% - going from diastole to systole, while stent 2Z3 had an increase in class II critical hoop stresses from 1.11% to 20.99% in the same cardiac cycle time points. In addition, stent 1B2, which has higher class II stress values than stent 2Z3 in diastole, induces less than half class II hoop stresses in systole than stent 2Z3.

An increase in spacing while all other parameters remain constant, as in stents 1B2 and 2B2, shows a decrease in class II stresses in both systole and diastole. Similarly, an increase in amplitude produces a decrease in class II stresses when comparing stents 1B1 and 1B2; with systolic values of 21.41% for the former, and 8.69% for the latter. Similar to the diastolic analysis of class II critical hoop stresses, stent 1A1 – short connector bars and small amplitude – produced the largest frequency of nodal stress values within the class II range. Stent 1A1 also showed the largest increase in class II stresses when compared with other small spaced, small amplitude stents (1Z1, 1A1, 1B1) with nearly a 15% increase. However, the largest disparity when varying radius of curvature is between stents 2A3 and 2Z3, with the former registering 35.87% of *class III critical hoop stresses (0% class II critical hoop stresses)*, while the former displayed a value of 20.99% of *class II critical stresses*. Similar to diastole, stents 1Z1 and 1B1, have nearly identical behavior (both in magnitude and trend) during systole.

5.5 Assessment of Radial Stresses on the Intima During Systole

Analysis of radial stresses at the intima during systole has revealed interesting additional information about stent design. Specifically, unlike the hoop stress component, systole caused the radial stresses to be lower than those observed during diastole. Stents were compared using the same classification system of critical radial stresses with the same thresholds as those used during diastole. These are shown below.


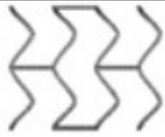
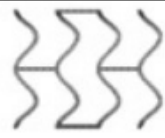




5.5.1 Critical Stress Definitions

- a) Class I critical stresses – defined to be stresses that are below – 120 kPa.
- b) Class II critical stresses – defined to be stresses that are below – 100 kPa (inclusive of class I).
- c) Class III critical stresses – defined to be stresses that are below – 80 kPa (inclusive of classes I and II).

As a point of reference, systolic pressure has a value of 16 kPa. Table 5.5 shows the distribution of class I, II and III critical radial stresses for the stented artery models studied in this thesis.

Table 5.5

Distribution of radial critical stresses according to stent design on the intima during systole. In comparison to diastole, all critical radial stress classes have decreased to below 1% in class I; in class II only stents 1Z1 and 1B1 exceed 5% of the area affected by the stent; in class III, stent 1Z1 induces stresses on 12.46% of the intima.

Radial Stress Comparison				
% Intimal Nodes Critically Stressed				
Stent	Stent Image	Class I (7.5XP _{sys})	Class II (6.25XP _{sys})	Class III (5XP _{sys})
1Z1		0.57	5.13	12.46
1A1		0.27	0.60	4.19
1B1		0.56	5.39	6.13
1B2		0.48	2.99	5.49
2A3		0.13	0.32	1.98
2Z3		0.07	0.20	3.80
2B2		0.29	0.55	4.71

5.5.1.1 Class I Critical Radial Stresses

In contrast to diastole, systolic class I critical radial stresses occur in less than 1% of the intima for all stents. This is a nearly a 15 – fold decrease for stent 1Z1 (largest decrease), and over a 3 – fold increase for stent 1A1 (smallest decrease). Figure 5.14 conveys this information more clearly.

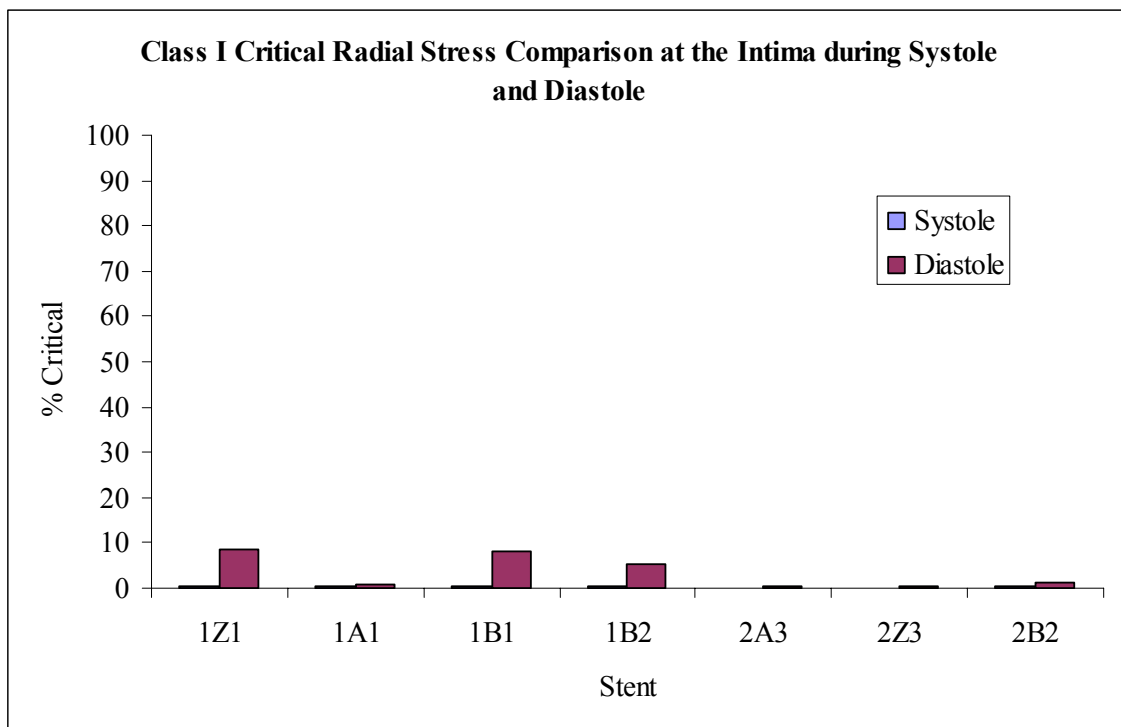


Fig. 5.14 Class I critical radial stresses at the intima according to stent design during systole and diastole. Note the decrease in stresses of nearly an order of magnitude for most stents. All systolic radial stresses are less than 1%.

Note that stent 1A1 is the only stent in the small connector bar, small amplitude group that did not exhibit an order of magnitude decrease when going from diastole to systole. Stents with large spacing and amplitudes “2” and “3” exhibited a relatively small change in stresses between diastole and systole.

Stent 2B2 had a relatively small change in class I stresses in going from diastole to systole. In contrast, stent 1B2 (smaller spacing) had a more significant change in class I stresses between diastole and systole. When varying only radius, radius “A” induced the lowest radial stresses. This is especially significant in stents with short connector bars and amplitudes (1Z1, 1A1, 1B1). A change in amplitude between stents 1B1 and 1B2 was much less significant in systole than in diastole (0.08% versus 2.82% respectively).

5.5.1.2 Class II Critical Radial Stresses

The most significant new information when comparing stents in class II critical radial stresses was a change in trend with stents 1B2, 2Z3 and 2A3. Specifically, increasing the amplitude from stent 1B1 to 1B2 produced a decrease in class II stresses – as opposed to an increase as observed in class II critical radial stresses during diastole. Furthermore, stent 1B2 exhibited the largest frequency of class II critical radial stresses during diastole. Stent 1B2 during systole induced class II stresses in 3% of the intima; less than 1B1 and 1Z1.

Similarly, stent 2A3 relative to class II radial stresses during systole does not exhibit the lowest incidence of stresses as it did during diastole. Moreover, it is stent 2Z3

– with sharp corners – that displays the lowest critical class II radial stresses with an incidence of 0.20%, whereas stent 2A3 has an incidence of 0.32%, and stent 2B2 has a value of 0.55%. Radial stresses in stent 1A1 during systole were consistent with radial stress observations during diastole, exhibiting a incidence of class II stresses of 0.60% during systole, and 3.50% during diastole. Figure 5.15 show this information.

In general, stents with large spacing and large amplitudes exhibited less incidence of class II critical radial stresses. An increase in amplitude translated into a decrease in stresses (during systole). Radii “Z” and “B” induced similar class II stresses during systole and diastole in stents 1Z1 and 1B1. The same radii in stents 2Z3 and 2B2 also induced similar class II stresses, yet there is also a variation of amplitude associated with that comparison.

5.6 Assessment of Hoop Stresses on the Adventitia During Systole

After analyzing the hoop stresses on the adventitia, it has been determined that no further information can be gained that was already obtained in the intima analyses. The same trends that were observed in the intima are also observed in the adventitia with the exception that the stresses are nearly 40 times lower. The same is true for hoop stresses at the adventitia during diastole, however the stresses are further reduced. Similarly, the radial stresses at the intima (during systole or diastole) do not provide any useful information when it comes to designing and comparing stents. The very nature of the boundary value problem being analyzed in this thesis, renders the radial stresses on the adventitia to be zero due to the boundary conditions applied (no external pressure).

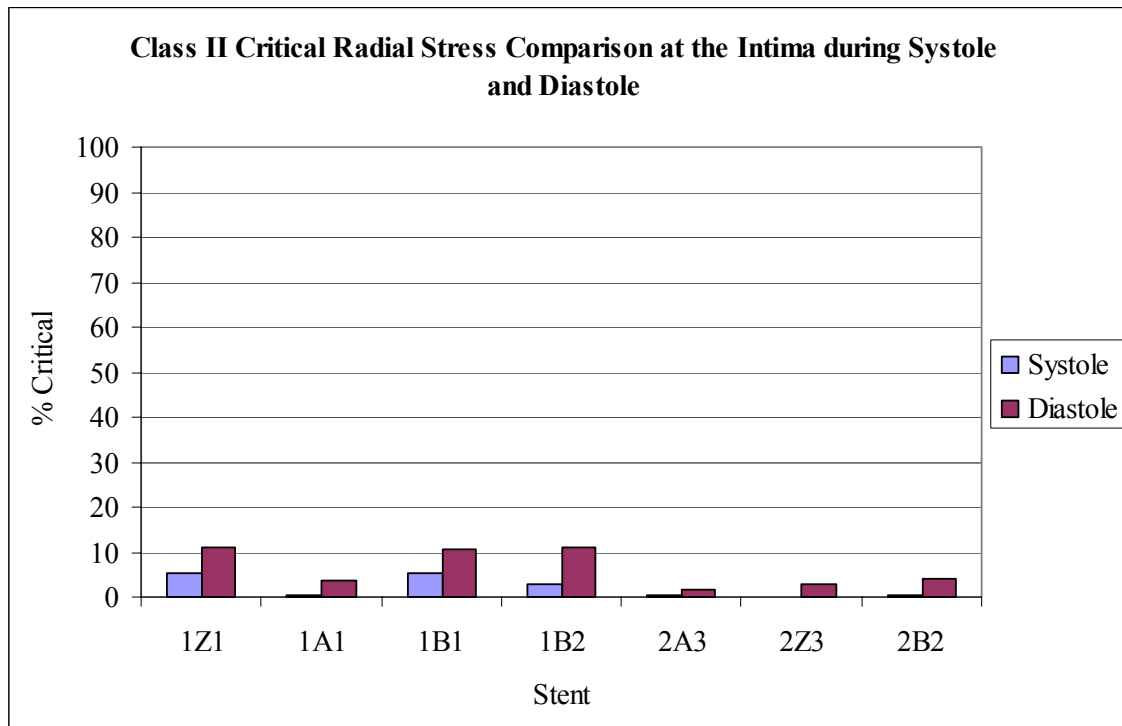


Fig. 5.15. Comparison of class II critical radial stresses at the intima according to stent design during systole and diastole. Note the decrease in magnitude of stresses when increasing the pressure from diastole to systole.

The results given by the finite element method regarding radial stresses on the adventitia are not identically zero due to the nature of approximation that the finite element method employs. Therefore, only the hoop stress results during systole at the

adventitia will be presented in this thesis for the sake of completeness. Similar to the intimal analyses, critical hoop stresses were defined for the adventitial analyses. These are described below.

5.6.1 Critical Stress Definitions


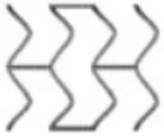





Three classes of critical hoop stresses for the adventitia were defined to be as follows (with no regard or implication to any biological response associated with any of the thresholds):

- a) Class I critical stresses – defined to be stresses that are above 13 kPa.
- b) Class II critical stresses – defined to be stresses that are above 11 kPa (inclusive of class I).
- c) Class III critical stresses – defined to be stresses that are above 9 kPa (inclusive of classes I and II). As will be shown below, only class I critical hoop stresses will be analyzed. No information is gained by analyzing classes II and III when evaluating the stent designs conceived in this thesis. Table 5.6 summarizes the incidence of nodal stress values in each of the aforementioned critical hoop stress classes.

Table 5.6

Summary of incidence of classes I, II and III critical hoop stresses on the adventitia during systole.

Note stents 1Z1, 1A1 and 1B1 have nearly 90% of the adventitia affected by class I critical stresses, whereas stents with larger connector bars have at most 20.94% of the adventitia affected.

Hoop Stress Comparison				
% Adventitial Nodes Critically Stressed				
Stent	Stent Image	Class I	Class II	Class III
1Z1		87.48	94.87	100.00
1A1		88.54	95.45	100.00
1B1		87.77	95.03	100.00
1B2		60.93	93.67	100.00
2A3		0.00	92.99	100.00
2Z3		3.00	92.94	100.00
2B2		20.94	94.81	100.00

Stents with large connector bars exhibited class I critical hoop stresses on the adventitia on 0%, 3% and 20.94% (designs 2A3, 2Z3 and 2B2 respectively). Variations of more than one parameter along the same path (all increasing, or all decreasing) magnifies differences between stents. In contrast, short connector bar designs imparted class I critical hoop stresses on 87%, 88% and 87% of the adventitia (stents 1Z1, 1A1 and 1B1 respectively).

When analyzing a variation in spacing while all other parameters are constant, there is a 3 – fold decrease in class I critical stresses when comparing stents 1B2 and 2B2 – values of 60.93% and 20.94% respectively. Similarly, an increase in amplitude as in stents 1B1 and 1B2, produces a decrease in class I stresses from 87.77% to 60.93%.

When varying the radius in small spaced stents with small amplitudes (stents 1Z1, 1A1, 1B1), stents 1Z1 and 1B1 affect similar areas of the adventitia with 87.48% and 87.77%. Recall that this same similarity between stent designs prevailed in the intima analyses. In addition, as was the case in the intima, stent 1A1 imparts class I critical hoop stresses (see table 5.6) in less area than stents 1Z1 and 1B1. When varying the radius of curvature in stents 2Z3 and 2A3, the latter radius minimized class I hoop stresses on the adventitia by not inducing any stresses while the former induced class I critical stresses on 3% of the adventitial area. Figure 5.16 is a summary of these observations.

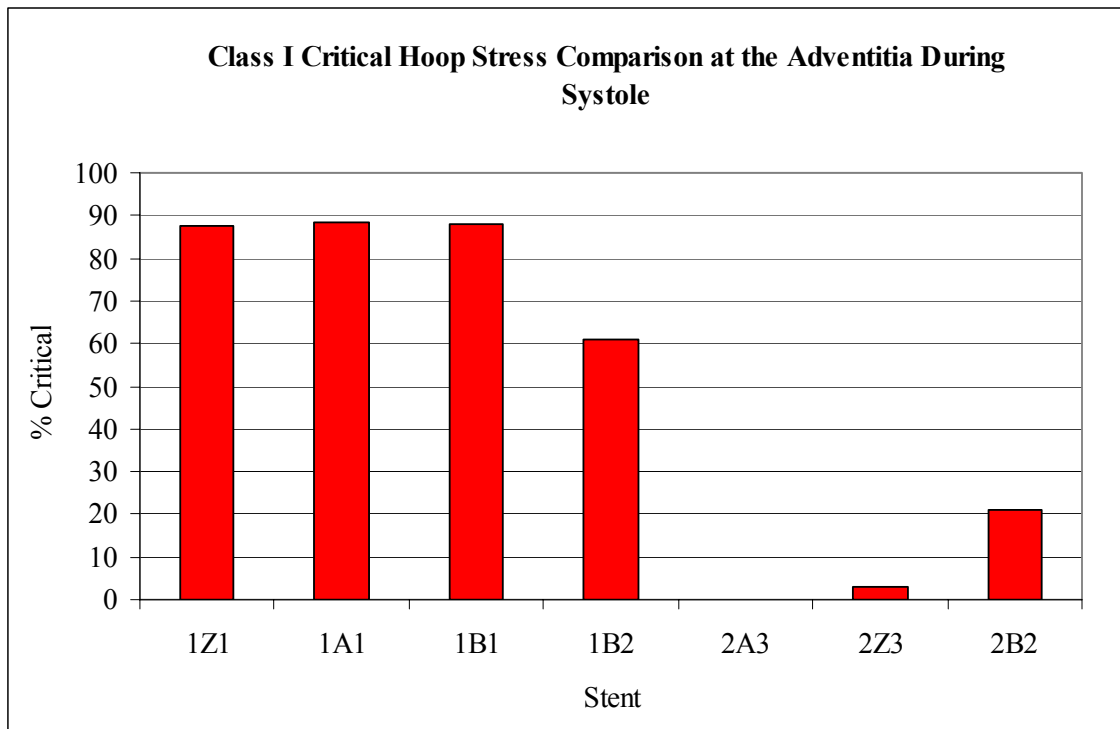


Fig. 5.16. Summary of class I critical hoop stresses on the adventitia during systole for the stent designs conceived in this study. Note the large disparity between stents with large spacing and stents with small spacing.

By analyzing class II critical hoop stresses on the adventitia, it can be appreciated that all stents in this study are similar regarding the area inflicted by class II stresses (see figure 5.17 below).

5.7 Assessment of RZ Shear Stresses on the Intima During Diastole

The significance of RZ shear in a stented vessel stems from the fact that endothelial cells align themselves in the direction of flow (respond to mechanical loads) (Moore and Berry, 2002). The presence of a stent in an artery, aside from altering the flow field (Berry et al., 2002), as has been shown previously in this document, the imparted hoop stresses by the stent can be in some instances 16 times greater than the average hoop stress predicted by the Law of Laplace. Therefore, the RZ component of shear may provide information as to how endothelial cells (as well as other biological entities) may respond to the presence of the stent. This is beyond the scope of this thesis, however, RZ shear plots are shown below in figure 5.18 and discussed qualitatively.

The highest magnitude shear stresses occur at the left and right edges of all stents. It is important to note that these results indicate that the RZ shear stresses are symmetric relative to a line bisecting the stents at the 45° degree angle line along the longitudinal axis (symmetric in both distribution and magnitude), as well as a line bisecting the stents in their geometric center perpendicular to the aforementioned 45° degree angular ray (symmetric in magnitude and distribution but opposite sign). Note how stents 1Z1 and 2A3 have the greatest disparity in magnitude of stresses and distribution. Stent 1Z1 has a relatively large incidence of stresses in the 10 kPa to 16.7 kPa magnitudes while stent 2A3 has a less dense stress population in those magnitudes. Also apparent is the relative sizes of the focal stress gradients at the stent edges. Note how stents 1Z1 and 1A1 have stress gradients that encompass a larger relative area than the stress concentrations created by stents 2Z3 and 2A3.

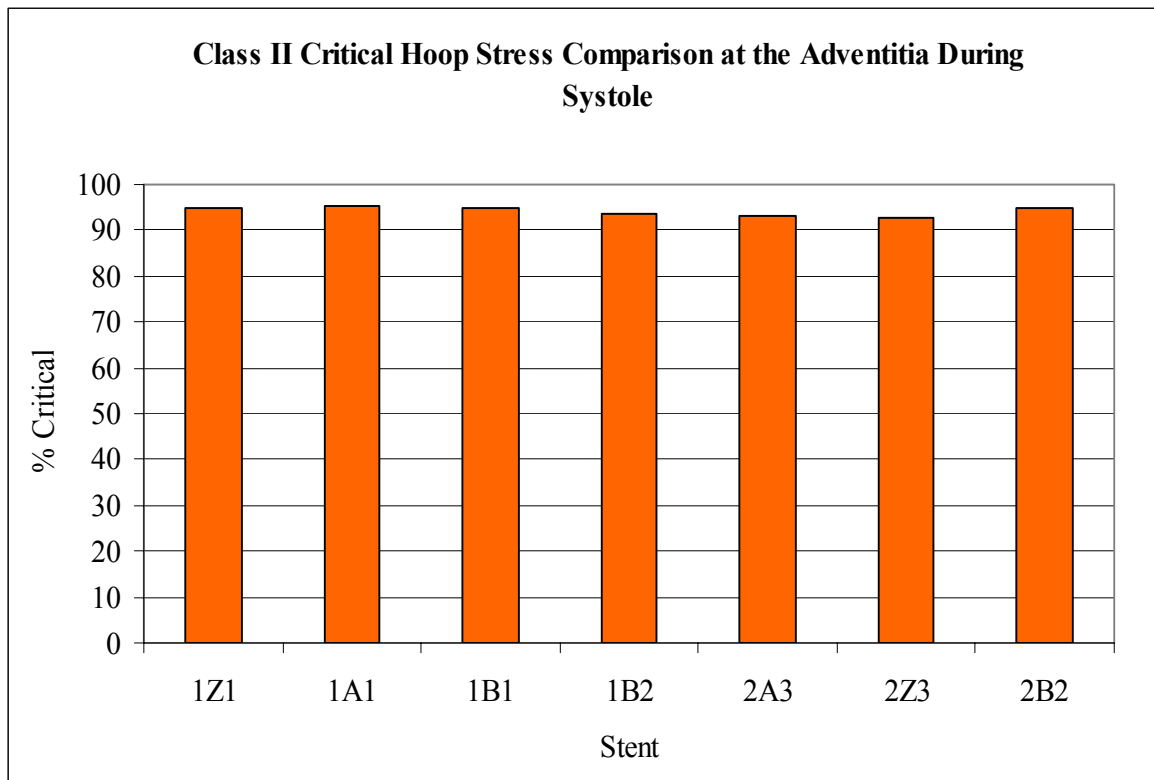


Fig. 5.17. Class II critical hoop stresses on the adventitia during systole. Note that all stents inflict class II hoop stresses on over 90% of the adventitial surface.

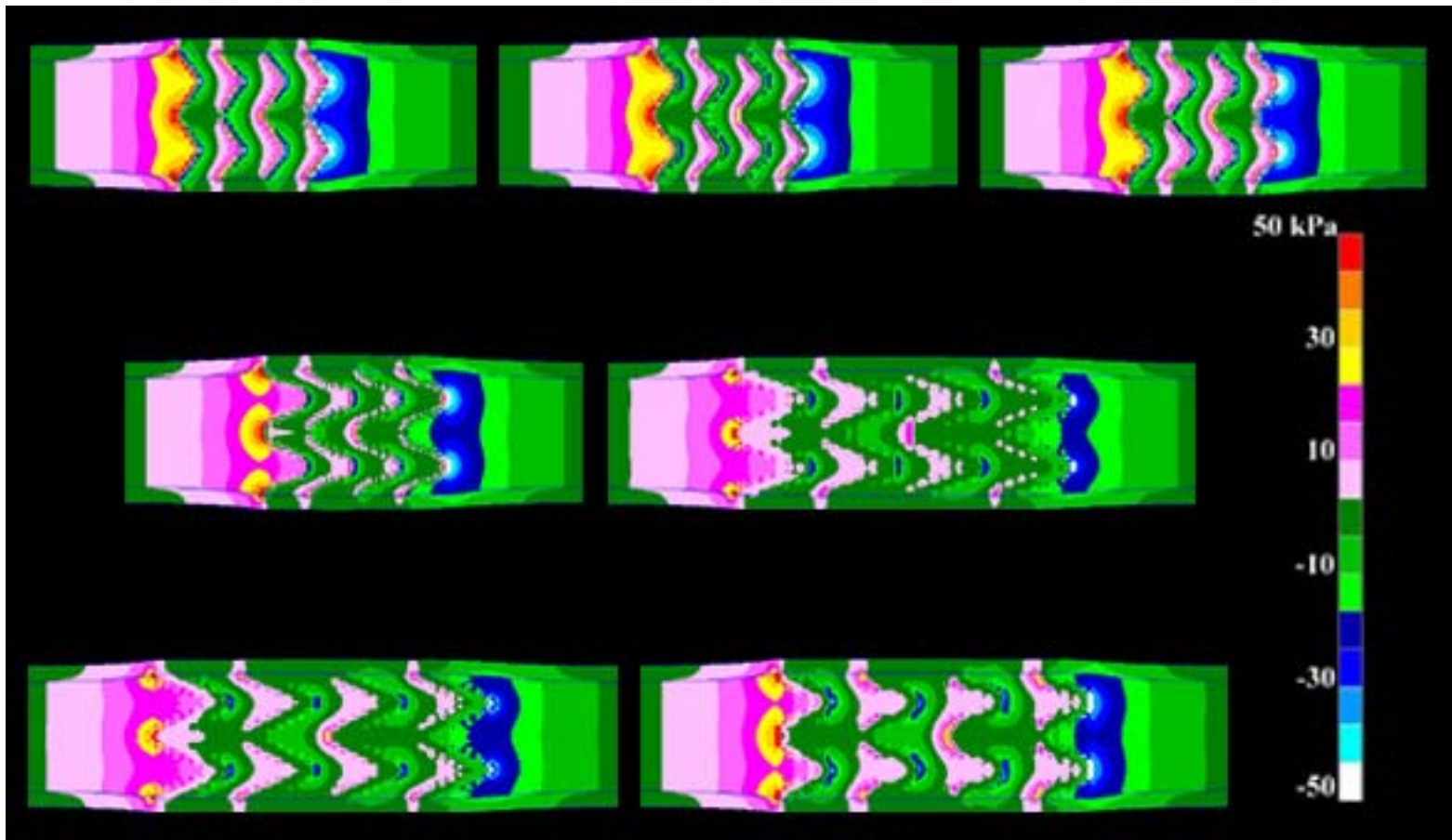


Fig. 5.18. RZ component of shear stress at the intima during diastole for all stents evaluated in this thesis. From left to right beginning at the top: stent 1Z1, 1A1, 1B1, 1B2, 2A3, 2Z3, 2B2. Note the decrease in stress intensity at the left and right edges of the stents when comparing designs with large spacing and amplitude relative to stents with small spacing and amplitude.

Stents with larger amplitudes and spacing inflict stress concentrations that are less severe than stents with low spacing and low amplitudes even when the radii are constant (1Z1 and 2Z3; 1A1 and 2A3). Similarly, stents with larger amplitudes while all else is constant (stents 1B1 and 1B2) induce less severe stress concentrations at the ends of the stents – again evidenced by the smaller stress concentration. When comparing the variation of spacing as in stents 1B2 and 2B2, both stents seem to create areas at the end struts affected by stress concentrations that are similar.

Variation of radius of curvature in stents 1Z1, 1A1 and 1B1 (while other parameters are constant) did not produce results that were qualitatively different. However, stents 2Z3 and 2A3 did show some differences in the area affected by the stress concentrations at the end struts with the former showing a larger area than the latter. This implies that a 0 mm radius of curvature will inflict more severe stress concentrations than larger radii of curvature.

5.8 Assessment of Radial Displacements on the Intima During Diastole

Analysis of radial displacements on the stented artery models will provide additional insight to complement the stress analyses already performed. All displacements are relative to the undeformed configuration as described in table 3.2. Figure 5.19 depicts all the displacement plots for all the stents at the intima during

diastole. As can be appreciated, all displacements caused by the presence of the stent in all stented artery models is in the range of 1.15 mm to 1.30 mm with a resolution of 0.01 mm. As can be seen, the stents in a macroscopic sense all have similar displacements, yet there are still differences that can be appreciated by the scale used herein, especially when comparing stents with long connector bars and stents with short connector bars.

Note that stent 2A3 has the lowest displacements – 1.22 mm at the center of the stent (the stiffest part of the structure), and 1.19 mm at the edges of the stent (the most compliant part of the structure) – relative to all the stents in this thesis. Conversely, stent 1Z1 has a displacement of 1.27 mm at the edges of the stent, a 0.08 mm change relative to the same spatial location in stent 2A3. Recall that stent 2A3 had the lowest class III and II critical hoop stresses and the lowest class I and II critical radial stresses. In general, stents with larger spacing and amplitude appear to be more compliant than the stents with low spacing and low amplitudes. Stents 1Z1, 1A1 and 1B1 on the other hand, are not very compliant having the highest displacement values of 1.27 mm on the stent imprint regardless of the radius of curvature that each stent has.

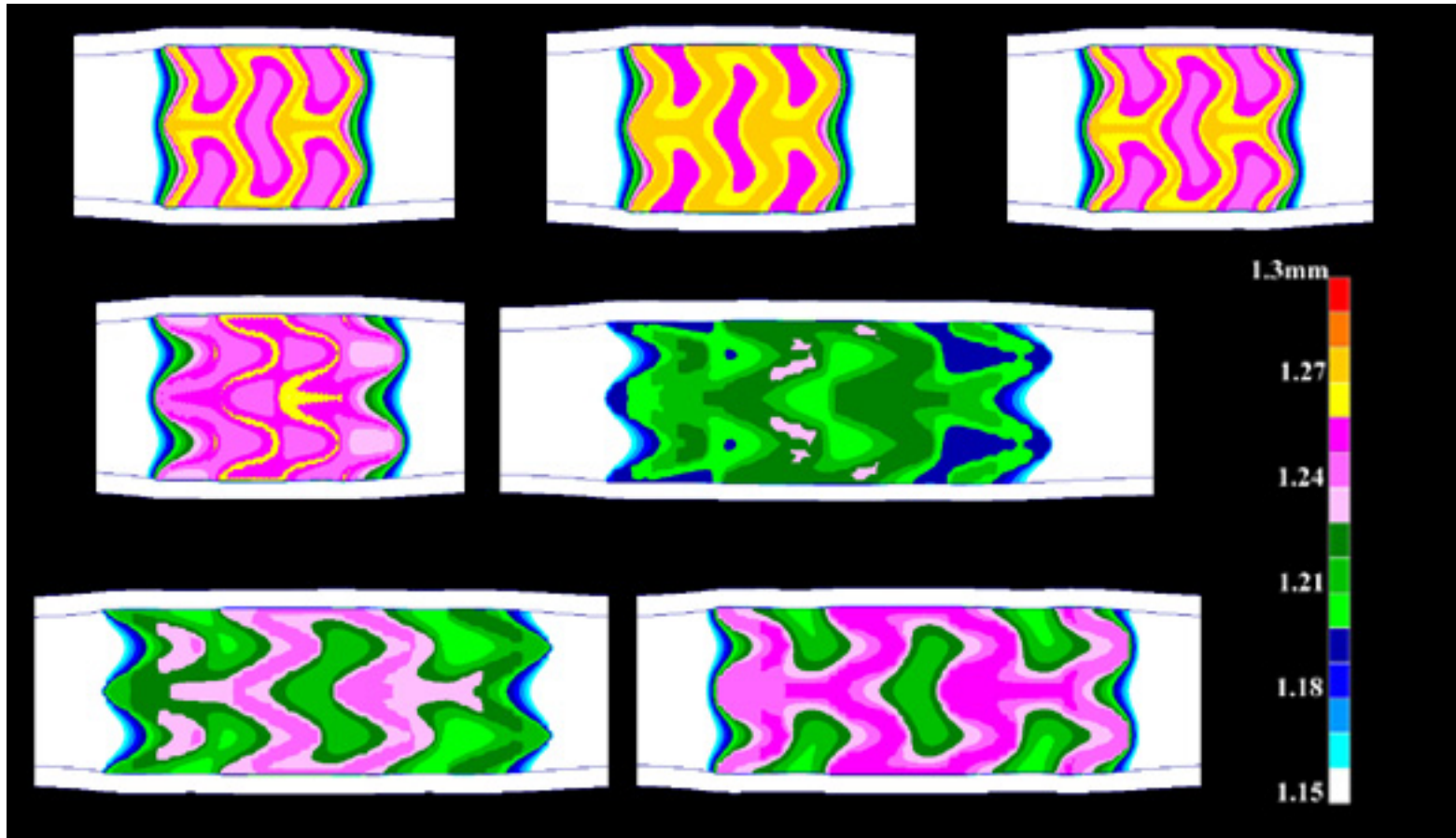


Fig. 5.19. Displacement maps of all stents at the intima during diastole. From left to right beginning at the top: stent 1Z1, 1A1, 1B1, 1B2, 2A3, 2Z3, 2B2. Units are in mm. Note how stent 2A3 has the lowest displacement of all stents (the most compliant stent) analyzed in this study. Stent 2A3 is also the stent with the lowest hoop stresses and radial stresses in all classes analyzed.

If one were to look at the effect of varying only the spacing of the stents as in stents 1B2 and 2B2, the latter has a maximum displacement of 1.25 mm at the middle of the stent while the former's maximum displacement at the center of the structure is 1.26 mm. Analyzing the effects of varying only the radius of curvature, the difference in displacements between stents 1Z1, 1A1 and 1B1 is not noticeable at a resolution of 0.01 mm. However, stent 1A1 had the highest class II and III hoop stresses, and close to the lowest radial stresses on classes I and II. When comparing stents 2Z3 and 2A3, the former creates a larger displacement at the intima than 2A3 at both middle and end struts. Stent 2Z3 has a displacement of 1.24 mm at the middle struts and 1.21 mm at the end struts. Stent 2A3 has a displacement of 1.22 mm at the middle struts and 1.19 mm at the end struts. Evidence suggests that stents with large amplitude and spacing are more compliant when designed to have larger radii.

Analyzing the effects of amplitude while other parameters are constant as in stents 1B1 and 1B2 resulted in the latter being more compliant exhibiting a displacement of 1.26 mm at the middle struts, and a displacement of 1.24 mm at the end struts. Stent 1B1 exhibited a displacement of 1.27 mm at both the middle and end struts. This is indicative that increasing the amplitude will allow compliance transitioning across the stent. It can be appreciated that stents with long connector bars and amplitudes, the radial displacement is a function of the axial position of the *stent struts*, whereas in

stents with short connector bars and short amplitudes, the radial displacement is uniform at the *stent struts*⁷.

5.8.1 Compliance Matching Results

By analyzing figure 5.19 it can be inferred that stents with large spacing and large amplitudes (stents 2*2, 2*3) are more compliant than stents with low spacing and low amplitudes. In addition, figure 5.19 also shows that stents with large amplitudes and large spacing exhibit characteristics of compliance matching. This becomes obvious when comparing displacements between stents 1Z1, 1A1 and 1B1 – all three stents exhibit the same amount of displacements at the middle struts and at the end struts, whereas stents 1B2, 2Z3, 2A3 and 2B2 all have different displacements at the middle struts and the end struts (see also figure 5.20). Stent 1B2 shows a 0.02 mm difference in displacement between the middle struts and end struts – 1.26 mm, 1.24 mm ; stent 2Z3 shows a 0.03 mm difference in displacement (1.24 mm, 1.21 mm); stent 2A3 also shows a 0.03 mm difference, although there are regions that exhibit a disparity of 0.04 mm (1.22 mm, 1.19 mm and 1.23 mm). Stent 2B2 with a lower amplitude than 2Z3 and 2A3 shows a difference of only 0.01 mm between middle and end struts (1.25 mm, 1.24 mm).

⁷ What this indicates is that stents with long connector bars and large amplitudes have the characteristic of allowing the edge struts to displace a larger amount than the middle struts.

5.8.2 Stent Breathing Results

“Breathing” of stents is a metaphor that describes how much change in displacement there is in a particular stent between systole and diastole. Figure 5.20 shows this behavior. When comparing stents 1Z1, 1A1 and 1B1, 0.01 mm in change in displacement is observed between diastole and systole. If the amplitude is increased, stent 1B2 shows a more noticeable change in displacement diastole and systole. Similarly in figure 5.20, stent 2Z3 shows approximately 0.04 mm in change in displacement, a 4 –fold increase from stents with low spacing and low amplitude in both middle and end struts. Stent 2A3 also displayed a 0.04 mm change in displacement – middle as well as end struts. When comparing stents 1B2 and 2B2 (figure 5.20), a larger amplitude will increase the breathing – a more compliant structure.

Generally, higher radial displacements – stents 1Z1, 1A1, 1B1 – have also yielded higher hoop stresses and radial stresses with the 1A1 caveat in radial stresses. Lower radial displacements in stents with long connector bars and larger amplitudes have induced lower radial and hoop stresses. It is interesting to note how a change of 0.08 mm at the edges of the stent (stent 2A3 relative to stent 1Z1) caused the former to induce class III hoop stresses on less than 6.5% of the intimal area, while the latter imparted over 80% of the intima with class III hoop stresses and an additional 17.08% of class II critical hoop stresses (see table 5.1 in section 5.1.1).

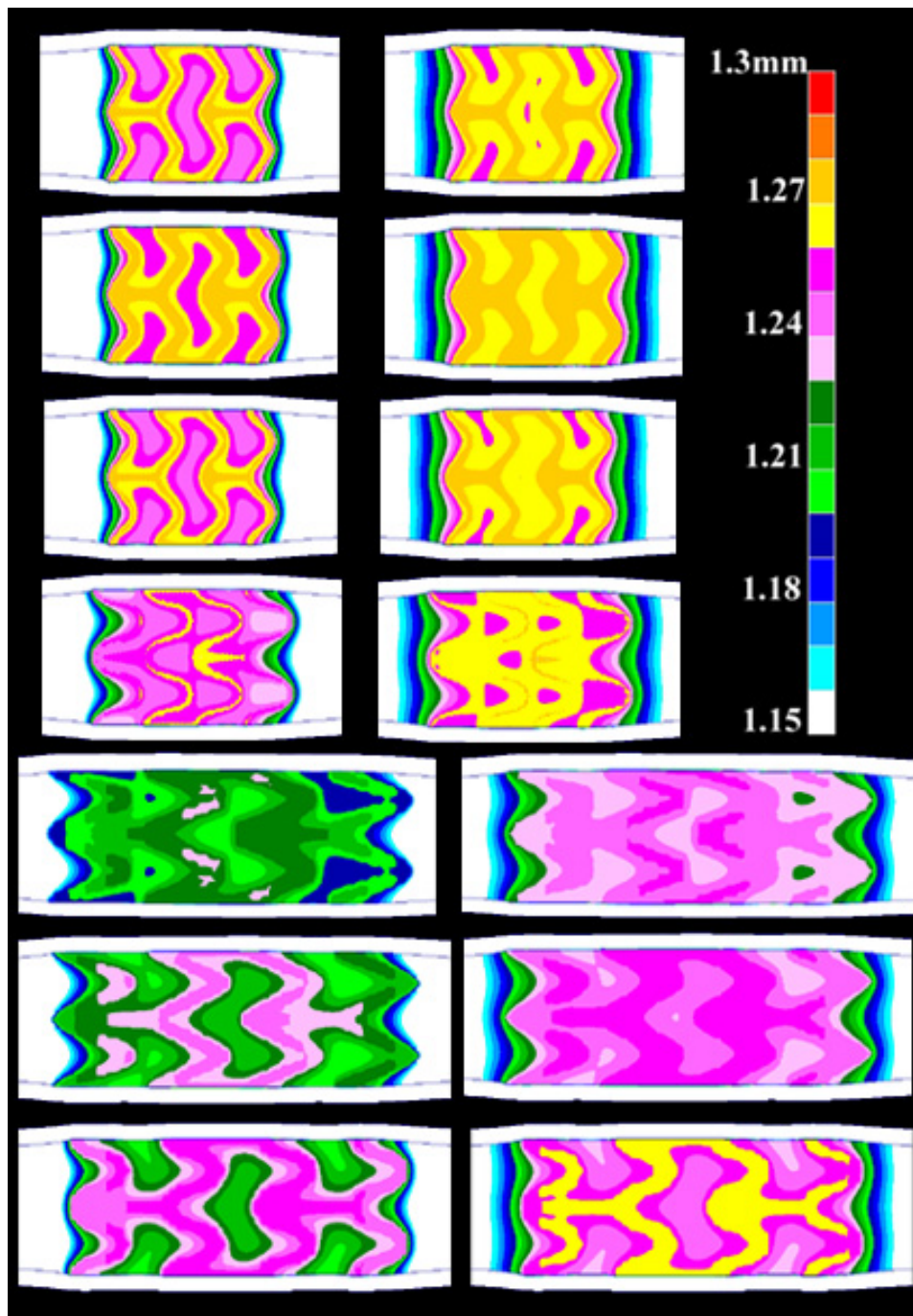


Fig. 5.20. Displacement plots of small spaced stents at intima during diastole (left column) and systole (right column). From top to bottom: Stent 1Z1, 1A1, 1B1, 1B2. Note how stents 1Z1, 1A1 and 1B1 do not exhibit compliance matching characteristics at the ends of the stent. In this group of stents, stent 1B2 exhibits the most “breathing”. Units are in mm.

6. SUMMARY

The aim of this study was to characterize the mechanical environment of an artery subjected to stenting. Implanting a stent with sufficient radial strength will cause an occluded artery to become patent. However, the presence of a stent will induce intense stress concentrations in the artery wall likely causing injury to the artery. Moreover, a stent often times denudes the endothelium provoking thrombus deposition further aggravating the fact that the stent is already a thrombogenic surface. Studies such as Edelman and Rogers (1998) have postulated that vascular injury acts as a stimulus and is a precursor to neointimal hyperplasia and eventual restenosis. Farb et al. (2002) showed that medial fracture caused by stent implantation invigorates the cascade of events culminating in restenosis.

There have been numerous studies performed where mechanical factors in stent design have been implicated in degree of injury and restenosis. Fontaine et al. (1994) concluded that stiffer stents maintain larger radial displacements for a longer period of time at the expense of eccentric greater late loss at follow-up. Large-scale clinical trials such as reported by Kastrati et al. (2001), showed evidence that restenosis rates are influenced by stent design. In addition to the altered mechanical environment, implanting a stent will also cause large-scale flow disturbances associated with the degree of compliance mismatch (Berry et al., 2002) as well as influence platelet deposition patterns near the vessel wall (Robaina et al, 2003), all of which have also been shown to depend on stent design.

The focus of this project was on the mechanical interaction of the artery wall and the implanted stent, and to infer design guidelines for future stent generations based on minimization of stresses. A stent design methodology was developed whereby 7 stents with a 10% oversize relative to an arterial systolic intimal diameter were conceived by parameterizing geometric features. The stents were then evaluated with respect to the biomechanical impact, paying close attention to the relationship between the influence of geometric features and the stresses imparted to the artery wall. Cyclical deflection between systole and diastole was also taken into consideration, as it is suggested that the expression of beneficial structural proteins by smooth muscle cells is increased in the presence of increased cyclical stretch such as the one experienced in a normal cardiac cycle (Kollros et al., 1987). A stent severely hinders cyclic stretch and therefore also hinders re-endothelialization (Sumpio et al., 1987; Sumpio et al., 1988).

6.1 Interpretation of Results During Diastole at the Intima

It was observed in all stent designs that the highest stress concentrations occurred at the far edges of the stent, the regions where the most severe compliance mismatch occurs. Stent 2A3, which has large spacing, a non-zero radius of curvature, and large amplitude, induced the lowest stresses – both hoop and radial stresses – on the intimal wall of the artery. It is therefore postulated that stent 2A3 will likely inflict the least amount of injury to the arterial wall, and consequently reduce the risk of in-stent restenosis the most out of all the stents evaluated herein. Additionally, stent 2A3 was the most compliant design, maximizing cyclical stretch in the artery between systole and

diastole. Finally, stent 2A3 displays behavior of compliance matching ends, which will reduce the intensity of the stress concentrations on the artery wall as previously shown by Mohammed et al. (2001). In addition, Berry et al. (2002) observed that compliance matching stents ameliorate the altered flow patterns resulting from stenting.

When analyzing the lowest threshold of hoop stresses, stent 2A3 was the best design inflicting only 6.44% of the intima with class III critical hoop stresses. In this same class, the closest stent – 2B2, with large spacing, large radius of curvature and medium amplitude – imparted much higher stresses affecting over 33% of the intima. In contrast, stents 1Z1 and 1B1 – small spacing, small amplitude zero and largest radius of curvature respectively – affected over ten times more intimal area than stent 2A3 (nearly 83%). Similarly, at a class II critical radial stress threshold during diastole, stent 2A3 induced compressive stresses on less than 2% of the intima, making it the best design in terms of minimization of stresses. It is therefore expected that stents with large connector bars, large amplitudes and a non-zero radius of curvature produce a stent that minimizes hoop stresses as well as radial stresses. Analyzing the shear stresses in the direction of flow (rz shear), it is evident that the shear experienced by the endothelium during normalcy is at least 5 orders of magnitude smaller than what it would experience once a stent is implanted. By referring to figure 5.20, it is evident that closely spaced stents induce a significantly larger stress concentration – magnitude and imprint – than stents with longer connector bars. This is attributed mainly to the increased stiffness of closely spaced stents. For example, comparing stents 2Z3 – largest spacing, 0 mm radius of curvature and the largest amplitude – and 1Z1 – smallest spacing, 0 mm radius of

curvature and smallest amplitude, it is shown that stress concentrations imparted by stent 1Z1 radiate to a larger area than stent 2Z3.

In contrast to Squire et al. (1999) which predicted stents with large spacing to impart higher stresses than stents with small spacing, evidence in this study suggests that stents with large spacing will benefit the host artery by imparting lower magnitude stresses, and therefore diminishing the risk of injury to the vessel. Stent 1B2 – which has the smallest spacing, the largest radius of curvature, and a medium amplitude, imparted over 70% of class III critical hoop stresses to the intima of the stented artery. In contrast, doubling the spacing, stent 2B2 is obtained and the intimal area affected is reduced to approximately 34%. This 50% reduction in area affected by class III hoop stresses is attributed to the increase in flexibility bestowed to the stent. A more flexible stent creates a more auspicious mechanical environment by reducing the degree of compliance mismatch between the stent and the artery; consequently, the magnitudes of the stresses are reduced and the stress gradients become less severe. Furthermore, observing the binary stress plots on figure 5.3, it is evident that the stiffest stents – stents with low spacing, low amplitude (1Z1, 1A1, 1B1) – have a noticeable increase in stress density, affecting regions between stent struts with nearly the same intensity as the regions in direct contact with the stent. In contrast, stents with long connector bars (2Z3, 2A3, 2B2) impart class III critical hoop stresses directly to the area in contact with the stent and not the regions in between stent struts.

Changes in radius of curvature are also important when designing stents. It can be inferred by figure 5.20 that stents with a non-zero mm radius of curvature have a

more blunt stress concentration than stents with a 0 mm radius of curvature. In a purely mechanical sense, it seems that sharp edges might inflict less injury than rounded edges when it comes to RZ shear stresses due to the smaller zone of influence over which stresses are increased. It is difficult to ascertain without further experimentation whether smaller puncture wounds – if formed – would cause more damage than larger dull stress concentrations. Furthermore, in a dynamic setting it is postulated that if a puncture wound is formed, it might propagate further with every cardiac cycle causing overall more damage than a blunt pierceless wound. In class III critical hoop stresses during diastole, a variation of radius of curvature in closely spaced stents (1Z1, 1A1, 1B1, 1B2) had a less obvious influence than in stents with large connector bars. Figure 5.2 distinctly shows stent 2Z3 – large spacing, 0 mm radius of curvature and large amplitude – imparting significantly more stresses to the intima of a stented artery model than stent 2A3 – large spacing, medium radius of curvature and large amplitude. This nearly 6 – fold increase in class III critical hoop stresses will likely inflict more harm to the artery than a stent with a blunt edge. Conversely, in closely spaced stents, class III critical hoop stresses at the intima during diastole were not very different amongst stents 1Z1, 1A1, 1B1 – increasing radius of curvature from 0 mm to 0.296 mm. Likewise, in class II critical hoop stresses, stents 1Z1 and 1B1 inflict nearly the same percentages of stresses to the intima during diastole (17%), while stent 2Z3 imparted class II hoop stresses to 1% of the intima at the same cardiac cycle phase – recall that stent 2A3 did not impart any class II critical hoop stresses, and approximately one sixth of stent 2Z3's class III critical hoop stresses . This provides additional clues that small spaced stents are stiff

structures likely to cause more damage than larger spaced – more flexible – stents. Curiously, class I and II radial stresses did not elucidate changes in stress magnitudes that were sensitive to radius of curvature. Figures 5.9 and 5.11 reveal that radial stresses are sensitive to spacing – low spacing had clearer stent stress imprints than large spaced stents (as well as higher magnitude stresses). Yet, all stents imparted a stress imprint at the stent edges – regions of most compliance mismatch – proportional to the magnitude of the radius of curvature. This reveals that radial stresses are more affected by contact stresses. Although contact areas were not quantified in this study, it is not difficult to realize that closely spaced stents will have a larger contact area, and therefore more regions affected by high compressive stresses, than stents that are more flexible – large connector bars.

Permutations in amplitude also cause noticeable changes in the stress fields imparted to the stented artery models. Comparing stents 1B1 and 1B2 – small spaced, same radius of curvature and smallest and middle amplitudes respectively – it is reasoned that stent 1B2 will inflict less injury to a vessel due to the increased flexibility achieved with a larger amplitude. Figure 5.20 supports this hypothesis by manifesting a smaller stress concentration area of influence – note how stent 1B1 has a continuous yellow patch of stress on the left edge of the stent – *circa* 23.3 kPa – while stent 1B2 has a smaller yellow patch coalescing with a magenta patch – *circa* 16.7 kPa. The influence of varying amplitude is also evident in class III critical hoop stresses. At diastolic pressure stent 1B1 imparts class III critical hoop stresses in approximately 10% more intimal surface than stent 1B2 (82% vs. 72%). Similarly, in class II critical hoop stresses

there was close to a 12% change in intimal area affected during the same cardiac cycle phase when comparing stents 1B1 and 1B2. Hoop stresses have a strong dependence on radial displacements relative to the unloaded configuration. Larger amplitudes, because they are more compliant, will cause a lower overall radial displacement than stents with smaller amplitudes. It is suggested that stents with large amplitudes are more apt to having larger deformations at the end struts because they have a larger moment arm (peak relative to trough where the connector bar is fused) and therefore the artery is capable of deflecting the ends of the stent to a larger degree in the process of reaching equilibrium. Stents with small amplitudes on the other hand, have a shorter moment arm and the force restoring equilibrium due to an oversized stent is likely to be higher, causing higher stresses on the artery wall. Comparing stent 2B2 – higher hoop stresses – with stent 2A3 – lower hoop stresses, smaller radius of curvature and larger amplitude – there is clear evidence of how the variation of parameters synergize yielding higher stresses (reduce all parameters), or lower stresses (increase all parameters). In radial stresses, this same comparison between stents 2B2 and 2A3 did not elucidate differences in stress – at the intima during diastole – greater than 3% in intima affected. It is not surprising therefore that stents 1B1 and 1B2 are also more similar than stents 2B2 and 2A3 due to the lack of synergy in variations of geometric features.

6.2 Interpretation of Results During Systole at the Intima⁸

Increasing the pressure from diastole to systole will cause an unstented artery to expand to a larger diameter and therefore increase the stresses. The hoop stresses will increase due to an enlarged diameter, and the radial stresses will become more compressive due to the increase in pressure load directly applied to the lumen of the vessel. In the case of a stented artery, a rise in pressure will also cause the diameter of the vessel to dilate, and therefore the hoop stresses are increased as a result of the augmented circumferential distention. Likewise, the radial component of stress in a stented artery will also increase in magnitude – become more compressive. However, the classification system for critical radial stresses was designed to show differences in stress due to the presence of a stent. A *decrease in critical* stresses is therefore manifested when increasing the pressure from diastole to systole because it is the contact pressure of the stent on the artery – which is decreased when the artery is dilated – that controls the most compressive stresses in a stented artery. While the class III critical hoop stresses at the intima during diastole elucidated several differences in stent design, systolic pressure caused all stents to behave in a similar manner when classified with class III hoop stresses. Namely, all stents except 2A3 – large spacing, middle radius of curvature, largest amplitude – imparted class III critical hoop stresses in over 80% of the intima, while stent 2A3 affected only 35% of the intima. While variation in parameters across all other stents was indistinguishable when compared with this class hoop stresses

⁸ Changes to critical stress levels are reflected in the publication in Appendix B.

at systole, it appears that stent 2A3 has a unique combination of parameters that indicate less affliction to the arterial wall. Differences between other stent designs are discernible however when comparing stents with class II critical hoop stresses. Stents endowed with more flexibility – larger spacing, larger amplitude – showed the same trends as those observed during diastole; namely, a decrease in stresses relative to shorter and stiffer stents. It is nevertheless peculiar that in spite of being classified as a flexible stent, stent 2Z3 – large spacing, 0 mm radius of curvature, large amplitude – imparted close to the same percentage of class II critical hoop stresses to the intima as stent 1Z1 – small spacing, 0 mm radius of curvature and low amplitude and exceeding the stresses imparted by stent 1B2 (small spacing, largest radius of curvature, medium amplitude). Note that stent 1B2 induced class II critical hoop stresses to a larger percentage of the intima during diastole than stent 2Z3 also at diastole. These results suggest that having a 0 mm radius of curvature can be very detrimental to the host artery, particularly in a dynamic setting where there is a 20 – fold increase in class II critical hoop stresses in every complete cardiac cycle (20% class II critical hoop stresses in systole; 1% class II critical hoop stresses in diastole for stent 2Z3). Stent 1B1 – largest radius of curvature, smallest spacing and amplitude – imparted once again nearly the same amount of stresses to the intima as stent 1Z1. This is supporting evidence that there could be a flexibility threshold whereby variation of parameters will not make a difference in stresses unless the threshold is exceeded. Similar to diastole, all other variations of enlarging spacing and amplitude – either one parameter at a time or more – the systolic critical hoop stresses behaved in the same fashion as the diastolic critical hoop stresses.

Unlike critical hoop stresses, critical radial stresses decrease when the pressure is increased from diastole to systole. As was mentioned above, radial stresses in artery will increase with an increase in pressure. However, due to the augmented dilation of the artery with systolic pressure, the contact pressure between the artery and the stent is reduced and therefore the *critical* radial stresses – stresses that are most likely to cause injury or an adverse biological response – are reduced during systole. Stents with smaller spacing (1Z1, 1B1, 1B2) exhibited a more pronounced disparity in intimal areas affected between systole and diastole than stents with larger spacing. This is attributed to differences in stent flexibility. Flexible stents – larger spacing and amplitude – have lower contact pressures due to the compliance of the structure when the artery is collapsing onto the stent. Stiffer stents do not have much displacement *due to bending*⁹ and therefore the artery's reaction force to the stent is higher producing higher contact stresses.

6.3 Cyclical Deflection Results

In addition to evaluating stresses, it is important to consider displacements in stented arteries. As was discussed earlier, stresses are highly influenced by displacements by virtue of the physical governing equations, and constitutive laws. In addition, the finite element method uses displacements as a primary – interpolated – variable, and therefore, it is the most accurate output of the method. As was alluded,

⁹ Stiffer stents have higher radial displacements. What is being described here are displacements due to a load that causes bending of the stent struts.

lower radial displacements induce lower stresses (all components). In addition, other studies have shown numerous inferences and speculations associated with displacements. In particular, it has been shown that cyclical radial displacements between systole and diastole experienced in normal, healthy arteries – sometimes metaphorically referred to as “breathing” – produces a beneficial reaction in the arterial wall. When the artery is prevented from experiencing this cyclical deflection, it has been shown by Vorp et al., (1999) that the production of E-selectin – a surface expressed molecule that heightens monocyte attachment – is reduced with a response to decreased cyclic flexing. Kollros et al., (1987) recognized that the hindrance of cyclic flexing halts smooth muscle cells from synthesizing beneficial structural proteins. It is therefore deduced from these studies that arteries will have a positive reaction with maximizing cyclical deflection when stented.

This study revealed radial displacements in the intima during systole and diastole on the order of 1.30 mm relative to the undeformed unloaded configuration (see table 3.1). Stents 1Z1, 1A1 and 1B1 exhibited close to no breathing so it is not surprising that they exhibited the highest hoop and radial stresses¹⁰. The displacement results make it clear that more flexible stents will impart lower magnitude stresses on the arterial wall due to the reduction in reaction force (restoring equilibrium) and contact stresses between the artery and the stent. Just as observed in hoop and radial stresses, stents with larger spacing, and in particular stent 2A3 – large spacing, middle radius of curvature and large amplitude – exhibit the most breathing and also imparts the lowest stresses on

¹⁰ Except for stent 1A1 in radial critical stresses.

the arterial wall. It is recognized that stent 2A3 is the best stent design relative to the population of stents analyzed herein. Furthermore, it is seen that a decrease in radius of curvature from stent 2A3 to 2Z3 – large spacing and amplitude, 0 mm radius of curvature – appears to stiffen the structure. Stents 2Z3 and 2A3 exhibit the same breathing in the ends of the stent, yet stent 2A3 has 0.02 mm more cyclic flexing in the middle of the structure than stent 2Z3. Such a small difference in displacement is perhaps not significant in terms of functionality of the stent, and furthermore, it might not be different in terms of injury imparted onto the vessel. Only with an experimental study could one have the opportunity to corroborate if the biological response is more vigorous or severe with one stent versus the other. Nevertheless, one is tempted to suggest that stent 2A3 is a better design based on these results and more likely to reduce the risk of intimal hyperplasia and eventual restenosis.

When varying spacing, stent 2B2 – large spacing, largest radius of curvature, medium amplitude – displayed less cyclic deflection between systole and diastole than stent 1B2 – smaller spacing, all else equal. This reduction in breathing is attributed to the reduced reaction force between the artery and the stent for the former design. While stent 1B2 exhibits larger cyclic deflections, it is thought that the smaller spacing in 1B2 will create larger reaction forces at the end struts than 2B2 –the more flexible stent. Since both stents have the same amplitude, the more compliant stent will elicit less of a need to deflect the end struts, than the stiffer stent. It is inconclusive whether stent 2B3 – not included in this thesis – with the largest radius of curvature, spacing and amplitude, would be a more compliant stent exhibiting increased breathing relative to stent 2A3.

Nevertheless, such stent would have an increased cyclical stretch relative to stent 2B2, due to its relative increase in amplitude. While it is postulated that having a larger radius of curvature would make it a more compliant stent, it is indeterminate until a numerical simulation is performed. Finally, the advantage of an increase in amplitude alone from stent 1B1 – small spacing, large radius of curvature and small amplitude – to stent 1B2, is obvious when observing figure 5.22. The former stent did not show any evidence of breathing at the stent edges, while stent 1B2 did.

6.4 Radial Displacement During Diastole at the Intima

Similar to the previous section, stents with large spacing induce the lowest displacements to the artery wall (relative to one cardiac cycle phase, and in the present discussion, diastole). This is attributed to the aforementioned increase in compliance associated with having longer connector bars. Just as larger amplitudes have larger moment arms allowing more deflection with less force, all else the same a longer connector bar will also increase the flexibility of the stent. Taking a moment at the center of a symmetrically loaded stent with contact forces around the circumference it is easily seen that larger connector bars will create larger moment arms and therefore the equilibrium restoring force originating from stent implantation and contact will be less than stents with short connector bars.

Stent 2A3 displayed the lowest radial displacements, imparting the lowest hoop stresses and radial stresses. The effects of varying geometric parameters were concordant with previous discussions. Namely, larger spacing and amplitudes rendered

more compliant stents imparting lower stresses to the artery wall. Differences when varying the radius of curvature were only noticeable in large spaced stents obeying the trends discussed above. Finally, stents with large amplitudes and spacing also exhibited evidence of compliance matching. It is evident in the displacement plots that edge struts of stent 1B2 deflect further than its center struts, while stent 1B1 does not exhibit this behavior. Furthermore, stent 2A3 is identified as the stent most likely to minimize harm to the arterial wall.

Lally et al. (2005) have reported that numerical results of tissue prolapse in an idealized stenotic artery treated with an S7 stent (Medtronic, AVE) exhibited “sufficient patency” and “superior scaffolding properties” when comparing a similar numerical model treated with an NIR stent (Boston Scientific). Their calculated tissue prolapse for the S7 stent was 0.056 mm while the simulations in this thesis show a tissue prolapse of 0.02 mm for stent 2A3 – recall that in this thesis a healthy artery was simulated and not a diseased one, so it is indeterminate whether or not stent 2A3 will remain patent on an actual artery (healthy or diseased, although in the case of the former it is likely that the stent in question will remain patent). However, it is inconclusive whether Lally et al., (2005) tissue prolapse calculations are representative of actual data from clinical trials. In addition, their constitutive law required an internal pressure of 13 MPa – over 128 atmospheres, or 97,500 mmHg – to be applied to the lumen of the artery for it to go beyond the nominal stent diameter. This most likely magnifies the differences in displacements and stresses that they reported between stent designs. In addition, note that their simulations – as a result of the increased stiffness in their arterial models,

produced stresses that are up to two orders of magnitude higher than those observed in this thesis. Material testing in this study required an internal pressure of less than 225 mmHg for the lumen of the artery to exceed the nominal stent diameter.

7. LIMITATIONS, FUTURE DIRECTIONS AND CONCLUSIONS

7.1 Limitations

Due to the high demand on computational resources, strict convergence criteria could not be applied to all models tested. Therefore, two different mesh densities are compared among the seven models tested (section 4.12). Trends observed in a model run at both densities were used to evaluate the effects of the different mesh densities. Based on these observations, it is believed that the effects of mesh density are not significant in comparing the models examined in this study – rankings of stents did not change relative to critical stresses, though this assumption is clearly an important limitation in this work.

The artery model employed herein is highly simplified, homogeneous and isotropic. Arteries are composed of heterogeneous distributions of constituents that possess a variety of mechanical properties. Thus, arteries are inhomogeneous and anisotropic. The constitutive model employed herein is therefore limited in its' ability to accurately model arterial mechanical behavior. It is assumed that in this comparative study, the simplified homogeneous isotropic model is sufficient to elucidate differences in stent design based on stresses imparted to the artery. However, evidence suggests that even a simple anisotropic model that allows for differing behavior in the circumferential and axial directions could reveal new insight. While axial stresses were generally not as high as the hoop stresses, there was no reliable connection between the hoop and axial stresses. Both were design dependent (axial stress data not shown). Therefore an anisotropic artery model, capable of exhibiting realistic behavior in both the hoop and

axial directions simultaneously, could result in a different understanding of the designs studied herein. In addition residual stresses were not included in this study. It is assumed that the stresses imparted by the stent are overwhelming to a degree that residual stresses would not change our conclusions. It is likely however that the stresses in the adventitia will exhibit a higher magnitude, while the intima would not show a significant decrease in stresses.

The software used in this study exhibited inconsistencies in processing the contact problem. It was not possible to obtain contact maps that were consistently on one body throughout this study. Namely, stents 1Z1, 1B1 and 1B2 exhibited contact maps on the artery while the rest of the stents showed the contact maps on the stent. It is expected that having consistent contact maps on one body or the other on all simulations, would affect the radial stresses by making them more similar (see radial stress results in section 5). Hoop stresses on the other hand, were not significantly affected. It is assumed that this limitation would not change our results significantly nor would it change our conclusions regarding stent hierarchy.

Only one degree of overexpansion was analyzed in this study and therefore we may only speculate how varying the stent oversize would affect our results. The hypothesis is that all stress magnitudes would increase because the artery would be subjected to a higher degree of overdistension. It is conjectured that radial stresses would be the most affected since it was observed that radial stresses for a stented artery model were highest during diastole (the greatest degree of oversize). In addition, a higher

degree of stent oversize would accentuate the contact pressures imparting a more compressive state of stress.

Arteries are often damaged in the stenting process; this would likely affect the stress distributions. Therefore, it is expected that the mechanical behavior of arteries would change as a result of remodeling. The purpose of this study however, was to elicit stent design criteria through use of the finite element method based on magnitudes of stresses imparted to the artery wall. The assumption is that the greatest degree of damage would be associated with the highest stresses and the lowest cyclical stretch of the artery. This limitation hinders our ability to speculate neointimal hyperplasia amounts and in-stent restenosis rates for the stents designed in this thesis.

The use of a homogeneous, non-diseased, non-curved arterial geometry is not realistic in a clinical setting. The use of a healthy rather than a diseased artery is more apt in this type of study (at the expense of lesion-specific geometries) given that we are characterizing general differences in stent design. Furthermore, the incorporation of plaque presence, and other attributes consistent with advanced atherosclerosis would change the stress fields each stent would impart on the artery wall. It is possible that some of the stents designed herein – while numerical evidence suggests that they will cause less harm by imparting lower magnitude stresses – might not be able to support the elastic recoil of an artery with a stenosis. Moreover, the measure of success of stents in a clinical setting is the ability to remain patent by having sufficient radial force, yet minimize the damage imparted to the artery and subsequently minimizing restenosis.

Finally, we used a porcine common carotid artery for mechanical properties, whereas we are trying to elucidate stent design criteria used in human coronaries. It is well known that there is much variability in the mechanical response of arteries – even within the same species. However, the make-up of arteries is similar, and it is postulated that conclusions drawn in this study are mostly unaffected by this limitation. More prevalent limiting criteria would include geometric idealization of healthy versus diseased arteries, and other shortcomings described herein.

7.2 Future Directions

Future directions of this study include an optimization of stress and displacement data whereby stresses imparted are minimized while cyclical deflection is maximized in order to design an optimal stent. Other extensions include modeling stenotic arteries with varying degrees of taper, as well as creating numerical simulations of a biological response to stenting. In addition, there are plans to create simulations using hybrid dynamic stents whereby there is a permanent as well as a biodegradable component to the stent. The biodegradable component is designed to give structural support and with a stent configuration optimal for avoiding thrombotic events in the acute stages of stent implantation. Once the biodegradable component is gone, the permanent component is designed to optimize re-endothelialization and compliance matching behavior.

7.3 Conclusions

The finite element method is a formidable tool that can be used to optimize stent design parameters resulting in stress distributions that minimize the impact of the stent on the artery wall. In this study, the variation of three design parameters was investigated. Stress distributions, concentrations, and gradients were all significantly affected by varying these parameters. The biologic response to the stress field induced by the stent is important to the success of the stenting procedure. Therefore, the ability to characterize the potential stress field induced by a particular design is critical to the stent design iteration process.

It is assumed that regions of high stress or high stress gradients are the most vulnerable to adverse biologic response. It is therefore concluded that stent 2A3 is the best overall stent design in the population of stents analyzed in this thesis. This stent is characterized by a large strut spacing, intermediate radius of curvature, and large amplitude. It produced the lowest hoop stresses as well as the lowest radial stresses on the intima and displayed the greatest flexibility when analyzing radial displacements. In addition, it demonstrated the greatest cyclic flexure and a smooth compliance transition region near the ends of the stent (compliance matching). These features suggest that stent 2A3 is the best candidate for minimizing the risk of restenosis through minimizing stresses, maximizing cyclical stretch of a stented artery and displaying compliance matching behavior. It is recommended that this stent design be implanted in porcine models and histological studies are performed whereby a biological response is correlated with the stent design. For comparison purposes, and to provide supporting

evidence to the claims made in this thesis, it is further suggested that stent 1Z1 also be manufactured and implanted in porcine models and growth and remodeling data is correlated with this stent design. Stent 1Z1 is characterized by tight strut spacing, zero radius of curvature, and low amplitude; traits that collectively contrast well with the more favorable 2A3 design.

REFERENCES

- American Heart Association, Dallas, Texas, 2004. Heart and Stroke Statistical Update: 2004 Update.
- Berry, J.L., Manoach, E., Mekkaoui, C., Rollan, P.H., Moor, J.E. Jr., Rachev, A., 2002. Hemodynamics and wall mechanics of a compliance matching stent: in vitro and in vivo analysis. *Journal of Vascular and Interventional Radiology* 13, 97-105.
- Carew, T.E., Vaishnav R.N., Patel D.J., 1968. Compressibility of the arterial wall. *Circulation Research* 23, 61-68.
- Chadwick, P., 1976. *Continuum Mechanics: Concise Theory and Problems*. Dover Publications Inc., New York.
- Chuong, C.J., Fung, Y.C., 1984. Compressibility and constitutive relation of arterial wall in radial compression experiments. *Journal of Biomechanics* 17, 35-40.
- Clark, J.M., Glagov, S., 1985. Transmural organization of the arterial media. The lamellar unit revisited. *Arteriosclerosis* 5, 19-34.
- Dobrin, P.B., Rovick, A.A., 1969. Influence of vascular smooth muscle on contractile mechanics and elasticity of arteries. *The American Journal of Physiology* 217, 1644-1651.
- Duerig T.W., Tolomeo, D.E., Wholey M., 2000. An overview of superelastic stent design. *Minimally Invasive Therapy & Allied Technologies* 9, 235-246.
- Edelman, E. R., Rogers, C., 1998. Pathobiologic responses to stenting. *The American Journal of Cardiology* 81, 4E-6E.

- Farb, A., Weber D.K., Kolodgie, F.D., Burke, A.P., Virmani R., 2002. Morphological predictors of restenosis after coronary stenting in humans. *Circulation* 105, 2974-2980.
- Fleisch, M., Meier, B., 1999. Management and outcome of stents in 1998: long term outcome. *Cardiology in Review* 7, 215-218.
- Fontaine, A.B., Spigos, D.G., Eaton, G., Das Passos, S., Christoforidis, G., Khabiri, H., Jung, S., 1994. Stent-induced intimal hyperplasia: are there fundamental differences between flexible and rigid stent designs? *Journal of Vascular and Interventional Radiology* 5, 739-744.
- Harrington, R.A., Kleiman, N.S., Kottke-Marchant, K., Lincoff, A.M., Tcheng, J.E., Sigmon, K.N., Joseph, D., Rios, G., Trainor, K., Rose, D., 1995. Immediate and reversible platelet inhibition after intravenous administration of a peptide glycoprotein IIb/IIIa inhibitor during percutaneous coronary intervention. *The American Journal of Cardiology* 76, 1222-1227.
- Holzapfel, G.A., 2000. *Nonlinear Solid Mechanics: A Continuum Approach for Engineering*. John Wiley and Sons, West Sussex, England.
- Holzapfel, G. A., Sommer, G., Regitnig, P., 2004. Anisotropic mechanical properties of tissue components in human atherosclerotic plaques. *Journal of Biomechanical Engineering* 126, 657-665.
- Holzapfel, G. A., Stadler, M., Gasser, T.C., 2005. Changes in the mechanical environment of stenotic arteries during interaction with stents: computational

- assessment of parametric stent designs. *Journal of Biomechanical Engineering* 127, 166-180.
- Humphrey, J.D., 2002. *Cardiovascular Solid Mechanics. Cells, Tissues, and Organs.* Springer, New York.
- Humphrey, J. D., Kang, T., Sakarda, P., Anjanappa, M., 1993. Computer-aided vascular experimentation: a new electromechanical test system. *Annals of Biomedical Engineering* 21, 33-43.
- Kastrati, A., Mehilli, J., Dirschinger, J., Pache, J., Ulm, K., Schuhlen, H., Seyfarth, M., Schmitt, C., Blasini, R., Neumann, F.J., Schomig, A., 2001. Restenosis after coronary placement of various stent types. *The American Journal of Cardiology* 87, 34-39.
- Kollros, P.R., Bates, S.R., Mathews, M.B., Horwitz, A.L., Glagov, S., 1987. Cyclic AMP inhibits increased collagen production by cyclically stretched smooth muscle cells. *Laboratory Investigation; A Journal of Technical Methods and Pathology* 56, 410-417.
- Kuntz, R.E., Gibson, C.M., Nobuyoshi, M., Baim, D.S., 1993. Generalized model of restenosis after conventional balloon angioplasty, stenting and directional atherectomy. *Journal of the American College of Cardiology* 21, 15-25.
- Lally, C., Dolan, F., Prendergast, P.J., 2005. Cardiovascular stent design and vessel stresses: a finite element analysis. *Journal of Biomechanics* 38, 1574-1581.
- Lawton, R.W., 1954. The thermoelastic behavior of isolated aortic strips of the dog. *Circulation Research* 2, 344-353.

- Migliavacca, F., Petrini, L., Colombo, M., Auricchio, F., Pietrabissa, R., 2002. Mechanical behavior of coronary stents investigated through the finite element method. *Journal of Biomechanics* 35, 803-811.
- Migliavacca, F., Petrini, L., Montanari, V., Quagliana, I., Auricchio, F., Dubini, G., 2005. A predictive study of the mechanical behaviour of coronary stents by computer modelling. *Medical Engineering and Physics* 27, 13-18.
- Mohammed, Z., Moore, J.E. Jr., Rachev, A., Berry, J., Manoach, E., 2000. Stress concentration reduction in stented arteries using compliance transitioning. *International Journal of Cardiovascular Medicine and Science* 3, 137-147.
- Moore, J. Jr., Berry, J.L., 2002. Fluid and solid mechanical implications of vascular stenting. *Annals of Biomedical Engineering* 30, 498-508.
- Morice, M.C., Serruys, P.W., Sousa, J.E., Fajadet, J., Ban Hayashi, E., Perin, M., Colombo, A., Schuler, G., Barragan, P., Guagliumi, G., Molnar, F., Falotico, R., 2002. A randomized comparison of a sirolimus-eluting stent with a standard stent for coronary revascularization. *The New England Journal of Medicine* 346, 1773-1780.
- Moses, J.W., Kipshidze, N., Leon, M.B., 2002. Perspectives of drug-eluting stents: the next revolution. *American Journal of Cardiovascular Drugs* 2, 163-172.
- MSC.Marc Volume A, 2004. MSC.Software Corporation, Santa Ana, California.
- MSC.Marc Volume B, 2004. MSC.Software Corporation, Santa Ana, California.
- Mudra, H., Regar, E., Klauss, V., Werner, F., Henneke, K.H., Sbarouni, E., Theisen, K., 1997. Serial follow-up after optimized ultrasound-guided deployment of Palmaz-

- Schatz stents. In-stent neointimal proliferation without significant reference segment response. *Circulation* 95, 363-370.
- Petrini, L., Migliavacca, F., Auricchio, F., Dubini, G., 2004. Numerical investigation of the intravascular coronary stent flexibility. *Journal of Biomechanics* 37, 495-501.
- Reddy, J. N., 1993. *An Introduction to the Finite Element Method*. McGraw-Hill, New York.
- Reddy, J.N., 2002. *Energy Principles and Variational Methods in Applied Mechanics*. John Wiley and Sons, New York.
- Roach, M.R., Burton, A.C., 1957. The reason for the shape of the distensibility curves of arteries. *Canadian Journal of Biochemistry and Physiology* 35, 681-690.
- Robaina, S., Jayachandran, B., He, Y., Frank, A., Moreno, M.R., Schoepfoerster, R.T., Moore, J.E. Jr., 2003. Platelet adhesion to simulated stented surfaces. *Journal of Endovascular Therapy* 10, 978-986.
- Rogers, C., Edelman, E. R., 1995. Endovascular stent design dictates experimental restenosis and thrombosis. *Circulation* 91, 2995-3001.
- Rogers, C., Tseng, D.Y., Squire, J.C., Edelman, E.R., 1999. Balloon-artery interactions during stent placement: a finite element analysis approach to pressure, compliance, and stent design as contributors to vascular injury. *Circulation Research* 84, 378-383.
- Slaughter, W., 2002. *The Linearized Theory of Elasticity*. Springer-Verlag New York.

- Squire, J.C., Rogers, C., Edelman, E.R., 1999. Measuring arterial strain induced by endovascular stents. *Medical & Biological Engineering & Computing* 37, 692-698.
- Sumpio, B.E., Banes, A.J., Levin, L.G., Johnson, G. Jr., 1987. Mechanical stress stimulates aortic endothelial cells to proliferate. *Journal of Vascular Surgery* 6, 252-256.
- Sumpio, B.E., Banes, A.J., Buckley, M., Johnson, G. Jr., 1988. Alterations in aortic endothelial cell morphology and cytoskeletal protein synthesis during cyclic tensional deformation. *Journal of Vascular Surgery* 7, 130-138.
- Topol, E.J., Lincoff, A.M., Kereiakes, D.J., Kleiman, N.S., Cohen, E.A., Ferguson, J.J., Tchong, J.E., Sapp, S., Califf, R.M., 2002. Multi-year follow-up of abciximab therapy in three randomized, placebo-controlled trials of percutaneous coronary revascularization. *The American Journal of Medicine* 113, 1-6.
- Versaci, F., Gaspardone, A., Tomai, F., Crea, F., Chiariello, L., Gioffre, P.A., 1997. A comparison of coronary-artery stenting with angioplasty for isolated stenosis of the proximal left anterior descending coronary artery. *The New England Journal of Medicine* 336, 817-822.
- Vorp, D.A., Peters, D.G., Webster, M.W., 1999. Gene expression is altered in perfused arterial segments exposed to cyclic flexure ex vivo. *Annals of Biomedical Engineering* 27, 366-371.
- Woods, T.C., Marks A.R., 2004. Drug-eluting stents. *Annual Review of Medicine* 55, 169-178.

APPENDIX A

```

%Program to Supply coordinates for stent creation
%given parameters such as radius of vessel, thickness
%of stent, angle between circular arc and straight line
%the corresponding sides of the formed right triangle
clear;
%clc;
figure(2);
r=2.375; %inner radius of stent
h=1.1875; %connector bar length
f=0.59375; %peak to peak distance of wave
t=0.10; %thickness of the stent
rho=0;
rho_o = rho + t/2; %radius of curvature of centerline stent
rho_1 = rho; %radius of curvature of sides of stent
rho_2 = rho + t;
c=2*pi*r; %circumference of the stent
n=8; %number of wavelengths around circumference -->choose from 8,16,24
d=c/n; %one wavelength
phi=(32.4816)*(pi/180); %angle in radians
Z = 1; % z-coordinate of origin
ksi = f - 2*rho_o*(1-cos(phi));
psi = d/2 - 2*rho_o*sin(phi);

p5=[0/r, Z-t/2];
p6=[0/r, Z+t/2];
p7=[(rho_2*sin(phi))/1, Z + (-t/2 + rho_2*(1-cos(phi)))];

```

$p8=[(\rho_1 \sin(\phi))/1, Z + (t/2 + \rho_1(1-\cos(\phi)))];$
 $p9=[(\rho_2 \sin(\phi) + \psi)/1, Z + (-t/2 + \rho_2(1-\cos(\phi)) + \kappa)];$
 $p10=[(\rho_1 \sin(\phi) + \psi)/1, Z + (t/2 + \rho_1(1-\cos(\phi)) + \kappa)];$
 $p11=[(d/2)/1, Z + -t/2 + f];$
 $p12=[(d/2)/1, Z + t/2 + f];$
 $p13=[(d/2 + \rho_1 \sin(\phi))/1, Z + (-t/2 + f - \rho_1(1-\cos(\phi)))];$
 $p14=[(d/2 + \rho_2 \sin(\phi))/1, Z + (t/2 + f - \rho_2(1-\cos(\phi)))];$
 $p15=[(d/2 + \rho_1 \sin(\phi) + \psi)/1, Z + (-t/2 + \rho_2(1-\cos(\phi)))];$
 $p16=[(d/2 + \rho_2 \sin(\phi) + \psi)/1, Z + (t/2 + \rho_1(1-\cos(\phi)))];$
 $p17=[p5(1)+d/1,p5(2)];$
 $p18=[p6(1)+d/1,p6(2)];$
 $p19=[p7(1)+d/1,p7(2)];$
 $p20=[p8(1)+d/1,p8(2)];$
 $p21=[p9(1)+d/1,p9(2)];$
 $p22=[p10(1)+d/1,p10(2)];$
 $p23=[p11(1)+d/1,p11(2)];$
 $p24=[p12(1)+d/1,p12(2)];$
 $p25=[p13(1)+d/1,p13(2)];$
 $p26=[p14(1)+d/1,p14(2)];$
 $p27=[p15(1)+d/1,p15(2)];$
 $p28=[p16(1)+d/1,p16(2)];$
 $p29=[p5(1)+2*d/1,p5(2)];$
 $p30=[p6(1)+2*d/1,p6(2)];$

 $p31=[-p7(1),p7(2)];$
 $p32=[-p8(1),p8(2)];$
 $p33=[p7(1)+2*d,p7(2)];$
 $p34=[p8(1)+2*d,p8(2)];$


```

%Number of points created in A-Z. In actuality, there are 4 points created
%when the surface is made for a total of 34. 34 does not include other
%points that will be created later.
n=30;

X1 =
[p32(1),p6(1),p8(1),p10(1),p12(1),p14(1),p16(1),p18(1),p20(1),p22(1),p24(1),p26(1),p2
8(1),p30(1),p34(1)];
Y1 =
[p32(2),p6(2),p8(2),p10(2),p12(2),p14(2),p16(2),p18(2),p20(2),p22(2),p24(2),p26(2),p2
8(2),p30(2),p34(2)];

X2 =
[p31(1),p5(1),p7(1),p9(1),p11(1),p13(1),p15(1),p17(1),p19(1),p21(1),p23(1),p25(1),p27(
1),p29(1),p33(1)];
Y2 =
[p31(2),p5(2),p7(2),p9(2),p11(2),p13(2),p15(2),p17(2),p19(2),p21(2),p23(2),p25(2),p27(
2),p29(2),p33(2)];

r1 = r + zeros(15,1);
plot(X1,Y1,'-o',X2,Y2,'-O')
%axis([-1 7 -1 4])
%axis square;
axis equal;
coord = zeros(30,3);
for i=1:1:n
    coord(i,:,:) = eval(sprintf('[r,(180/pi)*p%g(1)/r,p%g(2)]',i+4,i+4));
end

```

```

%Create File
fid = fopen('stent8A_cave.ses','w');

file_create = 'uil_file_open.go(
"C:\Julian\Patran\No_residual_stress\vessel_and_stent\matlab_stents\CAVE_FEM\STE
NT1\stent8A_cave.db" );
gen_comment1 = '$# Database version 3.2 created by 2004 12.0.044 successfully
opened.';
gen_comment2 = '$# Appending to existing journal file';
gen_comment3 = '$#
C:\Julian\Patran\No_residual_stress\vessel_and_stent\matlab_stents\CAVE_FEM\STEN
T1\stent8A_cave.db.jou at';
gen_comment4 = sprintf('$# %s',datestr(now));
file_pref1 = 'uil_pref_analysis.set_analysis_preference( "MSC.Marc", "Structural",
".dat", @';
file_pref2 = "'.t16", "No Mapping" );
gen_comment5 = '$# Changing results display tool settings - DeformedScale: Model=0.1
to';
gen_comment6 = '$# DeformedScale:True=1..';
geom_tol = 'ga_display_tolerance_set( "general", 9.9999997E-006 );

%create cylindrical coordinates
cyl_coord1 = 'STRING asm_create_cord_3po_created_ids[VIRTUAL]';
cyl_coord2 = 'asm_const_cord_3point( "1", "Coord 0", 2, "[0 0 0]", "[0 0 1]", "[1 0 0]",
asm_create_cord_3po_created_ids );
cyl_coord3 = '$# 1 Coord created: Coord 1';

% %Create Cylindrical surface

```

```

% cyl_surf1 = 'STRING asm_create_patch_xyz_created_ids[VIRTUAL]';
% cyl_surf2 = 'asm_const_patch_xyz( "1", "<0 120 10>", "[3.45 -10 0]", "Coord 1",
asm_create_patch_xyz_created_ids)';
% cyl_surf3 = '$# 1 Patch created: Patch 1';

% Must change to match r
cyl_surf1 = 'STRING asm_create_grid_xyz_created_ids[VIRTUAL]';
cyl_surf2 = 'asm_const_grid_xyz( "1", "[2.375 0 0]", "Coord 0",
asm_create_grid_xyz_created_ids)';
cyl_surf3 = 'STRING sgm_sweep_curve_rev_created_ids[VIRTUAL]';
cyl_surf4 = 'sgm_const_curve_revolve( "1", "Coord 0.3", 90., 0., "Coord 0", "Point 1",
sgm_sweep_curve_rev_created_ids)';
cyl_surf5 = 'STRING sgm_sweep_surface_e_created_ids[VIRTUAL]';
cyl_surf6 = 'sgm_const_surface_extrude( "1", "<0 0 5>", 1., 0., "[0 0 0]", "Coord 0",
"Curve 1", sgm_sweep_surface_e_created_ids)';

fprintf(fid,'%s\n%s\n%s\n%s\n%s\n%s\n%s\n%s\n%s\n%s\n',geom_tol,file_create,gen_
comment1,gen_comment2,gen_comment3,...
gen_comment4,file_pref1,file_pref2,gen_comment5,gen_comment6);
fprintf(fid,'%s\n%s\n%s\n%s\n%s\n%s\n',cyl_coord1,cyl_coord2,cyl_coord3,cyl_surf1,c
yl_surf2,cyl_surf3,cyl_surf4,cyl_surf5,cyl_surf6);

%Create strings for points
for i=1:1:n
    j=i+4;
    point_predecessor = 'STRING asm_create_grid_xyz_created_ids[VIRTUAL]';

```

```

point_string1 = sprintf('asm_const_grid_xyz( "%g", "[%g %g %g]", "Coord 1", @'...
    ,j,coord(i,1),coord(i,2),coord(i,3));
point_string2 = 'asm_create_grid_xyz_created_ids ');

point_comment = sprintf('$# 1 Point created: Point %g',j);

fprintf(fid,'%s\n%s\n%s\n%s\n',point_predecessor,point_string1,point_string2,point_co
mment);
end
fprintf(fid,'%s\n%s\n%s\n%s\n',point_predecessor,point_string1,point_string2,point_co
mment);

%Create manifold curves
m=2; %Number of man_curves to be created
j=5; %first point created in man_curve
w=29; %Last point in man_curve
man_curve_call = 'STRING sgm_curve_manifold__created_ids[VIRTUAL]';
for k=1:1:m
    man_curve = sprintf('sgm_const_curve_manifold_npoint( "%g", "Surface 1", "Point
%g:%g:2", sgm_curve_manifold__created_ids )'...
        ,k,j,w);
    man_curve_comm = sprintf('$# 1 Curve Created: Curve %g',k);
    fprintf(fid,'%s\n%s\n%s\n',man_curve_call,man_curve,man_curve_comm);
    j=j+1;
    w=w+1;
end
%Create line_2point for ends of stent per strut
L2p=4; %Counter for line_2points (global curve counter)
j=5; %first point used in line_2point

```

```

w=29; %Last point used in line_2point
for k=m:1:m+1
    line_2point_call = 'STRING asm_line_2point_created_ids[VIRTUAL]';
    line_2point = sprintf('asm_const_line_2point( "%g", "Point %g", "Point %g", 0, "",
50., 1, asm_line_2point_created_ids )'...
,k+1,j+1,j);
    line_2point_comm = sprintf('$# 1 Line created: Line %g',k+1);
    fprintf(fid,'%s\n%s\n%s\n',line_2point_call,line_2point,line_2point_comm);
    j=w;
end

%Create line_normal
line_normal_call = 'STRING asm_create_line_nor_created_ids[VIRTUAL]';
line_normal = 'asm_const_line_normal( "5", "Point 8 10 14 16 20 22 26 28", "Curve 1",
asm_create_line_nor_created_ids )';
line_normal_comm = '$# 8 Lines created: Line 5:12';
fprintf(fid,'%s\n%s\n%s\n',line_normal_call,line_normal,line_normal_comm);

%Break curves
break_curve_pt_call = 'STRING sgm_curve_break_poi_created_ids[VIRTUAL]';
break_curve1_pt = 'sgm_edit_curve_break_point( "13", "Point 8 10 14 16 20 22 26 28",
"Curve 2", TRUE, sgm_curve_break_poi_created_ids )';
break_curve_pt_comm = '$# 9 Curves Created: Curves 13:21';
question1 = '$# Question from application SGM';
question2 = '$# Do you wish to delete the original curves?';
answer = '$? YES';
delete_comm = '$# 1 Curve Deleted: Curve 2';
break_curve2_pt = 'sgm_edit_curve_break_point( "22", "Point 35:42", "Curve 1",
TRUE, sgm_curve_break_poi_created_ids )';

```

```

fprintf(fid,'%s\n%s\n%s\n%s\n%s\n%s\n%s\n',break_curve_pt_call,break_curve1_pt,break_curve_pt_comm,question1,question2,answer,delete_comm);
fprintf(fid,'%s\n%s\n%s\n%s\n%s\n%s\n%s\n',break_curve_pt_call,break_curve2_pt,break_curve_pt_comm,question1,question2,answer,delete_comm);
fclose(fid);

```

```

% load handel

```

```

% sound(y,Fs)**END PROGRAM

```

```

%This program calculates geometrically feasible stents

```

```

clear;

```

```

fid = fopen('stent_geometries_cave.xls','w');

```

```

h=1.8; %Minimum connector bar length

```

```

f=0; %Minimum peak to peak distance

```

```

rho = 0; %mimimum radius of curvature of stent

```

```

H=4; %Maximum value for peak-to-peak distance

```

```

inc_h = 1.6; %increment of connector bar length

```

```

inc_f = h/2;

```

```

inc_rho = f/4;

```

```

r=3.157; %Radius of stent

```

```

t2=0.15; %Thickness of stent

```

```

c=2*pi*r;

```

```

n=8;

```

```

d=c/n;

```

```

i=1;

```

```

i2 = 'valid iteration #';

```

```

h2 = 'h in mm';

```

```

f2 = 'f in mm';

```

```

rho2 = 'rho in mm';

```

```

d2 = 'wavelength in mm';
n2 = 'wavelengths around circ';
xi2 = 'xi';
psi2 = 'psi';
phi2 = 'phi in degrees';
fprintf(fid,'%s\t%s\t%s\t%s\t%s\t%s\t%s\t%s\t%s\n',i2,h2,f2,rho2,d2,n2,xi2,psi2,phi2);
while n<=24
    for h=1.8:inc_h:7.2
        for f=0:h/2:H
            for rho=0:f/4:f/2
                if d >= 4*(rho + t2/2)
                    d=c/n;
                    [phi,psi,xi] = solve(sprintf('xi = %g - 2*%g*(1 - cos(phi))',f,rho),sprintf('psi = (1/2)*%g - 2*%g*sin(phi)',d,rho),'phi=atan(xi/psi)');
                    xi=double(xi);
                    psi=double(psi);
                    phi=double(phi*(180/pi));

                    fprintf(fid,'%g\t%g\t%g\t%g\t%g\t%g\t%g\t%g\t%g\n',i,h,f,rho,d,n,xi,psi,phi);
                    i
                end
                i=i+1;
            end
        end
    end
    n=n+8;
end
fclose(fid);**END PROGRAM

```

```

clear all
close all
load johnsdata.txt
Lz=johnsdata(:,1);
P=johnsdata(:,2);
lamz=johnsdata(:,3);
rout=johnsdata(:,4);
Rout=.002509;
lamq_out=rout/Rout;
%Rin=.001196;

R_L=.0017212; % luminal radius in meters
R_X=.002509; % external radius in meters
Rvec=R_L:((R_X-R_L)/1000):R_X; % set of points every .1% of radius

P_L=P';
L_Z=Lz';

N_pts=max(size(P_L));
Rstep=(max(rout)-min(rout))/N_pts;
Rfirst=Rout/sqrt(sum(lamz)/N_pts);
R_of_adds=Rfirst:Rstep:rout(1);
n_of_adds=max(size(R_of_adds));

rout=[Rfirst:Rstep:rout(1) rout'];
P_L=[P(1)*(rout(1:n_of_adds)-rout(1))/(rout(n_of_adds)-rout(1)) P_L];

```



```

L_Z=[L_Z(1)*ones(1,n_of_adds) L_Z];
lamz=[lamz(1)*ones(1,n_of_adds) lamz'];
lamq_out=rout/Rout;
N_pts=max(size(P_L));

Alpha=lamz.^1.5-1;
zhiL=(lamz.^0.5).*(lamq_out);
Beta=zhiL.^2-1;
beta_max=max(Beta)*2;
N_pts=max(size(P_L));

%figure(1);clf;plot(Beta(1,:),P_L(1,:),''); title('generated data'); xlabel('beta');
ylabel('Pressure (Pa)')
%figure(2);clf;plot(Beta(1,:),L_Z(1,:),''); title('generated data'); xlabel('beta');
ylabel('Axial load (N)')
figure(1);clf;plot(rout/Rout,P_L(1,)/1000,''); title('generated data'); xlabel('outer radius
(mm)'); ylabel('Pressure (kPa)');hold on
figure(2);clf;plot(rout/Rout,L_Z(1,),''); title('generated data'); xlabel('outer radius
(mm)'); ylabel('Axial load (N)');hold on

N_pts=861; % cannot be changed with present code

P_L=zeros(1,N_pts); % the number of testing trajectories with constant stretch is
N_paths and the number of pts for each test is N_pts
L_Z=zeros(1,N_pts);
Alpha=zeros(1,N_pts);
Beta=zeros(1,N_pts);

```

```

alpha_max=4; % alpha and beta are as defined in the IUTAM 2004 presentation
lamz_max=(alpha_max+1)^(2/3); % lamz is the axial stretch. 'lam' for lambda.
zhiL_max=sqrt(beta_max+1); % greek letter zhi is for the 'inflation stretch'
mu=1; % approximate shear modulus for rubber in Pa

% data for axial stretch constant and increase diameter is in this first
% set of for loops
%c10=4328.1338;
%c01=0;
%c11=0;
%c20=-5317.6406;
%c30=13727.428;
a=46000; b=11966+12000; c=-506; d=-4777-16500;
c10=b; c01=d; c11=c; c20=(a-c)*0.5; c30=1650;

%lamz=1.59;
r_outer=zeros(1,N_pts);
for i=1:1:1
    zhiL=((1/N_pts):(1/N_pts):1)*(zhiL_max-1)+1;
    lamq_L=(lamz(i).^(-0.5))*zhiL;
%    I1=zeros(1,N_pts);
%    I2=zeros(1,N_pts);
    for j=1:N_pts
        Alpha(i,j)=lamz(i).^1.5-1;
        Beta(i,j)=zhiL(j).^2-1;
        lamq=sqrt(1/lamz(i)+R_X^2*(lamq_L(j)^2-1/lamz(i))./(Rvec.^2)); % lamq is the
hoop stretch. 'lam' for lambda and 'q' for theta
        I1=lamz(i)^2+lamq.^2+1./(lamz(i)*lamq).^2;
        I2=1/lamz(i)^2+1./lamq.^2+(lamz(i)*lamq).^2;

```

```

rvec=lamq.*Rvec;
r_outer(j)=max(rvec);
Bqq=lamq.^2;      % Brr is the radial-radial component of B, the left cauchy-
green deformation tensor
Bzz=lamz(i)^2+0*lamq;
Brr=1./(Bqq.*Bzz);
dWdI1=c10+c11*(I2-3)+2*c20*(I1-3)+3*c30*(I1-3).^2;
dWdI2=c01+c11*(I1-3);
trr=2*dWdI1.*Brr-2*dWdI2.*(1./Brr);
tqq=2*dWdI1.*Bqq-2*dWdI2.*(1./Bqq);
tzz=2*dWdI1.*Bzz-2*dWdI2.*(1./Bzz); % trr is the radial-radial component of
t, the cauchy stress with the Lagrange multiplier yet
%plot(j,rvec(1),'.')
rtmp=0.5*(rvec(2:1001)+rvec(1:1000));
dr=(rvec(2:1001)-rvec(1:1000));
trr_tmp=0.5*(trr(2:1001)+trr(1:1000));
tqq_tmp=0.5*(tqq(2:1001)+tqq(1:1000));
tzz_tmp=0.5*(tzz(2:1001)+tzz(1:1000));
P_L(i,j)=sum((tqq_tmp-trr_tmp).*dr./rtmp);
%      P_L(i,j)=P_L(i,j)+2*(rand(1,1)-0.5)*0.02*P_L(i,j); % rand function adds
some error to the calculated quantity
%      L_Z(i,j)=pi*sum((2*tzz_tmp-tqq_tmp-trr_tmp).*rtmp.*dr)-
pi*rvec(1)^2*P_L(i,j);
      L_Z(i,j)=pi*sum((2*tzz_tmp-tqq_tmp-trr_tmp).*rtmp.*dr);
%      L_Z(i,j)=L_Z(i,j)+2*(rand(1,1)-0.5)*0.02*L_Z(i,j);
end
end

```

```

figure(1);plot(r_outer/Rout,P_L(1,:)/1000,'g. '); title('generated data'); xlabel('outer hoop
stretch'); ylabel('Pressure (kPa)'); grid
figure(2);plot(r_outer/Rout,L_Z(1,:),'g. '); title('generated data'); xlabel('outer hoop
stretch'); ylabel('Axial load (N)'); grid **END PROGRAM

```

```

clc; tic
clear;
close all;
format short g;
warning off all

```

```

% Identify source filenames - located within same directory as m-files
stress_source_filename = 'cauchy_ri_dias_7xeA.rpt'
displ_source_filename = 'displ_ri_dias_7xeA.rpt'
displ_45_report_name = 'displ_ri_dias_7xeA_45.rpt' %ALWAYS DIASTOLE
%*****
% Settings used when writing to file
stent_name = '7xeA'; cycle_phase = 'Diastole';
vessel_wall = 'intima';
%*****
% Settings used to identify range of interest
stent_length = 9.00625;
stent_radius = 2.375;
reps = 6;
angle_tol = 0.03;
theta_nodes = linspace(0,90,57); %MESH SPECIFIC ANGLE LIST
theta_width = theta_nodes(2);

angles_list = [45]

```

```

%B IS 81, A IS 57 (CORNERS)
%B IS 41, A IS 29 (MIDDLE)
%*****
stress_source_file = load(stress_source_filename);
displ_source_file = load(displ_source_filename);
displ_45_report = load(displ_45_report_name);
%*****

%RUN CHECK FILES PROGRAM
[complete_message,vessel_ROI_L,vessel_ROI_R,centerlineZ,nearest_z_position_undef
_to_ROI_L,nearest_z_position_undef_to_ROI_R] = ...

check_files(stress_source_file,displ_source_file,displ_45_report,stent_length,stent_radiu
s)

%CONTINUE PROGRAM IF FILES ARE OK
if complete_message=='PASSED'

%*****
maximum = 'Max Stress'; mininum = 'Min Stress';

stress_matrix = [];
deform_config = [];

% create array out of STRESS input file corresponding to region of interest
h = waitbar(0,'What is the capital of Suriname?');
for i=1:length(stress_source_file)

```

```

    if stress_source_file(i,4)>= nearest_z_position_undef_to_ROI_L &
stress_source_file(i,4)<= nearest_z_position_undef_to_ROI_R
        stress_matrix = [stress_matrix; stress_source_file(i,:)];
    end
    waitbar(i/(length(stress_source_file)),h)
end
close(h)

% create array out of DISP input file corresponding to region of interest
h = waitbar(0,'Paramaribo!');
for i=1:length(displ_source_file)
    if displ_source_file(i,4)>= nearest_z_position_undef_to_ROI_L &
displ_source_file(i,4)<= nearest_z_position_undef_to_ROI_R
        deform_config = [deform_config; displ_source_file(i,:)];
    end
    waitbar(i/(length(displ_source_file)),h)
end
close(h)

nodeIDs = deform_config(:,1);

%CLARK'S conversion program

stress_withZdefs = [];
counter=0;
h = waitbar(0,'What is the capital of Namibia?');
for i=1:length(stress_matrix);%LOOP TO GET DEFORMED Z COORDINATES
    for j=1:length(nodeIDs);
        if stress_matrix(i,1) == nodeIDs(j,1);

```

```

        stress_matrix(i,4) = stress_matrix(i,4) + deform_config(j,8);
        counter = counter+1;
    end
end
waitbar(i/(length(stress_matrix)),h)
end
close(h);
%%%%%%%%%%%%%%%%%%%%%%%%%%%%%%%%%%%%%%%%%%%%%%%%%%%%%%%%%%%%%%%%%%%%%%%%END OF CLARK'S
CONVERSION PROGRAM

stress_matrix = sortrows(stress_matrix,4); %SORTED W.R.T Z
deform_config = sortrows(deform_config,4); %SORTED W.R.T Z

entity_id = stress_matrix(:,1);
x_undef = stress_matrix(:,2);
y_undef = stress_matrix(:,3);
z_undef = stress_matrix(:,4);
VM = stress_matrix(:,5);
r_stress = stress_matrix(:,6);
th_stress = stress_matrix(:,7);
z_stress = stress_matrix(:,8);
max_stress = stress_matrix(:,9);
mid_stress = stress_matrix(:,10);
min_stress = stress_matrix(:,11);
radius = sqrt(x_undef.^2+y_undef.^2);
z_def = deform_config(:,4) + deform_config(:,8);
radius_def = radius + deform_config(:,6);

for i=1:length(r_stress)

```

```

    angle(i) = atan(y_undef(i)/x_undef(i))*(180/pi);
    if angle(i) == -90
        angle(i) = 90;
    end
end
angle = angle';
stress_matrix = [stress_matrix angle radius radius_def];

stress_matrix = sortrows(stress_matrix,12); %Sorting by angle

fid = fopen('practice.xls','w');
fid2 = fopen('frequency.xls','w');

fprintf(fid,'Stress Measure\t Stent Number\t Cycle Phase\t Angle\t Vessel Wall
Position\t');
fprintf(fid,'Stress per unit length in kPa/mm\t Max Stress kPa\t Min Stress kPa\t');
fprintf(fid,'Stress per unit Volume MPa/mm^3\t stent_length mm\t reps\t angle_tol\t');
fprintf(fid,'Max R Value(deformed)\t Min R value\t');
fprintf(fid,'stent_lengthMOD mm\t Stress Source File\t Displ Source File\n');

fprintf(fid2,'Stress Measure\t Stent Number\t Cycle Phase\t Angle\t Vessel Wall
Position\t');
fprintf(fid2,'stent_length mm\t reps\t angle_tol\t');
fprintf(fid2,'stent_lengthMOD mm\t Stress Source File\t Displ Source File\t');
fprintf(fid2,'Frequency\t Bin\n');

```



```

for m = 1:length(angles_list)
    user_angle = angles_list(m)
    stress_col = [5:11];
    [ave_stress,stent_lengthMOD,stress_extras] = ...

stress_z_integral(user_angle,angle_tol,reprs,stress_col,stent_length,stress_matrix,centerlineZ);

%ri = 1.196; ra = 2.509; %INTIMAL AND ADVENTITIAL RADII
%volume = (theta_width*pi/180)*(ra^2 - ri^2)*stent_lengthMOD %VOLUME OF
QUARTER VESSEL USING STENT AS LENGTH

nbins=100;
for b=5:1:11
    stress_col=b;
    if stress_col==5
        stress_title='Von Mises Stress';
    elseif stress_col==6
        stress_title='Radial Stress';
    elseif stress_col==7
        stress_title='Hoop Stress';
    elseif stress_col==8
        stress_title='Axial Stress';
    elseif stress_col==9
        stress_title='Maximum Principal Stress';
    elseif stress_col==10
        stress_title='Mid Principal Stress';
    elseif stress_col==11

```



```

end
stress_col = [5:11];

[ave_surf_stress,total_surf_stress,stent_lengthMOD,G] = ...

theta_z_integral(radius,radius_def,theta_nodes,angle_tol,reps,stress_col,stent_length,stre
ss_matrix,centerlineZ);

for b=5:1:11
    %volume = pi/4*(ra^2 - ri^2)*(nearest_z_position_undef_to_ROI_R-
nearest_z_position_undef_to_ROI_L)
    % changed to undeformed ROI length - using all undeformed dimensions...
    stress_col=b;
    if stress_col==5
        stress_title='Von Mises Stress';
    elseif stress_col==6
        stress_title='Radial Stress';
    elseif stress_col==7
        stress_title='Hoop Stress';
    elseif stress_col==8
        stress_title='Axial Stress';
    elseif stress_col==9
        stress_title='Maximum Principal Stress';
    elseif stress_col==10
        stress_title='Mid Principal Stress';
    elseif stress_col==11
        stress_title='Minimum Principal Stress';
    end
end

```



```

    % MAYBE use a different volume
end
fprintf(fid,'\n');
fclose(fid);

fprintf(fid2,'\n');
fclose(fid2);

end
toc
'why?'
why
'But why?'
why
'Well that"s fantastic!!'

%print -f6; print -f7; print -f8; print -f9;**END PROGRAM

function
[complete_message,vessel_ROI_L,vessel_ROI_R,centerlineZ,nearest_z_position_undef
_to_ROI_L,nearest_z_position_undef_to_ROI_R] =
check_files(stress_source_file,displ_source_file,displ_45_report,stent_length,stent_radiu
s)
%CHECK FILES PROGRAM
%*****
%INPUT VARIABLES

```

```

stress_source_file;
displ_source_file;
displ_45_report;
stent_length;
stent_radius;
%*****

x_undef = displ_45_report(:,2);
y_undef = displ_45_report(:,3);
z_undef = displ_45_report(:,4);

for i=1:length(displ_45_report)
    angle(i) = atan(y_undef(i)/x_undef(i))*(180/pi);
    if angle(i)==-90
        angle(i)=90;
    end
end
angle=angle';

radius = sqrt(x_undef.^2 + y_undef.^2);
radial_deformation = displ_45_report(:,6);
theta_deformation = displ_45_report(:,7);
z_deformation = displ_45_report(:,8);
radius_def = radius + displ_45_report(:,6);
theta_def = angle + theta_deformation;
def_z = z_undef + displ_45_report(:,8);

node_ID = displ_45_report(:,1);

```

```

def_config_matrix =
[radius,angle,z_undef,radial_deformation,theta_deformation,z_deformation,...
 radius_def,theta_def,def_z,node_ID];
angle_tol=0.01;
axial_tol=0.001;
for i=1:length(def_config_matrix)
    if def_config_matrix(i,6) <= angle_tol & def_config_matrix(i,6) >= -angle_tol ;
        centerlineZ = def_config_matrix(i,3);
    end
end

vessel_ROI_L = centerlineZ - (stent_length/2 + 1/2*stent_radius);
vessel_ROI_R = centerlineZ + stent_length/2 + 1/2*stent_radius;

min_best_distance = 0.1;
for i=1:length(def_config_matrix)
    distance_to_target = abs(def_config_matrix(i,9)- vessel_ROI_L); %DEFORMED Z -
VESSEL_ROI
    if distance_to_target < min_best_distance
        min_best_distance = distance_to_target;
        nearest_z_position_def_to_ROI_L = def_config_matrix(i,9);
        nearest_z_position_undef_to_ROI_L = def_config_matrix(i,3);
        node_ROI_L = def_config_matrix(i,10);

    end
end

min_best_distance = 0.1;
for i=1:length(def_config_matrix)

```

```

distance_to_target = abs(def_config_matrix(i,9)- vessel_ROI_R);
if distance_to_target < min_best_distance
    min_best_distance = distance_to_target;
    nearest_z_position_def_to_ROI_R = def_config_matrix(i,9);
    nearest_z_position_undef_to_ROI_R = def_config_matrix(i,3);
    node_ROI_R = def_config_matrix(i,10);
end
end

node_found_L_S = find(stress_source_file(:,1)==node_ROI_L);
node_found_R_S = find(stress_source_file(:,1)==node_ROI_R);

node_found_L_D = find(displ_source_file(:,1)==node_ROI_L);
node_found_R_D = find(displ_source_file(:,1)==node_ROI_R);

if isempty(node_found_L_S)==1
    message_L_S = sprintf('The left edge should be at %0.5g (undeformed) and include
node ID %0.5g',...
    nearest_z_position_undef_to_ROI_L,node_ROI_L)
end
if isempty(node_found_R_S)==1
    message_R_S = sprintf('The right edge should be at %0.5g (undeformed) and include
node ID %0.5g',...
    nearest_z_position_undef_to_ROI_R,node_ROI_R)
end

if isempty(node_found_L_D)==1
    message_L_D = sprintf('The left edge should be at %0.5g (undeformed) and include
node ID %0.5g',...

```



```

        nearest_z_position_undef_to_ROI_L,node_ROI_L)
end

if isempty(node_found_R_D)==1
    message_R_D = sprintf('The right edge should be at %0.5g (undeformed) and include
node ID %0.5g',...
        nearest_z_position_undef_to_ROI_R,node_ROI_R)
end

if isempty(node_found_L_S)==1 | isempty(node_found_R_S)==1 |
isempty(node_found_L_D)==1 | isempty(node_found_L_D)==1
    complete_message = 'FAILED'
else
    complete_message = 'PASSED'
end **END PROGRAM

function [ave_stress,stent_lengthMOD,stress_extras] =
stress_z_integral(user_angle,angle_tol,reprs,stress_col,stent_length,stress_matrix,centerli
neZ)

%THIS PROGRAM WILL INTEGRATE THE STRESSES ALONG THE Z-AXIS
%DIRECTION TO COMPARE THE STRESS PLOTS ON EACH STENT AT A
GIVEN ANGLE

%*****
user_angle;%INPUT VARS
angle_tol;
reprs;
stress_col;

```

```

stent_length;
stress_matrix;
centerlineZ;
%*****

H=[];
for i=1:length(stress_matrix(:,12)); %LOOP EXTRACTING RELEVANT ANGLE
    if stress_matrix(i,12) >= (user_angle - angle_tol) & stress_matrix(i,12) <= (user_angle
+ angle_tol)
        H=[H; stress_matrix(i,:)];
    end
end

H_sorted=sortrows(H,4); %SORTING STRESS MATRIX WITH RELEVANT ANGLE
BY Z POSITION
H_1=H(1,:);
H_last = H_sorted((length(H)),:);
H_new = [H_1; H_sorted ; H_last]; %ADDING ROWS TO H FOR THE PURPOSE OF
FINDING A dz VALUE

z_width=[]; %LOOP TO DETERMINE dz VALUE: NOTE THAT dz IS NOT A
CONSTANT, AND IT IS A RECTANGLE
for i=2:(length(H_new) - 1)
    current = H_new(i,4);
    prior = H_new(i-1,4);
    next = H_new(i+1,4);

    nodeZ_width = (next - current)/2 + (current - prior)/2;
    z_width = [z_width; nodeZ_width];
end

```

end

H_Zwidth = [H_sorted z_width]; %CONCATENATING dz AS A COLUMN VECTOR
TO MODIFIED H

z_stress_area=0;

for i=1:1:length(H_Zwidth)

 z_stress_area = z_stress_area + H_Zwidth(i,stress_col)*H_Zwidth(i,15);

%INTEGRATION OF STRESSES ALONG Z

 %IN THE CURRENT CONFIGURATION!

end

z_length = sum(H_Zwidth(:,15)); %VALIDATING THAT SUM OF dz ADDS UP TO
TOTAL LENGTH

ave_stress_in_z = z_stress_area/z_length;

stent_edgeL = centerlineZ - (stent_length)/2;

stent_quarter = centerlineZ - (stent_length/2)/2;

stent_mid = centerlineZ;

stent_3quarter = centerlineZ + (stent_length/2)/2;

stent_edgeR =centerlineZ + stent_length/2;

A=[];

B=[];

C=[];

D=[];

E=[];

F=[];%VARIABLES TO ADD MIDDLE SECTIONS OF STENT AND THEN
ASSEMBLE

for i=1:1:length(H_Zwidth);

```

if H_Zwidth(i,4) < stent_edgeL;
    A = [A; H_Zwidth(i,:)];%LEFT SECTION WHERE THERE IS NO STENT
elseif H_Zwidth(i,4) >= stent_edgeL & H_Zwidth(i,4) < stent_quarter; %FIRST
QUARTER OF STENT
    B = [B; H_Zwidth(i,:)];
elseif H_Zwidth(i,4) >= stent_quarter & H_Zwidth(i,4) < stent_mid; %MIDDLE
SECTION OF STENT
    C = [C; H_Zwidth(i,:)];
elseif H_Zwidth(i,4) >= stent_mid & H_Zwidth(i,4) < stent_3quarter; %3/4
SECTION OF STENT
    D = [D; H_Zwidth(i,:)];
elseif H_Zwidth(i,4) >= stent_3quarter & H_Zwidth(i,4) < stent_edgeR; %4TH
QUARTER OF STENT
    E = [E; H_Zwidth(i,:)];
elseif H_Zwidth(i,4) >= stent_edgeR; %RIGHT SECTION WHERE THERE IS NO
STENT
    F = [F; H_Zwidth(i,:)];
end
end

% create original stent
stentORIG = [A;B;C;D;E;F];

%create extended stent
stentMOD = [A; B];
for i=1:reps %number of repetitions of internal part to add
    stentMOD=[stentMOD; C; D;];
end
stentMOD = [stentMOD; E; F];%ASSEMBLY OF MODIFIED STENT

```

```

for i=2:length(stentMOD)
    stentMOD(i,4)=stentMOD(i-1,4) + stentMOD(i,15);%WHAT IS THIS!!!!!!...
    %!!!!!!!!!!!!!!!!!!!!!!!!!!!!!!!!!!!!!!!!!!!!!!!!!!!!!!!!!!!!!!!!!!!!!!
end

z_stress_area_stentMOD=0;
for i=1:1:length(stentMOD)%INTEGRATION OF STRESSES OF MODIFIED STENT
ALONG THE Z DIRECTION
    z_stress_area_stentMOD = z_stress_area_stentMOD +
    stentMOD(i,stress_col).*stentMOD(i,15);
end
stent_lengthMOD = sum(stentMOD(:,15));%VALIDATING/VERIFYING MODIFIED
STENT LENGTH
ave_stress = z_stress_area_stentMOD./stent_lengthMOD;
stress_extras = stentMOD; %STRESSES IN MODIFIED STENT
**END PROGRAM
function [ave_surf_stress,total_surf_stress,stent_lengthMOD,G] =
theta_z_integral(radius,radius_def,theta_nodes,angle_tol,reprs,stress_col,stent_length,stre
ss_matrix,centerlineZ)

%INPUT VARIABLES*****
radius;
radius_def;
theta_nodes;
angle_tol;
reprs;
stress_col;
stent_length;

```

```

stress_matrix;
centerlineZ;
%*****

G=[];

for i=1:1:length(theta_nodes);
    user_angle=theta_nodes(i);
    [ave_stress,stent_lengthMOD,stress_extras] =
stress_z_integral(user_angle,angle_tol,reprs,stress_col,stent_length,stress_matrix,centerli
neZ);

    G=[G; stress_extras];
end
total_surf_stress = [0 0 0 0 0 0 0];
total_area = 0;
v = waitbar(0,'Calculating Average Stress Integrals');
for k=1:1:length(G)
    if G(k,12)==0 | G(k,12)==90;
        theta_width = theta_nodes(2)/2*pi/180; %THETA WIDTH IN RADIANS
    else
        theta_width = theta_nodes(2)*pi/180; %THETA WIDTH IN RADIANS
    end
    total_surf_stress = total_surf_stress +
G(k,stress_col)*G(k,14)*theta_width*G(k,15);
    total_area = total_area + G(k,14)*theta_width*G(k,15);
    waitbar(k/(length(G)),v)
end
close(v)

```

```
ave_surf_stress = total_surf_stress./(total_area);
```

```
%G(K,14) IS THE RADIUS IN THE DEFORMED CONFIGURATION!
```

```
**END RPROGRAM
```

APPENDIX B

Effects of Stent Design Parameters on Artery Wall Mechanics

Julian Bedoya, Clark Meyer, Lucas H. Timmins, Michael R. Moreno, James E. Moore
Jr.

Department of Biomedical Engineering
Texas A&M University
3120 TAMU
College Station, TX 77843-3120
(979) 845-3299
(979) 845-4450
jmoorej@tamu.edu

ABSTRACT

A stent is a device designed to restore flow through constricted arteries. These devices are tubular scaffolds with sufficient radial strength to prop the artery open that are delivered to the afflicted region and deployed using minimally invasive techniques. These devices are necessarily oversized, with diameters that are typically 1.05 – 1.40 times that of the artery. The presence of a stent can subject the artery to abnormally high stresses that can trigger adverse biologic responses culminating in restenosis. The primary aim of this investigation was to investigate the effects of varying stent design parameters on the stress field induced in the artery wall using the finite element method. Eight generic stent designs were constructed by varying stent strut spacing, radius of curvature, and ring amplitude. Two strut spacings, three amplitudes, and three different radii of curvature were studied. A non-linear hyper-elastic artery model was employed. Each stent was deployed in the artery model and evaluated using commercially available finite element analysis software. The stent designs employing large strut spacing, a non-zero radius of curvature, and large amplitude induced lower stresses over smaller regions of the artery than other configurations. Conversely, designs employing small strut spacing and small amplitude induced higher stresses over larger regions of the artery. Stent strut spacing was the dominant parameter in this study. All designs employing the small stent strut spacing induced higher stresses over larger areas than designs employing the large strut spacing. Increasing either radius of curvature or strut amplitude resulted in lower stresses. At larger strut spacing, sensitivity to radius of curvature was increased. With the larger strut spacing designs, the effects of varying amplitude could be offset by varying the radius of curvature and vice versa. The finite element method is a formidable tool that can be used to analyze the effects of stent design parameters on stress distributions in the artery wall. Evidence presented herein suggests that stent strut spacing should be as broad as possible. The amplitude parameter should also be maximized. Finally, sharp corners (zero-radius) should be avoided.

Keywords: Stress, Restenosis, Finite Element Analysis

INTRODUCTION

In the past century, cardiovascular diseases have claimed more lives in the United States than any other cause. The total cost associated with cardiovascular diseases in the year 2004 amounted to \$368.4 billion USD [American Heart Association, 2004].

Atherosclerosis is a progressive cardiovascular disease that most commonly afflicts the coronary, carotid and femoral arteries, as well as the abdominal aorta. Characterized by the buildup of atheromatous lesions, as this disease develops, blood flow is constricted and distal tissues become compromised and vulnerable to ischemia. Treatment options include bypass surgery, angioplasty, and stenting.

Implantation of vascular prosthetic devices called stents is a minimally invasive treatment option for patients afflicted with atherosclerosis. The relatively recent application of stents to the cardiovascular realm began in 1969, whereby stents were conceived to improve the outcome of angioplasty procedures. In an early clinical trial of stents (Benestent); the outcome of patients receiving angioplasty alone and the Palmaz-Schatz stent were compared [Versaci et al., 1997]. The study consisted of 516 patients of which 259 underwent angioplasty and stenting and 257 underwent angioplasty alone. It was found that 40% of the patients that underwent angioplasty required a repeat angioplasty due to restenosis. The stent group had a lower restenosis rate of 30%. Consequently, stenting procedures have become increasingly popular, with the market for stents estimated to reach \$5B for 2005 [Leon and Bakhai, 2003].

In efforts to reduce the risk of in-stent restenosis, designers have experimented with a variety of surface treatments and coatings. The most promising advancement for coronary applications has been the relatively recent development of drug-eluting stents (DES). Present DES incorporate anti-proliferative drugs such as Sirolimus (Rapamycin)

and Paclitaxel (Taxol). There is strong clinical evidence that drug eluting stents are a significant improvement to bare metal designs e.g. the RAVEL trial, which reported a 0% binary restenosis rate for patients receiving a Sirolimus eluting stent [Morice et al., 2002]. However, while present drug elution schemes have proven successful in coronary applications, similar success is yet to be observed in other areas, such as peripheral artery disease. Moreover, there is evidence [SIRIUS trial, Moses et al., 2002] that drug eluting stents are ineffective in the prevention of restenosis near the ends of the stent; a region that may be particularly vulnerable due to the compliance mismatch between the artery and the stent.

The recent breakthroughs in DES technology demonstrate the potential benefit of stents as a drug delivery platform. Continued optimization of the architectural and mechanical properties of stents could reduce the adverse effects associated with the stenting process itself. Indeed, it has been shown that stent design (bare metal) is a major risk factor for restenosis [Kastrati et al., 2001]. In a study of more than 4500 patients whose stent implantations were initially successful, binary restenosis (more than 50% reduction in diameter as determined angiographically) was shown to vary from 20% in some stents to nearly 40% in others. Thus, it can be seen that stent design influences treatment outcomes. Alternatively, optimization of design parameters (mechanical properties, geometry, etc.) could further reduce incidences of restenosis. DES, which incorporate conventional stent designs as delivery scaffolds may be inflicting unnecessary damage to the artery wall. While DES can be effective at reducing restenosis, the platforms used to deliver the drugs should still be optimized to reduce the initial trauma imposed by the treatment and facilitate the recovery process. It should also be noted that DES have not proven to be effective at treating peripheral artery disease. Understanding the role of biomechanics in restenosis would aid in the development of stents that are optimized to minimize the initial trauma typically associated with stenting, and facilitate a healthy recovery with minimal neointimal growth.

Computational methods such as finite element modeling provide an excellent means to investigate the mechanical implications of vascular stenting. Two dimensional linear

elastic models have been employed to investigate balloon expansion with stent and artery contact [Rogers et al., 1998]. Results of that study show that high inflation pressures, wide stent-strut spacings, and more compliant balloon materials cause markedly larger surface-contact areas and contact stresses between stent struts. It was determined that stent design and deployment protocols play an important role in stenting outcomes. Migliavacca and colleagues have used FEM in efforts to characterize the mechanical properties of stents. Migliavacca et al. [2002] investigated the influence geometry on the stent behavior. They determined that a stent with a low metal-to-artery surface ratio has a higher radial and longitudinal recoil, but a lesser degree of dogboning. The thickness of the stent also influences these important behaviors. Migliavacca et al. [2005] proposed a computational model that could be used to predict the mechanical behavior of coronary stents. Experiments to examine radial expansion and elastic recoil were conducted. Scanning electron microscopy was used to identify regions of plastic deformation. Results of the computational model were in satisfactory agreement with experiments. Prendergast and colleagues [Lally et al., 2005] have modeled the stent-artery interaction of commercially available stents (NIR – Boston Scientific; S7 – Medtronic AVE) on an idealized stenosed artery. The results indicated that the modular S7 stent design causes lower stress to an atherosclerotic vessel with a localized stenotic lesion compared to the slotted tube NIR design. These results correlated well with the clinical restenosis rates associated with respective stents. The testing methodology is proposed as a pre-clinical testing tool, which could be used to compare and contrast existing stent designs as well as aid in developing novel stent designs. Berry et al. [2002] examined stresses in the artery wall near the ends of the stent, in the region of compliance mismatch between the artery and the stent. It was determined that high stress concentrations are imposed at the ends of the stent, an area particularly susceptible to restenosis. Holzapfel et al. [2002] modeled the balloon expansion of a full 3-dimensional anisotropic diseased artery. It was proposed that this work provided a tool with the potential to improve procedural protocols and design of interventional instruments on a lesion-specific basis, and determine post-angioplasty mechanical environments, which

may be correlated with restenosis responses. In separate investigations, Holzapfel et al. [2004] characterized anisotropic plaque properties and modeled a 3-dimensional stent artery interaction with commercially available stents in a severely diseased iliac artery with 8 different vascular tissues. This work constitutes the most ambitious effort in the literature to model a diseased artery and could provide the basis for lesion specific clinical planning. All of the aforementioned computational studies have provided insight to our understanding of the implications of stenting. However, none of the aforementioned studies have attempted to provide specific stent design criteria for design iteration purposes.

Herein, we propose a computational method to evaluate the influence of specific stent design parameters on artery wall stress. It is acknowledged that the tools and methods developed for this study could be used to evaluate commercially available stents. In order to achieve more general and universally applicable results, we elected to investigate specific design parameters and employed generic stent designs developed using a parameterization algorithm. The stents employed in this investigation were designed parametrically in order to classify and evaluate geometric features commonly seen in commercially available stent designs as deleterious or beneficial to the mechanical environment of a stented artery. Stent geometries were uniquely defined using the following three parameters (Figure 1): strut spacing (h), axial amplitude (f), and strut radius of curvature at the crown junctions (ρ). Thus, the stents studied herein are generic designs consisting of concentric rings of sinusoid-like curves linked by straight bars of varying lengths (Figure 2). Using the finite element method, we tested these designs in a non-diseased, 3-dimensional, thick-walled, non-linear model of stent-artery interaction. The purpose of this investigation was to evaluate the impact of varying specific stent design parameters by assessing the impact of the resulting stent geometry on the stress field induced in the artery wall using the finite element method.

METHODS

Parametric Stent Development

Given the strong clinical evidence that stent design is a critical factor in the development of restenosis; we used the finite element method to provide insight that could potentially improve restenosis rates by extracting biomechanical evidence and applying it to stent design. Rather than evaluating actual stent geometries, we elected to investigate specific design criteria by developing generic stents, varying three specific design parameters. We then compared the resulting designs by evaluating their biomechanical impact in computational models of stented arteries.

The parameters of interest in this investigation were strut spacing (h), axial amplitude (f) and strut radius of curvature at the crown junctions (ρ). A Matlab (MathWorks, Natick, Massachusetts) subroutine was written to create the stent designs automatically. A separate program was then created to automate the generation of three-dimensional stents in Patran (MSC Software, Santa Ana, CA).

All stent designs had a constant wall thickness of 100 microns and an outer radius of 2.475mm, which was 10% larger than the systolic radius of the artery measured at the intima. For the purposes of this investigation, the stent models were labeled according to the design parameters incorporated within them. Names were composed based on the strut **S**pacings, **R**adius of curvature, and **A**mplitude (**SRA**). Spacing took values of either “1” or “2” to identify small or large spacings respectively (1.2 mm vs. 2.4 mm).

Similarly, radius of curvature is given an alphabetic symbol where “A” and “B” represent small and large radius of curvature respectively (0.15 mm vs 0.3 mm). The letter “Z” is used to identify stents with a zero radius of curvature. The amplitude was given a numerical symbol with magnitude proportional to its actual value, where “1” represents 0.6 mm, “2” represents 1.2 mm, and “3” represents 1.8 mm. A summary of the stent designs corresponding parameter values studied herein is given in Table 1.

Characterization of the Artery Model

A porcine common carotid artery was harvested with the aid of the School of Veterinary Medicine at Texas A&M University. Prior to harvest, measurements of the in vivo length of the common carotid were made using a micrometer. Measurements of the axial

length after harvest were also taken to determine the in vivo axial stretch ratio, which was approximately 59%. Additional measurements in the unloaded configuration were made by analyzing images of excised rings measuring approximately 1.5 mm in the axial direction. Once harvested, the artery was placed in phosphate buffered saline solution at 4 °C and transported back to the laboratory. The artery was cleaned and the perivascular tissue was carefully removed taking care not to damage the adventitia, or to puncture the artery.

A modified version of the Computer Aided Vascular Experimentation (CAVE) device described in Humphrey et al. [1993] was used to perform pressure-diameter and force-elongation tests on the artery specimen. The data acquired from these tests were subsequently used to develop a constitutive model. The CAVE device is able to extend, inflate and twist simultaneously a cylindrical specimen while acquiring pertinent load and displacement data in real time. Modifications to the original device include upgraded computer resources, a customized graphical user interface, and customized data processing and analysis capabilities. The system essentially consists of three subsystems. The first system consists of the hardware making up the mechanical components of the device, and is comprised of micro-step motors (Anaheim Automation, CA) and peristaltic pumps (Harvard Apparatus, Cole Parmer). The second and third systems include a non-contacting diameter measuring system consisting of a video dimension analyzer (VDA), and a control and data acquisition system (National Instruments) respectively.

Deformation of the diameter is measured in real time via the aforementioned CCD camera, a video dimension analyzer (VDA), a data acquisition system, a frame grabber board NI-1408 (National Instruments, Austin, TX), and a black and white monitor. Custom software in LabView (National Instruments, Austin, TX) was written to do all the acquiring and processing of data in real time. Data from the mechanical testing was used to determine the constants for the constitutive relation, which took the form:

$$W = C_{10} \cdot (I_1 - 3) + C_{01} \cdot (I_2 - 3) + C_{11} \cdot (I_1 - 3) \cdot (I_2 - 3) + C_{20} \cdot (I_1 - 3)^2 + C_{30} \cdot (I_1 - 3)^3$$

Where, $C_{10} = 25,466$ Pa; $C_{01} = -11,577$ Pa; $C_{11} = -506$ Pa; $C_{20} = 1703$ Pa; and $C_{30} = 1650$ Pa.

Ultimately, the artery model employed herein was characterized as a straight homogeneous isotropic circular cylinder with isotropic non-linear hyperelastic mechanical properties. Due to axisymmetry, only a quarter of the circumference of the artery and stent were modeled to save computational resources.

Application of Boundary Conditions

The finite element method was employed using MSC.Patran to develop the models with MSC.Marc as the non-linear solver (MSC Software). The boundary conditions applied to the boundary value problem included displacement boundary conditions, pressure, and contact. The vessel was stretched in the axial direction by 59% simulating the axial tethering that was measured in vivo. The vessel was then inflated by applying a pressure of 225 mmHg. This pressure dilated the artery enough such that the 10% oversized stent could be “implanted”. The stent was originally positioned outside the artery and then translated in the axial direction such that the stent and artery mid-points along that direction coincided. The pressure was then reduced to systole and subsequently to diastole. Contact occurs before systolic pressure is achieved. The boundary conditions on the stent beyond the translation step, included in-plane deformation for the struts similar to those applied to the artery, and an analytical contact boundary condition. Stent and artery models were constructed incorporating 20-node hexahedral elements. The displacements are interpolated using quadratic Lagrange functions, while the spherical stress is interpolated with a linear function. The contact bodies were defined by C^2 -continuous Non-Uniform Rational B-Splines surfaces (NURBS). The friction model available in MSC.Marc allows for adhesion; thus the “glue” option was used where once a node contacts a patch on the opposite body, the eight nodes on the face of a 20-node hexahedral element and the contacting node have multi-point constraint equations that restrict the future motion to be strictly in the normal direction. Although this friction condition adds non-symmetric stiffness contributions, these were taken to be symmetric.

It was confirmed through additional simulations (not shown) that this assumption led to less than 1% change in the maximum principal Cauchy stress field in the artery.

The computer cluster used to solve this boundary value problem consists of a head node with dual 2.8 Ghz 32-bit processors, 4GB of random access memory (RAM), 4 200GB hard drives with a RAID level 5 as a data back-up, ASUS motherboards with 800 Mhz front side bus speed. The slave nodes (15) consisted of single 2.8 GHz 32-bit processors, 2GB of RAM, 80GB of hard disk space, and ASUS motherboards with 800 Mhz of front side bus speed. The operating system of the computer cluster was RedHat 9. The version of Patran was 2005 release a, and Marc 2005 release a.

Evaluation Methods

Results of the finite element method with MSC.Patran and MSC.Marc are nodal values by default. The resulting table of nodal values can be plotted as a colormap of the model for qualitative analysis. The table can also be evaluated by manipulating the quantitative outputs. Both approaches are used herein to provide a more complete conception of the impact of stent design on stresses in the artery wall.

Seven stented artery models employing distinct variations of the stent parameters outlined above were developed. We tested stent segments that contained four concentric sinusoidal rings attached with straight connector bars oriented parallel to the axis. While each segment is the same diameter, the lengths vary according to the design parameters. It is assumed that the stresses at the ends of these segments (the two outer rings) correspond with those at the ends of the full length stent and that the stresses in the middle section (two inner rings), by symmetry, correspond with the stresses in the region of any two inner rings on a full length stent. Therefore, to compare the segments directly, we multiplied data in the central regions of each stent segment as necessary to model stents of equal length (least common multiple – approximately 30mm) and consequently equal stented area. To compare designs we evaluated the percentage of the

stented region subjected to critical stresses as defined in the methods below. This procedure provided an unbiased comparison relative to axial stent length. Data from 11.25° to 78.75° were used for the quantitative analysis.

Data corresponding to the stress field induced in the artery (at the intima and adventitia) and the radial displacement of the artery were acquired at diastolic and systolic pressures. Tensile circumferential (hoop) stresses were displayed in ranges designed to ease comparison of the colormap plots. Using these data, a percent of the vessel “critically stressed” was calculated according to the groupings. In performing this calculation it was necessary to compensate for the bias in the mesh (see below). The three groupings were defined as follows: Class I critical hoop stresses greater than 545 kPa (15.5 x Law of Laplace value of 35kPa) indicate the highest stresses observed among all stents. Class I critical stresses are regions of maximum stress and therefore regions where an adverse biological response is most likely to occur. Additional classifications are Class II critical hoop stresses greater than 510 kPa (14.5 x Law of Laplace value) and Class III critical hoop stresses greater than 475 kPa (13.5 x Law of Laplace value).

Using this classification system, the percent of the total nodes that correspond with these critical values is calculated as an approximation of the percent of the artery that is “critically stressed”. The purpose of the aforementioned classification system is to facilitate comparison of stent designs. There is no explicit assertion as to the implications or biological response resulting from the stresses within this system. We call them critical stresses based on the assumption that regions of highest stress are most vulnerable. Given this assumption, these Class I stresses would represent regions where adverse response to stenting is most likely to occur.

Convergence Criteria

The mesh convergence study consisted of a three-step process. The first step was to perform mesh refinements in the model of the artery alone – with no contact – observing the variation of maximum principal stress distributions. This was accomplished by

running simulations of a vessel being pressurized to 225 mmHg (30 kPa) and stretched by 59% in the axial direction - the measured in vivo length – while applying the aforementioned symmetry displacement boundary conditions in the xz and yz planes. The criterion used for the isolated vessel mesh convergence – alternatively, mesh independence – was that the maximum principal Cauchy stress field in the lumen and adventitia of the artery had to vary by less than 1%. The second step was to perform refinements in stents themselves by applying a pressure load on the outside of the stent and observing changes in displacements. This involved the application of a pressure load of 450 mmHg (60 kPa) to the outside surface of the stent and observing changes in displacement. The mesh was deemed converged when changes in displacement were less than 1% in radial displacement, which corresponded to stents with an element edge length of 0.10 mm.

The third phase of the mesh convergence was to run stented artery models while increasing the mesh density of the artery until the hoop stresses in the artery varied the least possible. Mesh density in the artery was increased and the stress field on the intima was examined for two cases. At diastolic pressure - intimal area subjected to Class I hoop stresses decreased from 1.1% to 0.7% in case I and from 1.8% to 1.3% in case II; intimal area subjected to Class II hoop stresses decreased from 86.8% to 83.3% in case I and from 86.2% to 83.6% in case II; and intimal area subjected to Class III hoop stresses decreased from 93.1% to 92.4% in case I and 93.1% to 92.6% in case II – using stents 1A1 and 1B1 respectively.

To optimize computational resources a non-uniform mesh of the vessel was constructed. The artery was divided into three regions in the axial direction. Within the end regions, a *one-way bias* was applied with larger elements specified at the ends of the artery and smaller elements specified at the outer edges of the central region. Within the central region a *two-way bias* was applied with larger elements specified in the center and smaller elements specified at the inner edges of the central region. Elements gradually change in length (along the axial direction) in transition from the larger specified elements to the smaller specified elements (Figure 3). This results in a high mesh density

in the region of the smaller elements; in this case, at the interfaces between the central region and the two outer regions.

RESULTS

Results of this finite element analysis of stented arteries suggest that stents with small strut spacing and low amplitude induce higher stresses in the artery than other designs. These designs e.g. stents 1Z1, 1A1, and 1B1, imposed Class I stresses (greater than 545 kPa) on greater than 4%, 1%, and 2% of the intimal area respectively. These stresses were predominantly focused near the apex of the struts at the ends of the stent. All other designs imposed Class I stresses on less than 1% of the intima. The 1Z1, 1A1, and 1B1 designs induced Class II (greater than 510 kPa) and Class III (greater than 475 kPa) stresses on over 86% and 93% of the intimal area respectively. Note that the critical stress distributions associated with the designs incorporating small strut spacing with low amplitude were relatively diffuse; whereas the critical stress distributions associated with designs incorporating large strut spacing with large amplitude were focused near the struts (Figure 4).

Stents with large strut spacing, a moderate radius of curvature, and large amplitude imposed lower circumferential stresses than all other designs in this study. These designs e.g. 2A3, and 2B3, did not induce Class I stresses and subjected smaller regions of the artery to Class II and Class III stresses. Class II levels for stents 2A3 and 2B3 were 1% or less; Class III levels for these designs were 26% and 15% respectively (Figure 5).

The aforementioned general observations are supported by inspection of the effects of the individual geometric parameters on critical stress distributions. Increasing stent strut spacing results in lower hoop stresses in the artery wall. To examine the effects of increasing the stent strut spacing parameter, we compare stent 1B2 with stent 2B2. The increase in strut spacing from 1.2mm to 2.4mm results in a reduction in area subjected to Class II stresses from 60% to 14%. The area exposed to Class III stresses changes from 92% to 67% with increased strut spacing. In fact, all stents with the 1.2mm spacing imposed Class II stresses over more than 60% of the intimal area while all stents with

the 2.4mm spacing imposed Class II stresses over less than 26% of the intima. (Figure 6, Table 2).

Increasing the amplitude parameter also resulted in lower circumferential stresses. This can be seen in the comparison between stents 1B1 and 1B2. Both of these stents have the small strut spacing and large radius of curvature. The increase in amplitude from 0.6mm (1B1) to 1.2mm (1B2) results in a change in Class III stresses from 2% to <<1%.

However, the Class II critical stresses differ considerably, 86% vs 60%. Further comparison using stents 2B2 and 2B3 – stents with the same radius of curvature as the 1B1 and 1B2 designs, but with larger strut spacing - provide similar evidence. In this comparison, the increase in amplitude from 1.2mm (2B2) to 1.8mm (2B3) results in a decrease in Class II stresses from 14% to <<1%, and a decrease in Class III stresses from 67% to 15%.

As with the strut spacing and amplitude, increasing the radius of curvature parameter also resulted in lower critical stress distributions. Designs incorporating large strut spacing with large amplitude i.e. the 2A3, 2B3, and 2Z3, were most sensitive to changes in this parameter. Here it can be seen that increasing the radius of curvature from 0mm (2Z3) to 0.15mm (2A3) results in a decrease in Class II stresses from 25% to <1%. Class III stresses decrease from 71% to 26% under the same conditions. A further increase in radius of curvature from 0.15mm (2A3) to 0.3mm (2B3) results in a further decrease in Class III stresses from 26% to 15%. Class II stresses under these conditions decrease from 1% to <<1%. Note that while the small strut spacing with small amplitude designs were not as sensitive to changes in radius; the zero-radius design induced higher Class I stresses than the non-zero-radius designs – greater than 4% versus approximately 2% or less.

Though strut spacing is clearly the dominant parameter, the effects of amplitude and radius of curvature, were in some cases offsetting. For example, stents 1Z1, 1A1, and 1B1 (small spacing, small amplitude) induced Class II stresses on over 86% of the intimal area, while stent 1B2 (small spacing, larger amplitude) imposed Class II stresses on less than 61% of the intima. When the small strut spacing is combined with zero-

radius of curvature the stress inducing effects of decreased radius of curvature are apparent at Class I level where the 1Z1 design imposed these high stresses over twice the area of any other design (4% vs 2%). While the effects of strut spacing could not be overcome by any other parameter in this study; the effects of amplitude and radius of curvature were similar at large strut spacing and thus could be offset. For example, consider the comparison between stent 2Z3 (zero radius, largest amplitude) and stent 2B2 (largest radius, smaller amplitude). The impact on Class III stresses differs by only 4% between these designs. The increased radius in the 2B2 design is sufficient to compensate for the lower amplitude; alternatively the larger amplitude in the 2Z3 design is sufficient to compensate for the lack of curvature. To further compare the effects of radius versus amplitude we systematically compare all stents with the large strut spacing. Stents 2B3 and 2B2 differ only in amplitude. The decrease in amplitude results in an increase in Class II stresses from $\ll 1\%$ to 14% and an increase in Class III stresses from 15% to 67%. Similarly, stents 2B3 and 2A3 differ only by radius. The decreased radius of the 2A3 design results in an increase in the Class II stresses from $\ll 1\%$ to $< 1\%$; and an increase in Class III stresses from 15% to 26%. This suggests that amplitude may have a stronger influence on the stress field than radius of curvature within the constraints of this study. However, if we further reduce the radius i.e. if we compare 2B3 with 2Z3, the Class II stresses increase from $\ll 1\%$ to greater than 25%; Class III stresses increase from 15% to over 71% respectively.

In general, stents that imposed higher stress on the artery wall also produced a larger final artery diameter, although the differences among designs studied herein were less than $90\ \mu\text{m}$. Within each model the greatest displacements occurred at the stent struts (Figure 7). The displacement associated with the region between the struts was typically within $60\ \mu\text{m}$ of the displacement at the struts. As implied above the greatest radial displacement was achieved with the 1A1, 1B1, and 1Z1 designs. Conversely, the lowest displacements were observed in the 2A3 and 2B3 designs near the ends of the stent. Finally, it can be inferred from the displacement maps that the stents with larger amplitude exhibit compliance matching behavior, i.e. these designs provide a smoother

compliance transition between the stented and unstented regions of the artery. Furthermore, these designs breathe; they exhibit a higher cyclic deflection through the cardiac cycle. The resulting change in displacement is approximately $40\mu\text{m}$ as compared to the $10\mu\text{m}$ deflections observed in the small strut spacing with small amplitude designs (data not shown).

DISCUSSION

The purpose of this investigation was to assess the effects of varying stent design parameters on artery wall stress using the finite element method. It is assumed that regions of high stress correspond with regions most likely to experience an adverse reaction. There is evidence that showed that medial fracture caused by stent implantation can invigorate a cascade of events culminating in restenosis [Farb et al. 2002]. Thus, in determining the most favorable stent configuration we consider first and foremost the reduction of stress in the artery wall. Subsequently, we consider radial displacement and cyclic deflection.

The design incorporating the large strut spacing, large radius of curvature and large amplitude (2B3) was superior to the other designs studied herein. With this design, critical stresses were imposed on less than 16% of the intima. These stresses were focused near the struts with some diffusion in the center of the stented region. Radial displacement of the artery between the struts at diastolic pressure was within $90\mu\text{m}$ of the maximum observed among all stents. This design also exhibited the greatest cyclic deflection ($40\mu\text{m}$) and a gradual transition in compliance at the ends of the stent.

Reducing the amplitude of the 2B3 design, e.g. 2B2, increases the maximum displacement but also increases the critical stress levels considerably. Whereas, increasing the radius of curvature of the 2B3 design, e.g. stent 2A3, increases the region of maximum displacement while maintaining a low stress distribution. Critical stresses in the 2A3 model covered only 26% of the intima. Thus, stent 2A3 is also an acceptable design for the reduction of stress and could be more favorable with respect to radial displacement. Further reduction of the radius of curvature to zero, e.g. 2Z3, only slightly

increases the area of maximum displacement and greatly increases critical stresses. Therefore, it is concluded that stents 2B3 and 2A3 are the best designs presented in this study.

Strut spacing is the most important design parameter studied in this investigation. All stents with the smaller strut spacing induced higher stresses over larger regions of the artery than any of the large strut spacing designs. The difference between the displacements achieved with the larger strut spacing and the smaller strut spacing were less than $90\mu\text{m}$; thus the gains in displacement observed in the small strut spacing designs are not worth the expense of the stresses induced. In general, small strut spacing results in high stresses that are diffuse, distributed across the entire stented region; whereas large strut spacing results in lower stresses that are localized near the stent struts. Moreover, the small strut spacing designs incorporating small amplitude exhibited less than $10\mu\text{m}$ of cyclic deflection. It has been shown that the production of E-selectin – a surface expressed molecule that heightens monocyte attachment – is reduced in response to decreased cyclic flexing [Vorp et al., 1999]. Re-endothelialization can also be hindered by stent induced reductions in cyclic stretch [Sumpio et al., 1987; Sumpio et al., 1988].

Increasing stent amplitude lowers stresses and provides a gradual transition in compliance from the central stented region to the ends of the stent. The highest stresses observed in this study were primarily located near the ends of the stents incorporating small strut spacing and small amplitude i.e. stents 1Z1, 1A1, and 1B1. Increasing the amplitude of these designs, e.g. stent 1B2, reduced the area exposed to high critical stresses and reduced the stiffness at the ends of the stent. The larger amplitude designs induced lower stresses throughout with the critical stresses appearing more concentrated in the central stented region and sparse near the ends of the stent. An increase in compliance near the ends of the stent is also evident in these designs as the lowest displacements occurred in these regions. Increased amplitude also contributes to an increase in cyclic deflection.

Sharp corners or zero-radius-of-curvature designs increase stresses throughout the stented region. In general, increasing the radius of curvature reduces stress. However, the area exposed to maximum displacement is also reduced. The highest stresses observed, irrespective of strut spacing, were in the models incorporating a zero radius. This includes stent 1Z1 among the small strut spacing designs and 2Z3 among the large strut spacing designs. Though the large strut spacing with large amplitude designs were generally better at reducing stress, the zero-radius design (2Z3) failed to reduce stresses in a comparable manner. The large strut spacing design incorporating the medium amplitude (2B2) actually induced similar critical stresses but over smaller areas and provided greater displacement than the zero-radius design with larger amplitude. This suggests that it may be better to reduce amplitude rather than radius.

Stent design involves many considerations including manufacturing, deployment, biocompatibility, and mechanical concerns. These considerations can constrain potential device developments. Based on our findings, a stent should have large axial strut spacing, large amplitude, and a large radius of curvature. However, such a design could provide heretofore unseen difficulty to manufacture or deploy. For example, self-expanding designs that are laser cut in the collapsed configuration are limited in the parameter configurations that are possible i.e. extending one parameter may inhibit another. Additional structural concerns include sufficient radial strength, the need to tack up intimal flaps, and fatigue behavior. In depth analysis of these design challenges is necessarily beyond the scope of this work, though it is acknowledged that the designs presented herein may be limited in their applicability.

A complete analysis of stent design effectiveness requires empirical evidence (e.g. clinical trials, animal studies), and an understanding of the mechanobiology of stented arteries. While the use of non-diseased model is not realistic from a clinical perspective, given the unique nature of a given lesion (soft lipid pool versus hard calcifications), the use of a healthy rather than a diseased artery model is preferred for this type of study. Incorporation of lesion properties would add specificity, perhaps limiting the applicability of this work. Additionally, arterial response to these stresses and potential

structural damage have not been specifically studied. Attempts to use computational modeling to investigate the development of neointimal hyperplasia have been initiated but are as yet necessarily simplified [Lally et al. 2005]. Nonetheless, advances in these areas represent important steps toward improving the ability to develop more informative models.

Since we used a generic model of stent design, the results of this study may have limited applicability to the myriad of stent designs either on the market or in development. Nonetheless, the premises outlined herein, e.g. avoid sharp corners, increase axial spacing, etc., can be applied to most designs. The material properties of the stent were characterized using a linearly elastic approximation, namely Young's modulus, for stainless steel. The use of other stent materials such as Nitinol requires more sophisticated modeling.

A non-linear hyperelastic constitutive model was employed to characterize arterial behavior. Roach and Burton [1957] showed that elastin and collagen were the primary contributors to the nonlinear characteristic behavior of arteries. Elastin is a highly extensible protein that can exhibit linear elastic behavior although with finite deformations. Collagen is much stiffer and is thought to prevent acute overdilation in arteries [Humphrey, 2002]. The artery model was further characterized as incompressible, homogeneous, and isotropic. Arteries are anisotropic and composed of heterogeneous distributions of constituents that possess a variety of mechanical properties. For the purposes of this comparative study, the simplified homogeneous model was sufficient to elucidate differences in stent design based on stresses imparted to the artery. In addition, residual stresses were not included in this study. It is assumed that the stresses imparted by the stent are high enough that inclusion of residual stresses would not alter our general conclusions. Finally, only one degree of overexpansion was analyzed in this study and therefore we may only speculate how varying the stent oversize would affect our results. While the absolute values of stress may be affected, it is expected that the relative rankings of the stents would be the same.

Due to the high demand on computational resources, strict convergence criteria could not be applied to all models tested. The results of the convergence tests performed on two of the eight models developed were compared as described in the methods section above. These models showed similar trends and results at the increased mesh density, with the largest differences in the more refined mesh occurring for Class II stresses (86.8% to 83.3% and 86.2 to 83.6%). Based on these observations, it is believed that the effects of mesh density are not significant in comparing the models using the techniques employed in this study. A more spatially refined study comparing artery wall stresses on a point-by-point basis would require greater mesh resolution and thus much greater computational resources.

CONCLUSIONS

The finite element method is a formidable tool that can be used to analyze the effects of stent design parameters on stress distributions in the artery wall. In this study, the variation of three design parameters was investigated. It was determined stent strut spacing should be as broad as possible. The amplitude parameter should also be maximized. Finally sharp corners (zero-radius) should be avoided. The biologic response to the stress field induced by the stent is important to the success of the stenting procedure. Therefore, the ability to characterize the potential stress field induced by a particular design is critical to the stent design iteration process.

It is assumed that regions of high stress or high stress gradients are the most vulnerable to adverse biologic response. It is therefore concluded that stent 2B3 is the best overall stent design in the population of stents analyzed in this study. This stent is characterized by a large strut spacing, large radius of curvature, and large amplitude. It produced the lowest stresses, substantial radial displacement, compliance matching behavior, and substantial cyclic deflection. These features suggest that stent 2B3 is the best candidate for minimizing the risk of restenosis. In contrast, stents characterized by tight strut spacing, zero radius of curvature, and low amplitude, may subject the artery to unnecessarily high stresses, allow little cyclic deflection, and impose a substantial

compliance mismatch near the ends of the stent, a region particularly vulnerable to restenosis.

REFERENCES

AmericanHeartAssociation (2004). "Heart and Stroke Statistical Update: 2004 Update."

Versaci, F., A. Gaspardone, et al. (1997). "A comparison of coronary-artery stenting with angioplasty for isolated stenosis of the proximal left anterior descending coronary artery." N Engl J Med **336**(12): 817-22.

Leon, M. B. and A. Bakhai (2003). "Drug-eluting stents and glycoprotein IIb/IIIa inhibitors: combination therapy for the future." Am Heart J **146**(4 Suppl): S13-7.

Morice, M. C., P. W. Serruys, et al. (2002). "A randomized comparison of a sirolimus-eluting stent with a standard stent for coronary revascularization." N Engl J Med **346**(23): 1773-80.

Moses, J. W., N. Kipshidze, et al. (2002). "Perspectives of drug-eluting stents: the next revolution." Am J Cardiovasc Drugs **2**(3): 163-72.

Kastrati, A., J. Mehilli, et al. (2001). "Restenosis after coronary placement of various stent types." Am J Cardiol **87**(1): 34-9.

Rogers, C., D. Y. Tseng, et al. (1999). "Balloon-artery interactions during stent placement: a finite element analysis approach to pressure, compliance, and stent design as contributors to vascular injury." Circ Res **84**(4): 378-83.

Lally, C., F. Dolan, et al. (2005). "Cardiovascular stent design and vessel stresses: a finite element analysis." J Biomech **38**(8): 1574-81.

Berry, J.L., E. Manoach, C. Mekkaoui, P.H. Rolland, J.E. Moore Jr., and A. Rachev, Hemodynamics and Wall Mechanics of a Compliance Matching Stent: In Vitro and In Vivo Analysis, *Journal of Vascular Interventional Radiology*, 13, p. 97-105, 2002.

Holzapfel, G. A., M. Stadler, et al. (2002). "A layer-specific three-dimensional model for the simulation of balloon angioplasty using magnetic resonance imaging and mechanical testing." Ann Biomed Eng **30**(6): 753-67.

Holzapfel, G. A., G. Sommer, et al. (2004). "Anisotropic mechanical properties of tissue components in human atherosclerotic plaques." J Biomech Eng **126**(5): 657-65.

Humphrey, J. D., T. Kang, et al. (1993). "Computer-aided vascular experimentation: a new electromechanical test system." Ann Biomed Eng **21**(1): 33-43.

- Farb, A., D. K. Weber, et al. (2002). "Morphological predictors of restenosis after coronary stenting in humans." Circulation **105**(25): 2974-80.
- Vorp, D. A., D. G. Peters, et al. (1999). "Gene expression is altered in perfused arterial segments exposed to cyclic flexure ex vivo." Ann Biomed Eng **27**(3): 366-71.
- Sumpio, B. E., A. J. Banes, et al. (1987). "Mechanical stress stimulates aortic endothelial cells to proliferate." J Vasc Surg **6**(3): 252-6.
- Sumpio, B. E., A. J. Banes, et al. (1988). "Alterations in aortic endothelial cell morphology and cytoskeletal protein synthesis during cyclic tensional deformation." J Vasc Surg **7**(1): 130-8.
- Lally, C. (2004). "Proceedings of IUTAM Symposium on Mechanics of Biological Tissue"
- Roach, M. R. and A. C. Burton (1957). "The reason for the shape of the distensibility curves of arteries." Can J Biochem Physiol **35**(8): 681-90.
- Humphrey, J. (2002). Cardiovascular Solid Mechanics Cells, Tissues, and Organs. New York, New York, Springer-Verlag New York, Inc.

ACKNOWLEDGEMENTS

The authors gratefully acknowledge the assistance of Drs. Jay Humphrey and John Criscione. This work was supported by NIH grant R01 EB000115.

TABLE AND FIGURE LEGENDS

Table 1. Design Parameters and Labeling Scheme. Generic stent designs were developed by varying three design parameters. Stents were identified by their design parameters or ‘SRA’ – Strut Spacing, Radius of curvature, and Amplitude. Possible values for each parameter were: strut spacing – ‘1’ or ‘2’ denoting a spacing 1.2mm or 2.4mm respectively; radius of curvature – ‘Z’, ‘A’, or ‘B’ denoting a radius of curvature of 0mm, 0.15mm, or 0.30mm respectively; and amplitude – ‘1’, ‘2’, or ‘3’ denoting an amplitude of 0.6mm, 1.2mm, or 1.8mm respectively. For example, stent 2Z3 had a strut spacing of 2.4mm with no radius of curvature (sharp corner) and amplitude of 1.8mm.

Table 2. Critical Stress Distribution. Class I stress distributions were highest in designs incorporating small strut spacing with small amplitude. All stents with the small strut spacing induced greater Class II stress distributions than stents with larger spacing. Stents with larger strut spacing, non-zero radius of curvature and large amplitude induced lower critical stress distributions than all other designs. Though the effects of strut spacing were clearly dominant the effects of radius of curvature and amplitude could offset e.g. 2Z3 versus 2B2.

Figure 1. Design Parameters. Generic stent showing the three parameters of interest: h is connector bar length (or strut spacing), ρ is the radius of curvature at the crown junctions, and f is the axial amplitude. These three parameters were varied to test their effects on artery wall stress.

Figure 2. Stent Designs. Renderings of the generic stent designs developed for this study. All stents were constructed by varying the three design parameters described herein.

Figure 3. Artery Model Mesh. The artery mesh developed for this study is non-uniform with higher density in the regions of interest. The artery was divided into three regions in the axial direction. Within the end regions, a one-way bias was applied with larger elements specified at the ends of the artery and smaller elements specified at the outer edges of the central region. Within the central region a two-way bias was applied with larger elements specified in the center and smaller elements specified at the inner edges of the central region. The stent model was placed completely within the central region.

Figure 4. Hoop Stress Distribution. For quantitative analysis three critical stress thresholds were established. Class I stresses, denoted by red in this illustration, are defined as stresses in excess of 545kPa. Class II stresses are defined as stresses in excess of 510kPa and are denoted by orange and red in this illustration. Class III stresses are defined as stresses in excess of 475kPa and are denoted by red, orange, and yellow-

orange in this illustration. Note that stent designs with small strut spacing and small amplitude induced more critical stresses in diffuse areas than those with large strut spacing and amplitude.

Figure 5. Binary Plot of Class III Critical Stress Distribution. Designs incorporating large strut spacing with large amplitude and non-zero radius of curvature (2A3 and 2B3) induced Class III stresses over less than 26% of the intima. Note also, the lower distribution near the ends of the stents with these designs, which exhibit gradual transition in compliance.

Figure 6. Binary Plot of Class II Critical Stress Distribution. The small strut spacing with low amplitude designs induced Class II stresses over more than 86% of the intimal area. Note the diffuse distribution with the low amplitude designs (1Z1, 1A1, and 1B1), versus the more localized distribution with the larger amplitude design (1B2).

Figure 7. Radial Displacement Map. Stent designs that induce the highest stresses also provide the greatest radial displacement in the stented region. However, differences in radial displacement between designs are small, approximately $90\mu\text{m}$. Note that the large spacing large amplitude designs exhibit greater compliance at the ends of the stent. These displacements are referenced from the unstented artery at diastolic pressure.

Stent (SRA)	Strut Spacing - h (mm)	Radius of Curvature - ρ (mm)	Axial Amplitude - f (mm)
1Z1	1.2	0	0.6
1A1	1.2	0.15	0.6
1B1	1.2	0.3	0.6
1B2	1.2	0.3	1.2
2Z3	2.4	0	1.8
2A3	2.4	0.15	1.8
2B2	2.4	0.3	1.2
2B3	2.4	0.3	1.8

Table 1. Stent Design Parameters and Labeling Scheme. Generic stent designs were developed by varying three design parameters. Stents were identified by their design parameters or ‘SRA’ – Strut Spacing, Radius of curvature, and Amplitude. Possible values for each parameter were: strut spacing – ‘1’ or ‘2’ denoting a spacing 1.2mm or 2.4mm respectively; radius of curvature – ‘Z’, ‘A’, or ‘B’ denoting a radius of curvature of 0mm, 0.15mm, or 0.30mm respectively; and amplitude – ‘1’, ‘2’, or ‘3’ denoting an amplitude of 0.6mm, 1.2mm, or 1.8mm respectively. For example, stent 2Z3 had a strut spacing of 2.4mm with no radius of curvature (sharp corner) and amplitude of 1.8mm.

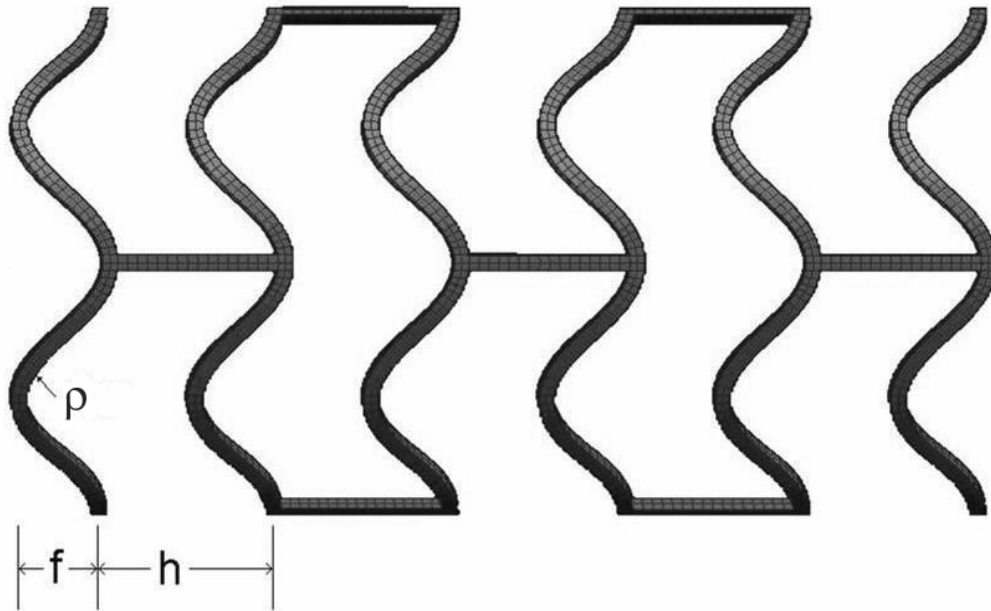


Figure 1. Stent Design Parameters. Generic stent showing the three parameters of interest: h is connector bar length (or strut spacing), ρ is the radius of curvature at the crown junctions, and f is the axial amplitude. These three parameters were varied to test their effects on artery wall stress.

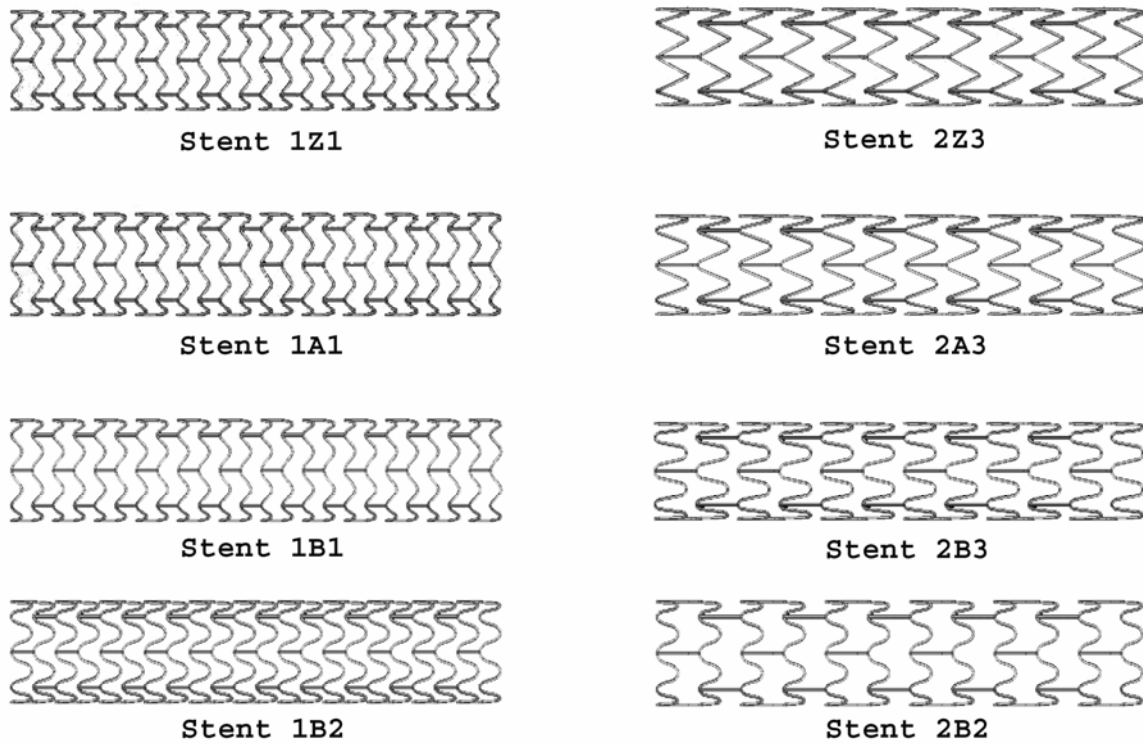


Figure 2. Stent Designs. Renderings of the generic stent designs developed for this study. All stents were constructed by varying the three design parameters described herein.

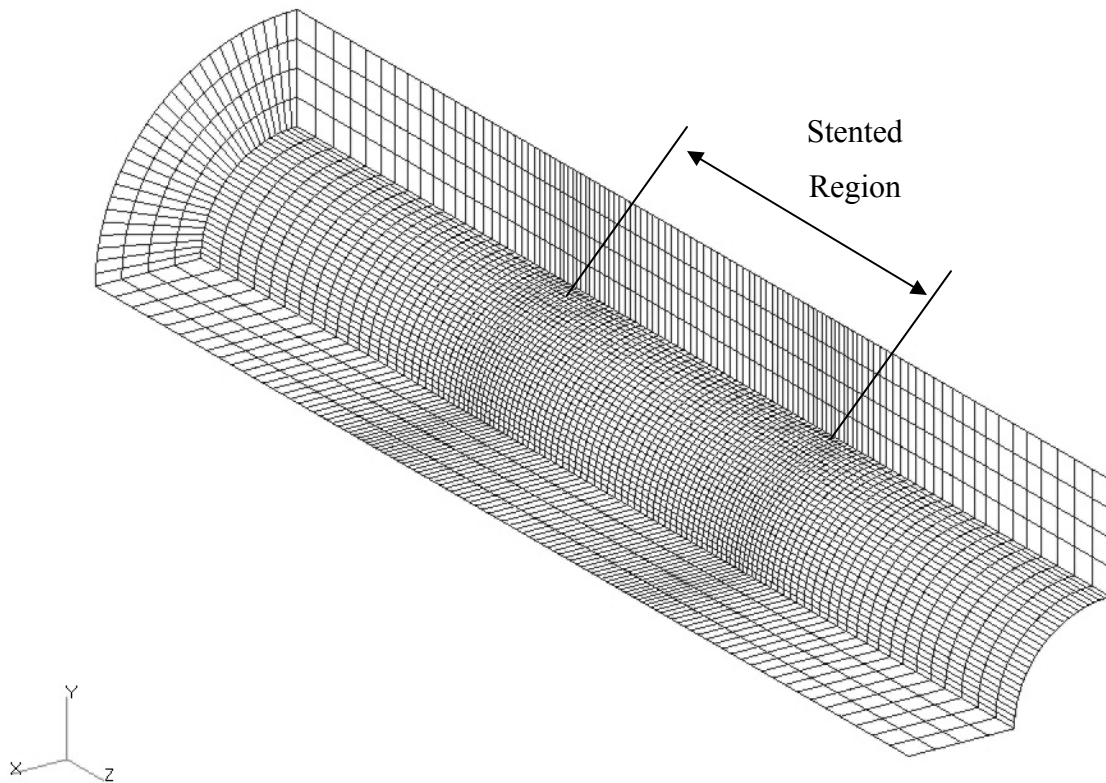


Figure 3. Artery Model Mesh. The artery mesh developed for this study is non-uniform with higher density in the regions of interest. The artery was divided into three regions in the axial direction. Within the end regions, a one-way bias was applied with larger elements specified at the ends of the artery and smaller elements specified at the outer edges of the central region. Within the central region a two-way bias was applied with larger elements specified in the center and smaller elements specified at the inner edges of the central region. The stent model was placed completely within the central region.

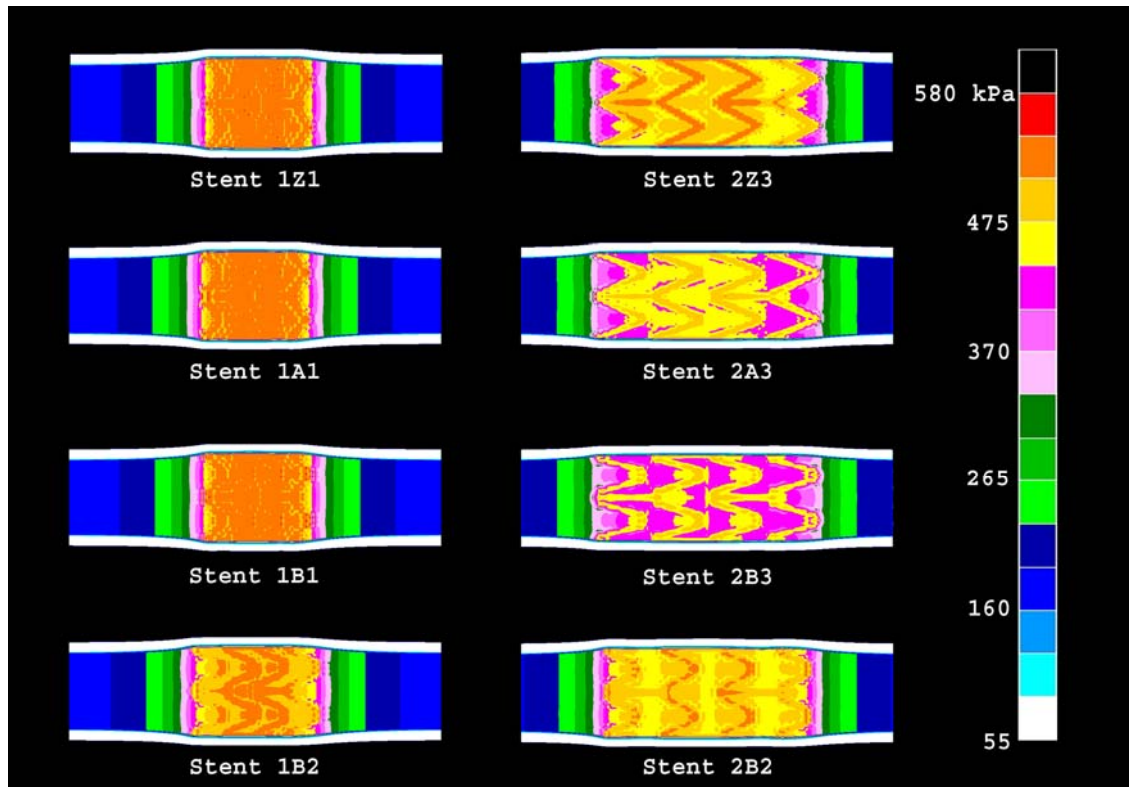


Figure 4. Hoop Stress Distribution. For quantitative analysis three critical stress thresholds were established. Class I stresses, denoted by red in this illustration, are defined as stresses in excess of 545kPa. Class II stresses are defined as stresses in excess of 510kPa and are denoted by orange and red in this illustration. Class III stresses are defined as stresses in excess of 475kPa and are denoted by red, orange, and yellow-orange in this illustration. Note that stent designs with small strut spacing and small amplitude induced more critical stresses in diffuse areas than those with large strut spacing and amplitude.

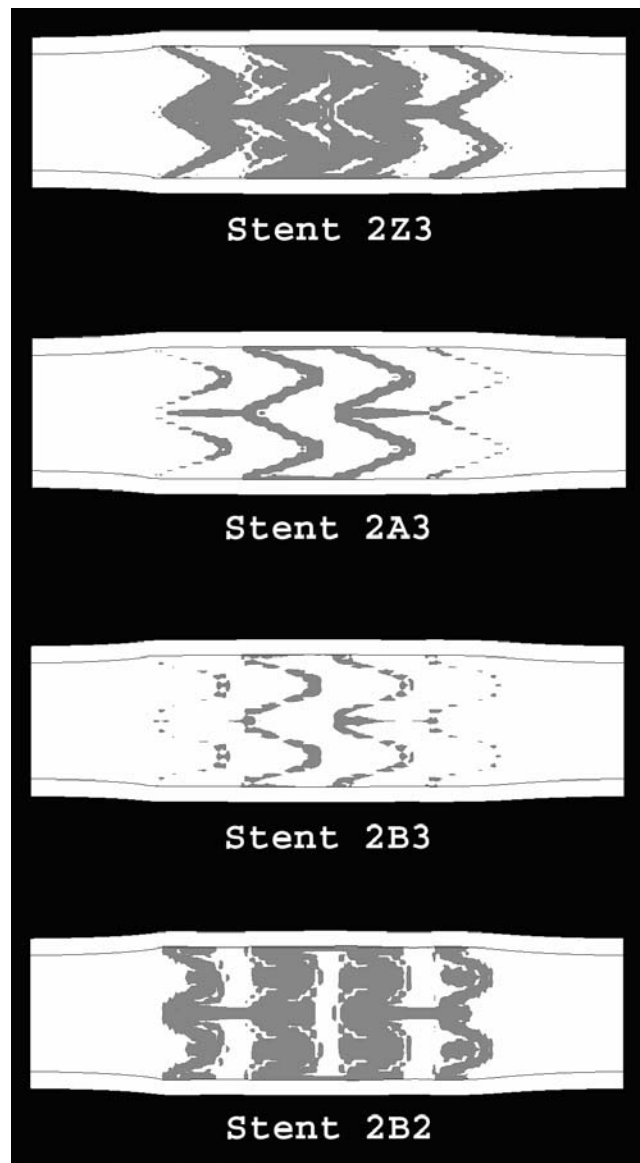


Figure 5. Binary Plot of Class III Critical Stress Distribution. Designs incorporating large strut spacing with large amplitude and non-zero radius of curvature (2A3 and 2B3) induced Class III stresses over less than 26% of the intima. Note also, the lower distribution near the ends of the stents with these designs, which exhibit gradual transition in compliance.

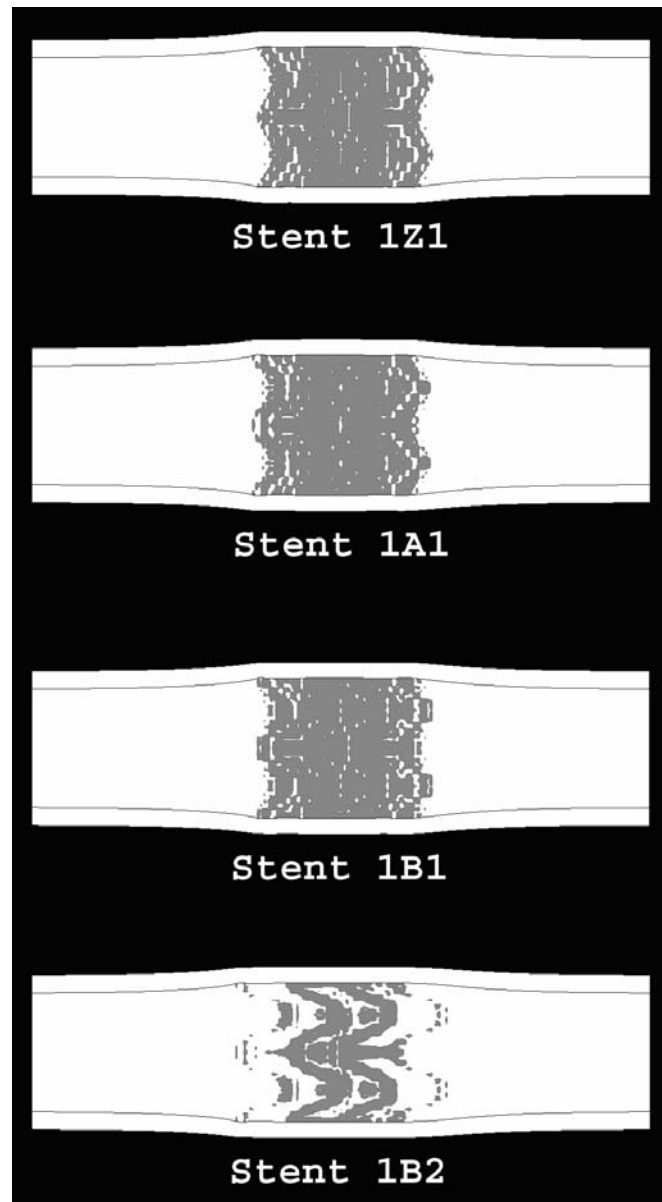


Figure 6. Binary Plot of Class II Critical Stress Distribution. The small strut spacing with low amplitude designs induced Class II stresses over more than 86% of the intimal area. Note the diffuse distribution with the low amplitude designs (1Z1, 1A1, and 1B1), versus the more localized distribution with the larger amplitude design (1B2).





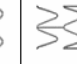



Hoop Stress Comparison - % Intimal Area Critically Stressed								
Stent (SRA)	1Z1	1A1	1B1	1B2	2A3	2Z3	2B2	2B3
Image								
Class I Stress > 545 kPa (15.5 x Laplace)	4%	1%	2%	<< 1%	0%	<< 1%	<< 1%	0%
Class II Stress > 510 kPa (14.5 x Laplace)	86%	87%	86%	60%	< 1%	25%	14%	<< 1%
Class III Stress > 475 kPa (13.5 x Laplace)	93%	93%	93%	92%	26%	71%	67%	15%

Table 2. Critical Stress Distribution. Class I stress distributions were highest in designs incorporating small strut spacing with small amplitude. All stents with the small strut spacing induced greater Class II stress distributions than stents with larger spacing. Stents with larger strut spacing, non-zero radius of curvature and large amplitude induced lower critical stress distributions than all other designs. Though the effects of strut spacing were clearly dominant the effects of radius of curvature and amplitude could offset e.g. 2Z3 versus 2B2.

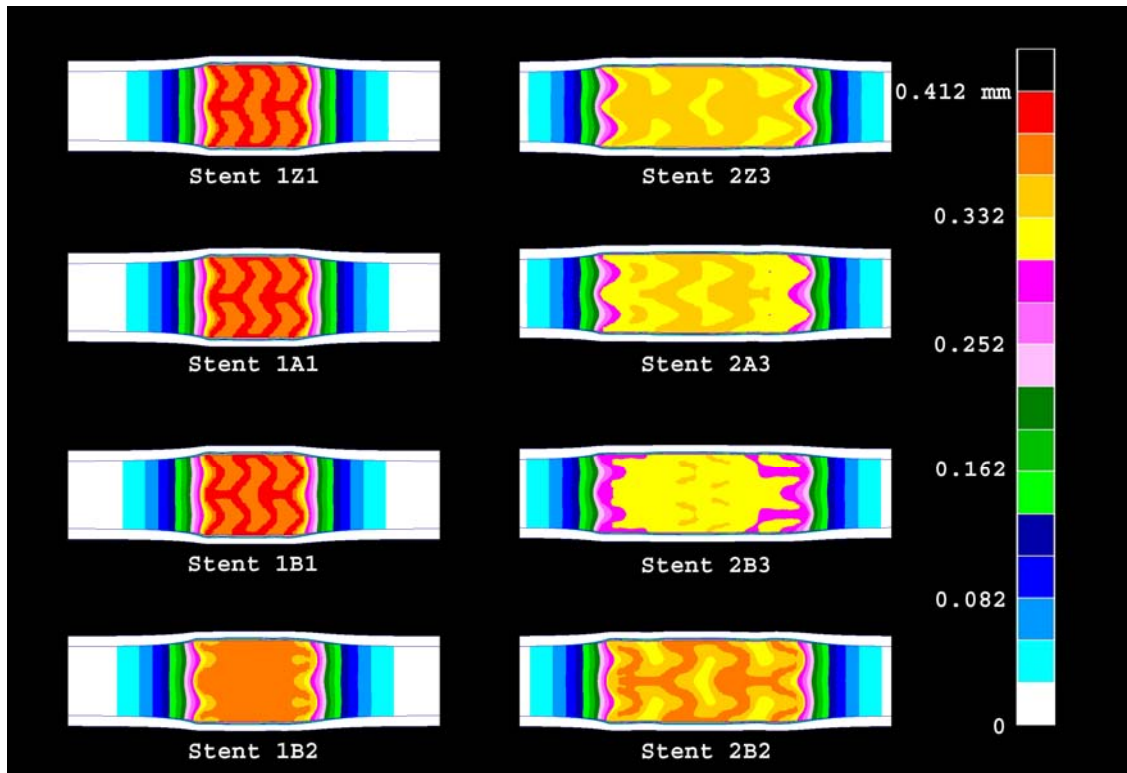


Figure 7. Radial Displacement Map. Stent designs that induce the highest stresses also provide the greatest radial displacement in the stented region. However, differences in radial displacement between designs are small, approximately $90\mu\text{m}$. Note that the large spacing large amplitude designs exhibit greater compliance at the ends of the stent. These displacements are referenced from the unstented artery at diastolic pressure.

VITA

Jose Julian Bedoya Cervera received his Bachelor of Science degree in mechanical engineering from Florida International University in Miami, FL in 2002. He entered the biomedical engineering department at Texas A&M University in August 2003. Mr. Bedoya received his Master of Science degree in May 2006. Currently, Mr. Bedoya is working as an analyst at Stress Engineering Services, Inc. in Houston, TX, doing oil and gas industry related work.

Mr. Bedoya can be reached at Stress Engineering Services, Inc., 13800 Westfair East Drive, Houston, TX, 77040. His e-mail address is Julian.Bedoya@stress.com, and his phone number is 281 955 2900.